INFORMATION TO USERS

This dissertation was produced from a microfilm copy of the original document. While the most advanced technological means to photograph and reproduce this document have been used, the quality is heavily dependent upon the quality of the original submitted.

The following explanation of techniques is provided to help you understand markings or patterns which may appear on this reproduction.

1. The sign or "target" for pages apparently lacking from the document photographed is "Missing Page(s)". If it was possible to obtain the missing page(s) or section, they are spliced into the film along with adjacent pages. This may have necessitated cutting thru an image and duplicating adjacent pages to insure you complete continuity.

2. When an image on the film is obliterated with a large round black mark, it is an indication that the photographer suspected that the copy may have moved during exposure and thus cause a blurred image. You will find a good image of the page in the adjacent frame.

3. When a map, drawing or chart, etc., was part of the material being photographed the photographer followed a definite method in "sectioning" the material. It is customary to begin photoing at the upper left hand corner of a large sheet and to continue photoing from left to right in equal sections with a small overlap. If necessary, sectioning is continued again – beginning below the first row and continuing on until complete.

4. The majority of users indicate that the textual content is of greatest value, however, a somewhat higher quality reproduction could be made from "photographs" if essential to the understanding of the dissertation. Silver prints of "photographs" may be ordered at additional charge by writing the Order Department, giving the catalog number, title, author and specific pages you wish reproduced.

University Microfilms

300 North Zeeb Road
Ann Arbor, Michigan 48106

A Xerox Education Company

THE UNIVERSITY OF OKLAHOMA

GRADUATE COLLEGE

DEVELOPMENT OF AN URBAN-RURAL ECOSYSTEM MODEL

A DISSERTATION

SUBMITTED TO THE GRADUATE FACULTY

in partial fulfillment of the requirements for the

degree of

DOCTOR OF PHILOSOPHY

BY

WILLIAM J. PARTON, JR.

Norman, Oklahoma

1972

DEVELOPMENT OF AN URBAN-RURAL ECOSYSTEM MODEL

APPROVED BY

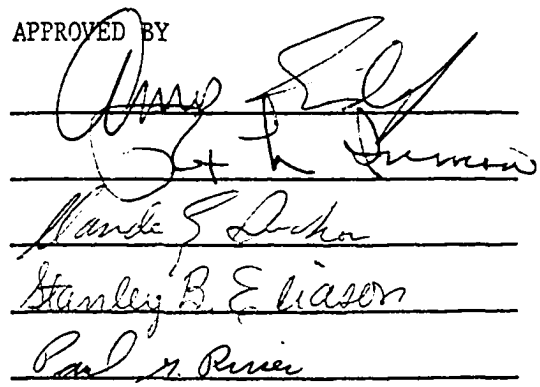

DISSERTATION COMMITTEE

ACKNOWLEDGMENTS

I wish to thank my advisor, Dr. Amos Eddy, for his suggestions and help in all phases of this study. I am also indebted to Mr. Martin Yerg for his numerous suggestions and critical proofreading of the manuscript. I would also like to thank Mrs. Margaret Eddy and Mrs. Molly Jameson for their work in managing the publication of this manuscript.

I am grateful to the National Center for Atmospheric Research (NCAR) for providing the computer time that was used to develop the model. I would also like to thank the Environmental Protection Agency (EPA) for providing the financial support that was used to publish this document.

TABLE OF CONTENTS

LIST OF TABLES

LIST OF ILLUSTRATIONS

DEVELOPMENT OF AN URBAN-RURAL ECOSYSTEM MODEL

CHAPTER I

INTRODUCTION

In the past few years, mankind has become increasingly aware of the fact that he is an integral part of a complex ecosystem. This ecosystem includes air, water, plant and animal life, and the environment that surrounds man. One of the most important things that he has learned is the fact that his activities can significantly modify the natural environment. This modification of nature has a profound effect upon man as well as upon the plant and animal life around him. This fact is illustrated by recent scientific studies that show the detrimental effects of air and water pollution on many life forms. The harmful effect of air pollution on man has been dramatically demonstrated in several acute air pollution episodes. These cases show an increase in illness that can be attributed to sharp increases in air pollution concentration. Some of the best known cases include Donora, Pa. (1948), London (1952), London (1962), and New York (1963). For these cases the increase above normal death rate ranged from 17 in the case of Donora to 4000 in the 1952 London smog. A study by Heimbach (1970) gives statistical evidence that lung cancer and emphysema are related to long term exposure in the presence of high air pollution levels. The harmful effects of air pollu-

tion (SO_2, NO_2, and O_3) on plant life is demonstrated by many authors (Middleton, 1955; Heck, 1965; Taylor et al., 1966; Hill et al., 1961). To cite one example: Thomas (1961) showed that alfalfa and grain crop loss due to SO_2 is directly proportional to the visible leaf damage. The recent large fish kill in the U.S. and the alarming increase in the mercury level of marine life demonstrate the harmful effects of water pollution.

With the ominous forecast that the world population will double in the next 30 years, and facts in mind such as those cited above, it seems necessary that man consider how this continuing use of environmental resources will modify the natural environment in the future. Mankind must also be cognizant of the fact that increases in the world population and industrial activity makes it necessary to consider the finite limits of vital natural resources such as clean air and water, fossil fuels and important minerals. The Committee on Natural Resources (1962) estimates that, with world-wide industrialization, 80% of the world supply of crude oil and natural gas would be consumed in 15 to 20 years and the same proportion of coal depleted in less than a century. If this estimate is correct, man will have the acute problem of developing new energy sources within the next 50 years since the industrial world uses coal, oil and natural gas as its primary sources of energy. It is apparent that it would be useful to develop a mechanism to help in the assessment of the long-term consequences of man's activities before the fact. One of the most promising approaches is the development of computer models which simulate the long term effect of man's endeavors. In recent years a number of scientific groups have started working on the development of computer models with such an objective.

Three of the most prominent ecosystem modelling groups are those organized by Van Dyne, (1971); Watt, (1969, 1971); and Forrester (1969, 1971). Van Dyne organized a group that is running the U.S. IBP Grassland Biome Project. His group is conducting a grassland field observation program that provides data for a Grassland Ecosystem Model which they are developing. Watt's group is involved in the development of a four-level human oriented hierarchical model which is primarily concerned with the state of California. The four levels included are: 1) a global model, 2) a North American model, 3) a regional model of California, and 4) sub-regional models. Forrester's group developed an Urban Dynamics Model (1969) and a World Simulation Model (1971).

Recent articles published by Watt (1971) and Forrester (1971) emphasize the importance of developing models capable of simulating the long-term influences of mankind upon the world ecosystem. Watt (1971) indicated that the present trend of the industrialization of underdeveloped countries will increase the rapid rate at which our natural resources are being depleted. This will cause, for one thing, a world-wide increase in air and water pollution. He showed that the per capita consumption of oil in some of the underdeveloped countries is increasing three times faster than it is in the highly industrialized countries. He also discussed some of the problems involved with the implementation of social changes to which mankind will have to adapt; problems such as natural resource depletion and increased air and water pollution. Forrester's (1971) results indicated doom for the world within 100 years unless there is a reversal of some of the present world-wide trends. The results of his model indicated that decreasing the birth rate and capital investment rate would cause the population growth, quality of life, natural resource consumption and pollution level to stabilize within the next 100 years.

An interesting point brought out in Forrester's paper is the fact that some social action programs which appear to be beneficial to mankind actually have detrimental long-term effects. For instance, Forrester's Urban Dynamics Model (1969) indicated that the construction of large low-income housing projects within the central urban areas has a detrimental effect on the evolution of an urban area. A concept implicit in both of these articles is the idea that the present life styles of mankind will have to be significantly modified if mankind expects successfully to survive the evolution of the ecosystem.

The urban-rural ecosystem computer model described in the following report has the potential for predicting some of the possible long-term consequences of man's planned and unplanned activities. It is also useful for studying certain implications of conscious management by man of the environmental resources in his ecosystem. The decision to develop an urban-rural ecosystem model is based upon the premise that most of the important interactions between man and his environment can be simulated using such a framework. For example, environmental problems such as air and water pollution and long term land utilization illustrate three of the major problems considered by an urban-rural ecosystem. This model is cast as a "management model" which uses linear programming and decision theory to optimize the effect of various management practices. Simulated evolution in the model depends upon the physical relationships which control the interactions between the different components of the system. These physical relationships are derived from state-of-the-art information about the physical sciences concerned. This ecosystem model differs from those of Watt and Forrester in that it deals primarily with the evolution in an urban-rural ecosystem and the associated human oriented city problems as opposed to national or global problems. The present

ecosystem model is set up so that it could easily be adapted for use in specific urban-rural systems and yet could be expanded to incorporate more realistic boundary conditions which might be available from other types of models.

The problem is organized with a basic structure which incorporates techniques capable of simulating the driving mechanisms which exist in a natural ecosystem. The model uses a variety of stochastic and deterministic concepts to simulate reality. Whenever possible, adaptability is considered in the selection of modelling techniques. For example, linear programming is presently used to optimize the water resource management and control air pollution emission rates in the urban area. The same techniques could be used for the other resource management problems such as optimum land utilization. Linear programming would also be useful when considering a transportation submodel for the ecosystem.

The methodology presently used in the model can also be made responsive to new information gained by further study of the real-world ecosystem. This information could be used to determine what state variables (parameters simulated by the model) and control parameters should be considered in an ecosystem model. For example, a study of the population dynamics of the urban area might indicate that a certain set of control parameters are those most important in influencing the evolution of an urban area. This set could easily be used to replace the control parameters presently used in the urban model. The addition of new state variables to the ecosystem can be accomplished by using modelling techniques that are used in the present ecosystem model. As an example, the existing ecosystem model only considers the growth of grass; however, other crops can be grown by using the basic botany model and incorporating crop

data to determine the exact relationship between a particular crop and the driving function that influences that crop. The present model only includes the state variable and control parameters that are needed for the desired level of complexity of the eocsystem.

The present ecosystem simulation program is intended to be used as a basic tool for the development of a more comprehensive computer model of an urban-rural ecosystem. Future development will require the addition of different components to the ecosystem and the utilization of large amounts of observed data for the calibration and validation of the model. The use of real-world data will determine what state variable and what values should be assigned to the coefficients used in the control mechanism. The model is structured so that the anticipated expansion associated with the development of a more comprehensive ecosystem can easily be handled without severely altering the present logic.

CHAPTER II

MODELLING CONCEPTS

This section will consider some of the concepts used in the development of the ecology model. Specifically, various types of models will be defined, some characteristics mentioned and explained and problems associated with model development will be discussed.

A model can be defined as abstraction of the real world and can be mathematical, verbal, graphical, pictorial, or mechanical. Mathematical models are of primary interest here for ecosystem modelling and any further reference to models will refer to the mathematical type. Models are useful in ecology because they abstract current knowledge about ecosystems and provide a mechanism to represent known and, sometimes, complex interactions in a format which can be accepted by a computer. Models provide an overall view of the system in operation. The computer representation of an ecosystem can be used to study the consequences of a variable set of assumptions and interactions. Modelling also can develop a means to elucidate certain characteristics presently observed in the ecosystem but only partially understood.

Characteristics of Models

Fig. 1 illustrates some of the characteristics used to describe various types of mathematical models. Each double-headed arrow represents

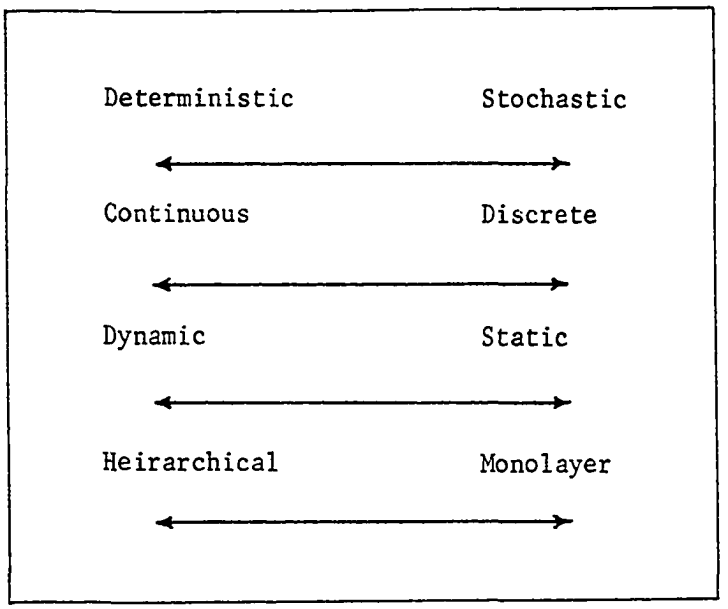

Fig. 1. Classification of mathematical models (Clymer, 1969).

a continuum of values between the extremes labeled at the tips. Most models are located at the extrema; for example, most models are either deterministic or stochastic. Each of the characteristics shown in Fig. 1 will be discussed in more detail, and following this discussion there will be a section that considers the problems involved in the development of a computer model for a real-world ecosystem.

A deterministic process can be defined as a process that will generate a unique set of results for a given set of initial conditions. A process that can be modelled by solving a differential equation with specified initial conditions is an example. A stochastic process can be described as one which can generate different sets of results from observations of a given set of initial conditions. The reason for this can be attributed to an uncertainty in the observed initial conditions as well as to an uncertainty about the mechanisms which drive the process. An example of a real-world problem that is represented by stochastic processes is weather prediction. The uncertainty about the actual state of the atmosphere at any given time along with a lack of precision in describing the mechanisms which drive the atmosphere makes it desirable for meteorologists to utilize stochastic processes in weather prediction. Deterministic phenomena are described using explicit equations, while stochastic phenomena must rely on statistical relationships such as cumulative frequency distributions, density distributions, mean values, variances, etc. An example of a deterministic process in the ecosystem model is the use of a radiation balance model to predict the surface temperature, while an example of a stochastic process is the utilization of a first order Markov chain to predict rainfall. The first order Markov chain relates the occurrence of rainfall at one time step to the occur-

rence or non-occurrence of rainfall at the previous time step.

A continuous model is a model which simulates state variables at any point in time and space (infinite number), while a discrete model simulates values for a finite number of points in time and space. A discrete model for predicting soil temperature profiles in the ground would predict soil temperature at specified time intervals for specified layers of soil. A continuous model would simulate the soil temperature at every point in time and at any point below the ground surface. In a sense, a discrete model can be considered as a special case of a continuous model. The difference between the results from discrete and continuous models should become less significant as the size of the increments considered by discrete models becomes smaller.

A static model can be defined as a model in which the control parameters remain constant, while in a dynamic model, the control parameters are allowed to vary. An example of a static model is one which uses differential equations with constant coefficients, while this same differential equation model would be dynamic if some mechanism permitted the coefficients of the equations to vary with evolution of the system. A dynamic model is capable of changing with evolution of a system while a static model only responds to the input variables which drive the model.

Complex ecosystems have a variety of time and space scales represented. Such systems can be divided into a discrete number of echelons characterized by different time and space scales. Lower echelons (smaller time and space scales) focus on details while the upper echelons encompass larger time and space scales. A hierarchical model is one that has more

than one echelon, while a monolayer model contains only one echelon. Hierarchical models are structured by considering all the different levels of activity in the system. The lower echelons usually have a small sphere of influence while the upper echelons have a larger sphere of influence. Hierarchical models contain submodels that are related to each other in terms of the relative time and space scales. A more detailed discussion of the importance of hierarchical structure can be found in an article by Clymer and Bledsoe (1969).

Another characteristic used in the description of models is the term modular. A computer model is modular when any of its submodels can easily be replaced by a new or updated package. This type of structure is advantageous because it enables one to alter any of the submodels without having to make major modifications to the overall structure of the model.

Modelling Problems

Some of the general problems encountered in the computer simulation of ecosystems are listed below and will be discussed in detail:

1. Components of the System
2. Conceptual Modelling
3. Modelling Techniques
4. Model Testing .

In modelling an ecosystem an important problem is the determination of the components which should be considered. A complete description of any real-world ecosystem requires that all of the components be considered; however, such a representation of most real-world ecosystems is impractical because of their complexity. The components chosen should describe the ecosystem for the specific purpose intended. The proposed model of an

urban-rural ecosystem contains 6 primary submodels that include: an Atmospheric component, a Hydrology component, an Urban component, a Zoology component, a Botany component and an Executive routine. These choices are based primarily upon an understanding of the importance of the different components to an urban-rural ecosystem. A more complete description could include transportation, sociology, and economics. These will not be included in the system at the present time, although they are implied.

Another important aspect of the development is the definition of reference systems. Some of the reference systems used for this purpose include:

1. Trophic levels (who-eats-whom levels)
2. Taxonomic lines (classification by natural relationships)
3. Biological vs. abiotic
4. Variable time and space scales.

A zoologist might consider trophic levels and taxonic lines to organize models concerning animal life while a biologist might classify a system with respect to the biological and abiotic aspects of the system. Meteorologists perceive the atmosphere with respect to the different time and space scales of atmospheric motion. Table 1 shows the breakdown of the scales of motion considered in the atmosphere. The scales of motion in the atmosphere run from the molecular scale (space scale of 10^{-6} m and time scales of less than a second) to the planetary scales (space scale greater than 1000 km and time scales of weeks). Meteorologists study the atmosphere by developing models to describe the different scales of motion. Each scale of motion requires different observational networks and instruments, different analysis techniques and different theories and principles for describing order in the data. The development

TABLE 1

CATEGORIZATION OF THE SCALES OF MOTION IN METEOROLOGY

Scales of Motion	Space Scale	Time Scale	Required Observation Network	Time Scale of Valid Forecasts	Associated Phenomena
Planetary Scale	>1000 km	days-weeks	500 km	3-5 days	1) General circulation patterns 2) Main air stream 3) Major circulation controls
Synoptic Scale	100-1000 km	days	100-500 km	1-3 days	1) Baroclinic waves 2) Cyclones and anticyclones 3) Fronts and air masses 4) Major frontal cloud systems 5) Hurricanes
Mesoscale	5-100 km	hours	5-10 km	up to 12 hr	1) Organized convective clouds 2) Squall-lines 3) Tornadoes 4) Cumulonimbus thunderstorm
Small Scale	.1 to 5 km	minutes	.5-1 km	up to 1 hr	1) Cumulus clouds 2) Rayleigh convection
Microscale	.01-100 m	sec-min	1-50 m		1) Turbulence 2) Micrometeorology of the lowest 10 m of atmosphere 3) Shearing flow and thermal convection
Molecular Scale	10^{-6} m	<sec			1) Molecular phenomena 2) Aerocolloidal particulate gas interaction 3) Atmospheric chemical reactions 4) Cloud droplet behavior

of a comprehensive model to describe atmospheric motion requires knowledge about the interactions between the different scales of motion. In meteorology, it is generally observed that each smaller scale of motion is partially controlled by the next larger scale of motion. The location of major frontal patterns in relationship to the general circulation pattern is an example of the dependence of a smaller scale of motion on the next larger scale of motion. A more complete discussion of the problems involved with atmospheric models can be found in articles by Lee (1966) and Hidy (1967).

Variable time and space scales are used for interdisciplinary ecosystem models because they are a basic reference system common to all components of the ecosystem. Categorization through the use of relative time and space scales permits simplification of complex systems by dividing them into a variety of submodels, each working with different time and space scales and each considering only those aspects of the system necessary to describe its main features. Two of the most important considerations include: 1) the determination of the critical time and space scales of observed phenomena and 2) the determination of the interactions between the different scales of processes involved in the system.

Another important problem is determining which techniques should be used to simulate the processes that drive the various components. Before such a determination one must decide whether to use a stochastic or deterministic modelling technique. This decision is based upon criteria previously described. The most important deterministic modelling techniques used in the urban-rural ecosystem model include: ordinary differential equations, partial differential equations and simple equations, while some of the stochastic modelling techniques used in the ecosystem model include: first order Markov chains, conditional probability

relationships, and a two-dimensional Gaussian diffusion model. The decision to use a particular technique is based on knowledge of the driving mechanisms and the characteristics associated with the different techniques. Some of the characteristics that should be considered include: round-off error, truncation error, relative accuracy, computational and dynamical stability and the amount of time required to run the model.

An important part of the development of a computer model of an ecosystem is its calibration and testing. Calibration is performed by using real-world data sources to determine the values for the driving parameters. Two of the testing techniques are termed sensitivity analysis and validation. Validation is performed by comparing simulated computer results with observed data sets. If the simulated computer results compare favorably with the observed data sets, then the model is considered validated. Validation which used a short time series of observed data would usually be considered much less significant than that which used a long time series. The calibration and validation should be tested using independent data sets. A sensitivity analysis demonstrates the response of a model to the parameters that control it. A sensitivity analysis can be performed empirically by running a numerical experiment where certain parameters are varied while others remain constant. Such analysis tests the stability of the model to variations of the control parameters and can also be used to validate subjectively a model that is calibrated and validated using a comparatively small time series of observed data. The use of a sensitivity analysis for validation is accomplished by running the model with different sets of data for the driving variables and comparing the computer simulated results with the results expected for the given set of driving variables.

CHAPTER III

STRUCTURE OF THE MODEL

The overall structure of the model is shown in Fig. 2. It contains five primary submodels: atmospheric, hydrology, urban, zoology, and botany submodels. These are controlled by a decision-making executive model that utilizes decision theory and linear programming techniques to study the consequences of various resource management practices on the evolution of the system. The overall system is modular and utilizes hierarchical structure. The hierarchical structure is based upon the time and space scales of the phenomena observed in the ecosystem. The model is discrete in order to make use of the capability of high speed digital computers to handle large complicated programs. The basic structure of the five primary submodels is static in nature; however, the overall system is dynamic because of the ability of executive routine to control the model to effect optimal management of the system. The atmospheric and urban submodels use both stochastic and deterministic processes while the zoology, botany, and hydrology models use deterministic processes.

A large variety of time and space scales are considered. The time scales are set up to simulate the evolution of the ecosystem for periods of time up to 30 years. These scales include hourly, daily,

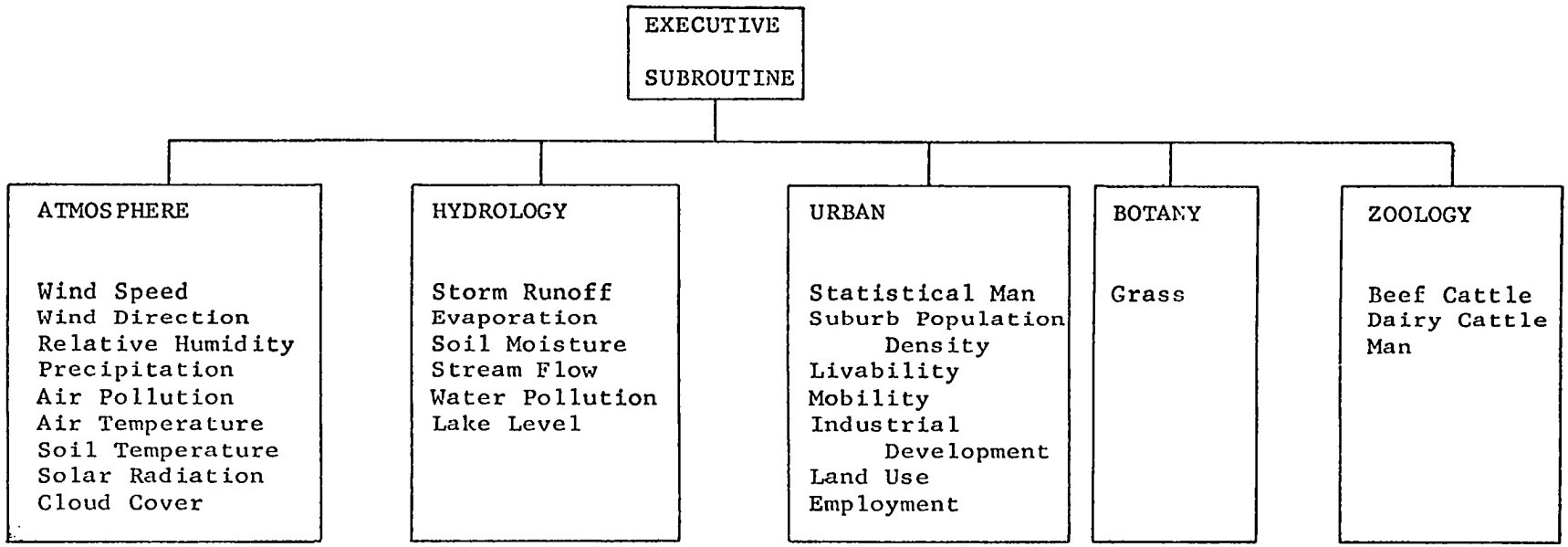

Fig. 2: Organization of the urban-rural ecology model.

monthly, and yearly time steps. The different space scales are considered by using a variety of grid networks in which grid points represent basic unit areas (.38 x .38 mi^2, 1x1 mi^2, and 16x16 mi^2). The grid networks are organized so that the smaller scale grids can be superimposed upon the larger grids. The overall dimensions of the model are illustrated in Fig. 3. Some of the important physical aspects include: 1) 128x128 mi^2 overall ecosystem, 2) 300 mi river system, 3) 24x18 mi^2 urban area with a 1 to 2 million population, 4) 25x25 mi^2 lake and 5) farm land broken down into 4x4 mi^2 plots. The important time and space scales for the different submodels are summarized in Fig. 4. A detailed description of the overall computer system and the six primary subsections of the model will follow.

Overall Computer System

The computer program is set up to run on the National Center for Atmospheric Research (NCAR) CDC 6600 computer system. The NCAR computing facilities are used because of the capability of the system to handle large numerical models (60,000 word core, ample tape and drum facilities, and DD80 scope output). Fig. 5 shows the flow diagram of the overall computer model. The large core capacity required necessitated the use of the overlay system which provides for "off line" storage of individual submodels that can be called into the "on line" computer system by the control program. The five primary submodels are programmed as individual overlays and are called separately into the "on line" computer system as a function of time and space scales of the individual submodels. The computer program uses 50,000 words of core, two magnetic tapes, and two drums. Forty-thousand words of core storage are used to establish a common block that stores data

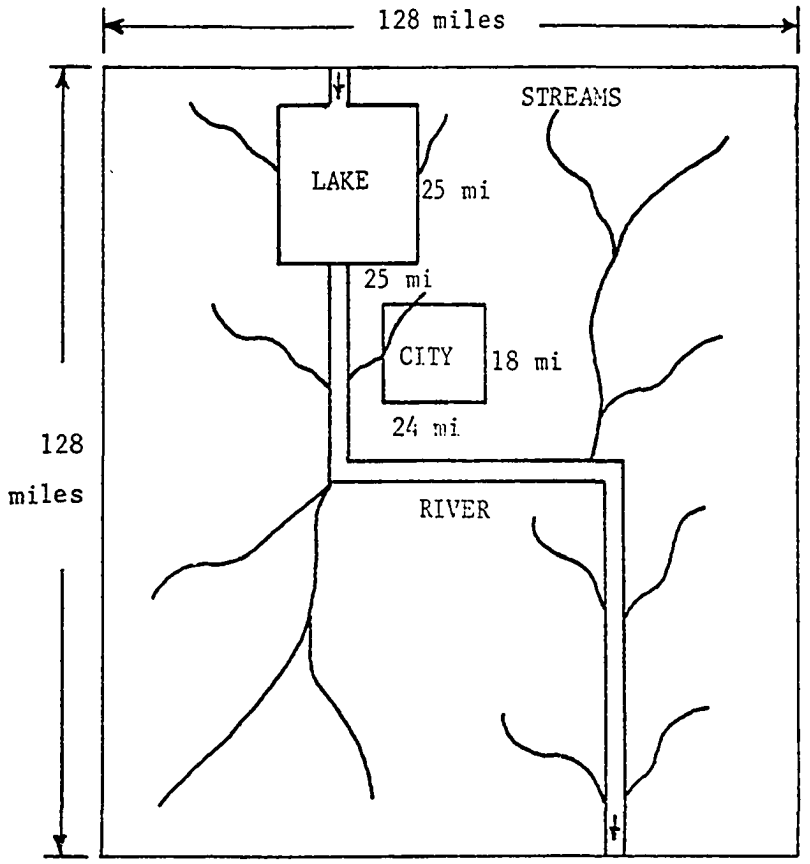

Fig. 3. Overall dimensions of the ecosystem.

	Atmospheric Model	Hydrology Model	Urban Model	Zoology Model	Botany Model
Time Scales	hourly daily	hourly daily	yearly	monthly	daily monthly
Space Scales (unit areas for the grid points)	4x4 mi^2 1x1 mi^2	4x4 mi^2 16x16 mi^2	.38x.38 mi^2 1x1 mi^2 6x6 mi^2	4x4 mi^2	4x4 mi^2

Fig. 4. Time and space scales considered by the five primary submodels.

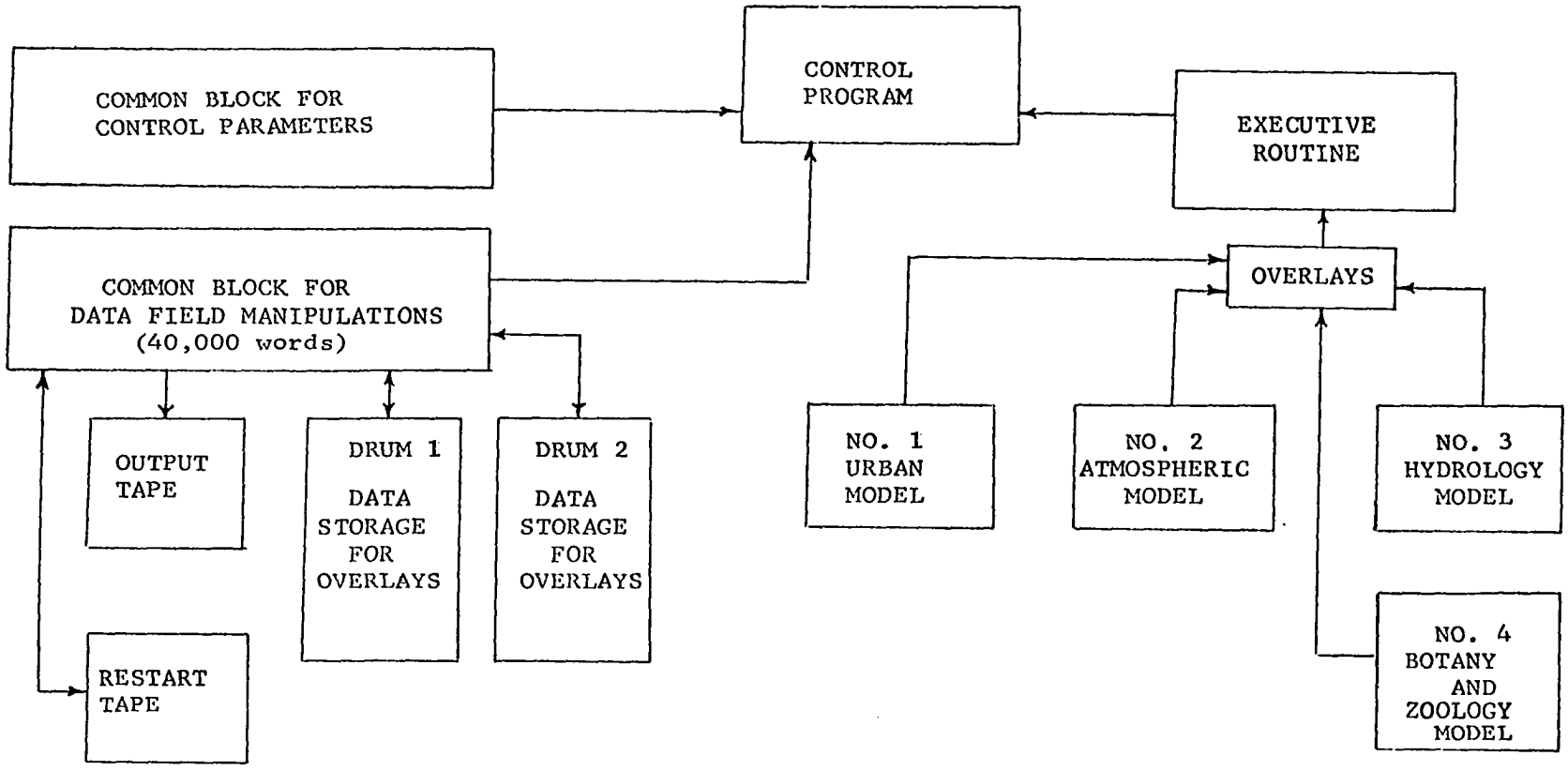

Fig. 5. Flow diagram of the overall structure of the computer model.

for use by the various overlays, while the two drums are used for recurrent data storage. Intermittent data storage for overlays 2, 3, and 4 are stored on drum 1, while drum 2 is used for overlay 1. Data stored in drum 1 is read into the common block prior to the use of overlays 2, 3, and 4 while the data on drum 2 is read prior to the use of overlay 1. Future growth of the model will require the use of additional drums for intermediate data storage. One of the magnetic tapes stores the output at the end of each time step, while the other magnetic tape is used in conjunction with the restart procedure available on the NCAR computer system. The restart procedure allows the computer program to be reactivated at the end of the last completed time step, so that studies which take a considerable amount of computer time to complete can be broken up and submitted on several occasions. This also permits one to stop the computation at a particular point in the evolution of the ecosystem and to change certain critical parameters to study the resulting effect.

Two of the most important characteristics of the overall program are the modular and hierarchical structure. The modular structure is illustrated by the use of the overlays to program the individual submodels. The substitution of new versions of old submodels and the addition of new submodels is accomplished easily by adding new overlays. The hierarchical structure is demonstrated by the use of the control program to direct overlay operations in which the individual submodels are called into the "on line" computer system as a function of the relative time and space scales. The individual overlays utilize hierarchical structure by containing submodels within the overlay that are organized with respect to time and space scales.

Atmospheric Submodel

The objective of the atmospheric submodel is to simulate daily weather observations for periods of time up to 30 years. The deterministic representation presently used in numerical weather prediction is generally capable of predicting large-scale weather patterns for periods of time up to a few days, while most of the smaller scale phenomena in meteorology can only be predicted for periods of time much less than 36 hours (Lee, 1966). The limited predictability of deterministic atmospheric models made it necessary to develop a stochastic atmospheric model which is capable of simulating consistent daily weather observations (5 inches of rain doesn't occur on a clear day) for long periods of time. This submodel simulates daily weather observations that are statistically comparable with the observed climatological data used in the calibration. Most of the parameters predicted by the atmospheric component are considered to be stochastic, while a few are represented as deterministic.

A list of the atmospheric parameters, the time and space scales associated with each parameter, and the processes used to simulate each parameter are shown in Table 2. The atmospheric parameters are represented on a variety of time and space scales because of their use in the model. In particular, the average air pollution field is predicted for the whole ecosystem using a large scale 32x32 grid and also for a small scale 40x40 grid (mesh size = 1x1 mi^2) that is centered about the urban area. Parameters such as the hourly urban heat island temperature and wind fields are predicted on a small scale 20x20 grid (mesh size = 1x1 mi^2) also centered on the urban area. The parameters that do not have any spatial variation are predicted as average values for the whole ecosystem.

TABLE 2

PARAMETERS SIMULATED BY THE ATMOSPHERIC MODEL

Parameters	Time Scales	Space Scales	Simulation Process
1. surface air temperature	hourly	20x20 grid (mesh size = 1x1 mi^2)	deterministic (radiation balance model)
2. 6 in. soil temperature	hourly	20x20 grid (mesh size = 1x1 mi^2)	deterministic (radiation balance model)
3. 1000 ft. air temperature	hourly	no spatial variation	stochastic
4. 1000 ft. wind speed	hourly	no spatial variation	stochastic
5. net radiation balance and short wave solar radiation	hourly	20x20 grid (mesh size = 1x1 mi^2)	deterministic (radiation balance model)
6. urban heat island	daily	20x20 grid (mesh size = 1x1 mi^2)	deterministic (radiation balance model)
7. urban heat island wind field	hourly	20x20 grid (mesh size = 1x1 mi^2)	deterministic (equations of motion)
8. average surface wind speed and direction	daily	no spatial variation	stochastic (first order markov chain)
9. average relative humidity	daily	no spatial variation	stochastic
10. average cloud cover	daily	no spatial variation	stochastic
11. rainfall distribution and amounts	daily	32x32 grid (mesh size = 4x4 mi^2)	stochastic (first order markov chain)
12. average air pollution	daily	32x32 grid (mesh size = 4x4 mi^2) 40x40 grid (mesh size = 1x1 mi^2)	deterministic (point source diffusion model)

Figure 6 illustrates the flow diagram of the atmospheric submodel as well as the sequence of predicting the atmospheric parameters. The wind direction and speed are the first parameters predicted at the start of each daily step. The predicted wind direction is used to forecast the relative humidity. Cloud cover is forecast using the predicted relative humidity and wind direction. The above parameters are used as input data for the air pollution field. The rainfall model, in turn, utilizes this field and all of the previously predicted parameters in forecasting the rainfall distribution for the ecosystem. All of these parameters are considered in the radiation balance model to predict hourly values of surface temperature, net radiation heat flux, short wave solar radiation, and the 6" soil temperature. The hourly surface temperature field for the urban area is used by the small scale wind model to get the urban heat island induced wind field. Climatological data from Oklahoma City (OKC) and National Severe Storms Laboratory tower data (Crawford, 1970) are used to derive the statistical relationships needed by the atmospheric submodel. The statistical relationships are determined as a function of time of year for three, four month periods (Nov., Dec., Jan., Feb., Mar., Apr., May, June, July, Aug., Sept., Oct,). These particular four month periods are chosen because of the relative homogeneity of the average monthly rainfall within these time periods.

Wind

The daily average wind direction is simulated using a first order Markov process specified through the use of a transition matrix (See Fig. 7) determined for OKC climatological data. Theory describing the first order Markov chain is found in a book by Lipschutz (1966). Three important properties of the use of the first order Markov chain in the present

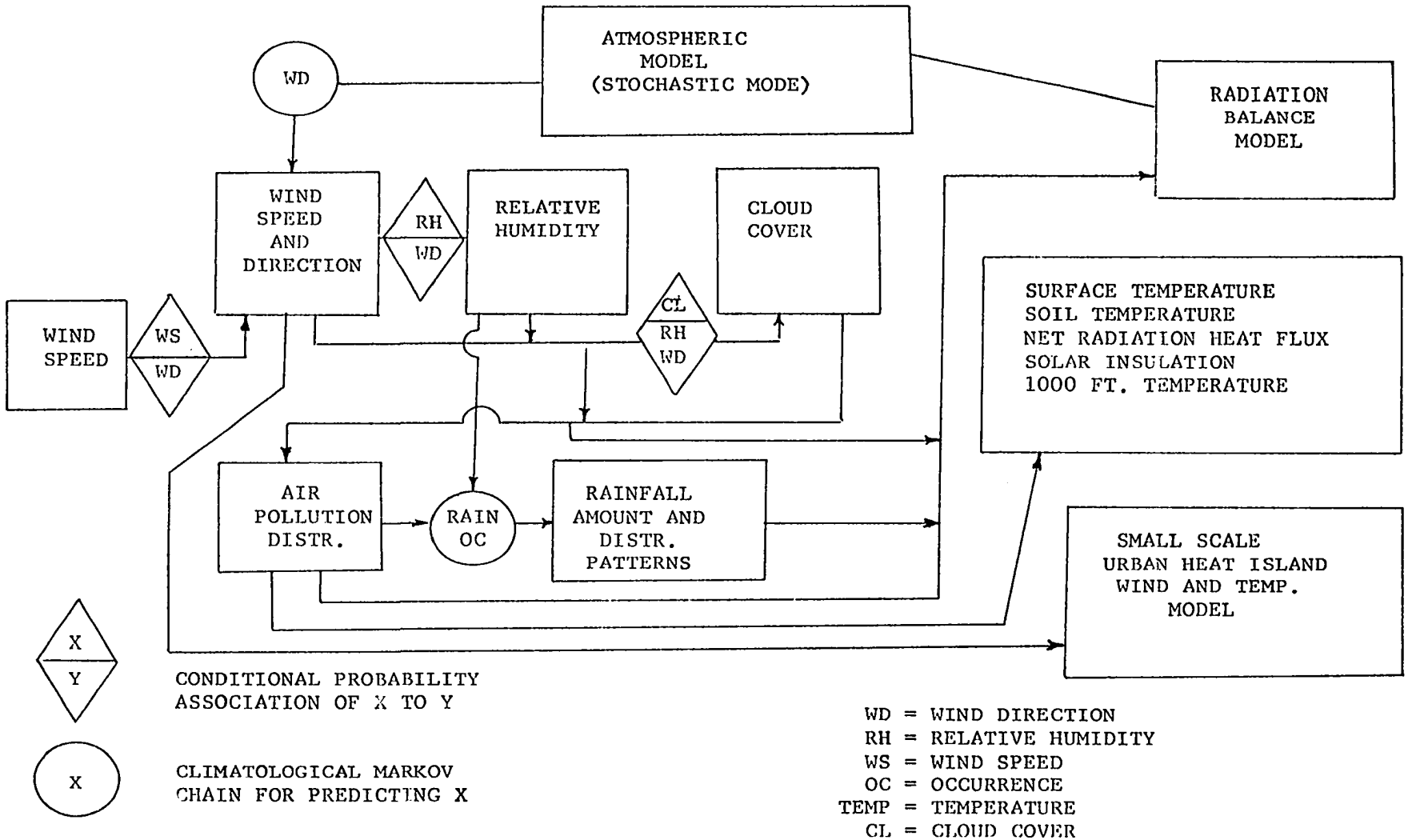

Fig. 6. Flow diagram for the atmospheric model.

$$P_{\Delta t} = \begin{matrix} A_{11} & A_{12} & A_{13} & \cdots & A_{15} \\ A_{21} & A_{22} & \cdots & \cdots & A_{25} \\ A_{31} & \cdots & \cdots & \cdots & A_{35} \\ A_{41} & \cdots & \cdots & \cdots & A_{45} \\ A_{51} & A_{52} & \cdots & A_{ij} & A_{55} \end{matrix}$$

where A_{ij} is the probability that the wind will change from direction "i" to direction "j" during time interval Δt.

Figure 7: The wind direction transition matrix.

study are:

1) After a sufficient number of time steps, a collection of the wind directions generated will represent the climatological wind rose,
2) The transition matrix required to make the forecast for time period $N\Delta t$ is given directly by $(P_{\Delta t})^N$,
3) Error propagation can be studied directly (Crawford et al., 1971).

The Markov chain forecasts the wind direction (to the nearest degree) in one of five class intervals (350^o-70^o, 71^o-150^o, 151^o-200^o, 201^o-270^o, and 271^o-349^o). The forecast is accomplished in the following manner. Let (D_t) be the probability distribution for the wind direction intervals at time t_o. Then, for example, the probability distribution $(D_{t+\Delta t})$ for wind direction at $t_o + \Delta t$ is given by

$$D_{t+\Delta t} = (D_{t_o})(P_{\Delta t}) = (P_{41}, P_{42}, P_{43}, P_{44}, P_{45})$$

where

(D_{t_o}) = (0,0,0,1,0) ... wind direction from class interval 4 at time t_o (known by observation)

$(P_{\Delta t})$ = the transition matrix (Fig. 7)

P_{ij} = the probability for the wind direction to be in class interval j at time $t_o + \Delta t$ when the wind direction is from class interval i at time t_o.

The forecast class interval of wind direction at $t + \Delta t$ ($t + 24$ hours) is obtained using rectangularly distributed random number between 0 and 1 and the cumulative frequency distribution (ogive) derived from the probabilities specified by $(D_{t+\Delta t})$. This is accomplsihed by using the generated random number as the ordinate of the ogive and then choosing the corresponding wind direction class interval from the abscissa (process illustrated in Fig. 8). This random process is used frequently to determine the predicted class interval for various parameters. Any further

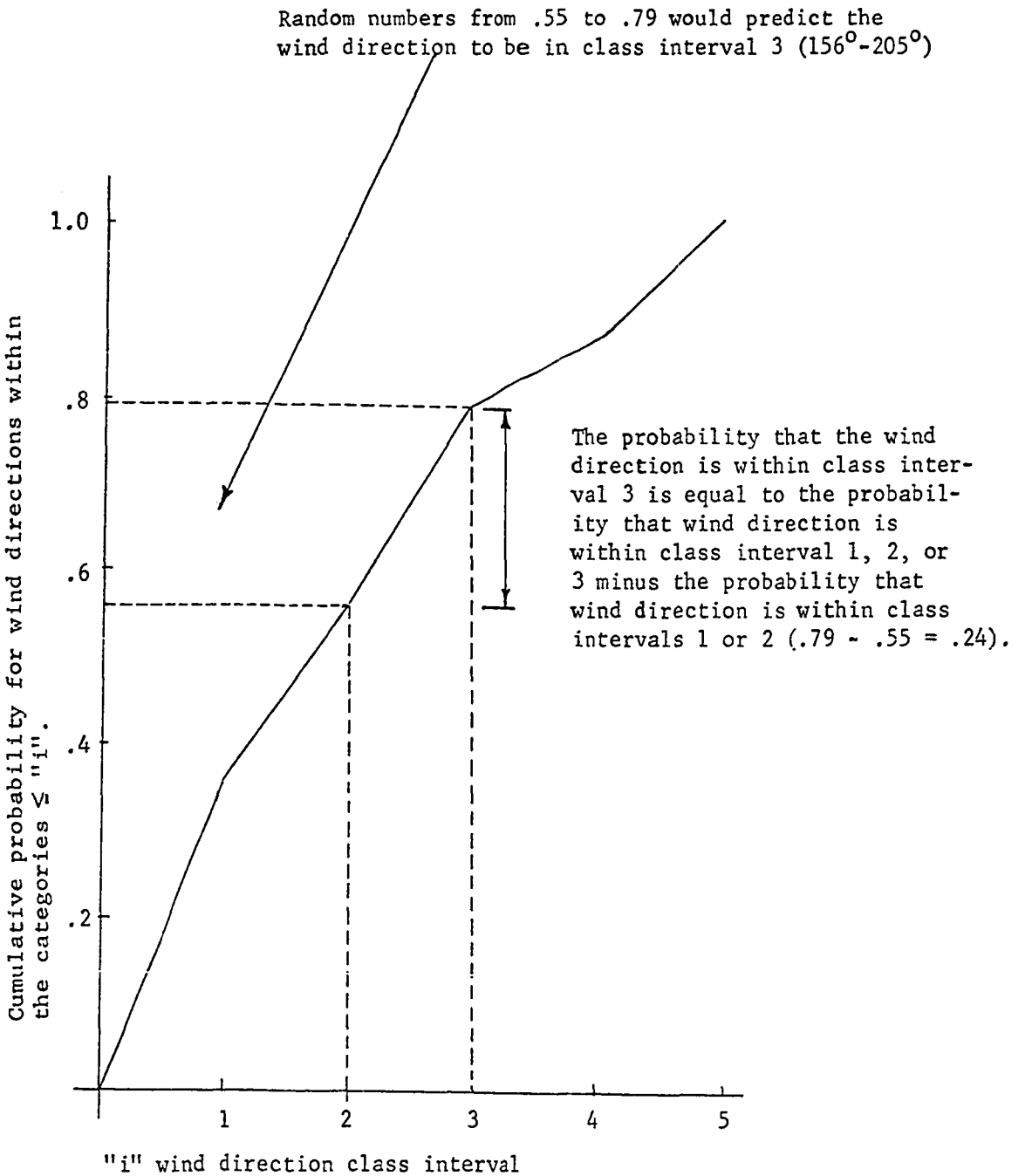

Fig. 8. Ogive for the wind direction class intervals at time t + 24 hours when the wind direction at time t is in class interval 1 (345° - 75°). This distribution is for the winter months (Nov., Dec., Jan., and Feb.).

reference to the use of a random process to select a class interval of quantity from a frequency distribution of that quantity will refer to random process demonstrated above.

The exact value of the wind direction (nearest degree) is determined by means of a statistical procedure which uses the probability for the class intervals of wind direction on either side of the predicted class interval. The statistical technique assumes that the cumulative distribution for wind direction within the predicted class of interval is generated from a normalized version of a special distribution in which the probability for the two wind directions that define the outer limits of a wind direction class interval are set equal to the probability of the wind direction class intervals that are adjacent to these wind directions. The probability for the wind directions within the class interval are then generated by assuming that there is a linear trend in the probabilities defined at the end point wind directions of the class interval. Fig. 9 demonstrated the special distribution that is used to generate the density distribution for wind directions within wind direction class interval 3 (statistics for the winter time period). The cumulative frequency distribution is generated from this density distribution and is used in conjunction with the random process illustrated in Fig. 8 to determine the exact value of the wind direction predicted for a particular wind direction class interval.

The average daily wind speed is forecast by using the predicted wind direction. Conditional probabilities for five class intervals of wind speed (0-5 mph, 6-10 mph, 11-15 mph, 16-20 mph, and 20-25 mph) are determined for the five class intervals of wind direction (OKC climatological data). The conditional probabilities of wind speed that correspond to the predicted wind direction class interval are used to construct

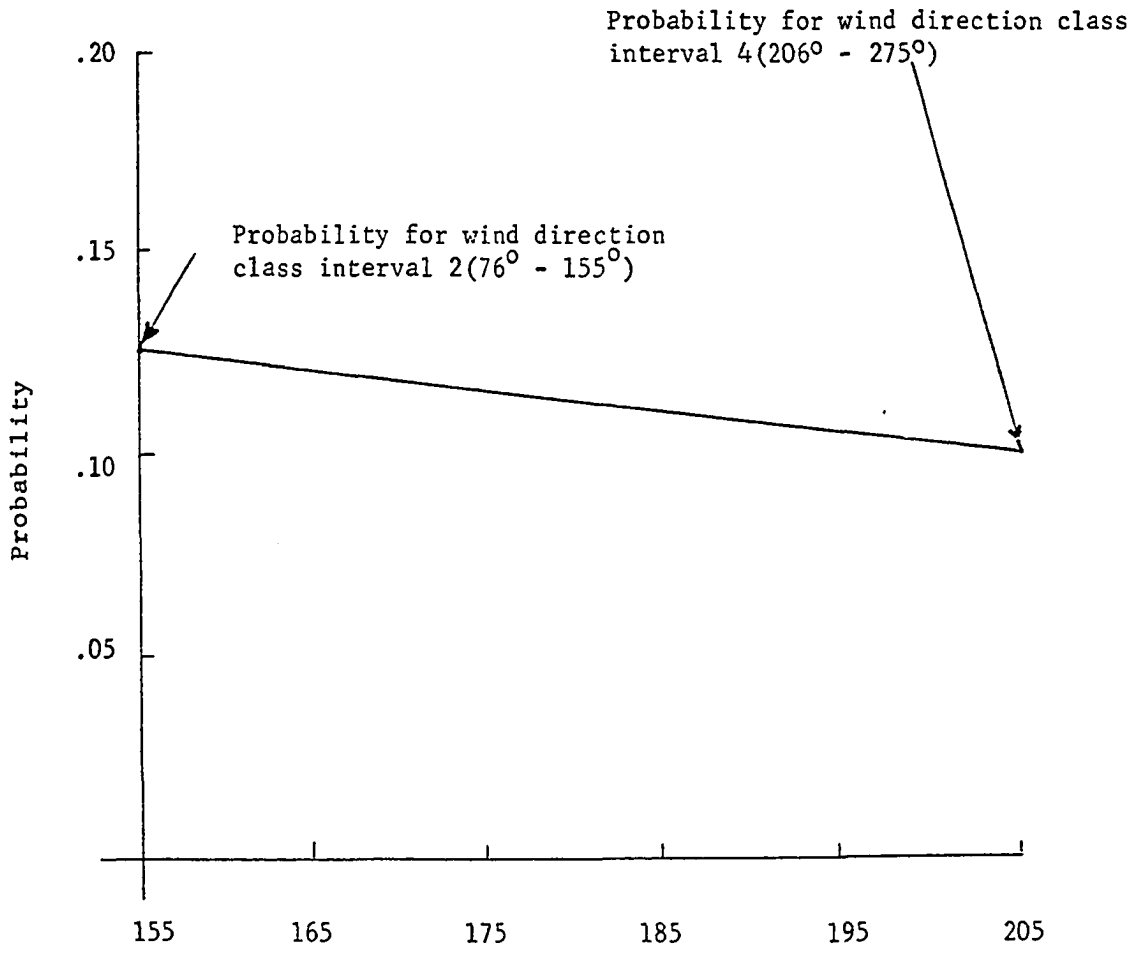

Fig. 9. Special frequency distribution used to generate the density distribution for wind direction within wind direction class interval 3. The special distribution is for the winter time period (Nov., Dec., Jan., and Feb.).

an ogive that is used in conjunction with a random process (process described in Fig. 8) to predict the class interval. The exact value of the wind speed is simulated by using a rectangular number generator in conjunction with the cumulative frequency distribution generated by assuming that each wind direction within the class interval has an equal probability.

Hourly average values of the surface and 1000 ft. wind speed are forecast as a function of the predicted daily average wind speed category. The wind speed category is used as input information for a table look up procedure which uses a table in which the average hourly surface wind speed and 1000 ft wind speed are presented for each hour during the day for the five average daily wind speed categories. This table is determined by comparing the daily average surface wind speed observed at OKC with the hourly average values of the surface wind speed and 1000 ft wind speed observed at the NSSL meso-network tower for the time period from June 1966 to May 1967. A complete description of the mesonetwork tower and the wind data for this time period (June 1966-May 1967) is presented in a report by Crawford (1970).

Relative Humidity

The average daily relative humidity is forecast from the predicted wind direction. Conditional probability distributions for five class intervals of relative humidity (0 to 20%, 21 to 40%, 41 to 60%, 61 to 80% and 81 to 100%) are determined for the different class intervals of wind direction (the conditional probabilities are determined using Oklahoma City climatological data). The conditional probability distribution that corresponds to the forecast wind direction is used in connection with a rectangular random number generator to determine the forecast relative

humidity class interval (technique illustrated in Fig. 8). The predicted value of relative humidity is determined by using the same technique that is used to get the exact value of the average wind speed.

Cloud Cover

Daily average cloud cover is predicted by using the forecast wind direction and relative humidity. Conditional probabilities for five class intervals of cloud cover (0 to .2, .21 to .40, .41 to .60, .61 to .80, .81 to 1) are calculated for the five class intervals of wind directions and relative humidity. The conditional probability distribution which correspond to the forecast wind direction and relative humidity is used in conjunction with a rectangular number generator to determine the class interval of cloud cover (technique shown in Fig. 8). The exact value of cloud cover is forecast by using the same technique that is employed to determine the exact value of mean daily wind speed.

Air Pollution

Daily average values of air pollution are determined at any position in the ecosystem by considering the dispersion of air pollution from specific point sources. The point source air pollution model suggested by Pasquill (1961) and modified by Gifford (1961) is represented by the following equation:

$$X(x,y,z,H) = \frac{Q_i}{2\pi\sigma_y\sigma_z U} \cdot \text{EXP}\left[-\tfrac{1}{2}\left(\frac{y}{\sigma_y}\right)^2\right]\left\{\text{EXP}\left[-\tfrac{1}{2}\left(\frac{z-H}{\sigma_z}\right)^2\right] + \text{EXP}\left[-\tfrac{1}{2}\left(\frac{z+H}{\sigma_z}\right)^2\right]\right\}$$

where

U = average wind speed (m/sec)

X = gas or aerosol concentration (gm^{-3})

Q_i = emission rate of pollutants (g sec^{-1}) for the Ith factory (I = 1, 2..., 16)

H = effective emission height (m)

σ_y = standard deviation of the plume concentration distribution in the horizontal (m)

σ_z = standard deviation of the plume concentration distribution in the vertical (m)

x,y,z = define the location in reference to the source of pollution (m).

The model assumes that the wind speed and direction and stability are constant throughout the mixing layer. σ_y and σ_z are functions of the stability and location in reference to the point source of pollution. The values of σ_y and σ_z are derived from tables illustrated by Turner (1969). The stability classification system suggested by Turner (1961) is used to determine the stability classification as a function of wind speed, solar radiation, and cloud cover. The stability classification runs from class A through F where A is most unstable and class F the most stable. The model simulates daily average SO_2 air pollution for a 40x40 grid (mesh size = 1x1 mi^2) centered on the urban area and a 36x36 grid (mesh size = 6x6 mi^2) that includes the whole ecosystem. The model uses the 1968 Houston, Texas SO_2 air pollution emission data (Report for Consultation on the Metropolitan Houston-Galveston Air Quality Control Region, 1969). A modified version of the method suggested by Turner (1964) is used to reduce the calculations needed to produce an air pollution field. A field of χ/Q values (χ = air pollution concentration, Q = air pollution emission rate) is calculated for a point source with the given meteorological conditions. This field is superimposed on the larger grid network at the location of each of the point sources and used to calculate the contribution of air pollution to the grid network

from each point source. This is accomplished by multiplying the χ/Q value at each grid point by the Q value that corresponds to the appropriate point source. This method assumes constant stack height for each of the point sources (i.e., an effective emission height of 10 meters is assumed).

Rain Model

Rainfall is simulated on a daily basis for a 36x36 grid network (mesh size = 6x6 mi^2). The rainfall model has three sections which include:

1) Prediction of the occurrence or non-occurrence of rainfall in the whole ecosystem,
2) Prediction of the average rainfall for the whole ecosystem if rainfall is forecast, and
3) Simulation of rainfall distribution for the grid network.

The occurrence of rainfall in the ecosystem is predicted by using a first order Markov process. Oklahoma City climatology data are stratified with respect to five class intervals of relative humidity and then used to calculate five first order Markov chains. The forecast value of the relative humidity determines which Markov chain is used on any particular day. The occurrence or non-occurrence of rainfall is predicted using the appropriate Markov chain, the occurrence or non-occurrence of rainfall anywhere in the ecosystem on the previous day, and the technique used to forecast the wind direction class interval. The occurrence or non-occurrence of rainfall is predicted for the ecosystem. The probability of the occurrence of rainfall is increased 10% for locations in the ecosystem that have air pollution levels greater than a specified critical level (40 $\mu g/m^3$). Gabriel and Neumann (1962) and others showed that Markov chains can be used successfully to simulate rainfall occurrence.

If rainfall is predicted for the ecosystem then the following method is used to determine the average rainfall amount for the whole ecosystem. Oklahoma City climatological data is used to develop a table which relates the average rainfall amount for rain days to the related humidity and wind direction. The average amount of rainfall is forecast by using this table in con unction with the predicted values of relative humidity and wind direction.

This section of the rainfall model also predicts the time periods when the average rainfall amounts will occur over the ecosystem. The frequency distribution for the number of rainfall periods as a function of the time of day (6-hour class intervals) is used in conjunction with a random number generator to predict the number of rainfall periods (technique illustrated in Fig. 8). The frequency distribution which relates the starting time period for measurable rainfall with the number of rainfall periods is used in conjunction with a rectangular random number generator to determine the starting time period for measurable rainfall (technique illustrated in Fig. 8). The frequency distributions used to determine the number of rainfall periods and the beginning of measurable rainfall are determined using Oklahoma City climatological data. The output from this section of the model predicts that the precipitation will start falling on the ecosystem during one of four periods and it will continue raining on the ecosystem for the period of time predicted by the model.

The third section of this model is used to simulate rainfall distribution for the grid network. This distribution is predicted using two types of patterns which include:

1) convective shower activity

2) large scale frontal rain

Rainfall is distributed in summer months (July and August) using convective shower activity while large scale frontal rain patterns are used for the other months of the year.

The convective shower activity is predicted using a modified version of area depth relationships suggested by Horton (1924). Eq. 1 and 2 describe the area depth relationship.

$$P = m(\exp(-kA^n)) \quad (1)$$

$$Z = m(1-knA^n(\exp(-kA^n)) \quad (2)$$

where

Z = rainfall along the boundary of area A

P = average precipitation with area A

m = rainfall at center of storm (in)

A = area (mi^2) contained in an isopleth of rainfall

k and n are constants (k = .01, n = .42).

The values of k and n are determined by fitting Eq. 2 to the experimental determined area depth relationship for convective showers in the Washita River Basin (Nicks and Hartman, 1965). Eq. 2 is used to specify the rainfall distribution around a convective storm that influences a 400 sq mi area. After specifying the number of convective storms (set equal to 18) and the average rainfall for each convective storm, Eq. 1 is used to determine the rainfall at the center of the convective storms (m). After the value of m has been determined, Eq. 2 is used to specify the rainfall distribution of convective storms that are distributed throughout

the grid system using a statistical process. The statistical process makes use of a cumulative frequency distribution which is determined with the probability distribution of a storm being centered at any of the grid points in the ecosystem. The probability for a storm to be located at a given point in the ecosystem increases 43% going south from the northern boundary of the ecosystem to the southern boundary. Similarly, there is a 43% increase going east from the western boundary of the ecosystem to eastern boundary. This particular frequency distribution is used to simulate the rainfall pattern observed in central Oklahoma. The cumulative frequency distribution is used in conjunction with a rectangular random number generator to determine the location of individual convective cells (technique illustrated in Fig. 8). The model has the capability of producing either circular or elliptical convective storm rain patterns. Such convective storms are oriented with the major axis parallel to the mean wind direction. The wind oriented elliptical rainfall patterns are obtained by rotating the coordinate system θ degrees (related to the wind direction) and then solving for A in Eq. 2 by defining an ellipticity and using the following three equations.

$$A = ab$$

$$x^2/a^2 + y^2b^2 = 1$$

$$e = a/b$$

where

A = area of ellipse

a, b = the semi-axes

e = the ellipticity (set equal to 1.66)

The rainfall at grid points that have air pollution concentration above a critical level (40 μ/m^3) have the predicted rainfall amount increased by 10%. On days when the convective shower mechanism is predicted to occur only at points with high air pollution, the model simulated rainfall for all the grid points in the ecosystem.

Rainfall amounts for large scale frontal activity are simulated for each grid point by using a Poisson distribution with a mean value equal to the predicted mean value for the whole ecosystem. This Poisson distribution is used in conjunction with a random number generator to determine grid point rainfall values (technique illustrated in Fig. 8). Grid points that show air pollution levels greater than a critical value (40 μ/m^3) have their rainfall amounts increased by 10%. The precipitation at each grid point is then multiplied by a factor which takes into account local influences. The precipitation factor varies quantitatively across the ecosystem in the same manner as the probabilities for locating convective storms in the ecosystem.

The 10% increase in occurrence of rainfall and the average rainfall amounts when the air pollution level is observed to be greater than 40 μ g/m^3 is included in this model because of recent statistical studies indicating that in urban areas, there is an increase in the probability for the occurrence of rainfall and also an increase in the relative frequency for large rainfall amounts. The increase in the number of ICE NUCLEI associated with air pollution is postulated as one of the causes for the modification of the rainfall pattern in urban areas. A fairly complete summary of the recent studies that look at the influence of urban areas upon the local rainfall pattern is presented in an article by Changnan (1969).

Radiation Balance Model

A modified version of a radiation balance model suggested by Myrup (1969) is used to predict hourly values of surface and soil temperature, net radiation heat flux and solar radiation. The primary equation used in the model is the energy balance equation at the surface of the earth, which is written as:

$$R_n = LE + H + S \tag{3}$$

where

R_n = net radiation flux (langly min^{-1})

LE = upward latent heat flux (langly min^{-1})

H = upward sensible heat flux (langly min^{-1})

S = downward flux of heat into the soil (langly min^{-1})

The terms on the right hand side of Eq. (3) are defined positive away from the interface. Physical relationships for each of the parameters in Eq. (3) are used to get a closed set of equations that can be solved for the surface temperature. Eq. (4) gives the net radiation term (R_n).

$$R_n = E \cdot (1 - \alpha) \cdot T_\gamma \cdot R_o \cdot (\sin\varphi\sin\delta + \cos\varphi\cos\delta\cos\gamma) - IR_n \cdot F + SH \tag{4}$$

where

E = parameter that modifies solar radiation as function of suspended particulate matter (non-dimensional)

F = parameter which modifies the infrared radiation loss as a function of local conditions (non-dimensional)

α = albedo (nondimensional)

T_γ = transmission coefficient for the atmosphere (non-dimensional = .664)

R_o = solar constant (1.98 Ly/min)

φ = latitude (radians)

δ = solar declination (radians)

γ = solar hour angle (radians)

IR_n = net infrared flux at the surface of earth (Ly/min)

SH = heat added to the air by man's activity (Ly/min)

Eq. (5) (Haurwitz, 1941) is used to describe albedo as a function of cloud cover.

$$\alpha = .17 + .53C \tag{5}$$

where

C = fractional cloud cover

The equation for net infrared radiation flux (IR_n) at the surface of the earth is presented by Haurwitz (1941) and can be written as

$$IR_n = (1 - .8C)IR_d \tag{6}$$

where C is the fractional cloud cover and IR_d is the long wave radiation from clear skies which is approximated using Swinbank's formula (1963) that can be written as

$$IR_d = .2447 - .195\sigma T^4 \tag{7}$$

where σ is the Stefan Boltzman constant and T is the absolute temperature. Swinbank's formula (1963) for IR_d is approximated by using a quadratic curve that agrees with the original equation within .3% and is written as:

$$IR_d = AT^2 + BT + C \tag{8}$$

where

$A = .739 \times 10^{-5}$ (Ly min^{-1} $^{o}K^{-2}$)

$B = -.2722 \times 10^{-2}$ (Ly min^{-1} $^{o}K^{-1}$)

$C = .3550 \times 10^{-1}$ (Ly min^{-1})

The turbulent fluxes of latent and sensible heat are written as:

$$H = (-\sigma C_p k^2 U / \ln(Z/Z_o)) \partial\theta / \partial \ln(Z) \quad (9)$$

$$LE = (-Lk^2 U / \ln(Z/Z_o)) \partial q / \partial \ln(Z) \quad (10)$$

where

H = turbulent flux of sensible heat (cal cm^{-2} min^{-1})

LE = turbulent flux of latent heat (cal cm^{-2} min^{-1})

k = von Karman constant (dimensionless)

θ = potential temperature (^{o}C)

σ = air density (.00123 gm/cm^3)

C_p = specific heat at constant pressure (.240 cal g^{-1} $^{o}C^{-1}$)

L = latent heat of evaporation (597.3 cal g^{-1})

Z = distance from interface (cm)

q = specific humidity (dimensionless)

U = wind speed (cm/min)

Z_o = roughness length (cm)

The equation for the fluxes of latent and sensible heat are derived assuming that the turbulent diffusivities for heat and water vapor are equal to the turbulent diffusivity of momentum for near neutral stability. The model also assumes that the turbulent fluxes of heat and water vapor are constant with height in the boundary layer. The soil heat flux(es) is represented using the following equation.

$$S = k_s \cdot \partial T_s / \partial Z \qquad (11)$$

where

S = soil heat flux (cal cm^{-2} min^{-1})

T_s = soil temperature (^oC)

k_s = soil thermal conductivity (cal cm^{-1} min^{-1} $^oC^{-1}$)

Z = soil depth (cm)

The calculation of the soil heat flux at any time requires the solution of the one dimensional Fourier heat conduction equation given as:

$$\partial T_s / \partial t = (k_s / \delta_s S_c)(\partial^2 T_s / \partial Z^2) \qquad (12)$$

where

t = time (min)

δ_s = soil density (1.75 gm/cm^{-3})

S_c = specific heat capacity (cal gm^{-1} $^oC^{-1}$)

The value of the specific humidity (q_o) within the canopy is estimated using the following equation;

$$q_o = RH\ (3.74 + 2.64\ (T_o/10)^2) \times 10^{-3} \qquad (13)$$

where

q_o = specific humidity

RH = fraction of total area occupied by transpiring plants

T_o = air temperature (^oC)

The soil thermal conductivity (k_s) and specific heat capacity (S_c) vary as function of the soil moisture. The following two equations are used to predict the variations of k_s and S_c as a function of soil moisture.

$$S_c = 1 \cdot W + .18\ (1 - W) \quad \text{(Munn, 1966)}$$

$$k_s \begin{cases} = .00045 \text{ cal/cm sec } ^oC & \text{if } SA < .20 \\ = .00080 \text{ cal/cm sec } ^oC & \text{if } .40 > SA \geq .20 \\ = .00100 \text{ cal/cm sec } ^oC & \text{if } .60 > SA \geq .40 \\ = .00300 \text{ cal/cm sec } ^oC & \text{if } .80 > SA \geq .60 \\ = .0045 \text{ cal/cm sec } ^oC & \text{if } SA \geq .80 \end{cases}$$

where

W = ratio of the volume of soil moisture to the volume of the soil

SA = ratio of the differences between the observed soil moisture and the soil moisture at the wilting point to the difference between the soil moisture at field capacity and soil moisture at the wilting point.

The variation of k_s and S_c as a function of soil moisture are determined by using information presented in a book by Munn (1966). The equations in the model are transformed into a finite difference format by using the physical model illustrated in Fig. 10. This model defined Z_o (cm) as the roughness length and Z_2 (3000 cm) as a height well above the canopy where the meteorological conditions can be assumed to be relatively constant. The soil temperature at depth "2d" (30.48 cm) is constant for each daily time step while the soil temperature at depth "d" (15.24 cm) is calculated using hourly time steps. The model also assumes that the air temperature is isothermal in the canopy from the surface to height Z_o. The value of the specific humidity at Z_2 (q_z) is constant for each daily time step while the temperature at Z_2 (T_z) is approximated using the following equation:

$$T_2 = \bar{T}_2 + A \cdot \cos\left((\pi/12)(TM + L)\right)$$

where

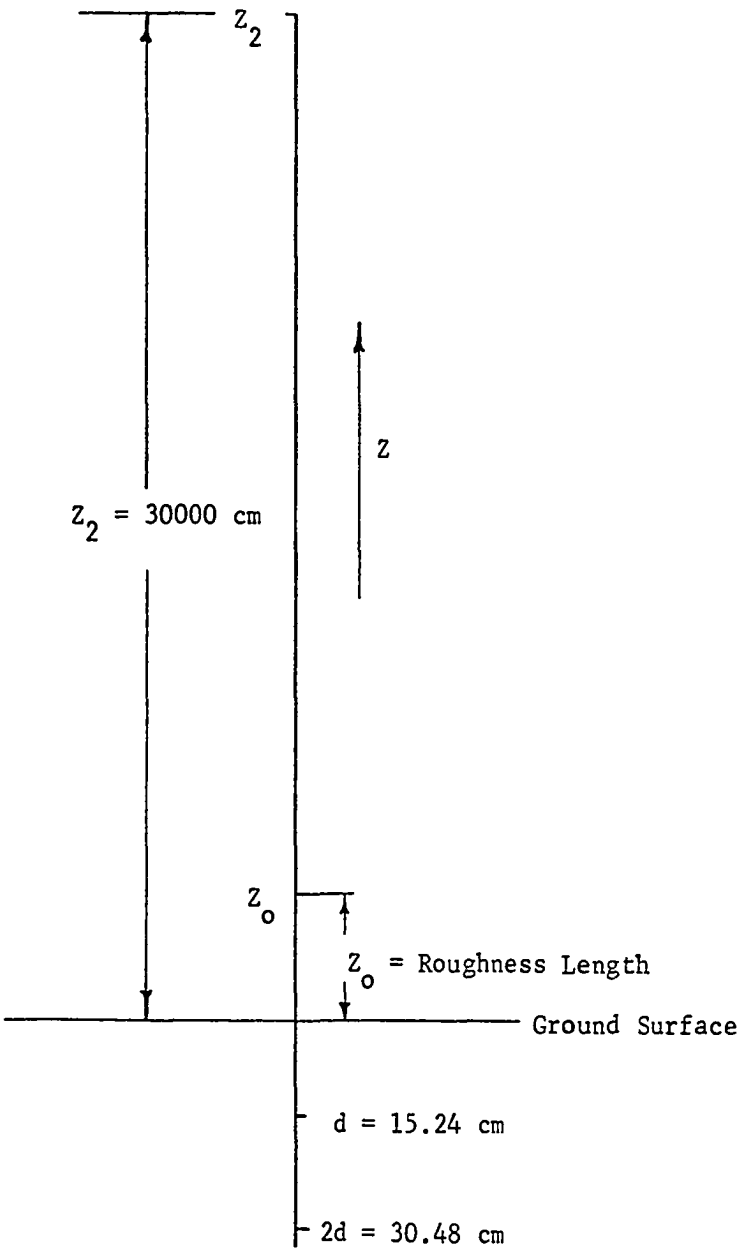

Fig. 10. The physical dimensions of the radiation balance model are presented in this figure.

$\bar{T}_2$ = average daily temperature at 30000 cm (^oC)

TM = time of day (hours)

L = lag of maximum temperature at 1000 ft (6 hours)

A = amplitude of cosine wave (nondimensional)

The phase of the cosine wave is such that the maximum temperature will occur in the late afternoon. Using this model, the finite difference equations for Eq. (9), (10), (11), (12) become:

$$H = (-\delta C_p k^2 U_2/(\ln(Z_2/Z_o))^2)(T_2 + \Gamma_d Z_2 - T_o) \tag{14}$$

$$LE = (-Lk^2 U_2/(\ln(Z_2 Z_o))^2)(q_2 - q_o) \tag{15}$$

$$S = (-k_s/d)(T_s - T_o) \tag{16}$$

$$T_s = (k_s/\delta_s s_c d^2)[(T_o^1 + 2T_b - 2T_s^1)\cdot\Delta t^1/(1 + \Delta t\cdot k_s/(\delta_s s_c d^2))] + T_s^1/(1 + \Delta t\cdot k_s/(\delta_s s_c d^2)) \tag{17}$$

where

Γ_d = dry adiabatic lapse rate ($.0001^oC\ cm^{-1}$)

U_2 = wind speed at 30000 cm (cm/sec)

T_o = air temperature within the canopy for time "t" (^oC)

q_2 = specific humidity at Z_2

q_o = specific humidity within the canopy

T_s = soil temperature at depth "d" for time "t" (^oC)

T_b = soil temperature at depth "2d" (^oC)

T_s^1 = soil temperatures at depth "d" for time t - Δt (^oC)

T_o^1 = air temperature within the canopy at time t - Δt (^oC)

Δt = integration time step (3600 sec)

Δt^1 = integration time step used to solve for T_s (1800 sec)

Equation 3, 4, 5, 6, 8, 13, 14, 15, 16, and 17 comprise a complete set which can be solved for T_o by determining the roots of a quadratic equation. The input parameters needed to solve the model include:

1) date, latitude and atmospheric transmission coefficient.

2) hourly wind speed at 1000 ft, 24-hour average temperature and specific humidity at 1000 ft, average daily suspended particulate concentration ($\mu g/m^3$) and the average daily soil temperature at 12 inches (T_b).

3) roughness length, soil heat capacity and conductivity, and the fraction of the total area occupied by transpiring plants (RH).

The average cloud cover and hourly wind speed at 1000 ft are predicted by the atmospheric model. The average values of T_2, q_2 and T_b are predicted using monthly climatology data that is linearly interpolated to determine daily values. The value of RH is approximated by using the ratio of actual evaporation rate to the potential evapotranspiration rate (see Hydrology Model) on the previous day, while the suspended particulate concentration is estimated from the air pollution model. The other parameters are fixed by the physical characteristics of the given location.

The effect of suspended particulate matter on incoming solar radiation is indicated by several recent articles. Roach (1961) and Monteith (1966) show that the incoming solar radiation is decreased by 1% for every 10 $\mu g/m^3$ of suspended particulate matter. The above relationship is used in this model to modify incoming solar radiation. The effect of local influences and suspended particulate matter on the infrared radiation loss is also considered in the model by using the F parameter (Eq. 4). The lack of understanding concerning the processes affecting the infrared radiation loss make it difficult to determine reasonable values for F.

This lack of understanding is illustrated by comparing two articles which discuss the effect of particulate matter on the IR_n radiation balance. An article by Roach (1961) indicates that the haze layer has the effect of warming up the air while an article by Shepard (1958) indicates that the haze layer has the effect of cooling the air. Consequently, in the present study, the F parameter in Eq. 4 is used to estimate the consequences of modifying the infrared heat loss.

The output from the radiation balance model includes an hourly forecast of air and ground temperature, the solar radiation, and the net radiative heat flux at the interface on a 20 x 20 grid network.

Urban Wind Model

The urban wind model is developed to simulate the wind field generated by the urban heat island. The urban heat island refers to the urban rural temperature difference studied by many authors Duckworth and Sandberg (1954), Sundborg (1950), and Bronstein (1968). The results of the articles indicate that the urban temperature excess is greatest in the early morning hours with light wind and clear sky conditions. The wind pattern induced by the urban rural heat island is dynamically similar to the sea breeze circulation. The urban wind pattern is considered as a perturbation on the large scale wind pattern and is primarily significant when the large scale wind speed is less than 5 kts. An article by Pooler (1963) gives observed data which indicate that the urban heat island wind pattern can be significant when the large scale pressure gradient is weak (wind speed < 5 kts).

Figure 11 illustrates an idealized model of the temperature structure associated with the urban rural heat island. This model assumes that the air within the heat island bubble (see Figure 11) is warmer than the environmental air outside of the bubble. The air temperature decreases from a maximum value at the center of the heat island bubble to the environmental temperature at the edge of the bubble. Outside of the urban rural heat island bubble the temperature is assumed to be horizontally homogeneous and to have a constant lapse rate. This simplified model is based upon observed data presented in articles on the urban rural heat island written by Duckworth (1954) and Bronstein (1968). The pressure pattern at the surface of the heat island bubble is calculated by using equation 18 and assuming that the pressure is constant on a horizontal surface tangent to the top of the heat island dome.

$$P_i(x,y) = P_o(1 - \delta_o Z(x,y)/T_o)^{g/R\delta_o} \cdot (1 - \delta_i(x,y) \cdot z(x,y)/T_i(x,y)) \qquad (18)$$

where

$P_i(x,y)$ = pressure at a point (x,y) (mb)

P_o = surface pressure outside of the dome (1000 mb)

δ_o = environmental lapse rate (.00003 $^\circ$K cm^{-1})

$z(x,y)$ = height of the dome at point (x,y) (30000 cm)

T_o = surface temperature outside the dome ($^\circ$K)

$\delta_i(x,y)$ = lapse rate inside the dome at point (x,y) (.00006 $^\circ$C cm^{-1})

g = specific gas constant (.8704 x 10^6 erg gm$^{-1} \cdot$C^{-1})

$T_i(x,y)$ = surface air temperature within the dome at point (x,y).($^\circ$C)

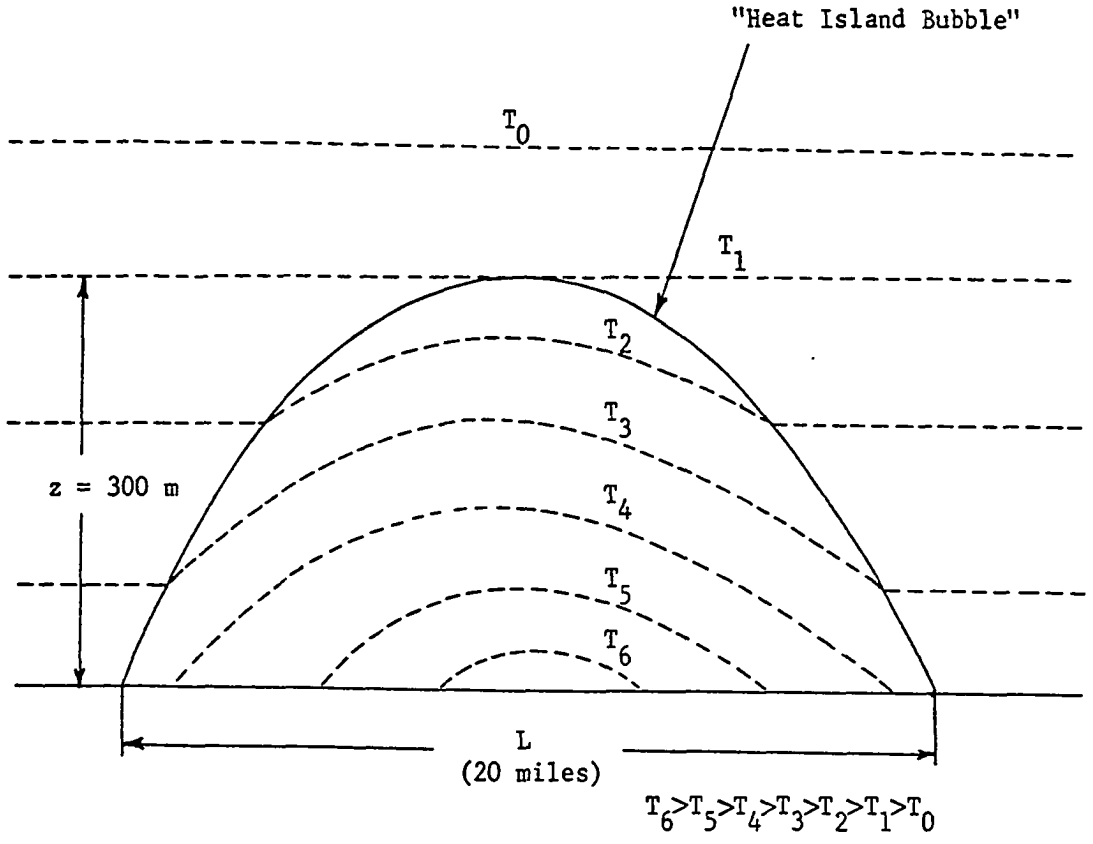

Fig. 11. Temperature structure of the urban heat island (dashed lines are isotherms).

Equation 18 is not valid if $\delta_o = 0$ or $\delta_i(x,y) = 0$; therefore, equations 19 and 20 are used respectively when $\delta_o < .5$°K/km and $\delta_i(x,y) < .5$°K/km

$$P_i(x,y) = P_o \cdot \exp(-gz(x,y)/RT_o) \cdot (1 - \delta_i(x,y) \cdot z(x,y)/T_i(x,y)) \quad (19)$$

$$P_i(x,y) = P_o \cdot (1 - \delta_o \cdot z(x,y)/T_o)^{g/R\delta_o} \cdot \exp(g \cdot z(x,y)/R \cdot T_i(x,y)) \quad (20)$$

The steady state horizontal equations of motion (equations 21 and 22) are solved in conjunction with the urban heat island surface pressure pattern to calculate the urban wind field.

$$u\partial u/\partial x + v\,\partial u/\partial y - fv + \alpha\ \partial p/\partial x - F_x = 0 \quad (21)$$

$$u\,\partial v/\partial x + v\,\partial v/\partial y + fu + \alpha\ \partial p/\partial y - F_y = 0 \quad (22)$$

where

u = zonal wind component (cm/sec)

v = meridional wind component (cm/sec)

α = specific volume ($gm^{-1}cm^3$)

p = pressure (dyne cm^{-2})

f = coriolis parameter ($.1 \times 10^{-3}$ sec^{-1})

F_x = zonal friction force per unit mass (dyne gm^{-1})

F_y = meridional friction force per unit mass (dyne gm^{-1})

F_x and F_y are function of location in the heat island dome and are given by the following equations:

$$F_x = -K(x,y)u + A(\partial^2 u/\partial x^2 + \partial^2 u/\partial y^2) \quad (23)$$

$$F_y = -K(x,y)v + A(\partial^2 v/\partial x^2 + \partial^2 v/\partial y^2) \quad (24)$$

where K(x,y) (sec^{-1}) is the drag coefficient and "A" ($5 \times 10^6 cm^2 sec^{-1}$) is the horizontal diffusion coefficient. K(x,y) is estimated by using the following equation:

$$K(x,y) = .4\ u^*/(\ln(z_a/z_o(x,y) + \frac{\alpha}{L}(z_a - z_o)z_a \quad (25)$$

where u^*(4.0 cm/sec) is the friction velocity, z_a(400 cm) is the height of the anemometer, $z_o(x,y)$(cm) is the roughness length as a function of location, α(4.6) is a quasi-constant and L(100 m) is the scale height. Values of α, u* and L are determined from tabulated data published in an article by Webb (1970). The roughness length is calculated using Lettau's equation (1969) given below.

$$z_o(x,y) = .5L(x,y).S(x,y)/A(x,y) \quad (26)$$

where

L(x,y) = mean height of the roughness element (cm)

A(x,y) = average horizontal area of the roughness element (cm^2)

S(x,y) = silhouette area of the average roughness element (cm^2)

The urban wind field is calculated using the following steps:

1) Determine the surface temperature inside the heat island bubble by using radiation balance model.

2) Solve for the surface pressure field P(x,y) using equations 18, 19, or 20 and then use equation 25 and 26 to determine the drag coefficient field (K(x,y)).

3) Calculate an initial guess field of u and v and then solve equations 21 and 22 for the final u and v field by using an interactive relaxation procedure.

Details of the relaxation technique and the derivation of the equations used in this model can be found in a report by Holyoke (1970).

Interactions with the Ecosystem

The atmospheric model interacts with the rest of the ecosystem by using the following input parameters:

1) ratio of the evaporation rate to the potential evapotranspiration rate (EVAP/EP).

2) soil moisture from 0 - 24".

3) Air pollution emission rate for the 16 factories (Q_ix-i = 1, 2, ...16)

EVAP/EP is used to estimate the percentage of area freely evaporating water(Radiation Balance model), while the soil conductivity and specific heat capacity are functions of the soil moisture from 0 - 24 inches. The values of Q_ix are determined by the air pollution control model (see the executive routine description) which calculates allowable air pollution emission rates (Q_ix) as a function of the desired production level for industry and the atmospheric parameters (wind speed and direction and cloud cover).

Hydrology Model

The hydrology model is concerned with the aspects of the hydrologic cycle that influence the evolution of an urban-rural ecosystem. Most of the water related parameters considered by the ecosystem are simulated. The structure is based upon empirical relationships derived from a comprehensive literature search. The hydrology model is deterministic

in structure, although the primary input variables are simulated by the basically stochastic atmospheric model.

The parameters predicted by the hydrology subsystem are listed below:

potential evapotranspiration
evaporation from soil surfaces
evaporation from the lake surface
storm runoff
infiltration
soil moisture for two layers (0-24" and 25-48")
ground water recharge
lake level
river system flow rate
water pollution

The time scales of most of the hydrology parameters are the same as the time scales of the affecting atmospheric variables. River and stream flow rates and water pollution are predicted for specific points along the river system using hourly time steps, while the remaining parameters are simulated for each grid point of a 32 x 32 grid (mesh size = 4 x 4 mi^2) using a 24-hour time step. Figure 3 shows the layout of the river system and the location of lake in reference to the urban area. Figure 12 shows a flow diagram of the hydrology model and a complete listing of all of the parameters considered. A detailed description of techniques used to predict the various parameters will follow.

Potential Evapotranspiration is defined as the amount of evaporation which would occur were there an adequate soil moisture supply at all times. A review of the literature indicates that there are a variety of methods for estimating potential evapotranspiration rate (Chow, 1964; Koler and Richards, 1962; Cartmill, 1970). Penmans format (1948) is used in this model because it estimates the potential evapotranspiration rate on a daily basis as a function of several of the meteorological

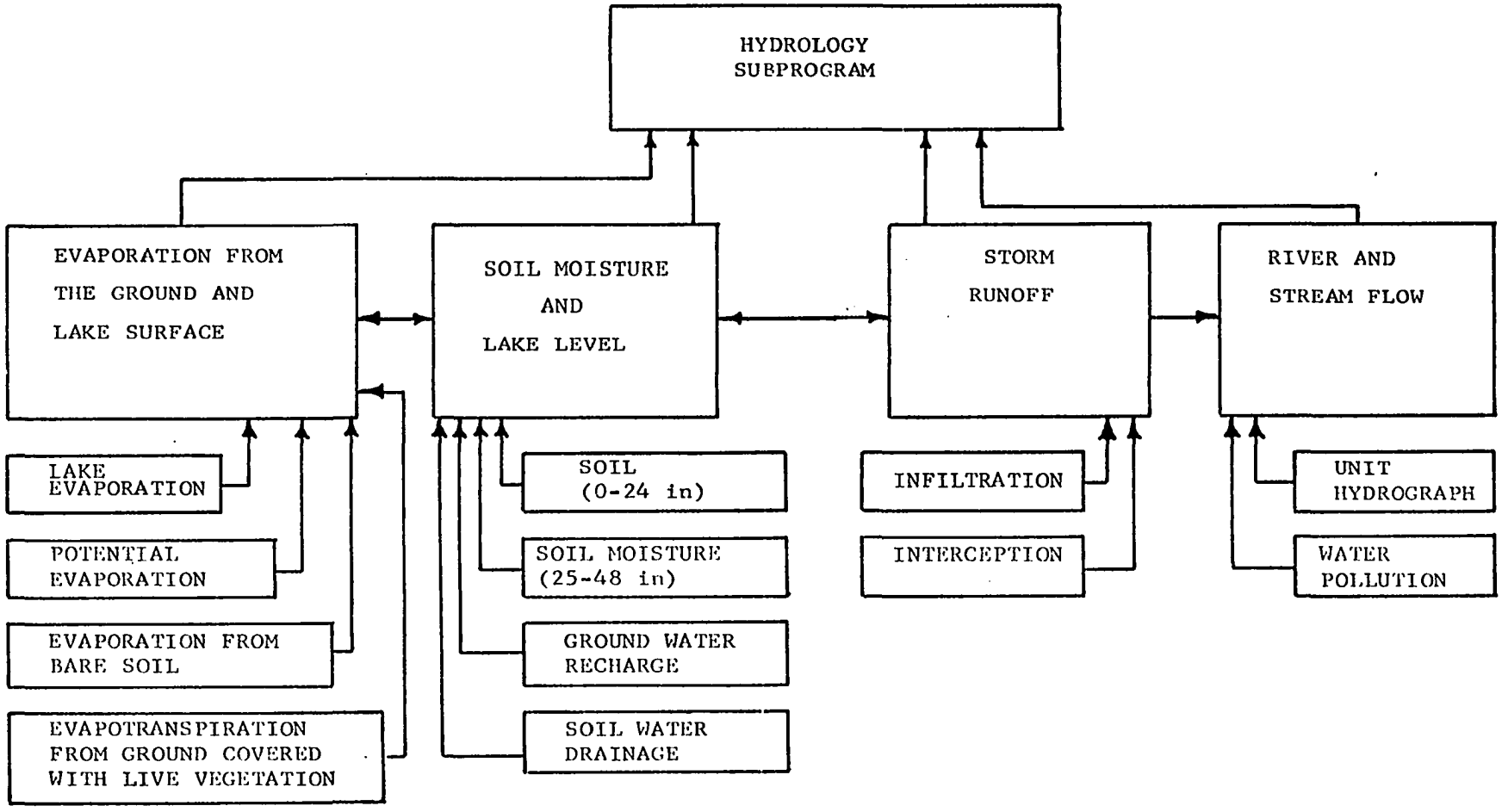

Fig. 12. Hydrology model flow diagram.

parameters predicted in atmospheric model (wind speed, cloud cover, relative humidity, surface air temperature and solar radiation). Penman's equation is written as:

$$EP = \frac{AH + .27\ E}{A + .27} \qquad (27)$$

where

$$E = .35(C_a - C_d)(1 + 0.0098W_z)$$

$$H = R(1-\gamma)(0.18 + 0.55CL) - B(0.56 - .092C_d^5)(0.10 + 0.90CL)$$

EP = evapotranspiration (mm/day)

H = daily heat budget at surface (mm/H_2O)

E = daily evaporation (mm)

A = slope of saturated vapor pressure curve of air at absolute temperature °F.

C_a = saturation vapor pressure at mean air temperature in mmHg

C_d = actual vapor pressure in mmHg

W_z = mean wind velocity at 2 meters above the ground in miles/day

R = mean monthly extraterrestrial radiation in mm of water evaporated per day

γ = albedo of the surface (.20)

CL = the percentage of time when there was no cloud cover (0-1)

B = a coefficient depending upon the air temperature ($B = \sigma T^4$ where T equal the average air temperature in °K and $\sigma = 2.01 \times 10^{-9}$ mm/day)

Evaporation rate is shown to be a function of many parameters. Cowan (1962) indicted that the evaporation rate is a function of root density, potential evapotranspiration rate and the soil water potential. Denmead and Shaw (1962) found that the evaporation rate is

a function of soil moisture content, and potential evapotranspiration rate, while Gardener (1960) indicated that evaporation rate is a function of soil suction, suction in the leaf, soil water content and soil type. Cooper (1969) indicates that the evaporation rate is equivalent to the potential evapotranspiration rate until the soil water potential decreases below -4 bars. Zahner (1966) showed that for soil water potential less than -4 bars, the evaporation rate is almost proportional to the moisture content of the soil for soil moisture conditions down to the wilting point. This model uses the ideas presented by Cooper (1969) and Zahner (1966) to estimate evaporation rate. The evaporation rate proceeds at the potential evapotranspiration rate until the soil water potential decreases below -4 bars. The evaporation rate then decreases linearly as a direct function of the ratio of available soil moisture to the available soil moisture capacity. The available soil moisture is equal to the difference between the actual soil moisture content and the soil moisture content at the wilting point. The available soil moisture capacity is equal to the difference between the soil moisture content at the field capacity and the soil moisture content at the wilting point. Figure 13 presents a graphical representation of this model for the soil types considered. The evaporation rate for a given soil type is calculated by using the ratio of the available soil moisture to the available moisture capacity (Figure 13) to determine the ratio of the evaporation rate to the potential evapotranspiration rate (EVAP/EP). The evaporation rate (EVAP) is then determined by multiplying EVAP/EP by the predicted rate of potential evapotranspiration. The method outlined above is used to estimate the evaporation rate of

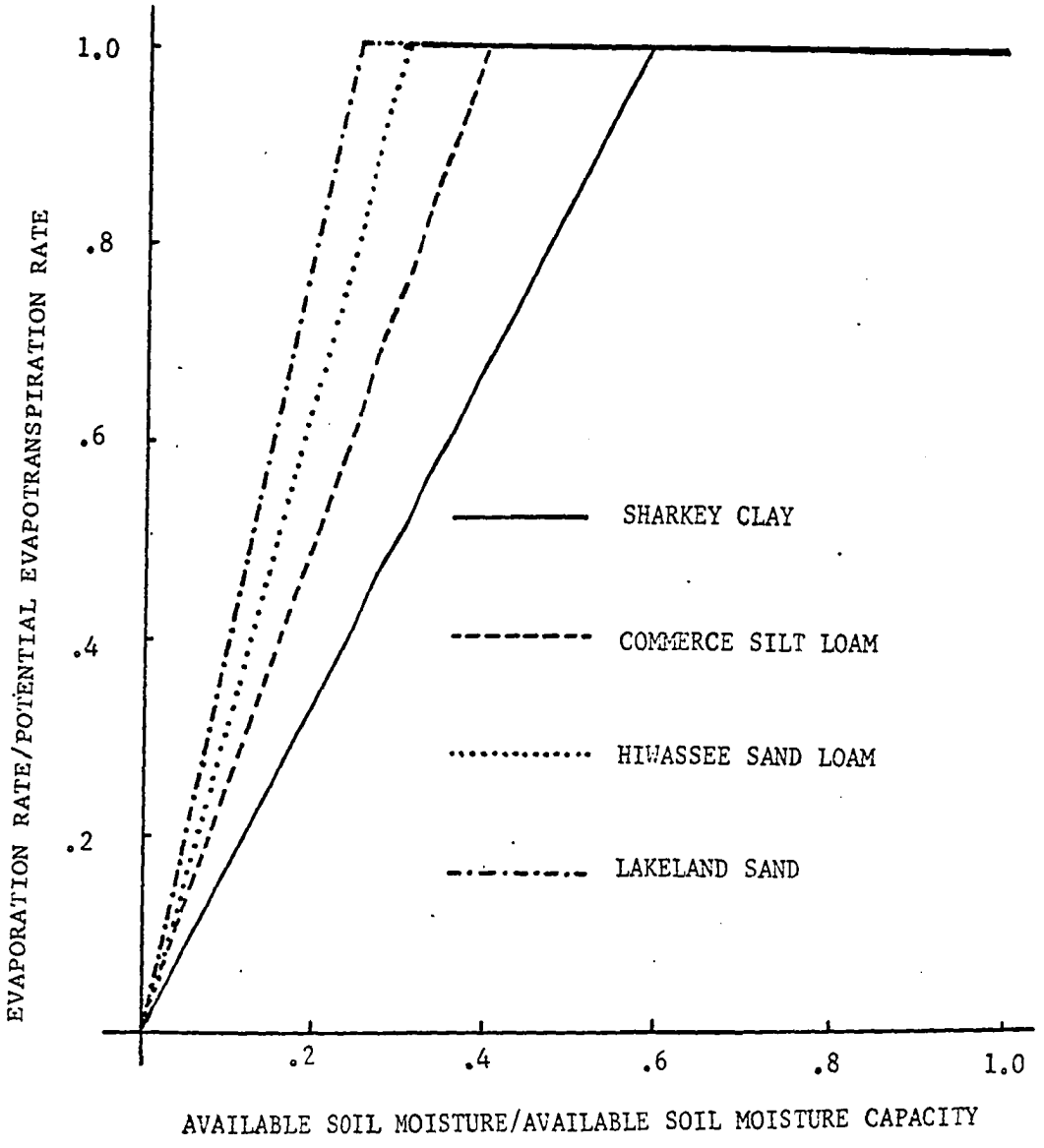

Fig. 13. Graph used to estimate evaporation rate as function of available soil moisture and soil type. This graph is based upon information presented in articles by Cooper (1969) and Zahner (1966).

water from land surfaces that are covered with live vegetation (transpiration water loss). A method of estimating evaporation rate from bare soil and soil that has non-live vegetation (EVAES) is devised from information in a paper by Cooper (1969). The technique used is to evaporate at the potential evapotranspiration rate until the available water in the top 6 inches of soil (ES_{12}) is evaporated and then set the rate equal to zero. This model does not consider the upward transfer of water by capillary action or water vapor transfer. The soil moisture characteristics for the four soil types considered by the model are presented in Table 3.

Evaporation from the lake surface is calculated from Equation 28 (Harbeck, 1954).

$$EVAPI = .00177\ w(e_w - e_a) \cdot 1.15 \qquad (28)$$

where

EVAPI = evaporation (inches/day)

w = mean wind speed (mph)

e_w = maximum vapor pressure (mb) at the lake surface

e_a = actual vapor pressure (mb) of the air at 1.5 meters

Storm runoff can be predicted using a variety of techniques (Kohler and Richards, 1962; Cartmill, 1970; Palmer, 1965; and Chow, 1964). This model uses a technique suggested by the U.S. Soil Service (1957). Equation 29 predicts storm runoff as a function of total storm rainfall, land use, hydrologic conditions of the soil and soil type.

$$RN = \frac{(P - .2S)^2}{P + .8S} \qquad (29)$$

TABLE 3

SOIL MOISTURE CHARACTERISTICS FOR THE FOUR SOIL TYPES CONSIDERED IN THE MODEL

Soil Characteristics	SOIL TYPES: Sharkey Clay	Commerce Silt Loam	Hiwassee Sandy Loam	Lakeland Sand
Wilting Point (soil moisture % by volume)	26	9	10	5
Field Capacity (soil moisture % by volume)	41	27	18	9

TABLE 4

This table[1] illustrates the variation of the "S" factor in Equation 29 as a function of soil type and the hydrolic condition of the soil.

Soil Type	PASTURE LAND with Poor Hydrologic Conditions	Fair Hydrologic Conditions	Good Hydrologic Conditions	Bare Soil
Sharkey Clay	89	84	80	89
Commerce Silt Loam	86	79	74	87
Hiwassee Silt Loam	79	69	61	82
Lakeland Sand	68	49	39	72

[1] The values of "S" illustrated in this table are presented in Chow's (1964) book.

where

RN = storm runoff (inches)

P = total storm rainfall minus the interception (inches)

S = a factor which is a function of soil type, land use, and the hydrological condition of the soil (see Table 4)

Storm runoff from an area that contains streets and buildings (city area) is calculated using the following equation.

$$RNCIT = RN \cdot (1-CIT_i) + RAIN \cdot .80 \cdot CIT_i$$

where

RNCIT = storm runoff from a region that is part of the city.

RN = storm runoff from the region not occupied by the building and streets.

CIT_i = ratio of area occupied by building and streets to the total area for the ith large city block.

RAIN = rainfall on a particular grid point.

Interception is calculated by using Equation 30. This equation is known as Horton's Equation (Bruce and Clark, 1966).

$$INTER = a + bP^n \qquad (30)$$

where

INTER = interception (inches)

P = total storm rainfall (inches)

a,b,n = constants which are a function of vegetation height and type.

(a = .005h, b = .08h, n = 1, h = height of vegetation (ft)--for meadowgrass)
(a = .05h, b = .05h, n = 1, h = height of vegetation (ft)--for small grain crops)

Interception loss is equal to zero for regions that contain bare soil, while the interception water loss by streets and buildings is not considered.

Infiltration is estimated by using Equation 31. This equation is used to determine the total amount of water infiltrated into the soil moisture layer from 0 - 24" for 24-hour time periods. The model layer (0 - 24"), and storm runoff all occur during the same twenty-four hour time period.

$$IN = SR - .85 \cdot INTER - RN \tag{31}$$

where

IN = infiltration (inches)

SR = storm rainfall (inches)

Soil moisture is predicted for a two layer model (0 - 24" and 25 - 48"). This two layer model is used because of empirical field evidence indicating that the soil evaporation loss is confined primarily to the top 24" of the soil (Cartmill, 1970). The soil moisture available for evaporation from the top two layers (SMT, SMB) is predicted using equations 32 and 33.

$$SMT = SMTI - EVAPZ + IN - DRANT + IRG \tag{32}$$

where

EVAPZ = EVAP·ST + EVABS·SBS

SMT = soil moisture in top layer (inches)

SMTI = soil moisture from previous time step (inches)

EVAPZ = evaporation from the soil (inches) by transpiration and by the base soil techniques

DRANT = drainage from the top layer (inches)

IN = infiltration (inches)

IRG = water added to the soil by irrigation (inches)

EVAP = transpiration water loss (inches)

EVABS = water loss from bare soil (inches)

ST = ratio of the area occupied with freely transpiring plants to the total area

SBS = ratio of the area occupied with base soil or dead plants (non-transpiring) to total area (the total area referred to by ST and SBS is the area not occupied by streets and buildings)

$$SMB = SMBI + DRANT - DRANB \quad (33)$$

where

SMB = soil moisture in bottom layer (inches)

SMBI = soil moisture from previous time step (inches)

DRANB = drainage from bottom layer into the ground water (inches)

This simplified model assumes that the recharge rate for the ground water is equal to the drainage from the bottom soil moisture layer. The soil moisture is only simulated for the part of each grid point that does not contain concrete, asphalt or houses.

A literature search indicated that there are a variety of equations for estimating soil moisture drainage (Gardner, 1968; Ogata and Richards, 1957; and Black, Gardner, and Thurtell, 1969). In most of the equations the drainage is a function of soil moisture content and soil type. This model uses Black, Gardner, and Thurtell's equation (1969) for predicting drainage (Equation 34).

$$DRAN = C \cdot EXP(.7(S-D)) \quad (34)$$

where

$$D = (-1.6 + FLD)$$

FLD = the field capacity for the soil type (cm of water for a 24 inch soil layer)

DRAN = drainage from a layer of soil (cm/day)

S = soil moisture for the 0-24 inch layer (cm)

$$C = \begin{cases} .21 \text{ for sharkey clay} \\ .25 \text{ for commerce silt loam} \\ .30 \text{ for Hiwassee sandy loam} \\ .35 \text{ for Lakeland sand} \end{cases}$$

The soil moisture from 0 - 6 inches is also predicted by the model. This soil moisture layer receives water by the infiltration of rain water (Equation 31) and loses water at the potential evapotranspiration rate until evaporation water loss from the layer exceeds the critical value (ES_{12}) that is a function of the potential evapotranspiration rate (ES_{12}=1.0" for $E_p < .08$", ES_{12}=.85" for $.16 > E_p \geq .08$", and ES_{12}=.75" for $E_p \geq .16$"). The evaporation from this layer is set equal to zero after the amount of available water in the layer is less than or equal to ($1-ES_{12}$). Soil water drainage from this layer is not considered. The available soil moisture in the layer is not allowed to be greater than 1 inch and is never allowed to become negative. The available soil moisture does not exceed 1 inch because the model assumes that the field capacity is exceeded with available soil moisture conditions greater than 1 inch. If the available soil moisture exceeds 1 inch, then the excess water (available soil moisture - 1 inch) drains into the lower layer (soil moisture from 0 - 24 inches). The soil moisture from 0 - 6 inches is calculated independent of the soil moisture from 0 - 24 inches and 25 - 48 inches.

The lake level is estimated using equation 35. This model assumes

that the lake has a constant area and uniform depth of water and no water flux through the bottom or sides.

$$LK = LKI - EVAPI/12 + RN + RNET \tag{35}$$

where

LK = lake level (feet)

LKI = lake level from previous time step (feet)

EVAPI = evaporation from lake surface (inches)

RN = runoff into the lake (feet)

RNET = change in the lake level due to difference between the flow of water into the lake and the flow of water from the dam into the river (feet)

The river and stream flow rates are calculated at seven specific points along the river system using a two hour time step. The flow rates are determined by breaking the ecosystem up into small watersheds of about 900 sq miles and then calculating the contribution each watershed made to the stream flow rates. The streams then flow into the river. Figure 14 shows the position of the streams and river and also indicates the location of small watersheds (the area enclosed in the dashed line blocks are the watershed areas). Water flows into the lake (Point 1) at a constant rate (Function of time of year) and then flows out of the dam into the river (Point 2) at a rate controlled by the water control model (see description of Executive Routine). The water control model also determines the amount of water used by the consumers. The water used by the consumers (city, industry and agriculture) is taken out of the river just below the dam, while the water pollution emitted and water returned by consumers is emitted into the river at

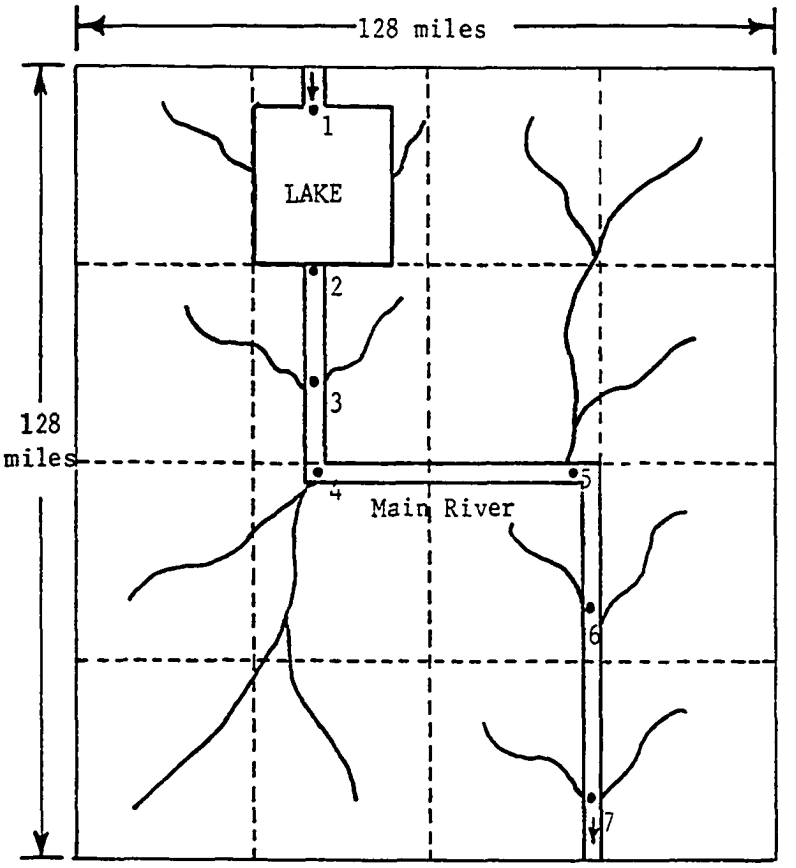

Fig. 14. The physical characteristics of the hydrology model are presented in this figure. The area enclosed in the dashed line blocks are the watershed areas. Numbers 1-7 refer to the points along the river where river flow is calculated.

this same point. The water pollution emitted at this point is simply advected down the river without modifying the water pollution concentration. The individual watersheds use the synthetic unit hydrograph proposed by Mockus (1957) to estimate the flow rate vs time for each rain storm. Figure 15 illustrates the synthetic unit hydrograph used in the model. The flow rate vs time is determined from Figure 15 by using the values of q_p and T_p determined from the following equations.

$$q_p = \frac{484\ AQ}{T_p} \tag{36}$$

$$T_p = .5D + 2.4D_e^2 \tag{37}$$

where

q_p = peak rate of flow for a given storm (CFS)

A = drainage area (sq mi)

Q = average runoff in inches

D_e = unit hydrograph storm duration (number of hours that rainfall is observed)

T_p = elapsed time from the beginning of the hydrograph to the peak flow rate

D = duration of excessive rainfall ($D_e/3$)

Equations 36 and 37 are presented in Chow's Handbook of Applied Hydrology (1964). The value of D_e if assumed to be equal to the predicted duration of the rain storm. Values of q_p and T_p are calculated for the different watersheds and are then used in conjunction with the unit hydrograph (Figure 14) to calculate the flow rate vs time for each watershed that reports measurable storm runoff. The start of water flow out of a watershed for a particular storm is delayed TMI/2

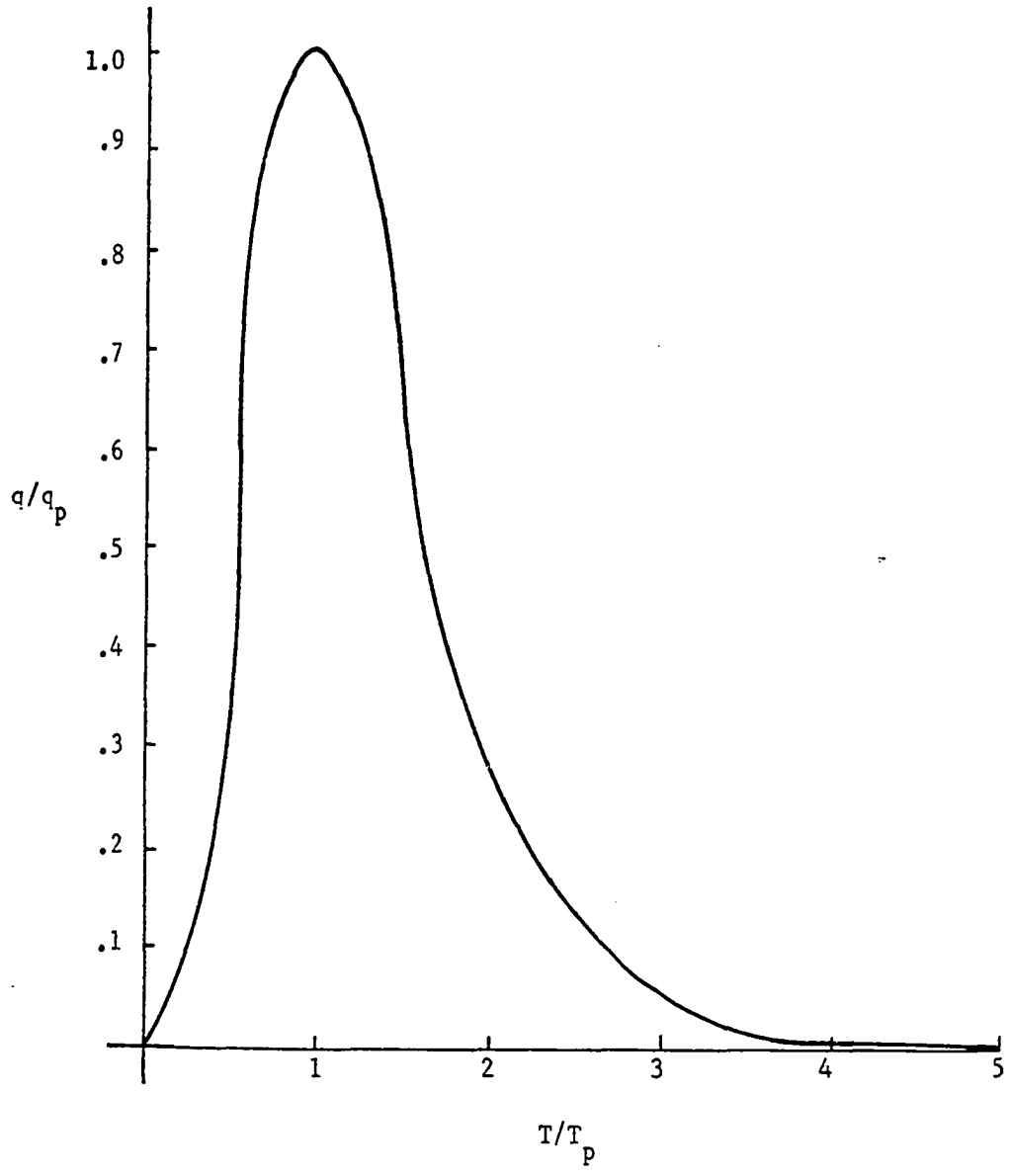

Fig. 15. Non-dimensional unit hydrograph where q = rate of flow, q_p = peak rate of flow, T = time from beginning of hydrograph rise, and T_p = T at peak rate (from Mockus, (1957)).

(TMI = time period when rainfall occurs-hours) after the rainfall starting time. The atmospheric model predicts the starting time and duration for all the rain storms. The progressive average lag technique is used to route the water down the streams and through the river. This technique predicts the water flow at the downstream point by smoothing the unit hydrograph at the upstream point using a running mean over "n" hours (n=6 for the streams, n=10 for the river) and then lagging the modified unit hydrograph by the number of hours it takes for the water to travel from the upstream point to the downstream point.

Interaction with the Ecosystem

The Hydrology model interacts with the ecosystem by using the following input parameters:

1) rainfall, relative humidity, cloud cover, wind speed, and average air temperature.
2) state of the plants (live or dead), height of the plants, and the amount of water being added to the soil by irrigation.
3) water flowing from the dam and the amount of water flowing at point where the consumers take their water out of the river.
4) the percentage of area in each grid point (mesh size=4x4 miles^2) that contains streets and buildings

The parameters in 1), 2), 3) and 4) are simulated by the atmospheric model, botany model, water control model (see Executive Routine description) and the Urban model respectively.

Urban Model

The urban model is organized to simulate population dynamics, changes in the characteristics of identifiable societal subgroups, land use, and industrial development of an urban area. The model is primarily concerned with the population dynamics and the growth of a city. The city has specific boundaries and is divided into suburbs which have boundaries within the city. Both the city and suburb boundaries move in response to the evolution of the urban area. Each suburb has city blocks within it, and a "statistical man" representing individuals in a particular suburb. Subroutines determine the population for every city block and the characteristics of each individual in the city. Attributes are subdivided into different classes and a histogram of classes is maintained showing the number of people in each class for each suburb. The characteristics given a statistical man are chosen from a frequency distribution of properties associated with the suburb in which he lives. The model provides two mechanisms (diffusion and discontinuous movement) that allow a statistical man to move in response to the environmental 'livability' of his suburb. Each suburb in the city keeps records of the local population total, frequency distribution of characteristics, housing distribution, birth rates and death rates. This urban model uses both stochastic and deterministic processes in the simulation of evolution of the different parameters considered. Some aspects of the structure of the model have been influenced by Forester's Urban Dynamics Model (1970).

The urban model is designed to consider the evolution of an urban area for periods of time up to 30 years by using one year time steps.

The model can handle an urban area which is contained within a 36 x 26 sq mi region. The model uses a large scale 6 x 6 grid (mesh size 6x6 mi^2) in which each grid point is considered a large city block. Each large city block is subdivided into a small scale 16 x 16 grid (mesh size .38x.38 mi^2) in which each grid point is considered a small city block. Small city blocks are used as the basic grid size in population dynamics of the urban model.

The flow diagram of the urban model (see Figure 16) partitions the model into five different sections which include: 1) statistical man, 2) city and suburb boundaries, 3) suburb dynamics, 4) population dynamics and 5) industry. Each of these sections will be described in detail and the interactions between them will be emphasized.

Statistical Man

A "statistical man" is defined in the model as an individual who has seven attributes to describe him. These seven attributes include:

age
sex
race
educational level
occupation
family income
health

Each of these attributes is divided into different class intervals. Age is divided into seventeen five-year categories and one category for those over 85. Sex and race are both divided into two class intervals (sex -- male, female; race -- white, non-white). Educational level is divided into eight classes which consider the number of years of school

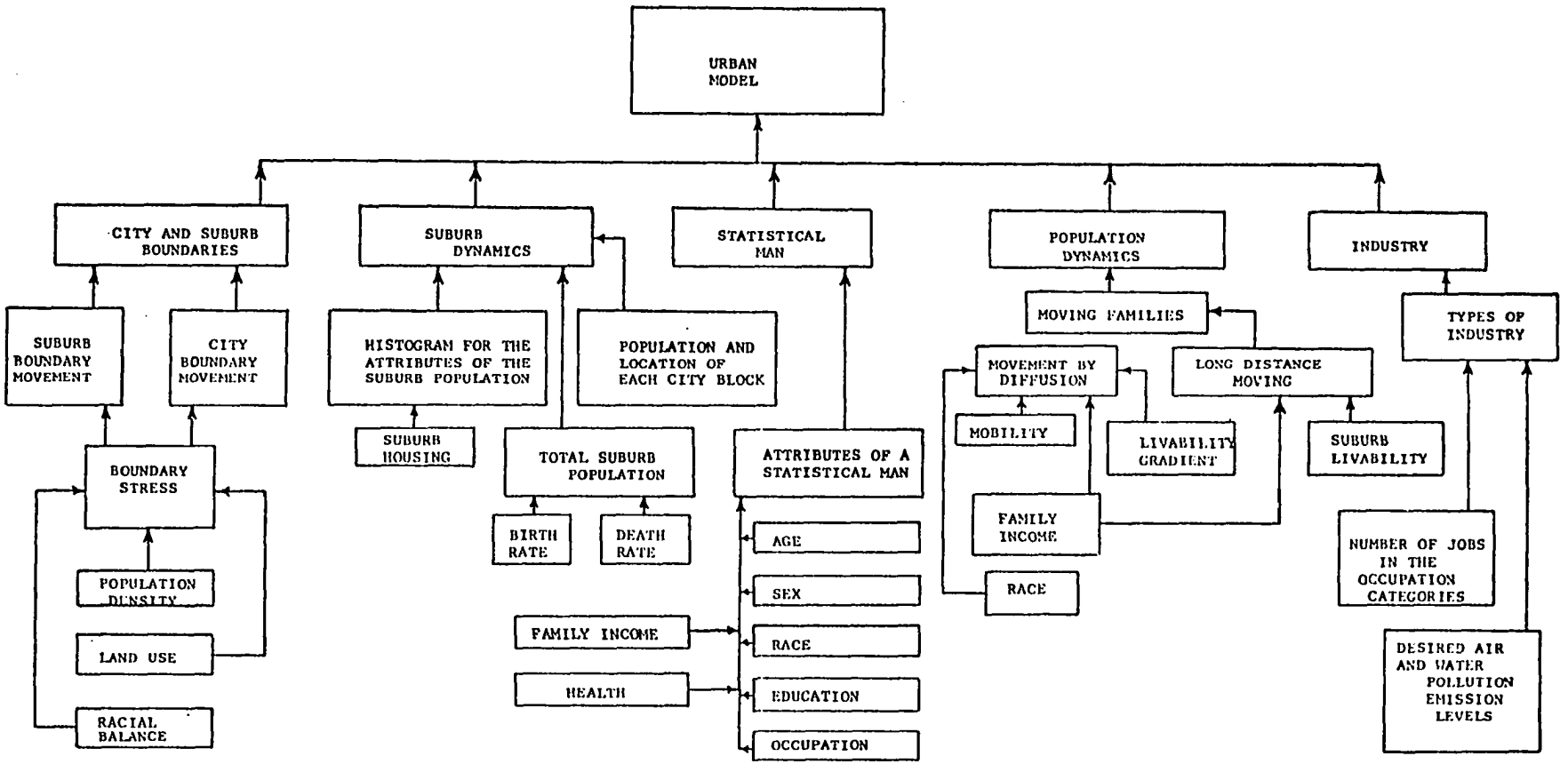

Fig. 16. Flow diagram of the Urban Model.

completed. Occupation is divided into four class intervals that include: managerial-professional, worker, underemployed and unemployed. The family income is divided into 14 categories of total yearly family income. The mortality rate per thousand population is the health parameter which is divided into six class intervals of mortality rate. The individual suburbs maintain histograms that record the number of people in each class interval associated with seven attributes of the people living within the suburbs. These histograms are used to calculate the frequency distributions of the properties of the people in each suburb.

When people in the city move from one suburb to another, they carry their seven attributes with them. The attributes of an individual are selected from the frequency distribution of the attributes associated with the suburb from which he is moving by using the following statistical scheme. The race, sex, educational level, health and age class interval of an individual are selected by using random process in conjunction with the frequency distributions of these attributes. The individual's status in the working force (member or non-member) is determined as a function of age and sex. If an individual is less than 15 years old, he is considered a non-member of the working force (unemployed). The status of people $\geq$ 15 years old is determined by using frequency distributions which relate the sex and age of an individual to position in the working force. The status category is chosen by using a random process in conjunction with the frequency distribution that corresponds to the sex and age of the individual. If an individual is a non-member of the working force, his expected family income is chosen by using a

random process in conjunction with the income frequency distribution of the individual's suburb. If the individual is a member of the working force, his income is chosen as a function of his education and age. This is accomplished by using frequency distribution that corresponds to the age and education of the individual. An individual who is a non-member of the working force is assigned to the unemployable occupation class interval. The occupation of the members of the working force are chosen as a function of sex and income by using frequency distributions that relate sex and income to the occupation of an individual. The occupation category is chosen by using a random process in conjunction with the frequency distribution that corresponds to the sex and family income of an individual. The present model provided for movement of people in groups of three. If an individual is selected to move to another suburb, he takes with him two other people that have the same race, wealth, education, family income and health. The attributes of age and sex for the two other individuals will be chosen randomly from the appropriate suburb frequency distributions of age and sex, while the occupation of the two individuals is set as unemployable. The movement of three people at a time is designed to simulate the movement of family units. The family units that move by this technique have a finite possibility of being all female or all male. The technique for moving family units is designed to minimize the computer time needed to move the people around the city. When a group of individuals move from one suburb to another, they take their attributes from and place them in the histogram of the attributes for the suburb they are moving to.

Individuals born in each suburb are given attributes randomly selected from the frequency distribution of attributes associated with each suburb. When an individual dies in the system, his attributes (other than age) are selected randomly from the suburb's frequency distribution of attributes and then removed for the histogram of attributes associated with the suburb. The age of a dead person is determined by the process described in the suburb dynamics subsection. The model is organized so that newborn people in the suburb can have their attributes chosen from frequency distributions associated with suburbs other than their own.

City and Suburb Boundaries

The urban model defines the city and suburb boundaries using the basic grid network that is used to define the population of the city. Each "small city block" is classified by means of a numerical code. Three classes exist: part of a particular suburb at present, a potential portion of a suburb once the city has expanded to include the block, or zoned for non-urban use. A suburb boundary is defined between two adjacent city blocks when the code of two city blocks indicates that the blocks are in different suburbs. Similarily, a city boundary is defined when the code of two adjacent blocks indicates that one of the blocks is part of the city and the other block is not.

The city and suburb boundaries move in response to the gradient of stress across the boundary. The boundary stress is a function of population density, land utilization, and racial balance. Equation 38 is used to calculate the gradient of stress.

$$\nabla_{xy} L_B = A \cdot \nabla_{xy}(LV) + B \cdot \nabla_{xy}(PD) + C \cdot \nabla_{xy}(RB) \qquad (38)$$

where

L_B = livability at the boundary between suburbs

A,B,C = control constants (A=100, B=2.0, C=40)

PD = population

LV = % of land occupied by houses in a suburb

RB = non-white population %

$$\nabla_{xy} = i\frac{\partial}{\partial x} + j\frac{\partial}{\partial y}$$

The boundary between two adjacent small city blocks moves one city block toward the region with better livability conditions if the critical value (100) of the gradient of boundary stress between the two is exceeded. If the boundary stress between a particular grid point and the points that surround it is exceeded for more than one of the surrounding grid points the boundary moves in the direction of the grid point with the highest boundary stress. This process adds a new city block to the suburb that has the higher value of stress. The original population of this block is removed and randomly distributed in the suburb that lost the land. The block is then given a population equal to the original population plus one-half of the population discontinuity at the original suburb boundary. The new people for this city block are selected randomly from the population of the suburb that has just gained the land. The boundaries of the suburbs are allowed to move in the city and out into any portion of the rural area which is zoned for potential urban use. For testing purposes, 6 x 6 mi^2 blocks adjacent to the city are zoned for expansion if the gradient of the

boundary stress along a 6 mile section adjacent to the city exceeds a critical level. This critical level will be controlled by the many factors that influence land utilization (industrial land needs, available financial backing for new developments, urban development, etc). The suburb boundary model determines the percentage of each large city block that is occupied by streets and buildings calculated by using the following equation.

$$CIT_i = NCIT_i/256$$

where

$NCIT_i$ = the number of small city blocks in the ith large city blocks that are part of the city

This equation is set up to work with large city blocks that have a mesh size of 4×4 mi^2.

Suburb Dynamics

The urban model divides the city up into basic areas that are known as suburbs. Each suburb is set up so that the attributes of the people within a suburb are fairly homogeneous. Family income and race distribution are the primary factors considered in organizing suburbs as homogeneous regions. The overall characteristics of suburbs within the urban model include:

1. A grid network that defines the suburb population for each "small city block" within the suburbs,

2. A grid network that defines the location of the "small city blocks" contained in each suburb,

3. Histograms that record the number of people within the different categories associated with the attributes of the people within each suburb,

4. Histograms that record the number of housing units for categories of housing,

5. Total suburb population.

The suburb age distribution and total population are controlled by a model that utilizes five year survival rates. Every fifth year the model ages the people five years, allows the population to die as a function of the survival rate, and then assigns the people born into this suburb during the last five years to the 0 - 4 years old age group.

The number of births per year in a suburb is calculated using the annual birth rate and an estimated value of the total population of the suburb that is updated each year. The estimated value of the total suburb population is determined using constant birth rates and death rates for each suburb. The constant death rate used is only an approximate value since the number of deaths determined by the five year survival tables is a function of the age distribution suburb.

The population of the individual suburbs is also modified by people moving from one suburb to another. The total city population is calculated by adding up the population of the individual suburbs. The total population of the city is the primary parameter that determines the desired municipal water utilization rate and water pollution emission rate. The model assumes that the desired value of these rates is a direct function of the total urban population.

The housing submodel uses the classification system suggested by Forrester (1970) and predicts the number of housing units in three housing categories which include:

premium housing
worker housing
underemployed housing

The model assumes that premium housing degenerates into worker housing, while worker housing will degenerate into underemployed housing. The mathematical formulation of the model is summarized by the following differential equations:

$$\frac{\partial}{\partial t}(PH) = P_C \cdot PH - P_D \cdot PH \tag{39}$$

$$\frac{\partial}{\partial t}(WH) = W_C \cdot WH + P_D \cdot PH - W_D \cdot WH \tag{40}$$

$$\frac{\partial}{\partial t}(UH) = W_D \cdot WH + U_C \cdot UH - U_D \cdot UH \tag{41}$$

where

PH = the number of premium housing units (.0015 mi^2 ea)

WH = the number of worker housing units (.001 mi^2 ea)

UH = the number of underemployed housing units (.001 mi^2 ea)

P_C = premium housing construction rate

P_D = premium housing loss rate (aging of premium housing)

W_C = worker housing construction rate

W_D = worker housing loss rate (aging of worker housing)

U_C = underemployed housing construction rate

U_D = underemployed housing loss rate (aging of underemployed housing)

The occupation distribution uses the classification system suggested by Forrester (1970). The occupation of the working class is divided into three classifications which include:

Managerial-professional
Worker
Underemployed

The occupation submodel modifies the occupation distributions of the different suburbs by transferring people in the underemployed classification to the worker classification and people in the worker classification to the managerial-professional classification. Only upgrading of the population is considered in this model. Once the occupational level of an individual is improved, there is no mechanism in this model that will allow the individual to lower his occupational level. The mathematical representation of this model is shown in equations 42, 43, and 44:

$$\frac{d}{dt}(UN) = - I_V \cdot UN \tag{42}$$

$$\frac{d}{dt}(W) = + I_V \cdot UN - I_W \cdot W \tag{43}$$

$$\frac{d}{dt}(MP) = + I_W \cdot W \tag{44}$$

where

UN = number of people in the underemployed classification

W = number of people in the worker classification

MP = number of people in the managerial-professional classification

I_V = underemployed to worker transfer rate

I_W = worker to managerial-professional transfer rate

This model uses the occupation classification system suggested by Forrester (1970).

The occupation classification of an individual is highly correlated to the educational level and income of an individual. This correlation makes it necessary to modify the education distribution and income

distribution when the occupation distribution is modified. This model considers that people in the underemployed group will have an education level below the seventh grade and a yearly income less than $5000. People in the worker classification will have an educational level above the eighth grade but below a high school degree and an income greater than or equal to $5000 but less than $10,000. People in the managerial-professional level will have an education level greater than a high school degree and an income level greater than or equal to $10,000. The above classifications are used in conjunction with the following differential equations to modify the education and income distribution.

$$\frac{d}{dt}(E_1) = - I_V \cdot E_1 \tag{45}$$

$$\frac{d}{dt}(E_2) = + I_V \cdot E_1 - I_W \cdot E_2 \tag{46}$$

$$\frac{d}{dt}(E_3) = + I_W \cdot E_3 \tag{47}$$

$$\frac{d}{dt}(I_1) = - I_V \cdot I_1 \tag{48}$$

$$\frac{d}{dt}(I_2) = I_V \cdot I_1 - I_W \cdot I_2 \tag{49}$$

$$\frac{d}{dt}(I_3) = + I_W \cdot I_3 \tag{50}$$

where

E_1 = number of people with education level < eighth grade

E_2 = number of people with education level $\geq$ eighth grade but $\leq$ high school level

E_3 = number of people with education level > high school level

I_1 = number of people with income < \$5000

I_2 = number of people with income $\geq$ \$5000 but < \$10,000

I_3 = number of people with income $\geq$ \$10,000

I_V = underemployed to worker transfer rate

I_W = worker to managerial-professional transfer rate

The first order differential equations used in this section are solved using the Euler finite difference scheme (1 year time steps).

Population Dynamics

The urban model uses a stochastic-deterministic process to predict the movement of people within the city. Families of three are moved around the city using either a diffusion technique or a long distance moving technique. The diffusion technique moves people several blocks at a time while the long distance moving technique can transport people across the city in one relocation. The people change their residence in response to environmental conditions.

The model predicts the movement of people from each of the small city blocks. A specified percentage of the people at each small city block are considered eligible for relocation at each time step. This percentage is a function of the livability of the city block. The functional relationship and the equation for livability are presented in Equations 51(a) and 51 (b). These equations define livability such that high values of livability mean poor living conditions.

$$PM_i = \begin{cases} 2 & \text{if } XLV_i \leq 160 \\ 5 & \text{if } 200 \geq XLV_i > 160 \\ 7 & \text{if } 240 \geq XLV_i > 200 \\ 9 & \text{if } 280 \geq XLV_i > 240 \\ 15 & \text{if } XLV_i > 280 \end{cases} \tag{51a}$$

$$XLV_i = LI \cdot AP_i + L2 \cdot HD + L3 \cdot RD + L4 \cdot PD \tag{51b}$$

where

PM_i = % of people at the ith city block that are eligible for movement

XLV_i = livability for the ith city block

AP_i = average annual air pollution ($\mu g/m^3$) at the ith city block

HD = % of underemployed housing units in the suburb

RD = % of non-white people in the suburb

PD = population per city block

L1,L2,L3,L4 = control coefficients

(L1 = 0.0, L2 = 70., L3 = 100., L4 = .5)

The attributes of each eligible individual are determined using the technique outlined in the section describing the attributes of a statistical man. If the individual has income less than $5000 or if his occupation classification is non-employable then he is not permitted to move in the city. If the individual's income is greater than or equal to $10,000, he is allowed to move using the discontinuous movement technique. Racial discrimination is introduced by permitting only a certain percentage (PR) of the individuals who are non-white and have this income level to move if the diffusion technique takes them

outside of their suburb. If the individual has an income greater than $10,000, the "P" percentage of the people move using the diffusion technique while (100 - P) percentage of the people will move using the long distance moving technique. If an individual is allowed to move, he takes with him two other individuals. If the family moves out of one suburb, they take their statistical attributes with them. The diffusion technique moves people in response to the gradient of livability such that they move toward more desirable regions. Livability gradient is a function of air pollution, housing distribution, population density, and racial distribution and is calculated using Equation 51 (c).

$$\nabla_{xy}(XLV_i) = P_1 \cdot \nabla_{xy}(AP_i) + P_2 \cdot \nabla_{xy}(HD) + P_3 \cdot \nabla_{xy}(PD) + P_4 \cdot \nabla_{xy}(RD) \qquad (51c)$$

where

P_1, P_2, P_3, P_4 = control coefficients

($P_1 = 0.0$, $P_2 = 130$, $P_3 = 6$, $P_4 = 150$)

The livability gradient is found in the form of a magnitude (L) and direction (θ). An ellipse is placed such that one of the foci lies near the position of the individual to be moved and the major axis is oriented using "θ" such that the other focal point lies down the gradient of "L" toward more desirable living conditions. The mobility of a person determines the exact position of the ellipse. Higher mobilities increase the distance from the center point of the ellipse to position of the individual (see Figure 17). The mobility of a

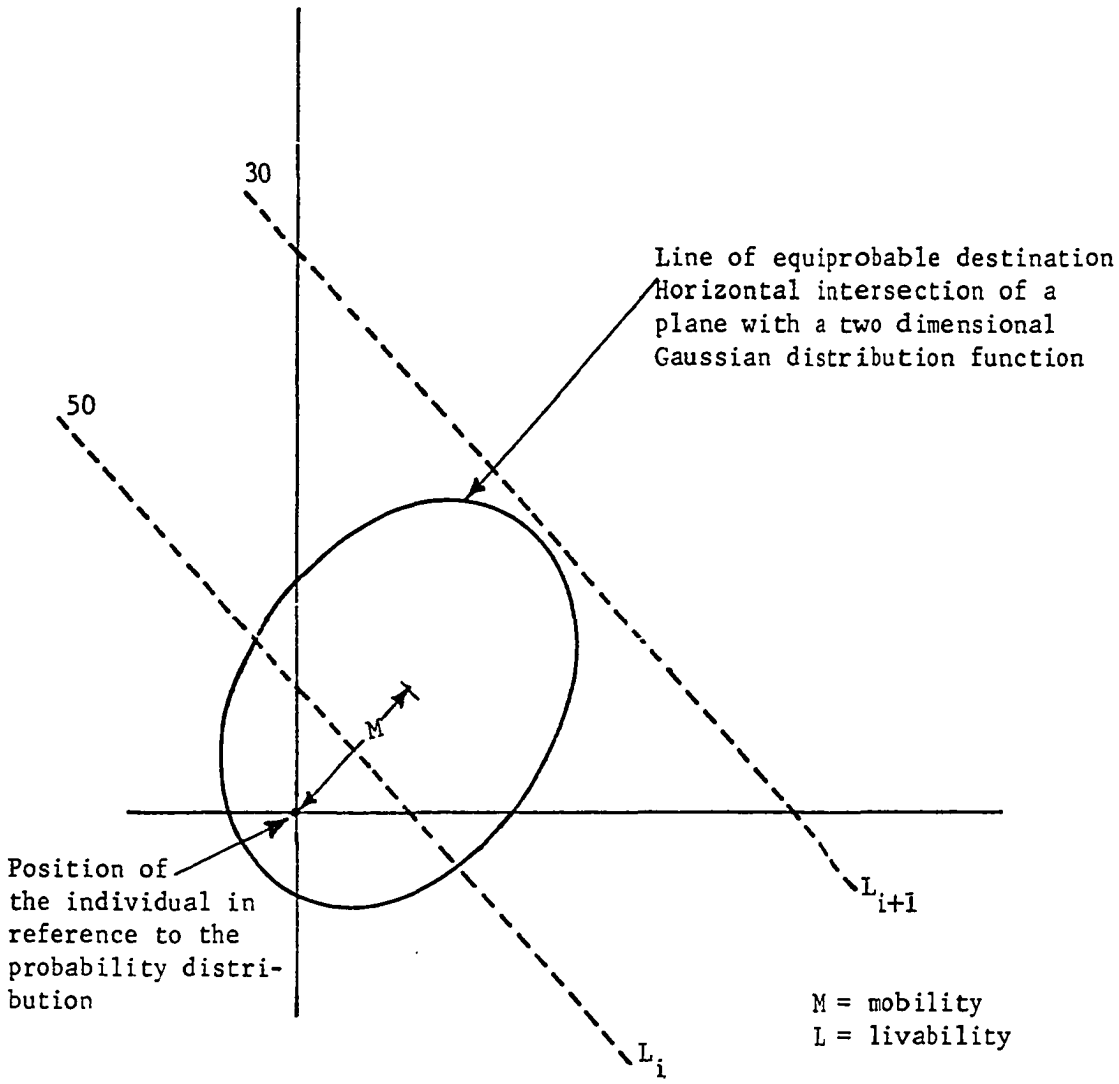

Fig. 17. Position of the probability distribution for movement of people as a function of the mobility of the individual and livability gradient are shown in this figure.

person is defined using Equation 52.

$$M = Z_3 \cdot IN + Z_4 \cdot ED \tag{52}$$

where

IN = income level of an individual

ED = educational level of an individual

M = mobility

Z_3, Z_4 = control coefficients

($Z_3 = .40$, $Z_4 = .40$)

The ellipse is one of a set of lines of equiprobable destination and is defined using Equation 53.

$$P_{xy} = \frac{1}{2\pi\sigma_a\sigma_b} \exp\left[-\tfrac{1}{2}\left\{ \frac{(x \cos\theta + y \sin\theta)^2}{\sigma_a^2} + \frac{(-x \sin\theta - y \cos\theta)^2}{\sigma_b^2} \right\} \right] \tag{53}$$

where P_{xy} is the probability that the individual will move to a position defined by x and y, while σ_a, σ_b define the ellipticity.

The actual move takes place by using a random process in conjunction with the frequency distribution derived from P_{xy}. If the individual moves from his suburb, then a complete set of attributes is transferred from the histogram of his old suburb to the appropriate histogram of his new suburb.

The long distance moving technique transports people directly from suburbs with poor livability conditions to suburbs that have better livability conditions. The attributes of the people chosen for long

distance moving are taken out of the local suburbs histograms and stored in temporary storage array. After the people at all of the small city blocks have been given a chance to move, the people stored in the long distance moving array are distributed randomly in the two suburbs that have the best livability (L_t) with each suburb receiving 50% of the people. The attributes of the new people are then located in the appropriate histograms of the two suburbs. The livability of a suburb is defined by Equation 54.

$$L_{t_j} = \frac{\sum_{i=1}^{M_j} R_1 \cdot Po(i)_j + R_2 \cdot AP(i)_j + R_3 \cdot RD(i)_j}{M_j} \qquad (54)$$

where

L_{t_j} = average livability of the jth suburb

M_j = number of small city blocks in the jth suburb

$Po(i)_j$ = population for the ith city block

$AP(i)_j$ = air pollution for the ith city block

$RD(i)_j$ = percentage of non-white population at the ith city block

R_1, R_2, R_3 = control constants

($R_1 = 1.$, $R_2 = 2.0$, $R_3 = 130.$)

Industry

The industry submodel simulates the industrial development of the urban area. The model is patterned after a model suggested by Forrester (1970). The model divides industry into three categories which include:

new business
mature business
declining business

A new business ages into a mature business, while a mature business ages into a declining industry. The different types of industries employ a specified number of people in each of the three working force occupation categories. Equations 55, 56, and 57 present a mathematical description of the industry model and are solved using the Euler finite difference scheme (1 year time step).

$$\frac{d}{dt}(NB) = H_C \cdot NB - H_D \cdot NB \tag{55}$$

$$\frac{d}{dt}(MB) = H_C \cdot NB - Q_D \cdot MB \tag{56}$$

$$\frac{d}{dt}(DI) = Q_D \cdot MB - Q_C \cdot DI \tag{57}$$

where

NB = number of new businesses

MB = number of mature businesses

DI = number of declining industries

H_C = new business construction rate (yr^{-1})

H_D = new business aging rate (yr^{-1})

Q_D = mature business aging rate (yr^{-1})

Q_C = declining industry destruction rate (yr^{-1})

The industrial submodel predicts the number of industries in each classification, the number of jobs in each of the working force occupation categories, and water utilization rates. This model predicts

water pollution emission rates and the water utilization rates desired by industry and the city, by using the following equations:

$$P_{MX_I} = ((NB + MB + DI)/NBIS)150 .$$

$$I_{MX} = ((NB + MB + DI)/NBIS)2000 .$$

$$M_{MX} = ((POPT/NPOP)2000 .$$

$$P_{MX_M} = ((POPT/NPOP)50 .$$

where

NBIS = the total number of industries at the beginning of a simulation

NPOP = the total population of the city at the beginning of a simulation

P_{MX_M}, P_{MX_I} = the maximum water pollution rate desired by the city and industry (lb/sec)

M_{MX}, I_{MX} = the maximum water flow rates desired by the city and industry (CFS)

Interactions with the Ecosystem

The average annual air pollution field is the only input parameter used by the urban model. The air pollution field causes people to move toward regions where the air pollution is lower.

Botany Model

The botany model is organized to simulate the growth of grass in the ecosystem. A deterministic model simulates the total above and below ground biomass for warm season grass fields as a function of time of year. The basic structure of the model is derived from a grassland ecosystem model developed by Bledsoe, et al (1971). The primary driving parameters which influence the growth of grass are soil moisture,

precipitation, soil and air temperature, incoming solar radiation, and wind speed. Most of these parameters are influenced by the stochastic atmospheric model.

The locations of grass fields are specified on a 32 x 32 grid (mesh size = 4 x 4 mi^2) that divides the ecosystem into grid points which represent potential crop producing fields that have a 16 sq mile unit area. The model uses hourly time steps to simulate the above ground biomass and below ground biomass for each grid point that is growing grass. The grass in each field is either consumed by grazing cattle or harvested and stored for use by the dairy cattle and feed lot cattle. The model has the option of providing water for irrigation of the crop producing fields. The flow diagram in Figure 18 illustrates the organization of the Botany model.

In describing the model, the terms primary and secondary state variables will be used frequently. Primary state variables describe the state of the system. Secondary state variables influence the evolution of a system; however, they do not define the actual state of the system.

Primary State Variables The four which define the state of the grassland system are above ground living biomass, below ground biomass, standing dead and litter. The sum of above ground living biomass, standing dead and litter is equal to the total above ground biomass. Above ground living biomass refers to living plant matter above the ground surface, while below ground biomass refers to root biomass. Standing dead includes all non-living biomass that is standing above the ground, while litter is non-living biomass that is lying on the ground surface. These four

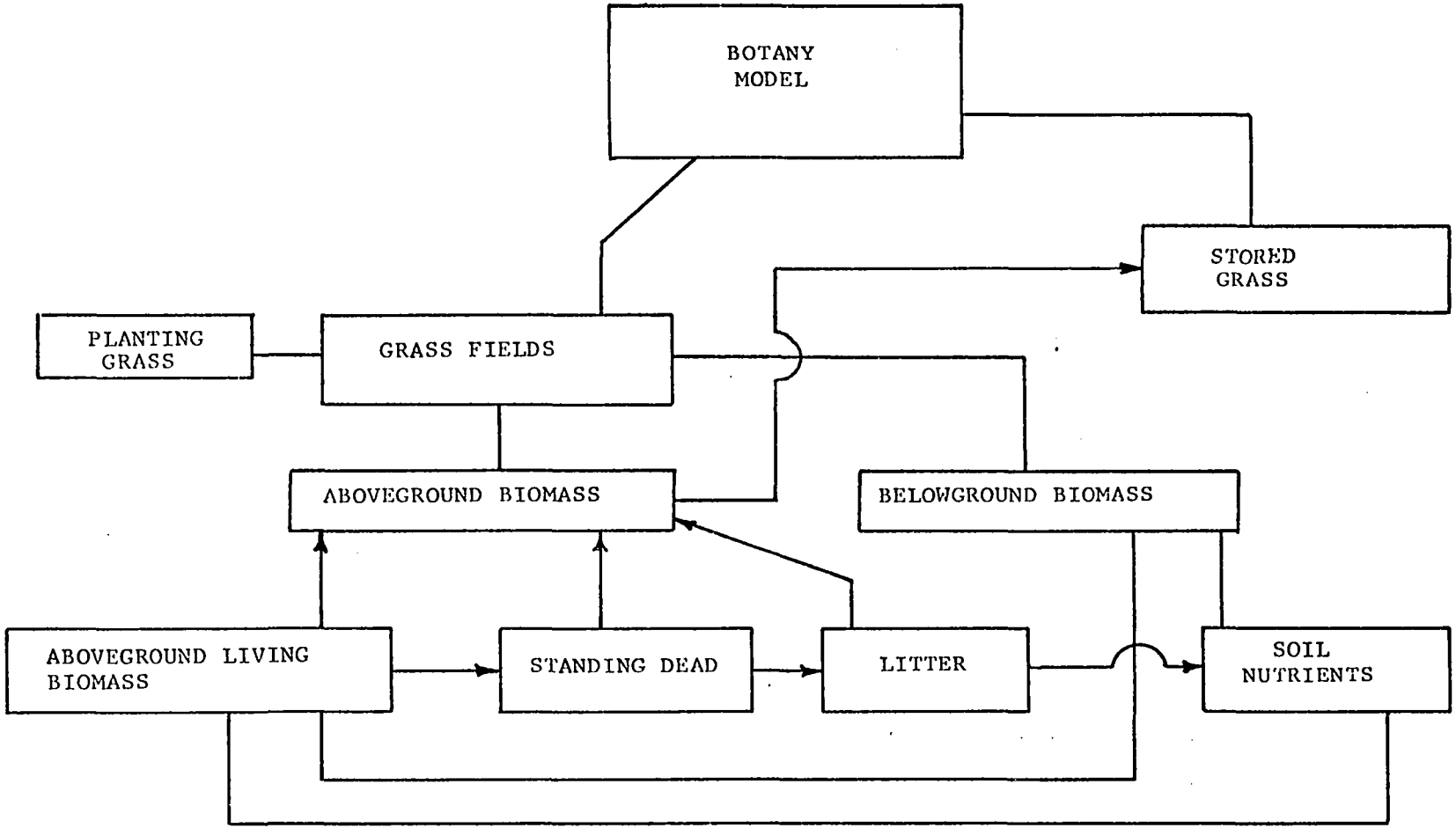

Fig. 18. Flow diagram of the botany model. Boxes connected by lines with arrow heads indicate that material from one box flows into the other. Boxes connected by lines indicate that the two boxes influence each other.

state variables are simulated as a function of time by solving the following first order differential equations using the Euler finite difference scheme (1 hour time step).

$$\dot{ABM} = CPH \cdot ABM \cdot PHO - (TBG + DAG + HAR) \quad (58)$$

$$\dot{ASD} = DAG - (SA \cdot ASD + HS) \quad (59)$$

$$\dot{LIT} = SA \cdot ASD - (HL + HM + LC \cdot LIT) \quad (60)$$

$$\dot{BBM} = TBG - (DB + RB \cdot RBM + HB) \quad (61)$$

where

ABM = above ground biomass (gm/cm^2)

BBM = below ground biomass (gm/cm^2)

ASD = standing dead (gm/cm^2)

LIT = litter (gm/cm^2)

$\dot{ABM}, \dot{BBM}, \dot{ASD}, \dot{LIT}$ = time rate of change of the primary state variables ($gm/sec\ cm^2$)

CPH = conversion factor for photosynthate function

PHO = net photosynthesis rate (net gm of CO_2 fixed per unit plant green tissue)

TBG = net translocation rate of photosynthate material to the BBM (gm/cm^2 sec)

DAG = death rate of ABM (gm/cm^2 sec)

HAR = harvest rate of ABM (gm/cm^2 sec) by cattle

SA = shattering rate of standing dead (sec^{-1})

HS = harvest rate of standing dead (gm/cm^2 sec) by cattle

HL = harvest rate of litter ($gm/sec\ cm^2$) by cattle

HM = harvest rate of litter by microfaune ($gm/sec\ cm^2$)

LC = leaching rate of plant litter into soil by rain water (sec^{-1})

DB = death rate of below ground biomass ($gm/sec\ cm^2$)

RB = respiration rate of below ground biomass (sec^{-1})

HB = harvest rate of below ground biomass ($gm/cm^2\ sec^{-1}$)

Equations 58-61 indicate that the time rate of change of the primary state variables are a function of the present values of the primary and secondary state variables. The secondary state variables at any time are determined from empirical equations which depend on the present values for the primary state variables and the abiotic parameters. The abiotic parameters which influence the model include: wind speed, canopy air temperature, ground temperature, net incoming solar radiation, soil moisture and rainfall.

Secondary State Variables The most influential secondary state variable is the net photosynthesis rate (PHO). In this model PHO is primarily a function of soil moisture, canopy air temperature, and solar radiation. Three equations are used to predict PHO as a function of the effective solar radiation (RP) and canopy air temperature (TC). Equation 62 is used for moderate solar radiation conditions (RP > .001 cal/cm^2 sec) and moderate canopy air temperature conditions (OC < TC < 44C).

$$PHO = MS \cdot (AMM \cdot HPM \cdot Z2) \cdot NS \cdot CR \cdot LA \cdot PPH1 \qquad (62)$$
$$\left(\frac{PPH2 \cdot RP}{1+PPH2 \cdot RP} - \frac{PPH2 \cdot PRP}{1+PPH2 \cdot PRP}\right) \cdot$$
$$\left\{(PTC - TC) \cdot Z1^{(-PPH3 \cdot (PTC - TC))}\right\}$$

where

TC = air temperature in the canopy (°C)

MS = moisture stress index (0-1)

NS = nutrient stress index (0-1)

LA = leaf area index (0-3)

CR = fractional cover of grass (0-1)

AMM = excess growth coefficient (0-1)

HPM = seasonal growth coefficient (0-1)

PPH1 = peak photosynthesis rate (sec^{-1})

PPH2 = parameter associated with sunlight response

RP = solar radiation effective for photosynthesis (cal/cm^2 sec)

PRP = threshold of positive photosynthesis response to sunlight (cal/cm^2 sec)

PTC = threshold of positive photosynthesis response to temperature (°C)

PPH3 = parameter associated with temperature response of photosynthesis during normal daylight and moderate temperature

Z1,Z2 = constant control coefficients

Equation 63 is used for low solar radiation (RP < .001 cal/cm sec) and moderate canopy air temperature conditions.

$$PHO = -MS \cdot NS \cdot CR \cdot LA \cdot PPH4 \cdot \left\{ \frac{(PRP-RP)}{PRP} \cdot \left(\frac{TC}{PTC2}\right)^{PPH5} \cdot \right. \quad (63)$$
$$\left. EXP\left[\left(\frac{PPH5}{PPH6}\right) \cdot \left(1 - \left(\frac{TC}{PTC2}\right)^{PPH6}\right)\right] \right\}$$

where

PPH5 = parameter associated with temperature response of photosynthesis during limited sunlight

PPH6 = parameter associated with temperature response

PTC2 = parameter associated with temperature response (position of peak photosynthesis)

PPH4 = peak photosynthesis rate under these conditions

When the temperature is greater than 44°C or less then 0°C PHO is set equal to zero. All of the parameters except MS, AMM, HPM, and RP are set equal to constant values in this model. The following equations are used to determine the values for the non-constant coefficients.

$$MS = \frac{1}{\pi}\tan^{-1}\left[\tan(.4\pi)\cdot(SHO-PMS1)/PMS2\right] + .5 \qquad (64)$$

where

SHO = percentage of soil moisture by volume for the top 24 inches (SHO=(SMT+WLT)/24.)

PMS1 = control coefficient (inflection point of curve)

SMT = the soil moisture available for evaporation from the 0-24 inch layer (inches)

PMS2 = control coefficient (slope of curve)

WLT = soil moisture from 0-24 inches at the wilting point (inches)

$$AMM = -\frac{1}{\pi}\tan^{-1}\left[\tan(.4\pi)(ABM-ABM1)/ABM2\right] + .5 \qquad (65)$$

where

ABM1 = control coefficient (inflection point)

ABM2 = control coefficient (slope of curve)

$$HPM = -\frac{1}{\pi}\tan^{-1}\left[\tan(.4\pi)\cdot(ZM-ZM1)/ZM2\right] + .5 \qquad (66)$$

where

ZM = number of months elapsed since the beginning of the growing season

ZM1 = control coefficient (inflection point)

ZM2 = control coefficient (slope of curve)

$$RP = SRPK \cdot \left(\frac{SR}{SRPK}\right)^{PRP10} \tag{67}$$

where

SRPK = net short wave solar radiation (cal/cm^2 sec) at (11:00 LST)

SR = net short wave solar radiation (cal/cm^2 sec)

PRP10 = control coefficient

TBG, DAG, SA, LC, DB, TC and RB are the other non-constant secondary state variables for equations 58-61. The following equations will be used to simulate these parameters.

$$TBG = \begin{cases} (.105-BBM)(PBT1-PBT2 \cdot BBM) \cdot ABM \cdot MS \cdot 100 \\ \quad \text{if } BBM > 1000 \text{ gm/m}^2 \\ 0.0 \\ \quad \text{if } TS \leq 0 \\ MAX[0., (PBT1-PBT2 \cdot BBM) \cdot ABM] \cdot MS \\ \quad \text{if } TS \geq 0C \text{ and } ABM \geq 5 \text{ gm/m}^2 \\ -MAX[0., PBT4(BBM-PBT5)] \cdot MS \\ \quad \text{if } TS \geq 0C \text{ and } ABM < 5 \text{ gm/m}^2 \end{cases} \tag{68}$$

$$DAG = (1-MS) \cdot PDA1 \cdot ABM \left[\frac{1}{\pi} \tan^{-1} \{\tan(.4\pi) \cdot (TS-PDA2)/PDA3\} + .5 \right] \tag{69}$$

$$\cdot \left[\frac{1}{\pi} \tan^{-1} \{\tan(.4\pi) \cdot (ZM-PDA4)/PDA5\} + .5 \right] \cdot 40.$$

$$LC = .035 \, PR \tag{70}$$

$$SA = .22 \times 10^{-3} \cdot WND \qquad (71)$$

if WND $\leq$ 223.5 cm/sec, SA = .005

$$RB = PRB \cdot (44.-TS) \cdot EXP[(44.-TS)/7.0] \qquad (72)$$

if TS > 44C, RB = 0.0

$$DB = RB \cdot BBM \cdot (1-MS) \cdot 1.5 \qquad (73)$$

$$TC = \begin{cases} T + 10 \cdot (SR/SRPK) \\ \quad \text{if } SR \geq .0002 \text{ cal/cm}^2 \text{ sec} \\ \quad \text{and WND} \leq 223.5 \text{ cm/sec} \\ \\ T \text{ otherwise} \end{cases} \qquad (74)$$

where

PDA1,PDA2,PDA3,PDA4, PRB = control coefficients

WND = wind speed (cm/sec)

PR = rainfall rate (cm/sec)

TS = soil temperature at 6 inches ($^{\circ}$C)

T = air temperature at 1.5 meters ($^{\circ}$C)

The equations describing the botany model are based upon the equation used by Pawnee Grassland Model (Bledsoe, 1970). The constant coefficients used for the model are different from those used in Pawnee Grassland Model because the Pawnee model is concerned with a short grass prairie, while the model presented here is used to grow grass on a tall grass

prairie. The values for the constant coefficients used in the botany model are derived from the calibration and validation process which used the 1970 Osage site data (Risser, 1971) and are presented in Appendix D. In the process of adopting the Pawnee model for a tall grass prairie, some of the equations describing the Pawnee model are changed to include grassland dynamics needed for a tall grass prairie (equations 62, 63, 69, 73). The model simulates the vegetation height as function of the total standing crop (ABM + ASD) using the following equation:

$$HVT = 12. + \frac{34.}{\pi} \cdot ARCTAN(\pi \cdot 0.002(SC-300.)$$

where

HVT = average height of the vegetation in inches

SC = standing crop biomass (gm/m^2)

The irrigation water demand for a particular field is calculated using the following equation:

$$AIRG_i = (1.5-AVM_i)\ AREA_i/(86400. \cdot 1728.)$$

$$\text{if } AIRG_i \leq 0.0;\ AIRG_i = 0.0$$

where

$AIRG_i$ = the daily irrigation water demand for the ith field ($Ft^3\ sec^{-1}$)

AVM_i = the daily average available soil moisture in the ith field (inches)

$AREA_i$ = the area of the ith field ($inches^2$)

The maximum amount of water flow desired by agriculture (A_{MX} - see description of water control model) is determined by summing up the irrigation demand by all of the ith fields ($A_{MX} = \sum_{i=1}^{n} AIRG_i$; n=the number of fields), while the water added to a particular grid point (mesh size = 4 x 4 mi^2) in a field (IRG) is estimated using the following equation:

$$IRG = (A/A_{MX})AIRG_i(86400/AREA_i/(144.)/12.$$

where

IRG = the water added to a grid point in the ith field (in.)

A = the amount of water flow allocated to agriculture on a particular day (Ft^3 sec^{-1} - see water control model)

Interaction with the Ecosystem

The Botany Model interacts with total ecosystem by using the following input parameters:

1) hourly wind speed (WND), air temperature (T), 6" soil temperature (TS), and net short wave solar radiation (SR); along with the rainfall rate (PR)
2) the soil moisture available for evaporation from the 0-24 inch layer (SMT - see description of the hydrology model)
3) the harvest rates of ABM (HAR), ASD (HS), and LIT (HL) by the cattle.

The parameters in 1), 2), and 3) are simulated by the atmospheric

model, the hydrology model and Zoology model respectively.

Zoology Model

The Zoology model is designed to simulate the production of milk and meat for consumption by people in the urban area. The model has dairy and beef cattle herds for producing milk and meat. The cattle are fed by grazing in the grass fields or by eating cut grass in feed lot areas. The zoology model is deterministic in structure and is primarily responsive to the output from the botany model. It is run using monthly time steps.

The structure of the zoology model is shown in Figure 19. Feed lot cattle, range cattle (yearling cattle) and breeding cattle are the three types considered in the beef herds. The breeding cattle produce calves in the spring (April, May and June) which comprise the range cattle herd. Both the breeding cattle and the range cattle graze on the grass fields from April through September. During this time period the breeding and range cattle consume ABM, ASD and LIT with equal preference until the biomass in a particular category reaches a critical value (ABM < 50 gm/m^2, ASD < 25 gm/m^2 and LIT < 25 gm/m^2). When this critical value is reached, the cattle replace this aspect of their diet by selecting grass from the other categories using ASD, ABM and LIT in descending order. If there is insufficient grass for grazing the cattle are transported to another grass field, or moved to the feed lots (see description of Range Management model). If the range cattle are moved to feed lots, the breeding cattle are fed cut grass. The age and weight of the range cattle are recorded on a monthly basis.

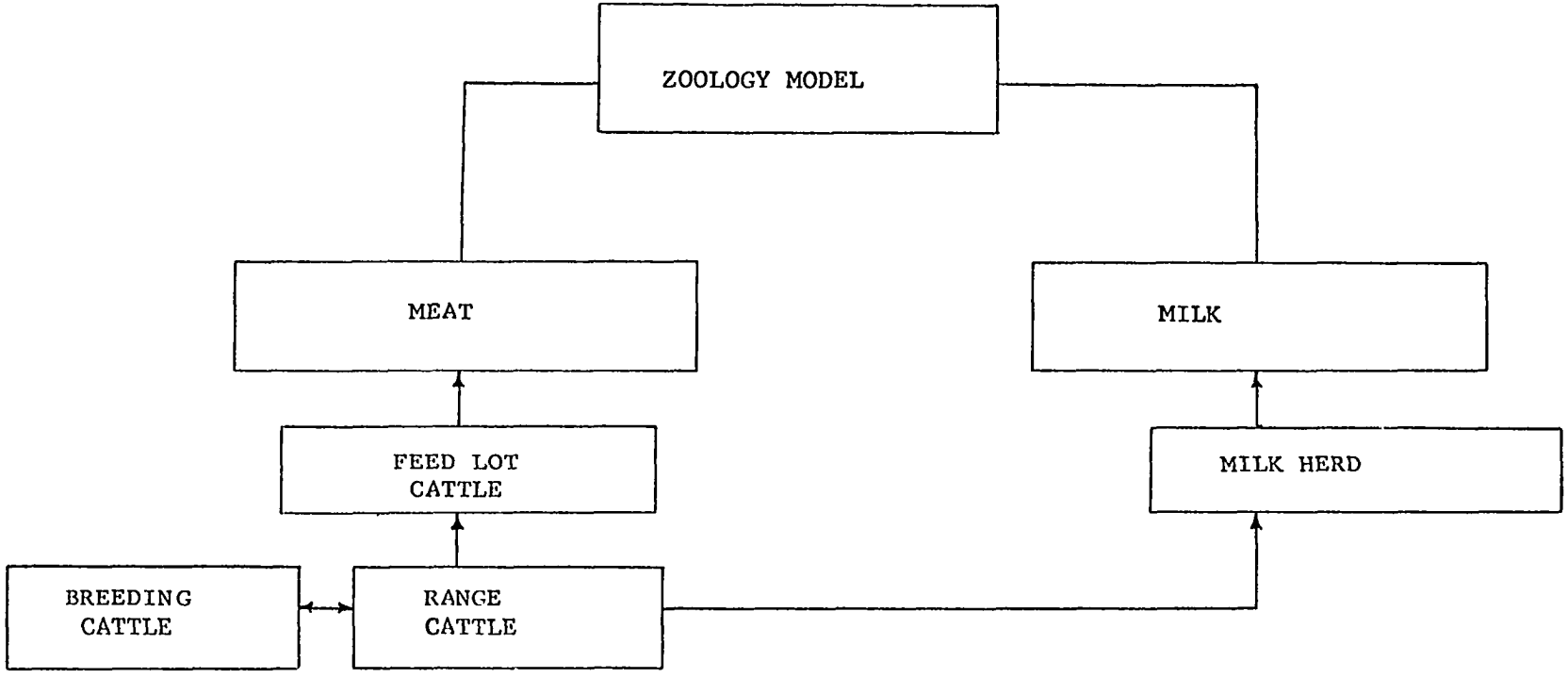

Fig. 19. This figure presents a flow diagram of the zoology model. Boxes connected by lines with arrow heads indicate a flow of biomass from one category to another.

During the growing season (March - November) the location, areal extent of the grazing land, and amount of grass consumed are recorded for each range cattle herd and its accompanying breeding herd. The amount of grass consumed by a grazing herd in a particular field is determined using the following equations:

$$HAR = NGZ*NLB*0.33/(86400.*NAREA)$$

$$HS = NGZ*NLB*0.33/(86400.*NAREA)$$

$$HL = NGZ*NLB*0.33/(86400.*NAREA)$$

where

NGZ = the total number of cattle grazing in the field

NLB = grams of grass consumed by a cow in a day (23560 gm/day)

NAREA = total area in the field (cm^2)

HAR,HS,HL = the harvest rate for live grass, standing dead and litter by cattle in the field ($gm/sec\ cm^2$)

HAR, HS and HL are modified if the amount of biomass in ABM, ASD or LIT reaches the critical level (read previous discussion).

From October until March the breeding cattle are fed cut grass. At the beginning of October the range cattle are put into feed lots where they are fed hay until they reach a certain weight or age. The age and average weight of the feed lot cattle are recorded on a monthly basis until the cattle reach the weight at which they are slaughtered for meat. The number of breeding cattle is regulated as a function of the demand for meat. Increases in the breeding cattle herd will come from feed lot cattle that have reached a certain weight. Breeding cattle have a constant weight and their age is not recorded. Feed lot cattle produce water pollution that influences the river system. The daily water

pollution rate desired by the feed lots (PMX_A - see description of the water control model) is calculated using the following equation:

$$PMX_A = NFDC \cdot 0.0035$$

where

PMX_A = the maximum daily water pollution rate desired by the feed lots

NFDC = the total number of feed lot cattle

If the water pollution rate allocated to the feed lots by the water control model is less than PMX_A then the cost of producing cattle increases as direct function of the amount of water pollution that is not allowed to be emitted into the river.

Milk herds are fed cut grass. The amount of milk produced is a function of the number of cows in the herd. An increase in the herd size will come from the feed lot cattle.

Interaction with the Ecosystem

The zoology model interacts with the total ecosystem by using the following input parameters:

1) the feed lot water pollution rate (P_A) allowed by the water control model,
2) the location and number of grazing cattle in the grazing fields.

The parameters in 1) and 2) are simulated by the water control model and the range management model respectively.

Executive Model

The executive model (control program) is set up to monitor and act upon the intermediate results from the interactions among the five primary submodels and also to optimize the resource management of the ecosystem. The executive model uses linear programming, decision theory, and simple logic. A flow diagram of the executive model is given in Figure 20. Linear programming optimizes the use of resource variables subject to linear constraints. This is accomplished by optimizing an objective function that considers both the utility of the resource variables and the linear relationships which contain them. Decision theory is used to determine the least cost action from a series of possible alternatives. Each action has a specified cost related to a parameter called the state of nature. The state of nature has classifications which are related experimentally to observed stochastic variables. The relationship between the cost of each action and the state of nature are summarized in a cost (utility) matrix, while the relationship between the state of nature and the observed stochastic variables are summarized in climatology matrices.

Specifically the executive model uses linear programming to optimize the allocation of the water resources and also to optimize industrial production subject to air pollution constraints. Decision theory is used to determine the optimal (least cost) range management policies, while Boolean logic is used to manipulate the simple geophysical and biological constraints.

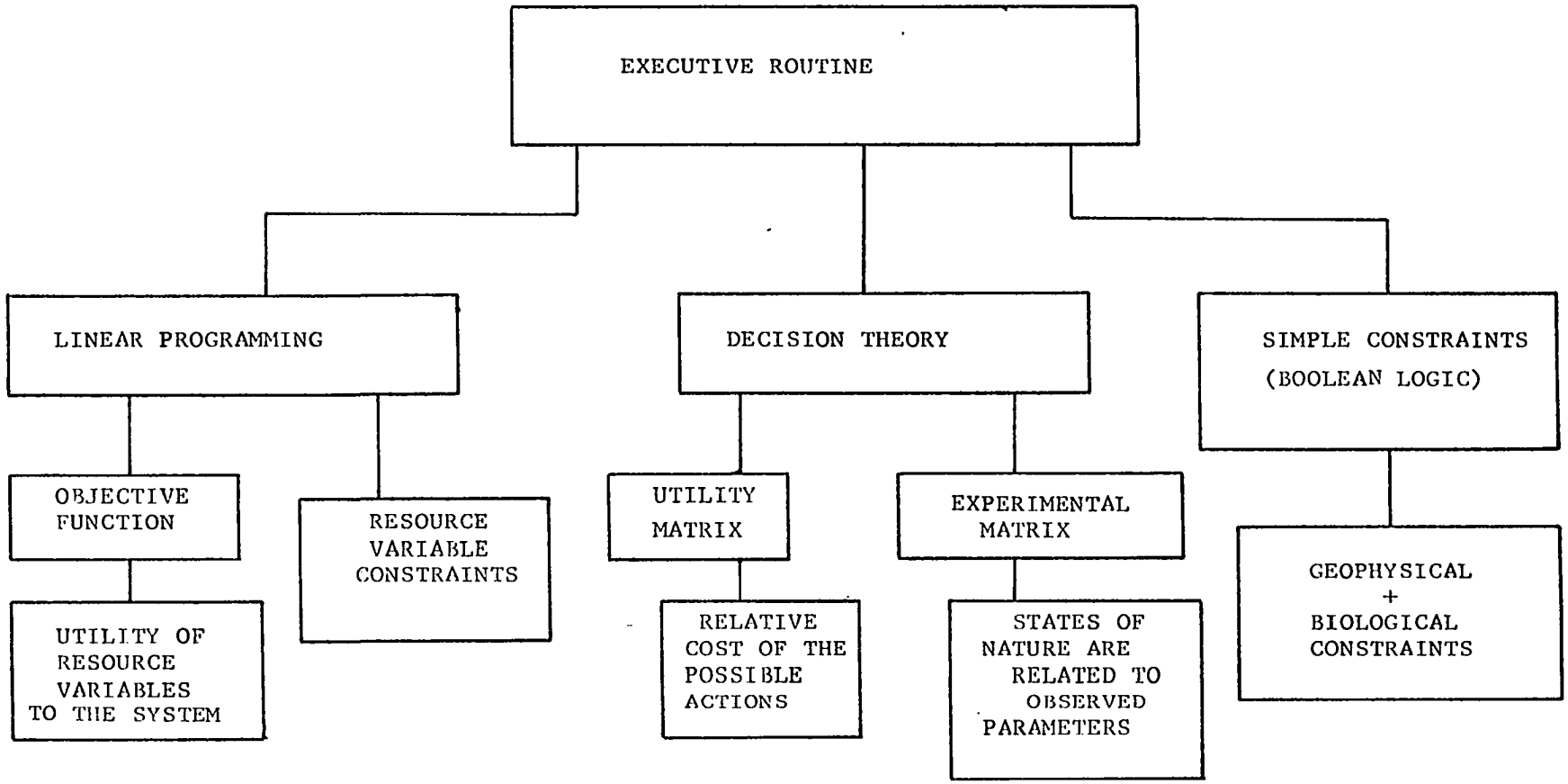

Fig. 20. Overall structure of the executive subroutine is shown in this figure.

Water Resource Management

The model for controlling the use of water resources in the ecosystem is shown in Figure 21. It considers a lake-stream-river complex in which the use of existing water resources is optimized. The assumption is made that the water flowing into the lake comes from rainfall runoff and controlled upstream water sources. The maximum amount of lake water available for use by the system is controlled as a function of the lake level. The water flowing from the lake is either used by the city, industry and agriculture, or allowed to flow freely down the river. A specified percentage used by the consumers (city, industry, agriculture) is returned to river and contains pollution generated by the consumers. The linear programming model constrains the results so that water flow and pollution levels below the city will be within acceptable limits. The mathematical representation of this model in the linear programming format is represented below.

Maximize $[Q = K_1M + K_2A + K_3I - K_4WFD + K_5P_M + K_6P_A + K_7P_I]$

subject to the following constraints:

$$M + A + I + R = WFD$$

$$H_1M + H_2M + H_3I + R \geq R_D$$

$$P_M + P_A + P_I \leq K_8(H_1M + H_2M + H_3I + R)$$

$$WFD \leq ZZWL$$

$$I \geq I_{MN}$$

$$M \geq M_{MN}$$

$$A \geq A_{MN}$$

$$P_M/PMX_M = M/M_{MX}$$

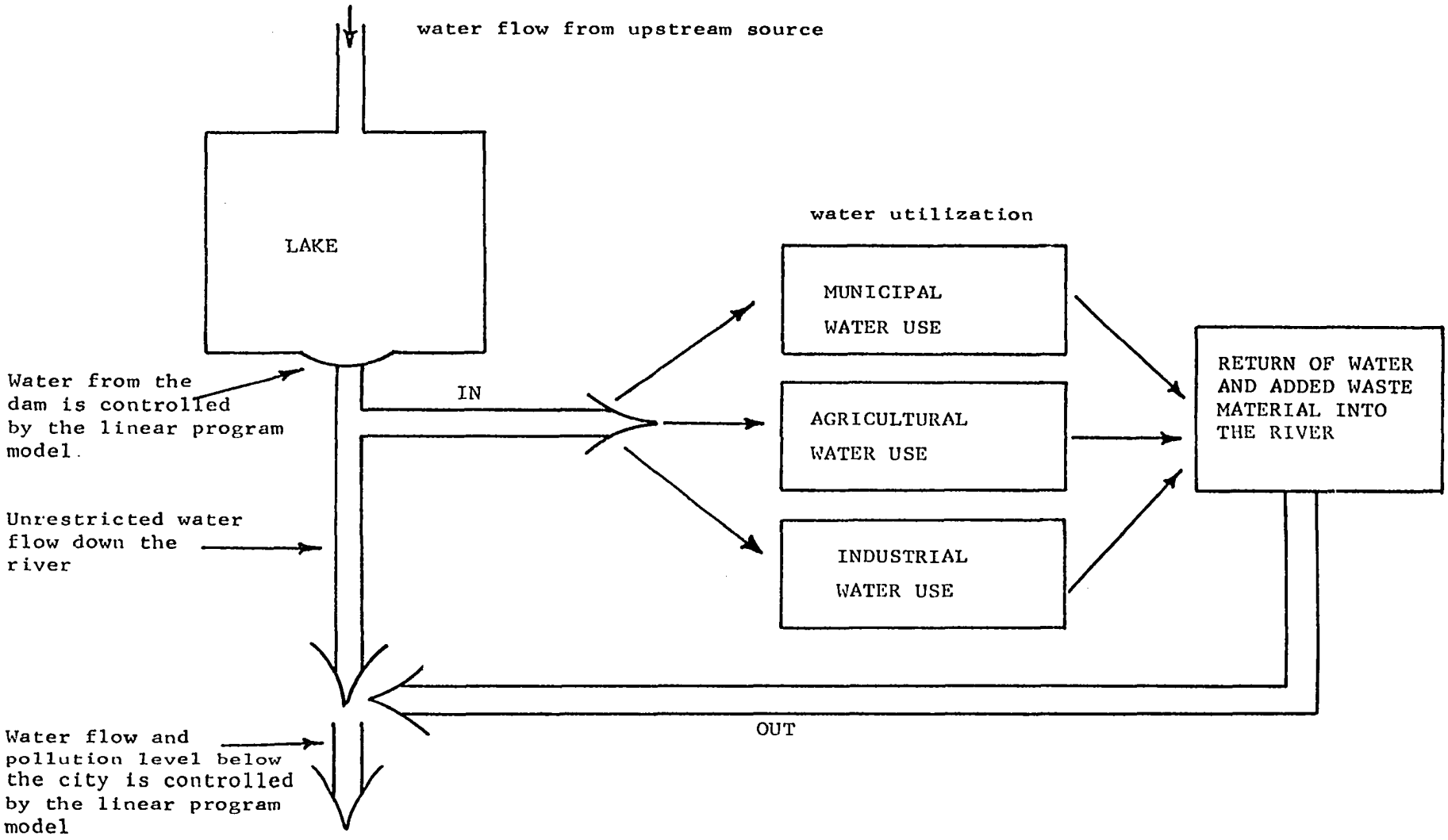

Fig. 21. Overall structure of the linear program model for water management in the ecosystem is presented.

$$P_I/PMX_I = I/I_{MX}$$

$$R_D \geq RMN_D$$

where

M = water used by the city ($ft^3\ sec^{-1}$)

A = water used by agriculture ($ft^3\ sec^{-1}$)

I = water used by industry ($ft^3\ sec^{-1}$)

R = water flowing freely down the river ($ft^3\ sec^{-1}$)

WFD = water flow from the lake ($ft^3\ sec^{-1}$)

H_1, H_2, H_3 = percentage of water returned by the three consumers (M,A,I)

RMN_D = the minimum allowable water flow below the city (ft^3 sec)

R_D = water flow below the city ($ft^3\ sec^{-1}$)

P_M, P_A, P_I = water pollution returned to the river by the three consumers (lb/sec)

$ZZWL$ = maximum amount of water allowed to flow from the lake ($ft^3\ sec^{-1}$), ZZWL is a function of the lake level (see Appendix F for functional relationship)

M_{MN}, A_{MN}, I_{MN} = the minimum water flow rate desired by the consumers ($ft^3\ sec^{-1}$)

PMX_M, PMX_A, PMX_I = the maximum water pollution rate desired by the consumers ($lb\ sec^{-1}$)

M_{MX}, A_{MX}, I_{MX} = the maximum water flow rate desired by the consumers ($ft^3\ sec^{-1}$)

K_8 = permissible pollution level (lb per ft^3 of water)

The model assumes that the water allocated to the consumers is taken out of the river system at a point just below the dam, while the water and pollution returned to the river by the consumers is emitted at this same point. The water allocated to the city is used to satisfy municipal

water demand for drinking water and sewage control. Industrial water demand is used to satisfy the water needs of industry in the city, while the water allocated for agriculture is used to irrigate crop land. Water pollution emitted by the city and industry come from untreated sewage and industry wastes, while the water pollution emitted by agriculture comes from a feed lot near the city. The maximum amount of water and maximum water pollution emission rates desired by the consumers corresponds to the levels of consumption needed to satisfy all of their needs, while the minimum amounts of water and minimum water pollution emission rates desired by the consumers are the lowest level of consumption which the consumers can use without being forced to shut down completely. The average daily water consumption rates for the consumers are determined by using the primal simplex algorithm that has positive upper bounds on the basic variables to solve the water control linear programming model once every twenty-four hours. The input parameters needed by the model are the lake level, desired water consumption rates for the consumers, and the desired water pollution emission rates of the consumers. The desired water consumption rates and water pollution emission rate for the city is a function of the total population of the city, while these same rates for industry are a function of the industrial activity in the city. The desired water consumption rate for agriculture is a direct function of irrigation water demand while the desired water pollution emission rate is a direct function of the number of cattle in the feed lot.

The output from the linear programming model gives the daily average water flow rates that are allocated for the three consumers and

specified the amount of water to be released from the lake. The model also specifies the water pollution emission rate allowed the consumers and determines the river flow rate below the point where water control model is utilized.

Interaction with the Ecosystem

The water control model interacts with the rest of the ecosystem by using the following input parameters:

1) the lake level (LK)

2) PMX_M, PMX_I, M_{MX}, and I_{MX}

3) A_{MX}

4) PMX_A

The parameters in 1), 2), 3), and 4) are simulated by the hydrology model, urban model, botany model and the zoology model respectively.

Air Pollution Control

The production level of factories that emit air pollution are optimized using linear programming model that maximizes the factory production subject to linear constraints that require the air pollution concentration (gm/m^3) to be below specified critical levels at the air pollution monitoring points in the city. Figure 22 shows the location of the factories and the air pollution monitoring points. The location of the factories and the desired air pollution emission rates for each factory are determined from the 1968 SO_2 air pollution data from the city of Houston, Texas (Report for Consultation on the Metropolitan Houston-Galveston Interstate Air Quality Control Region, 1969). The model assumes that the air pollution emission rate for a given factory

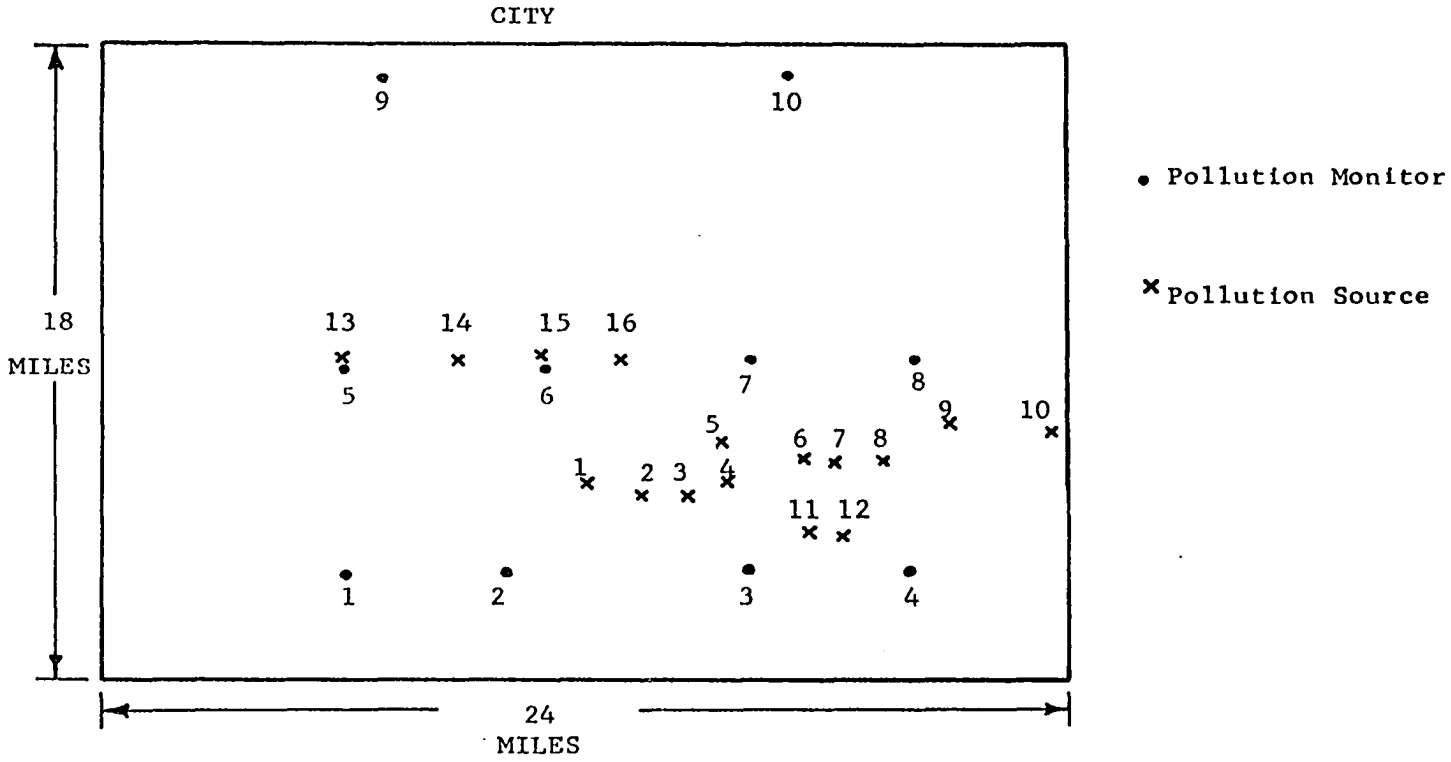

Fig. 22. Position of the air pollution monitor points and SO_2 air pollution source. The SO_2 air pollution sources are chosen to approximate the important SO_2 air pollution sources in Houston, Texas, while the pollution monitoring points are chosen arbitrarily.

is proportionate to the production rate of the factory. Thus, a factory producing at its peak production rate will be emitting air pollution at its peak rate. The mathematical description of the linear programming model is given below.

Maximize $$[Z = \sum_{i=1}^{16} P_i K_i]$$

$$P_i = X_i Q_i$$

subject to the following constraints

$$\sum_{i=1}^{16} \frac{P_i}{X_i} S_{ij} \leq PMX_j$$

$$P_i = \leq P_i^{MX}$$

where

"i" refers to the 16 factories emitting air pollution

"j" refers to the 10 air pollution monitoring points

Z = profit (dollars sec^{-1})

K_i = profit parameter for the type of product produced by the ith factory (dollars per unit produced)

P_i = the production rate of the products of the ith factory (number of units per sec)

X_i = the number of production units per gram of pollution emitted by the ith factory (units/gm)

$S_{ij} = \chi_{ij}/Q_i$ value at the jth monitoring point caused by the ith pollution source (sec m^{-3})

χ_{ij} = the air pollution concentration of the jth monitoring point caused by the ith factory (gm/m^3)

Q_i = the air pollution emission rate of the ith factory (gm/sec)

P_i^{MX} = the maximum production level for the ith factory (units/sec)

PMX_j = maximum allowable air pollution concentration at the jth monitoring point (gm/m^3)

The values of P_i^{MX} are determined using the following equation:

$$P_i^{MX} = ((NB + MB + DI)/NIND) \cdot P_i^o$$

where

NB = number of new businesses in the city (see Urban model)

MB = number of mature businesses in the city (see Urban model)

DI = number of declining industries in the city (see Urban model)

NIND = the total number of industries at the beginning of the simulation

P_i^o = the desired production rate (# of units per sec) of the ith factory at the beginning of the simulation

The average daily production rate for each factory in the city is determined by using the primal simplex algorithm to solve the air pollution control model once every twenty-four hours. The input values needed to solve the model include the desired production levels of the factories and the χ_{ij}/Q_i for each of the pollution monitoring points. The χ_{ij}/Q_i values are determined from the air pollution model in the atmospheric subroutine by using the predicted twenty-four hour average wind speed and wind direction as input values for the air pollution model. The technique used to solve for the χ_{ij}/Q_i values is presented in the description of the atmospheric submodel. The desired production level of each of the factories is a direct function of the level of industrial activity, which is determined by the industry submodel in

the urban subroutine. The predicted production levels determined by the air pollution control model are compared with P_i^{MN} (P_i^{MN} = the minimum profitable production level for the ith factory) to determine if the recommended production levels are less than the minimum profitable production levels. If the predicted production level is less than P_i^{MN} then the production rate of the ith factory is set equal to zero. Otherwise the production levels predicted by the air pollution control model are not modified. The direct relationship between the production level of a factory and the air pollution emission rates of a factory is used to predict the twenty-four hour average air pollution emission rate for each factory. These emission rates are used by the atmospheric subroutine to predict the air pollution field in the urban area.

Interaction with the Ecosystem

The input parameters utilized by the air pollution control model are listed below.

1) χ_{ij}/Q_i

2) NB, MB, DI

The parameters in 1) are simulated by the atmospheric model while the parameters in 2) are simulated by the urban model.

Range Management

The executive routine uses decision theory and simple constraints to determine optimal range management actions for the range cattle herds. The model is set up so that there are four possible management actions which include:

1) keeping the cattle in their present grazing area without supplying additional food,
2) keeping the cattle in their present grazing area and providing all the food required for a month,
3) moving the cattle to a new grazing area,
4) moving the cattle to the feed lots.

The range management model uses daily and monthly time steps in formulating management policies. The total above ground biomass is checked daily and the cattle are permitted to graze on the grass if there is sufficient food (ABM < 50 gm/m^2, ASD < 25 gm/m^2, LIT < 25 gm/m^2). If there is insufficient grass the cattle are fed only cut grass until the end of the month. If the grass becomes insufficient for grazing at any time during a monthly period, then a decision must be made at the end of the month either to keep the cattle on the grazing area or to move the cattle elsewhere. Decision theory, using a cost matrix and climatology matrix, determines which of these alternative actions is optimal (least cost). The cost matrix relates the cost of each action to the state of nature, which is the grass growing potential for the next month. If the grass growing potential is very good for the next month, then the least cost action is to keep the cattle in the present grazing area, while with poor growing conditions the least cost action is to move the cattle to another area. The climatology matrix relates the grass growing potential for the next month (state of nature) to the forecast average soil moisture for the next month. This matrix demonstrates that high values of soil moisture are related to good growing conditions while low values are related to poor growing conditions. The forecast

soil moisture for each month is determined by using the following equation:

$$FSM = \frac{(SMT + \nabla SML(t) + SMT)}{2} \tag{75}$$

where

FSM = forecast average soil moisture available for evaporation

SMT = observed soil moisture available for evaporation at the beginning of the month

∇SML = the climatological change in soil moisture from the beginning of the month to the end of the month (function of time of year - see Appendix F)

The technique by which the cost matrix and the experimental matrix are used to determine the optimal action is presented by Chernoff and Moses (1959). If the decision is made to keep the cattle in the present grazing area, then the cattle are fed stored forage for the next month. A decision to move the cattle means that the cattle go either to a new grazing area or to the feed lot. The cattle are moved to a new grazing area if there is such an area where the total above ground biomass is greater than 150 gm/m^2. If none of the grazing areas satisfy this condition then the cattle are moved to the feed lots. If the yearling cattle are transferred to the feed lot before the yearling cattle are scheduled to be born, then the model assumes that the unborn cattle are born on the last day of the month that the cattle are in a grazing field. Once the cattle are transferred to the feed lot, they are not allowed to be returned to the grazing fields.

Interactions with the Ecosystem

The range management model interacts with the ecosystem by using

SMT and the above ground biomass (ABM, ASD, and LIT) in the grazing fields as input parameters. SMT is determined for the field where the cattle are located by the hydrology model while ABM, ASD, and LIT are determined by the botany model.

CHAPTER IV

TESTING THE MODEL

Validation and sensitivity analysis are the two techniques used to test the urban-rural ecosystem model. Validation, which is a simple comparison of simulated computer results with observed data sets, is the most common technique used to test models. Deterministic models attempt to reproduce observed data sets exactly, while stochastic models produce data that reproduce certain statistical properties of observed data. A sensitivity analysis demonstrates the response of the model to variations in the parameters that control it. The results of a sensitivity analysis are used to provide a preliminary validation of models that do not have sufficient observed data available. A more thorough discussion of the attributes of sensitivity analysis and validation is presented in Chapter II.

A thorough testing of the model would require that validation procedures and sensitivity analysis be performed on the total ecosystem model. This type of testing procedure is unfeasible because of 1) data acquisition problems, 2) the immense amount of data required to perform such a testing procedure, 3) the time needed to complete such a task, and 4) the dubious value of performing a complete testing procedure on the ecosystem model in its present state of development. A total ecosystem model of an urban-rural system would have to be expanded to

include components not considered in the present ecosystem model before a complete testing scheme would produce meaningful results. It is interesting to note that a complete sensitivity analysis of the total ecosystem would require that over 100 parameters be altered individually to ascertain their effect upon the model.

Validation and sensitivity analysis are used to thoroughly test selected segments of the ecosystem model. An important criterion in the selection of segments of the model to be tested is the relative availability of observed data. The testing procedure performed on the model also demonstrates how the critical parameters in the different subroutines influenced the evolution of the urban-rural ecosystem. A list of the tests performed on the five main subroutines and the executive routine are presented in this chapter, along with a summary of the results. A more detailed discussion of the results of the testing scheme and the figures and tables illustrating these results are presented in Appendices A-F. A complete summary of the input data used for the five main subroutines and executive routine are also presented in the appendices.

Atmospheric Subroutine

The atmospheric subroutine used both stochastic and deterministic modelling techniques to simulate daily observation of the atmospheric parameters. A model that combines both stochastic and deterministic modelling techniques is considered a stochastic model and is validated by comparing statistical attributes of the model output with those of observed data sets. In addition to the validation procedure, a sensitivity analysis which demonstrates the effect of the control parameters on the model could also be performed.

The testing scheme used on the atmospheric model is a validation procedure in which the data simulated from a fourteen-year run of the model is used to determine the frequency distribution and average monthly values for the parameters predicted by the model. These statistical attributes for the simulated data are compared with the same statistical attributes determined from observed climatological input data. Five years of daily weather observation at Oklahoma City (1965 - 1970) and one year of NSSL tower data (1967 - 1968) are used as the input climatological data for the model. In addition to the validation procedure, a sensitivity of the deterministic segments of the atmospheric subroutine is also run. The sensitivity analysis is performed in order to provide a preliminary validation of the deterministic segments. A more thorough validation procedure is not performed on the deterministic segments of the atmospheric model because of the lack of observed data sets.

Specifically, the wind direction, relative humidity and cloud cover are tested by comparing the seasonal and yearly frequency distributions generated from simulated data with the appropriate frequency distributions derived from climatological data. The wind speed is examined by determining the seasonal and yearly average values as a function of wind direction for the simulated data and that comparing these average values of wind speed with those determined from climatological data. The stochastic rainfall model is tested by comparing monthly average number of rain days, monthly average rainfall, and the frequency distribution of rainfall amounts with the appropriate statistics generated from the climatological input data. The spatial distribution of rainfall in the ecosystem is illustrated by comparing the average monthly rainfall amounts for three of the grid points in the ecosystem. Monthly average values for the maximum and minimum air temperature determined from the

simulated data are compared with the average monthly maximum and minimum air temperature at Oklahoma City (1931 - 1967). The results of the above testing procedures indicate a favorable comparison between the frequency distributions and average monthly values of the parameters determined from the simulated data and those generated from the climatological data.

The deterministic air pollution model, radiation balance model and urban heat island wind are examined using sensitivity analysis. The sensitivity of the air pollution model to various wind speeds and stability classifications is demonstrated by changing these parameters and observing the simulated air pollution fields. The sensitivity of the radiation balance model to the twelve input parameters is ascertained by altering each of the parameters separately and observing the effect upon the simulated daily maximum and minimum air temperature. The urban heat island effect is demonstrated by comparing the simulated air temperature at a point in an urban area with the simulated air temperature at a point in a rural area. The sensitivity of the urban-rural temperature difference to cloud cover, wind speed and time of year are also demonstrated. The sensitivity of the urban heat island wind model is shown by changing the urban minus rural temperature difference and observing the wind fields produced by these variations.

In general, the results of the sensitivity analysis demonstrate that submodels of the atmosphere routine respond to variation of the driving parameters in a manner consistent with subjective judgement.

Hydrology Model

Hydrology model uses deterministic modeling techniques to simulate the hydrologic response to the driving atmospheric parameters. The valida-

tion of such a deterministic model can be achieved by driving the model with an observed time series of atmospheric parameters and then comparing the simulated time series of hydrology parameters with the observed time series of hydrology parameters that correspond to the driving atmospheric time series. Another technique for validation would be to drive the hydrology model with a stochastic atmospheric simulation model that uses climatological data from a particular area as input data and then compare the statistical attributes of the simulated time series of hydrology parameters with the statistical attributes of an observed time series of hydrology parameters. The observed time series of hydrology parameters would have to be observed at a point where the climatological input data for the atmospheric simulation model is observed. In addition to the above validation procedures, a sensitivity analysis of the model could also be performed. Neither of the two validation schemes are used because of data acquisition problems. A sensitivity analysis is not performed because the farily simple mathematical representations used in the model would cause the results of a sensitivity analysis to be trivial and inherently obvious.

The hydrology model is tested by demonstrating its ability to simulate a reasonable hydrologic response to the driving atmospheric parameters. This is accomplished by using the data generated from a 14-year simulation of the atmospheric and hydrology models to calculate average monthly values for the hydrology parameters. These average values are compared with the average values for the atmospheric parameters. The hydrology parameters tested in this manner include:

soil moisture (0-6, 0-24, 25-48 in)

soil water drainage

storm runoff

potential evapotranspiration

actual evaporation

lake evaporation

river flow

A 30-day time sequence manifesting the response of the soil moisture, evaporation rate and river flow to rainfall in ecosystem is also demonstrated. The effect of soil characteristics upon storm runoff is illustrated by calculating the average monthly runoff for several points in the ecosystem that have different runoff characteristics. The results of the testing procedure for the hydrology model indicate that the hydrologic parameters respond to the driving atmospheric parameters in a consistent manner.

Urban Model

The urban model could be tested by performing a validation procedure and a sensitivity analysis on the model. The validation procedure is not run on the model because of data acquisition problems and the fact that the model needs to be expanded before the results of a validation procedure would be meaningful. A type of sensitivity analysis is performed on the model. This testing scheme demonstrates the response of the model to its four primary driving mechanisms which include boundary movement, population dynamics, industrial development and suburb dynamics. This is accomplished by performing a series of 15-year computer simulations of the urban model in which the parameters that control the driving mechanisms are altered individually. The effects of changing the control parameters are demonstrated by showing the influence of the parameters upon the evolution of the city and

suburb boundaries, population density of the city, industrial development of the city, and the frequency distributions of the attributes associated with each suburb. The 1960 census data for the U.S. and Houston, Texas is used to specify the initial values assigned to the parameters in the urban model. A complete listing of the initial conditions of the model and the conditional probability relationships used in the model are presented in Appendix C.

Specifically, the boundary movement is examined by varying the parameters which define the boundary stress and by changing the critical boundary stress values that determine when boundary movement will occur. In particular, the effect of altering the race parameter in the boundary stress equation and increasing the critical boundary stress values are illustrated. The population dynamics is tested by varying the influence of the parameters which define the livability of the suburbs and influence the two mechanisms (diffusion and discontinuous movement) by which a "statistical man" can move within the city. The testing procedure demonstrates the effect of altering the air pollution and population density terms in the livability gradient equation, and the parameter which controls the percentage of people who move either by discontinuous or diffusion moving techniques. Industrial development is examined by changing the rate parameters that control the growth of industrial activity within the urban area. In particular, the effect of both increasing and decreasing the rate of growth of new industries is shown. Suburb dynamics is tested by changing the rate parameters that control the housing distribution and the attributes of the inhabitants of the suburbs. The effect of modifying the rate parameter which increases the educational level of the people and the effect of increasing the construction rate of new houses are both demonstrated in

the testing scheme. The results of the testing procedure for the urban model indicate the modelling mechanisms and control parameters considered by the model are very useful in simulation of the dynamics of an urban area.

Botany Model

Validation and sensitivity analysis are both used to test the deterministic botany model. The validation procedure compares a simulated time series of the primary state variables (ABM, BBM, LIT, and SD) with the 1970 warm season biomass data for the IBP Osage site (Risser, 1971). The sensitivity of the botany model to soil moisture, soil and air temperature, wind speed and solar radiation is demonstrated by a numerical experiment which ran the botany model for a series of one-year simulations that utilize different data sets for the listed driving variables. The effect of the overall ecosystem on the botany model is shown in a two-year computer simulation in which the botany model is run with the overall ecosystem. The results of this simulation are illustrated by a time series of ABM, LIT and SD for four warm season grass fields. The first field is irrigated and not grazed, the second is permitted to grow without any modifications, while the last two are grazed by cattle. A ten-year computer simulation of the botany model is run in order to determine the monthly average values of the primary state variables for the four grass fields. The results of the validating scheme and sensitivity analysis provide a preliminary validation of the warm season grass botany model. An even longer time series of observed data is desirable to provide a more convincing validation.

Zoology Model

Validation and sensitivity analysis techniques could be used to test the zoology model. A validation scheme is not used because of data acquisition problems and the fact that the model is not sufficiently developed to justify the use of normal validation techniques. A type of sensitivity analysis is used to demonstrate the response of the model to the input variables. The results from a four-year simulation of the total ecosystem model is used to indicate the responses of the model to the input variables. The evolution of the zoology model is illustrated by a time series of 1) the number of grazing and feed lot cattle, 2) the average weight of grazing and feed lot cattle, and 3) the available grazing grass. The effect of different range management policy decisions are also demonstrated by this time series. A ten-year computer simulation of the zoology model is used to determine the average monthly values of the number of grazing and feed lot cattle and the average monthly weight of the grazing and feed lot cattle. The results of this testing method indicate that the zoology model responds to the input parameters in a reasonable manner.

Executive Model

The executive model is organized to control the interactions between the five primary submodels and to optimize resource management. This type of model is not validated by comparing observed data sets with simulated data sets because the model is intended to be used to demonstrate the effect of different management strategies on the evolution of the ecosystem. The model is tested by running a sensitivity analysis on the three primary submodels of the executive model and by showing the

influence these submodels have on the overall ecosystem.

The sensitivity of the air pollution control model to wind direction, maximum air pollution level permitted at the monitoring points, and the objective function coefficients (coefficients indicate the relative importance of the different factories) is demonstrated by altering these parameters separately and observing their influence upon the optimal production level permitted by the air pollution control model. A two-year computer simulation in which the air pollution model is run in conjunction with the air pollution control model is used to determine the average monthly production level of the urban factory complex and the average annual air pollution field for the urban area. A comparison of the average annual air pollution concentrations for controlled and uncontrolled air pollution emission rates is also presented.

The sensitivity of the water control model to the objective function coefficients and the maximum amount of water permitted to flow out of the lake (WFD) is illustrated by changing these parameters separately and observing their influence upon the amount of water allocated to the consumers (City, Industry, and Agriculture) and the water pollution emission rates allowed. A ten-year time simulation of the overall computer model is used to determine average monthly values of water allocated to the various consumers, average monthly values of the ratio of the water received by the consumers to the water desired by the consumers, and a similar ratio of water pollution allowed for agriculture to the water pollution emission rate desired by agriculture. The average values of the above parameters are compared with the monthly average lake level. A ten-year trend in the average annual water consump-

tion by the consumers and the average annual ratio of water consumption to water demand are also presented.

The sensitivity of decision theory aspect of the range management model to the cost and climatology matrices is demonstrated by altering the cost and climatology matrices and observing the changes in the optimal management strategies. A ten-year computer time series in which the zoology model is controlled by the range management model is used to demonstrate the evolution of range management policy decisions.

The results of the testing procedure for the three submodels of the executive model illustrate the potential of the executive model for controlling the evolution of the ecosystem and optimizing the use of the resources in the system.

CHAPTER V

SUMMARY

A balanced ecosystem model that considers the interactions of a representative selection of the major components of an urban-rural ecosystem was developed. The ecosystem model was organized to simulate the evolution of an urban-rural ecosystem for periods of time up to 25 years. The model is intended to be used to determine the consequences of alternative management decision upon the urban-rural ecosystem and is specifically designed to be useful in studying a variety of real world problems associated with this ecosystem.

After developing the model a testing procedure was performed on the model in order to provide a preliminary validation. Validation and sensitivity analysis were used to thoroughly test selected segments of the model, while the other segments were tested by demonstrating the manner in which critical parameters in these segments influence the evolution of the ecosystem. Validation and sensitivity analysis were used to test the different parts of the atmospheric submodel. Results showed that this submodel could be used successfully to simulate time series of daily weather observation and to study some of the characteristics of the urban-rural heat island phenomena. The other submodels in the ecosystem were tested by demonstrating the responses of the submodels

to the input parameters. Results showed that the submodels responded to the input parameters in a consistent manner. The interactions among the different components of the ecosystem were demonstrated by illustrating the computer output for different case studies. A complete validation of the total system model was not performed because of data acquisition problems and the immense amount of data required to perform such a testing procedure.

In the process of developing the ecosystem model, a variety of modelling problems developed. Two of these were determining which components should be considered in the ecosystem and balancing the representation of the ecosystem so that the different systems have comparable levels of complexity. The decision to use the components considered was based upon the apparent representativeness of the different components and the level of complexity desired for the overall ecosystem. Determining which modelling techniques should be used to represent the pheonomena observed in the ecosystems was also a problem. The results of this project demonstrated that a variety of techniques were needed to represent the different components in the urban-rural ecosystem. In particular, this model demonstrated how stochastic processes can be used to represent social systems and how linear programming can be used to optimize resource management.

The ecosystem model was designed for utilization by urban-rural areas and federal agencies such as HUD, HEW, and EPA. A city could use it to determine the effect of specific management decisions upon the evolution of the city and its surrounding area. Federal agencies (HUD, HEW, and EPA) could use the model to determine the effect of

their policy decisions upon particular urban areas. For example, EPA could determine the effect of enforcing air and water pollution laws upon the economy of different urban areas in the country. This is a relevant problem since blanket enforcement of air and water pollution standards throughout the country will cause economic inequities. These inequities are associated with the fact that the ability of the atmosphere to diffuse air pollution varies significantly from one area to another, and the fact that the amount of water available for diluting water pollution varies significantly from one local to another.

The influence of man upon the evolution of the urban-rural ecosystem is one of the most important facts demonstrated by this computer model. Results of a ten year simulation of the ecosystem model (see Appendix F) illustrated the dramatic influence that man's decisions have upon the evolution of the ecosystem. In particular, the simulation demonstrated the effect of man upon the water flow in ecosystems and the dependence of man upon availability of an adequate water supply. These results and the process of developing the model have demonstrated that the predictive value of the results from this model is limited by the uncertainty about man's actions in the future and that realistic models of the biological and geophysical aspects of the ecosystem can be developed. The development of management models that use realistic geophysical and biological subsections is desirable since they can be used to simulate the effect of man's possible actions on the evolution of the ecosystem. Results from this type of endeavor should be used to guide mankind in planning future activity. This is necessary since

mankind has the ability to significantly modify his natural environment. It is particularly important in the light of recent evidence which indicates potential disaster for man if he fails to change his present living style within the next 50 years (Forester, 1971; Watt, 1971). I believe that the use of management models such as the one presented in this paper is essential in order for man to avoid potential disaster associated with his modification of the natural environment and his rapid consumption of natural resources.

GENERAL REFERENCES

Air Quality Criteria for Sulfur Dioxides. DHEW, PHS, March 1967.

Air Quality Criteria for Particulate Matter, Summary and Conclusions, DHEW, PHS, Feb., 1969.

Bendat, J.S. and A.G. Piersol, Measurement and Analysis of Random Data, John Wiley and Sons, Inc., New York, 1958.

Clarke, A.B. and R.L. Disney, Probability and Random Processes for Engineers and Scientists, John Wiley & Sons, Inc., New York, 1970.

Clymer, A.B., The Modelling and Simulation of Big Systems, Proc. Simulation and Modelling Conference, Pittsburgh, Pa., April 21-22, 1969.

Clymer, A.B., The Modelling of Hierarchical Systems, Proc. Conference on Applications of Continuous Systems Simulation Languages, in Francisco, June 30, 1969.

Clymer, A.B. and Bledsoe, L.J., A Guide to the Mathematical Modelling of an Ecosystem, Paper presented at Ford Foundation Sponsored Workshop on Ecological Effects of Weather Modification, Albuquerque, New Mexico, June 16-27, 1969.

Committee on Natural Resources, Energy Resources, Natl. Acad. Sci., Natl. Res. Counc. Publ. 1000-d 141, Washington, D.C., 1962.

Eddy, A., and Parton, W.J., 1970. An Atmosphere-Oriented Ecosystem Simulation Model, Oklahoma Academy of Sciences.

Fensterstock, J.C. and R.K. Fankhauser, Thanksgiving 1966 Air Pollution Episode in the Eastern United States, U.S.D.HEW, PHS, July, 1968.

Forrester, J.W., Counter Intuitive Behavior of Social Systems, Technology Review, Jan. 1971.

Greenburg, L., et al., Report of an Air Pollution Incident in New York City, November 1963, Public Health Reports 78:1061-64.

Heimbach, J.A., 1971, The Correlation of Polluted Air with Tree Growth and Lung Disease in Humans, Comput. Biol. Med., 1, 243-253.

Hidy, G.M., Adventures in Atmospheric Simulation, Bul. Am. Met. Soc., 48, 143-159.

Landsberg, H.H., et al., 1963, Resources in America's Future, Published for Resources for the Future, Inc., John Hopkins Press.

Lee, Ray, An Organizational Solution of the Weather Forecasting Problems, Bul. Am. Met. Soc., 47, 438-444.

Lorentz, E.N., 1969, The Predictability of a Flow which Possesses Many Scales of Motion, Tellus, 21, 389-307.

Ministry of Health, Mortality and Morbidity During the London Fog of December 1952, Report by a Committee of Department Officers and Expert Advisers Appointed by the Minister of Health. Report on Public Health and Medical Subjects, No. 95, H.M. Stationery Office, 1954.

Parton, W.J. and A. Eddy, 1970, A Numerical Model of Human Population Dynamics Influenced by a Polluted Environment, Proc. AMS 2nd Natl. Conf. on Weather Modification.

Schrenk, H.H., et al., Air Pollution in Donora, Pa., Epidemiology of The Unusual Smog Episode of October 1948. Public Health Bulletin, No. 306, Federal Security Agency, Washington, D.C., 1949.

Scott, J.A., The London Fog of December 1962. Med. Officer 109-250, 1963.

Taha, H., 1971, Operations Research, An Introduction, the MacMilliam Co., New York.

Van Dyne, G., Analysis of Structure, Function and Utilization of Grassland Ecosystems, A Progress Report and Continuation Proposal to Natl. Sci. Foundation Grant GB - 1309 6-A, July, 1971.

Watt, K.E. and N.R. Glass, Land Use, Energy, Agriculture and Decision Making, A Report to N.S.F., Office of Interdisciplinary Research, Grant No. GI-27, May 28, 1971.

Weather and Climate Modification, 1965, Report of Special Commission of Weather Modification, National Science Foundation.

ATMOSPHERE

Bornstein, R.D. 1968. Observations of the Urban Heat Island Effect in New York City, J. Applied Metero. 7:575-582.

Chandler, T.J. 1962. Diurnal, Seasonal and Annual Changes in the Intensity of London's Heat Island, Met. Mag., London, 91: 146-153.

Changnon, S.A. 1969. Recent Studies of Urban Effects on Precipitation in the United States, Bul. of Am. Met. Soc., 56:44-421.

Chernoff, H. and L.E. Moses. 1959. Elementary Decision Theory, New York, John Wiley & Sons, Inc. 364 pp.

Clark, C.O. 1945. Storage and the Unit Hydrograph, Transactions ASCE Vol. 110, pp 1419-1488.

Court, A. 1961. Area-Depth Rainfall Formulas, Journal of Geophysical Research, 66(6):1823-1831.

Crawford, K.C. and H.R. Hudson. Behavior of Winds in the Lowest 1500 Feet in Central Oklahoma: June 1966-May 1967, ESSA Technical Memorandum ERLTM-NSSL 48, August 1970.

DeMarrais, G.A. 1961. Vertical Temperature Difference Observed Over an Urban Area, Bul. of Am. Metr. Soc., 12(8).

Denmead, O.T. and R.H. Shaw. 1962. Availability of soil water to plants as affected by soil moisture content and meteorological conditions. Agron. J. 54. pp 385-390.

Duckworth, F.S. and J.S. Sandberg 1954. The Effect of Cities Upon Horizontal and Vertical Temperature Gradients, Am. Metr. Soc. Bul., 35(5):198-207.

Dyer, A.J. and B.B. Hicks, 1968. Global Spread of Volcanic Dust from the Bali Eruption of 1963, Quarterly Journal of the Royal Meteorological Society, 94(402).

Ellsaesser, H.W. 1971. Air Pollution: Our Ecological Alarm and Blessing in Disguise, Transactions, American Geophysical Union, 53(3):92-99.

Gabriel, K.R. and J. Newmann. 1962. A Markov Chain Model for Daily Rainfall Occurrence at Tel Aviv. Quarterly Journal of Royal Meteor. Soc., 88:90-95.

Gardner, W.R. 1968. Availability and Measurement of Soil Water, Chapter 5 from "Water Deficits and Plant Growth, (ed.) T.T. Kozlowski, Academic Press, New York and London.

Gifford, F.A. 1961. Uses of Routine Meteorological Observations for Estimating Atmospheric Dispersion, Nuclear Safety, 2(4):47-51.

Hidy, G.M. Adventures in Atmospheric Simulation. Bul. Am. Metr. Soc., 48:143-159.

Holyoke, D. 1970. Model of Thermally Induced Wind Over a City Heat Island, Term Project for Ecology Modelling Class (Spring, 1970) at the Univ. of Oklahoma.

Horton, R.E., 1924, Discussion of "The distribution of intense rainfall and some other factors in the design of storm-water drains," by Frank A. Marston, Proc. Am. Soc. Civil Engrs. 50, pp. 660-667.

Horton, R.E. 1919. Rainfall Interception, Monthly Weather Review. 44:603-6234.

Haurwitz B., 1941. Dynamic Meteorology, McGraw Hill Book Co., New York.

Lee, Ray. An Organizational Solution of the Weather Forecasting Problem. Bul. Am. Metr. Soc. 47:438-444.

Lettau, H. 1969. Note on Aerodynamic Roughness--Parameter Estimation On the Basis of Roughness-Element Description, J. of Appl. Met., Vol. 8, No. 5.

Lipschutz, S. 1966. Theory and Problems of Finite Mathematics, New York, McGraw Hill Book Co., 339 pp.

Ludwig, J.H., et al., 1970. Trends in Urban Air Quality, Transactions, American Geophysical Union, 51(5).

Monteith, J.L. 1966. Local Differences in the Attenuation of Solar Radiation Over Britain. Quar. J. Royal Met. Soc. Vol. 92(392):254-262.

Munn, R.E. Descriptive Micrometeorology, Academic Press, New York, 1966.

Myrup, L.O. 1969. A Numerical Model of the Urban Heat Island, J. of Applied Meteorology, 8(6):863-873.

Nicks, A.D. and M.A. Hartman, 1966. Variations of Rainfall Over a Large Gaged Area. Transactions of ASAE, 9(3):437-440.

Ogatta G., Richards, L.A. 1957. Water Content Changes Following Irrigation of Bare Soil That is Protected From Evaporation, Soil Science Soc. of Am., Proceedings Vol. 21, No. 4 pp. 355-356.

Pasquill, F. 1961. The Estimation of the Dispersion of Windborne Material, Meteorological Magazine, 90(1063).

Pochop, L.O. Dynamics of the Atmosphere in the Grassland Ecosystem.

Pooler, F., Jr. 1963. Airflow over a City in Terrain of Moderate Relief, J. Appl. Met., 2:446-457.

Singer, S.F. 1970. Global Effects of Environmental Pollution, Transaction, American Geophysical Union, 51(5).

Summers, P.W. 1965. An Urban Heat Island Model, Paper presented at the First Canadian Conference on Micrometeorology, Toronto, April, 1965.

Sundborg, A. 1950. Local Climatological Studies of Temperature Conditions in an Urban Area. Tellus, 2(3):222-232.

Swinbank, W.C. 1963. Long-Wave Radiation from Clear Skies. Quart. J. Royal Metero. Soc. 89:339-348.

Turner, D.B. 1961. Relationships Between 24-hour Mean Air Quality Measurements and Meteorological Factors in Nashville, Tennessee, Air Poll. Cont. Assoc., 11:483-489.

Turner, D.B. Workbook of Atmospheric Dispersion Estimates, DHEW, PHS, 1969.

Webb, E.K. 1970. Profile Relationships: The Log-Linear Range and Extension to Strong Stability, Quarterly Journal Royal Metero. Soc., 96(407).

Whitman, W.C. and G. Wolters, 1967. Microclimatic Gradients in Mixed Grass Prairie, In Ground Level Climatology, Amer. Ass. Advanced Sci. Publ. 86:165-185.

"Upper Air Climatology of the United States, Part 1," Tech. Paper #32, U.S. Dept. of Commerce, Weather Bureau, June 1957.

BOTANY

Air Pollution Injury to Vegetation, DHEW, PHS, 1970.

Bledsoe, L.J., R.C. Francis, G.L. Swartzman and J.D. Gustafson. 1971. PWNEE: A grassland ecosystem model. Range Sci. Dept. Sci. Ser. No. 64. Colorado State University, Fort Collins, 179 p.

Burzlaff, D.F. The Role of the Abiotic Factors in the Structure and Function of the Grassland Ecosystem, Proceedings of the Information Synthesis Project, Grassland Biome, Range Science Dept., Science Series No. 2, Colorado State University, pp. 117-123, 1969.

Cochran, W.G., 1963. Sampling Techniques, John Wiley and Sons, New York, 413 p.

Francis, R.C., et al. A Study of Weight Estimation Method of Botanical Analysis, Tech. Rep. #117-U.S. IBP Grassland Biome.

Heck, W.W. et.al. Interaction of Environmental Factors on the Sensitivity of Plants to Air Pollution, JAPCA, 15:511-515.

Hill, A.C. et al. Plant Injury Induced by Ozone, Phytopathology 51:356-363, June, 1961.

Kline, J.R. Soil Chemistry as a Factor on the Function of Grassland Ecosystems, Proceedings of the Information Synthesis Project, Grassland Biome, Range Science Dept., Science Series No. 2, Colorado State University, pp. 71-88, 1969.

Middleton, J.T. et al. Airborne Oxidants as Plant-Damaging Agents, National Air Pollution Symposium, Stanford Research Institute, 1955.

Research Progress Report, 1968. Eastern Oklahoma Pasture Station, Muskogee, Oklahoma, Progress Report P-584, May, 1968, Oklahoma State University.

Research Progress Report, 1969. Eastern Oklahoma Pasture Station, Muskogee, Oklahoma, Progress Report P-611, May, 1969, Oklahoma State University.

Risser, P.G. 1970. Comprehensive network site description, OSAGE. Range Sci. Dept., Sci. Ser. No. 44., Colorado State University, Fort Collins, 5 p.

Risser, P.G. 1971. OSAGE Site, 1970 report, primary production. Range Sci. Dept., Sci. Ser. No. 80. Colorado State University, Fort Collins, 41 p.

Taylor, O.C. and I.M. Eaton. Suppression of Plant Growth by Nitrogen Dioxide. Plant Physiol. 41:132-135. Jan., 1966.

Terwillinger, Charles, Jr., Physical Properties of Grassland Soils and their influence on Primary Productivity, Proceedings of the Information Synthesis Project, Grassland Biome, Range Science Dept., Science Series No. 2, Colorado State University. pp. 65-70, 1969.

Thomas, M.D. Effects of Air Pollution on Plants, World Health Organization, Monograph Series, No. 46, Columbia University Press, New York, 1961.

Whitman, W.C. Microclimate and its Importance in Grassland Ecosystems. pp. 40-64, 1969.

HYDROLOGY

Black, T.A., W.R. Gardner and G.W. Thurtell. The Prediction of Evaporation, Drainage and Soil Water Storage for a Bare Soil, unpublished paper; Dept. of Soil and Water Sciences; Univ. of Wisconsin, Madison, Wisconsin.

Bruce, J.P. and R.H. Clark. 1966. Introduction to Hydrometeorology Oxford, New York. Pergamon Press.

Cartmill, R. 1970. "Forecasting the Volume of Storm Runoff Using Meteorological Parameters," Ph.D. Dissertation. Dept. of Meteorology, Univ. of Oklahoma, 1970.

Chow, V.T. 1964. Handbook of Applied Hydrology, McGraw-Hill Book Co., New York.

Cooper, C.F. Hydrology and Water Balance of Semi-Desert Soils, paper prepared for the Ford Foundation Workshop, Modelling Ecological Influence of Weather Modification, June 16-27, 1969; Albuquerque, New Mexico.

Cowan, I.R. 1962. Transport of Water in the Soil-Plant Atmosphere System, J. Appl. Ecol., 2:221-239.

Denmead, O.T., Shaw, R.H., 1962. Availability of Soil Water to Plants as Affected by Soil Moisture Content and Meteorology Conditions, Agronomy Journal, Vol. 54, pp. 385-390.

Gardner, W.R., 1968. Availability and Measurement of Soil Water, In T.T. Kozlowski's, WATER Deficits and Plant Growth, Academic Press, New York.

Gardner, W.R. 1960. Dynamic Aspects of Water Availability to Plants, Soil Science, 89:63-73.

Harbeck, G.E., Jr., et al. 1954. Water Loss Investigations, Vol. 1 Lake Hefner Studies, Technical Report. U.S. Geological Survey Paper 269.

Kohler, M.A. and M.M. Richards, 1962. Multi-Capacity Basic Accounting for Predicting Runoff from Storm Precipitation, Journal of Geophysical Research, 67(13):5187-5197.

Louchs, D.P. Stochastic Methods of Analyzing River Basin Systems, Research Project Technical Completion Report, OWRR Project No. c-1034 Department of Water Resources Engineering, Cornell University, August, 1969.

Mockus, V. Use of Storm and Watershed Characteristics in Synthetic Hydrograph Analysis and Application, U.S. Soil Conservation Series, 1957.

Palmer, W.C. 1965. Meteorological Drought, Research Paper No. 45, U.S. Department of Commerce Weather Bureau.

Penman, H.L. 1948. Natural Evaporation from Open Water, Bare Soil, and Grass, Proc. Royal Society, London, Ser. A., 193:120-145.

Penman, H.L. 1963. Vegetation and Hydrology. Technical Communication No. 53. Commonwealth Bureau of Soils, Harpenden, Rarnham Royal, Bucks, England.

Phosphate Study of Six Texas Rivers, Univ. of Texas Medical Branch, Galveston, Texas.

Pierce, L.T. 1958. Estimating Seasonal and Short-term Fluctuations in Evapo-Transpiration from Meadow Crops, Bul. Am. Met. Soc., 39(2).

Project Skywater, 1970 Annual Report, United States Department of the Interior, Bureau of Reclamation, February 1971.

Report for Consultation on the Metropolitan Houston-Galveston Interstate Air Quality Control Region, DHEW, PHS, Oct. 1969.

Roach, W.T. 1961. Some Aircraft Observations of Fluxes of Solar Radiation in the Atmosphere. Quart. J. Royal Meter. Soc. 87:346-363.

Ross, L.W. 1970. Simulation of Air and Water Pollution Dynamics: A Survey, Simulation, 14(4):165-171.

Shepard, J. 1958. The Effect of Pollution on Radiation in the Atmosphere, Int. J. of Air and Water Poll., Vol. 1.

U.S. Soil Conservation Service, National Engineering Handbook, Sec. 4, Supplement A. Hydrology, 1957, (3rd Edition in press, 1963).

Zahner, R. 1966. Refinement in Empirical Functions for Realistic Soil-Moisture Regimes under Forest Cover, Int. Symposium For Hydrol., Pergamon Press, N.Y., 261-274.

URBAN REFERENCES

Blumenfeld, H. The Modern Metropolis, Scientific American, 213(3): 64-74.

Davis, K. 1965. The Urbanization of the Human Population, Scientific American, 213(3):41-54.

Diehl, W.D. Farm-Nonfarm Migration in the Southeast: A Costs-Return Analysis, Journal of Farm Economics, Feb. 1966.

Forester, J.W. 1969. Urban Dynamics, the MIT Press, Cambridge, Mass.

Glazer, N. The Renewal of Cities, Scientific American, 213(3):195-208.

Mid-Planning Statement, The Model City Program, Houston, Texas, Jan., 1970.

Reid, George W. A Systems Approach to Urban Planning, Oklahoma Economic Development Foundation, Inc., Norman, Oklahoma.

Sjoberg, G. The Origin and Evolution of Cities, Scientific American, 213(3):55-64

Watt, K.E. A Model of Society, Environmental Systems Group, Institute of Ecology, University of California, Davis, California, April, 1969.

Wolman, A. The Metabolism of Cities, Scientific American, 213(3): 179-190.

ZOOLOGY

Elder, W.C. and B.B. Tucker. Pasture Management: Biennial Report of Progress for 1966 & 1967 on Forage Crop Grazing Studies and Fertility Tests, Processed Series P-583, April, 1968, Oklahoma State University.

Elder, W.C. and B.B. Tucker. Pasture Management: Grazing Studies and Forage Crop Fertility Tests, Biennial Report of Progress, 1964-1965, Processed Series P-530, March, 1966, Oklahoma State University.

APPENDIX A

APPENDIX A

RESULTS OF THE TESTING SCHEME PERFORMED ON THE ATMOSPHERIC MODEL

This section will present the results of the procedure used to test the atmospheric model. Sensitivity analysis and the comparison of observed data with simulated computer results are the two techniques used to test the model. The results from a 14-year simulation of the atmospheric model are used to generate frequency distributions and average monthly values of the atmospheric parameters which are compared with appropriate statistics calculated from a five year time series (1965-1969) of daily weather observation at Oklahoma City. A fairly long time series of simulated data are used to improve the probability that statistical attributes calculated from the simulated time series would be representative of the long-term statistical attributes of the parameters simulated by the models. A comparison of the statistical attributes calculated from the simulated and observed data should indicate that there is little difference between them since the observed data are used to calculate the climatalogical input data for the simulation model. The sensitivity analysis demonstrates the response of the radiation balance model, air pollution model and the urban heat island wind model to variations in the parameters that influence them. A complete summary of the climatological data used in the model is presented

in Tables 5-12. The data presented in Tables 7-12 are determined by statistically analyzing the five year time series of daily observations at Oklahoma City (1965-1969). The data are subjectively modified in cases where there were insufficient data to justify some of the results indicated by the statistical analysis. The utilization of subjective analysis to determine data presented in the tables is indicated by a "#" in the upper right hand corner of the numbers. The significance of the frequency distribution presented in the tables is indicated by the number of observations that are used to calculate each frequency. The superscript in the upper right hand corner of each frequency or average value gives the number of observations used to calculate the frequency or average value. Most of the numbers presented in the tables are calculated using a significant number of observations (30 or greater), however, some of them are calculated using only one or two observations. The data for the 1000 ft. average monthly air temperature and relative humidity (Table 5) are determined by using the 10-year climatalogical mean value for Oklahoma City (Upper Air Climatology of the US, 1957), while the average monthly 12-inch soil temperature (Table 5) is determined by subjectively modifying the average 12-inch soil temperatures observed in North Dakota. The average hourly surface and 1000 ft. wind speed are presented as a function of the average daily wind speed in Table 6. Table 6 is determined by comparing one year June 1966-May 1967) of the National Severe Storms Laboratory's hourly tower data (Crawford, 1970) with the daily average wind speed observed at Oklahoma City. The numbers in the far right hand column are the number of observations that are

TABLE 5

AVERAGE MONTHLY VALUES OF THE 12-INCH SOIL TEMPERATURE

AND

THE 1000 FT. AIR TEMPERATURE AND RELATIVE HUMIDITY

PARAMETERS	J	F	M	A	M	J	J	A	S	O	N	D
1000 ft Air Temperature[1](°C)	4.5	5.6	7.8	13.4	17.3	22.7	24.5	25.0	21.0	16.4	8.8	5.8
1000 ft Relative Humidity[2](%)	55	53	54	55	64	61	59	54	51	51	50	48
12-inch Soil Temperature[3](°F)	29	34	42	50	58	68	71	74	69	56	44	34

[1]Average monthly 1000 ft air temperature observed at Oklahoma City (Upper Air Climatology of the US, 1957).

[2]Average monthly 1000 ft relative humidity observed at Oklahoma City (Upper Air Climatology of the US, 1957).

[3]Average monthly 12-inch soil temperature estimated from Whitman's (1969) soil temperature data.

TABLE 6

AVERAGE HOURLY SURFACE AND 1000 FT WIND SPEEDS (KT) AS A FUNCTION OF AVERAGE DAILY WIND SPEED AND THE TIME OF DAY[1] (LST)

	Average Daily Wind Speed	TIME(Local Standard Time) 00	1	2	3	4	5	6	7	8	9	10	11	12
1000 ft average wind speed for Nov.,Dec.,Jan., and Feb.	0-5	12	12	12	11	9	9	10	10	9	9	9	7	6
	5.1-10	15	15	14	15	14	15	15	15	15	15	14	12	10
	10.1-15	26	27	26	27	28	28	28	28	27	26	26	23	21
	15.1-20	31	32	32	32	32	31	30	30	28	26	22	19	19
	20	35	35	34	33	33	34	35	36	34	33	32	30	29
1000 ft average wind speed for Mar.,Apr.,May, and June	0-5	12	13	14	13	11	10	10	11	11	9	8	5	7
	5.1-10	21	21	20	20	20	19	20	19	18	12	11	10	10
	10.1-15	26	27	27	27	26	25	25	24	23	18	18	15	15
	15.1-20	35	35	33	31	30	31	32	33	31	28	25	23	23
	20	47	44	44	40	45	27	30	36	39	37	35	32	35
1000 ft average wind speed for July,Aug.,Sept., and October	0-5	11	11	10	9	8	9	8	8	7	7	13	5	5
	5.1-10	18	18	18	18	18	18	17	16	15	12	10	9	10
	10.1-15	29	29	29	29	27	27	26	24	21	19	16	15	15
	15.1-20	34	32	34	32	33	32	29	27	26	24	18	18	18
	20	41	35	35	41	38	38	41	38	36	30	25	25	30
Average surface wind speed for Nov.,Dec.,Jan., and Feb.	0-5	3	3	3	3	3	2	2	2	2	3	4	5	5
	5.1-10	5	5	4	4	4	4	5	4	7	6	7	7	9
	10.1-15	9	9	9	9	9	9	10	11	10	12	13	13	13
	15.1-20	11	12	13	13	14	13	13	12	13	14	18	18	15
	20	18	17	17	16	18	18	19	18	17	19	20	19	19
Average surface wind speed for Mar.,Apr.,May, and June	0-5	2	1	1	1	1	3	2	1	3	3	4	3	4
	5.1-10	4	3	3	3	3	3	3	4	5	5	9	6	6
	10.1-15	7	7	7	7	7	7	7	7	9	9	9	10	10
	15.1-20	16	15	15	15	15	15	16	17	15	15	22	15	14
	20	20	18	17	17	17	14	15	14	20	17	17	21	18
Average surface wind speed for July,Aug.,Sept., and October	0-5	3	3	2	3	2	2	3	4	4	4	4	3	4
	5.1-10	5	4	5	5	4	4	5	5	6	6	7	6	7
	10.1-15	8	8	8	8	7	7	8	8	10	11	12	12	12
	10.1-20	12	12	11	12	11	11	11	12	13	14	11	13	12
	20	14	10	10	17	16	17	20	16	18	19	17	19	21

TABLE 6 continued

	Average Daily Wind Speed	TIME (Local Standard Time) 13	14	15	16	17	18	19	20	21	22	23	No. of Observations Used
1000 ft average wind speed for Nov.,Dec.,Jan., and Feb.	0-5	5	6	6	7	7	8	9	10	12	13	13	7
	5.1-10	11	13	13	14	11	12	14	15	16	18	18	48
	10.1-15	22	19	21	20	20	22	24	26	27	28	27	37
	15.1-20	23	23	23	24	24	24	24	24	25	25	25	24
	20	29	32	42	44	28	31	30	32	21	30	28	5
1000 ft average wind speed for Mar.,Apr.,May, and June	0-5	7	7	6	7	8	9	12	13	14	16	18	2
	5.1-10	13	12	14	11	10	11	12	14	16	18	19	35
	10.1-15	16	16	17	16	17	19	20	22	25	27	27	61
	15.1-20	24	23	24	27	25	26	27	29	31	32	32	24
	20	31	29	33	29	30	32	34	36	41	39	38	1
1000 ft average wind speed for July,Aug.,Sept., and October	0-5	5	5	6	6	7	7	7	9	9	11	12	9
	5.1-10	10	12	11	11	13	13	14	16	17	18	19	79
	10.1-15	15	16	16	16	17	18	19	21	23	24	24	29
	15.1-20	19	17	23	22	24	21	29	32	33	32	32	3
	20	36	37	36	33	37	38	41	40	39	44	29	1
Average surface wind speed for Nov.,Dec.,Jan., and Feb.	0-5	4	5	4	5	3	2	2	2	3	4	4	7
	5.1-10	9	7	7	9	6	5	5	4	4	5	5	48
	10.1-15	14	13	13	13	11	9	9	9	10	11	10	37
	15.1-20	16	16	15	15	14	12	10	10	10	9	9	24
	20	21	21	20	19	16	15	12	11	11	12	12	5
Average surface wind speed for Mar.,Apr.,May, and June	0-5	4	4	4	4	4	4	3	2	2	3	2	2
	5.1-10	6	6	9	6	5	5	3	3	3	3	3	35
	10.1-15	11	10	10	10	9	8	7	8	7	7	7	61
	15.1-20	16	19	18	18	14	16	14	14	14	14	15	24
	20	22	21	21	19	18	17	15	18	17	16	15	1
Average surface wind speed for July,Aug.,Sept., and October	0-5	4	4	4	4	4	3	3	2	2	3	3	9
	5.1-10	8	10	8	9	7	6	5	5	5	5	5	79
	10.1-15	12	11	12	11	11	9	8	7	7	6	7	29
	15.1-20	14	11	16	14	12	9	10	9	11	11	10	39
	20	24	27	19	20	23	24	22	22	23	26	16	1

[1]The average hourly wind speeds are determined by comparing one year (June 1966 - May 1967) of NSSL's hourly tower data (Crawford, 1970) with the daily average wind speeds observed at Oklahoma City.

TABLE 7

FREQUENCY DISTRIBUTIONS FOR THE DAILY AVERAGE WIND SPEED[1] AS A FUNCTION OF OBSERVED TWENTY-FOUR HOUR AVERAGE WIND DIRECTION

	Average Daily Wind Direction	WIND SPEED (MPH) 0 - 5	5.1-10	10.1-15	15.1-20	> 20
Nov. - Feb.	345-75	.051[10]	.358[70]	.410[80]	.164[32]	.051[3]
	76-155	.119[10]	.571[48]	.285[24]	.012[#]	.012[#]
	156-205	.043[9]	.289[60]	.478[99]	.174[36]	.014[3]
	206-275	.106[7]	.409[27]	.303[20]	.136[9]	.045[3]
	276-345	.054[6]	.309[34]	.400[44]	.20[22]	.036[4]
Mar. - June	345-75	.016[3]	.273[50]	.497[91]	.180[33]	.032[6]
	76-155	.048[6]	.362[45]	.467[58]	.112[14]	.008[#]
	156-205	.024[6]	.142[36]	.474[120]	.335[85]	.024[6]
	206-275	.05[3]	.250[15]	.516[31]	.150[9]	.033[2]
	276-345	.056[3]	.321[17]	.339[18]	.150[8]	.132[7]
July - Oct.	345-75	.051[6]	.431[50]	.431[50]	.068[8]	.017[2]
	76-155	.112[18]	.544[80]	.285[42]	.040[6]	.007[#]
	156-205	.022[6]	.333[90]	.551[149]	.088[24]	.003[#]
	206-275	.058[2]	.44[15]	.44[15]	.029[#]	.029[#]
	276-345	.145[7]	.312[15]	.375[18]	.125[6]	.041[2]

[1]The frequency distributions are calculated by using five years of daily weather observations at Oklahoma City (1965-19

[10] The number in the upper right hand corner of each frequency is the number of observations used to calculate the frequency.

[#]The symbol means that the indicated frequency of wind speed is estimated subjectively.

TABLE 8

WIND DIRECTION TRANSITION MATRIX FOR THE AVERAGE DAILY WIND DIRECTION AS A FUNCTION OF TIME OF YEAR[1]

	Average Daily Wind Direction At Time = t	Wind Direction at time t + 24 Hours				
		345-75	76-155	156-205	206-275	276-345
Nov. - Feb.	345-75	.370[74]	.170[35]	.250[50]	.066[13]	.128[25]
	76-155	.277[23]	.253[21]	.289[24]	.048[4]	.144[12]
	156-205	.241[50]	.053[11]	.429[89]	.125[26]	.140[29]
	206-275	.303[20]	.060[4]	.318[21]	.106[7]	.212[14]
	276-345	.254[28]	.109[12]	.209[23]	.145[16]	.272[30]
Mar. - June	345-75	.453[83]	.224[41]	.158[29]	.071[13]	.098[18]
	76-155	.178[22]	.292[36]	.455[56]	.024[3]	.048[6]
	156-205	.173[44]	.098[25]	.577[46]	.098[25]	.036[9]
	206-275	.366[22]	.216[13]	.183[11]	.116[7]	.113[8]
	276-345	.226[12]	.150[8]	.207[11]	.226[12]	.226[12]
July - Oct.	345-75	.370[43]	.293[34]	.181[21]	.043[5]	.08[10]
	76-155	.089[13]	.500[73]	.342[50]	.041[6]	.027[4]
	156-205	.149[40]	.118[32]	.646[174]	.048[13]	.056[15]
	206-275	.294[10]	.088[3]	.352[12]	.058[2]	.176[6]
	276-345	.208[10]	.083[4]	.250[12]	.166[8]	.270[13]

[1]The wind direction transition probabilities are calculated by using a five year time series of daily weather observations at Oklahoma City (1965-1969).

[74]The numbers in the upper right hand corner of each probability is the number of observations used to calculate the probability.

TABLE 9

FREQUENCY DISTRIBUTIONS OF THE AVERAGE DAILY RELATIVE HUMIDITY[1] AS A FUNCTION OF THE OBSERVED DAILY AVERAGE WIND DIRECTION AND THE TIME OF YEAR

		RELATIVE HUMIDITY (%)				
	Average Daily Wind Direction	0-20	21-40	51-60	61-80	81-100
Nov. - Feb.	345-75	.005#	.030[6]	.326[64]	.274[73]	.265[52]
	76-155	.011#	.011#	.321[27]	.356[30]	.297[25]
	156-205	.004#	.076[16]	.394[82]	.346[72]	.178[37]
	206-275	.014#	.119[8]	.447[30]	.298[20]	.119[8]
	275-345	.009#	.054[6]	.441[49]	.387[43]	.108[12]
Mar. - June	345-75	.005#	.043[8]	.315[58]	.456[84]	.179[33]
	76-155	.008#	.008#	.282[35]	.556[69]	.145[18]
	156-205	.004#	.039[10]	.381[97]	.523[133]	.051[13]
	206-275	.016#	.147[9]	.508[31]	.295[18]	.032[2]
	276-345	.009#	.481[9]	.481[26]	.240[13]	.092[5]
July - Oct.	345-75	.008#	.025[3]	.427[50]	.470[55]	.008[8]
	76-155	.011#	.011#	.445[65]	.475[70]	.119[10]
	136-205	.004#	.044[12]	.551[149]	.37[100]	.03[8]
	206-276	.027#	.027#	.675[25]	.243[9]	.027#
	276-345	.020#	.061[3]	.428[21]	.428[21]	.016[3]

[1]The frequency distributions of relative humidity are calculated by using a five-year time series of daily weather observations at Oklahoma City (1965-1969).

[6]The number in the upper right hand corner of each frequency is the number of observations used to calculate the frequency.

#The symbol means that the indicated frequency of relative humidity is estimated subjectively.

TABLE 10

THE FREQUENCY DISTRIBUTIONS OF DAILY AVERAGE CLOUD COVER[1]

AS A FUNCTION OF THE DAILY AVERAGE WIND DIRECTION AND RELATIVE HUMIDITY

	Relative Humidity (%)	Cloud Cover (%)				
		0-20	21-40	41-60	61-80	81-100
Wind Direction (345-75)	0-20	.625[10]	.1875[3]	.063[#]	.063[#]	.063[#]
	21-40	.058[#]	.352[6]	.117[2]	.235[4]	.235[4]
	41-60	.372[64]	.133[23]	.186[32]	.128[22]	.18[31]
	61-80	.132[28]	.080[17]	.141[30]	.179[38]	.466[99]
	81-100	.010[#]	.010[#]	.010[#]	.063[6]	.905[86]
Wind Direction (76-155)	0-20	.625[10]	.187[3]	.063[#]	.063[#]	.063[#]
	21-40	.500[5]	.200[2]	.10[#]	.10[#]	.10[#]
	41-60	.283[36]	.173[22]	.149[19]	.165[21]	.228[29]
	61-80	.071[12]	.088[15]	.147[25]	.225[38]	.468[79]
	81-100	.018[#]	.018[#]	.018[#]	.018[#]	.928[51]
Wind Direction (156-205)	0-20	.625[10]	.1875[3]	.063[#]	.063[#]	.063[#]
	21-40	.526[20]	.105[4]	.131[5]	.105[4]	.131[5]
	41-60	.426[140]	.195[64]	.125[41]	.103[34]	.149[49]
	61-80	.137[42]	.154[47]	.150[46]	.219[67]	.337[103]
	81-100	.016[#]	.016[#]	.032[2]	.133[8]	.800[48]

Table 10 continued

		0-20	21-40	41-60	61-80	81-100
Wind Direction (206-275)	0-20	$.625^{10}$	$.187^{3}$	$.063^{\#}$	$.063^{\#}$	$.063^{\#}$
	21-40	$.473^{9}$	$.210^{4}$	$.157^{3}$	$.105^{2}$	$.011^{\#}$
	41-60	$.465^{40}$	$.128^{11}$	$.162^{14}$	$.069^{6}$	$.174^{15}$
	61-80	$.276^{13}$	$.191^{9}$	$.212^{10}$	$.126^{6}$	$.191^{9}$
	81-100	$.090^{\#}$	$.090^{\#}$	$.180^{2}$	$.272^{3}$	$.363^{4}$
Wind Direction (276-345)	0-20	$.625^{10}$	$.187^{3}$	$.063^{\#}$	$.063^{\#}$	$.063^{\#}$
	21-40	$.611^{11}$	$.11^{\#}$	$.11^{\#}$	$.11^{\#}$	$.055^{\#}$
	41-60	$.625^{60}$	$.156^{15}$	$.062^{6}$	$.104^{10}$	$.052^{5}$
	61-80	$.220^{17}$	$.142^{11}$	$.202^{17}$	$.168^{13}$	$.202^{17}$
	81-100	$.245^{\#}$	$.045^{\#}$	$.045^{\#}$	$.090^{2}$	$.773^{17}$

[1]The frequency distributions of cloud cover are calculated by using a five-year time series of daily weather observations at Oklahoma City (1965-1969).

[10]The number in the upper right hand corner of each frequency is the number of observations used to calculate the frequency.

[#]The symbol means that the indicated frequency of cloud cover are estimated subjectively.

TABLE 11

THE PROBABILITY FOR RAINFALL[1] AS A FUNCTION OF THE OCCURRENCE OR NON-OCCURRENCE OF RAINFALL ON THE PREVIOUS DAY, THE OBSERVED AVERAGE DAILY RELATIVE HUMIDITY AND THE TIME OF YEAR

Average Daily Relative Humidity	Nov, Dec, Jan, Feb		Mar, Apr, May, Jun		Jul, Aug, Sep, Oct	
%	No-Rain	Rain	No-Rain	Rain	No-Rain	Rain
0-20	.001[#]	.002[#]	.001[#]	.002[#]	.001[#]	.002[#]
21-40	.028[1]	.038[#]	.009[#]	.018[#]	.056[1]	.078[#]
41-60	.025[6]	.133[2]	.048[10]	.162[6]	.071[20]	.167[5]
61-80	.130[25]	.196[9]	.291[64]	.381[37]	.297[49]	.378[34]
81-100	.506[41]	.585[31]	.767[23]	.828[34]	.72[13]	.999[11]

[1]The probability for rainfall is calculated by using a five-year time series of daily weather observations at Oklahoma City (1965-1969).

[6]The number in the upper right hand corner of the rainfall probabilities is the number of observations used to calculate the probability.

[#]The sumbol means that the rainfall probability is estimated subjectively.

TABLE 12

AVERAGE DAILY RAINFALL[1] (INCHES) FOR RAINDAYS AS FUNCTIONS OF AVERAGE DAILY WIND DIRECTION AND RELATIVE HUMIDITY AND THE TIME OF YEAR

	Average Daily Wind Direction	Average Daily Relative Humidity (%)				
		0-20	21-40	41-60	61-80	81-100
Nov. - Feb.	345-75	.01[#]	.01[#]	.02[1]	.27[4]	.18[16]
	76-155	.01[#]	.01[#]	.24[#]	.25[#]	.279[11]
	156-205	.01[#]	.07[#]	.09[1]	.09[13]	.242[36]
	206-275	.01[#]	.01[#]	.01[#]	.06[7]	.250[8]
	276-345	.01[#]	.01[#]	.02[#]	.244[5]	.170[15]
Mar. - June	345-75	.01[#]	.01[#]	.12[#]	.38[7]	.482[33]
	76-155	.01[#]	.01[#]	.216[#]	.350[1]	.765[9]
	156-205	.01[#]	.05[#]	.32[2]	.33[7]	.664[23]
	206-276	.01[#]	.01[#]	.075[2]	.25[7]	.350[15]
	276-345	.01[#]	.01[#]	.075[1]	.25[6]	.350[9]
July - Oct.	345-75	.01[#]	.01[#]	.12[#]	.40[3]	.45[15]
	76-155	.01[#]	.01[#]	.228[#]	.48[1]	.620[21]
	156-205	.01[#]	.08[#]	.104[#]	.301[12]	.620[53]
	206-276	.01[#]	.01[#]	.090[#]	.17[#]	.190[8]
	276-345	.01[#]	.01[#]	.075[#]	.50[3]	.600[9]

[1]The average daily rainfall for raindays is calculated by using a five-year time series of daily weather observations at Oklahoma City (1965-1969).

[4]The number in the upper right hand corner of each of the average daily rainfall amounts is the number of observations used to calculate the value.

[#]The symbol indicates that the average daily rainfall amount is estimated subjectively.

used in calculating the average wind speed values presented in each of the rows of the table. The air pollution field for the 14-year simulation is set equal to 8 $\mu g/m^3$, however, the occurance or non-occurance of rainfall is simulated with the assumption that high air pollution (greater than 40 $\mu g/m^3$) values exist in ecosystem.

The comparison of the observed and simulated wind direction frequency distribution (Figure 23)is satisfactory. Both the simulated and observed frequency distributions show that wind directions from 120 to 200 are the most probable. The observed and simulated average wind speed as a function of wind direction is shown in Figure 24. The results show a favorable comparison; however, observed average wind speeds are generally lower than the simulated average wind speeds. This is because the frequency distributions used to predict the wind speed in the model are modified to take into account the fact that the wind speed for the five years of observed data used as input data for the model is below the long term average for wind speed at Oklahoma City. Some of these important features indicated by Figure 24 are that average wind speed is greatest in the spring months (April, May, and June), lowest during the fall (October, November and December) months and that the average wind speed is greatest for wind directions from south (140-200) and north (300-370).

The comparisons of the observed and simulated frequency distributions of cloud cover and relative humidity are shown in Figures 25 and 26. Inspections of the cloud cover frequency distribution show that the observed and simulated frequency distributions compare favorably. The "student t" test (Panofsky, 1965) is used to determine if the

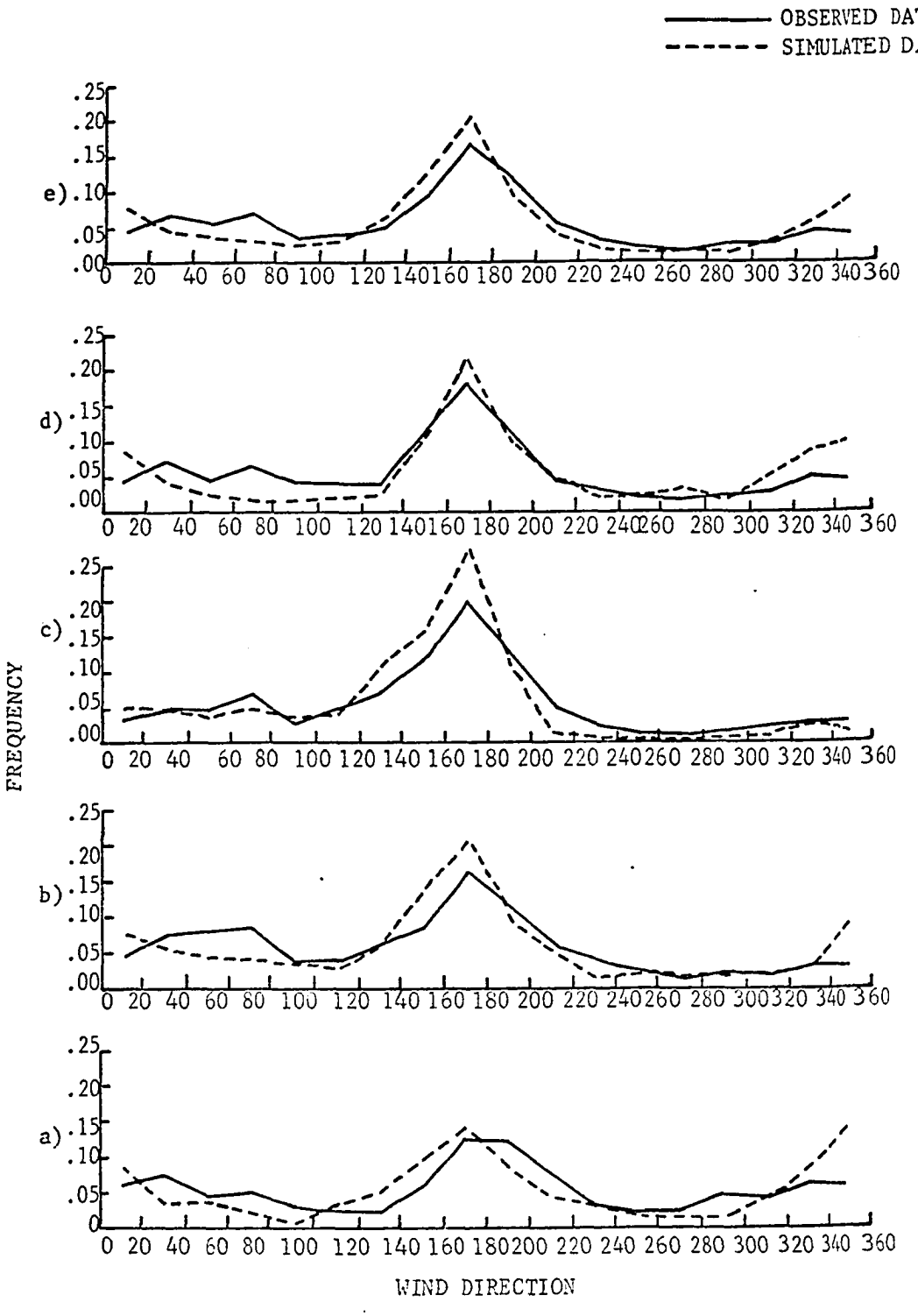

Fig. 23. Frequency distribution of wind direction for January, February, and March (a); April, May and June (b); July, August, and September (c); October, November, and December (d); and the annual frequency distribution (e) are presented in this figure. The average number of observations used to calculate the probability for the 18 wind direction class intervals in (a), (b), (c), and (d) is equal to 25 for the observed data and 75 for the simulated data. Similarly, in graph (e), the average number of observations for the observed data is 100 and 280 for simulated data.

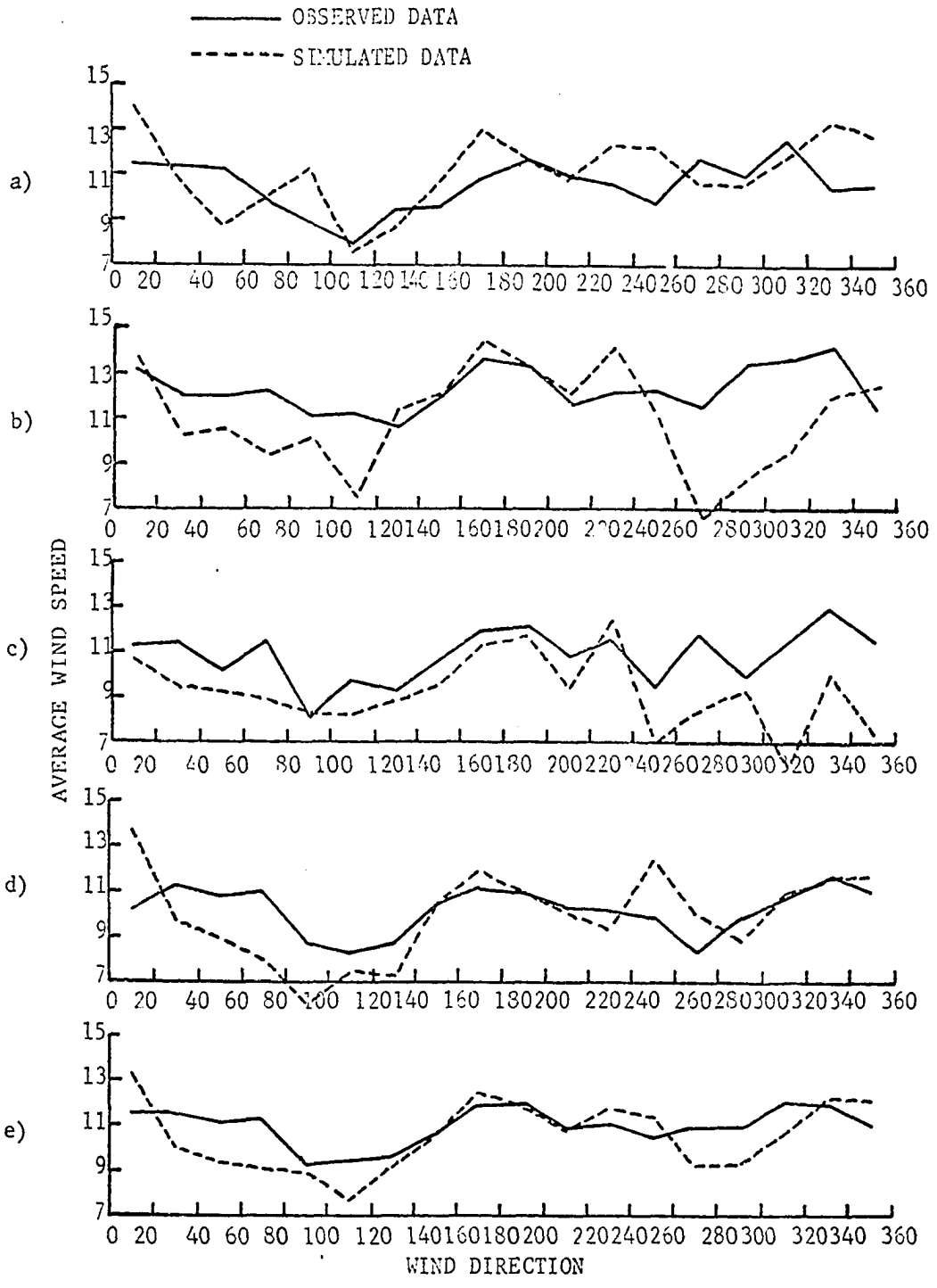

Fig. 24. The average wind speed as a function of wind direction for January, February, and March (a); April, May, and June (b); July, August, and September (c); October, November, and December (d); and January through December (e) are presented in this figure. The average number of observations used to calculate the average wind speed for the 18 wind direction class intervals in (a), (b), (c), and (d) is equal to 25 for the observed data and 70 for the simulated data. Similarly, in graph (e), the average number of observations for the observed data is 100 and 280 for the simulated data.

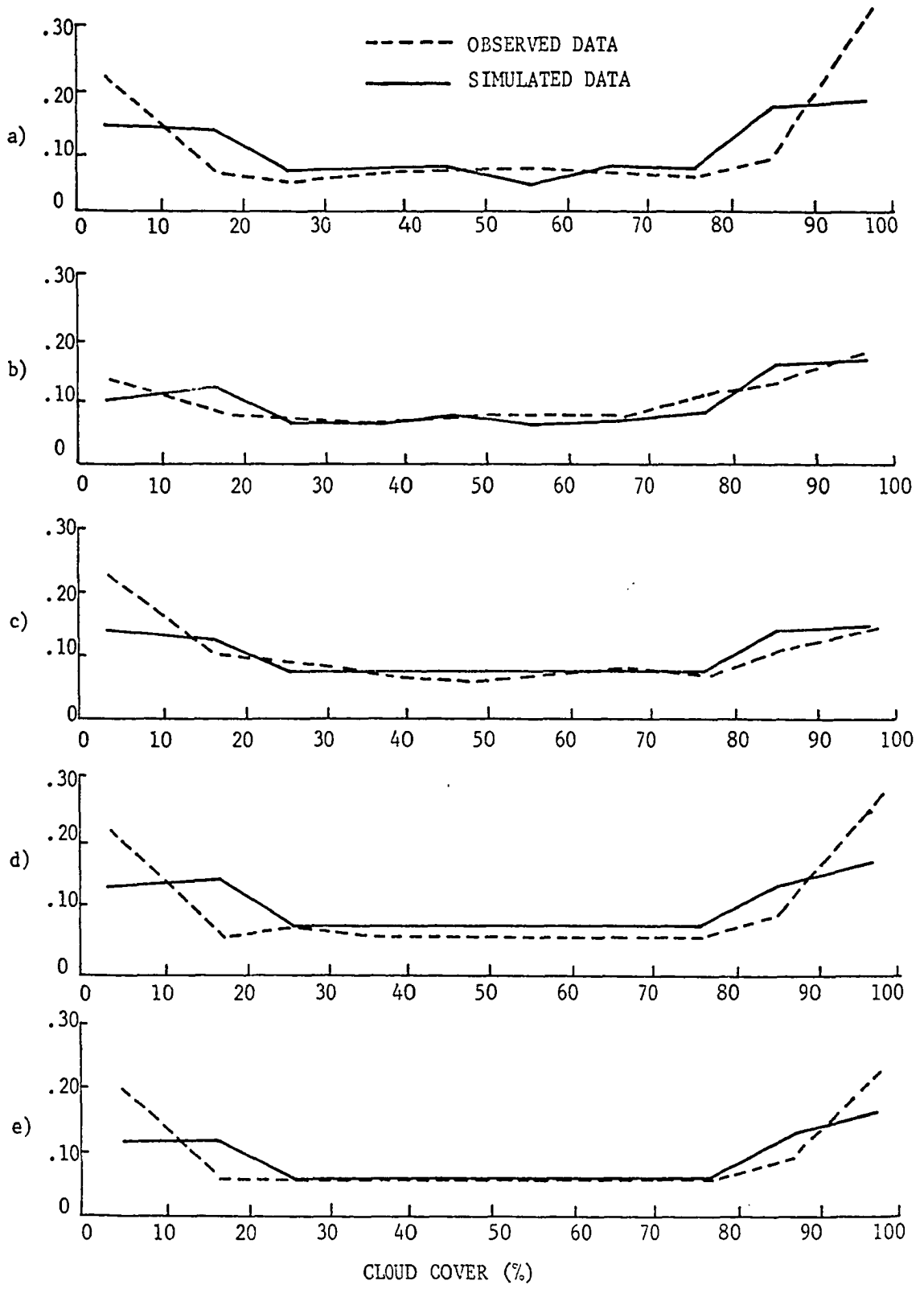

Fig. 25. Frequency distributions of cloud cover for Jan., Feb., and Mar. (a); Apr., May, and June (b) July, Aug., and Sep. (c); Oct., Nov., and Dec. (d); and the annual frequency distribution (e) are presented in this figure. The average number of observations used to calculate the probabilities in the 10 class intervals of cloud cover in (a), (b), (c), and (d) is 45 for the observed data and 126 for the simulated data. In graph (e) the average number is 180 for the observed data and 504 for the simulated data.

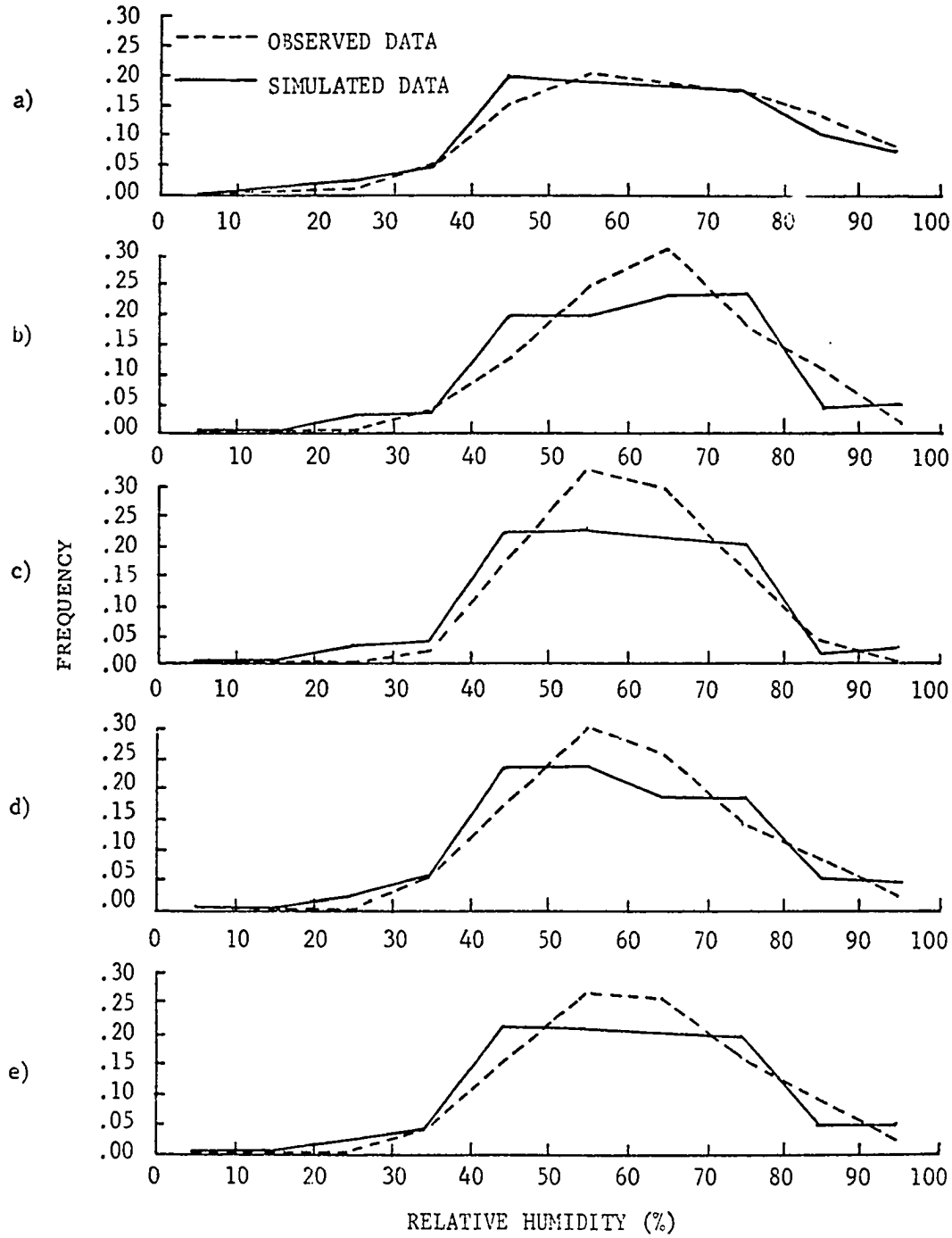

Fig. 26. Frequency distributions of relative humidity for January, February, and March (a); April, May and June (b); July, August, and September (c); October, November, and December (d); and the annual frequency distribution (e) are illustrated in this figure. The average number of observations used to calculate the probabilities in the 10 class intervals of relative humidity in (a), (b), (c), and (d) is 45 for the observed data and 126 for the simulated data. In graph (e) the average number is 180 for the observed data and 504 for the simulated data.

difference between the observed and simulated probabilities for the cloud cover class intervals are significant. The combined results form graphs (a), (b), (c), (d), and (e) in Figure 25 show that there is a significant difference (values are outside the 95% confidence limits) between the observed and simulated probabilities for the cloud cover class intervals in 10 of the 50 different comparisons that are tested. The observed discrepancy is most likely attributed to the fact that a large number of the probabilities in the frequency distribution used as input data for the simulation model are subjectively estimated because of insufficient data (see Table 11). Both the observed and simulated frequency distributions indicate that the winter, fall and spring months have higher probabilities for cloud cover greater than 70%. The observed and simulated frequency distributions for relative humidity (Figure 26 compared very favorably. They both showed that the winter and spring months have higher relative humidity than the summer and fall months, while the relative humidity from 45 to 75% have the highest probability of occurrence.

The rainfall model is tested by considering the spatial distribution of rainfall in the ecosystem and by comparing statistical attributes of the rainfall at a particular point in the ecosystem (this point represents the rainfall at Oklahoma City) with the statistical attributes derived from observed data at Oklahoma City. The model is set up to simulate rainfall in the ecosystem such that the annual average rainfall amounts will increase from the northwest to the southeast across the ecosystem. Two techniques are used to simulate the rainfall distribution in the ecosystem. The frontal rain mechanism

distributes rainfall across the ecosystem using a poisson distribution while, the convective shower mechanism distributes rainfall across the ecosystem by using randomly placed "unit area storms." A typical type of pattern for both of these types of rainfall is presented in Figure 27. The spatial distribution of rainfall is demonstrated in Figure 28 which shows the average monthly values for three points in the ecosystem (southeast, central and northwest). The results show that average monthly rainfall is least in the northwest and greatest in the southeast. The only discrepancy in this figure is that during the months of July and August, the rainfall is lower at the point in the central section than it is in the northwest. This discrepancy is attributed to the fact that during the months of July and August rainfall occurs as convective shower activity which has the property such that the rainfall for the whole ecosystem will be distributed over less than 20% of the area. The convective shower simulation mechanism causes the monthly rainfall observed at any point in the ecosystem to be subject to large variations. These large variations are a likely cause for the discrepancy observed between the mean rainfall amounts observed at the central and northwest point. The fact that the probability for a convective shower to be located in the central section is 20% greater than the probability in the northwest make it likely that a longer time simulation of the model would show that the average monthly rainfall during July and August is greater in the central section than the northwest.

The rainfall at the central point in the ecosystem is used to compare the monthly average rainfall, frequency distribution of rainfall amounts, and the average monthly number of rain days with the appropriate

a)

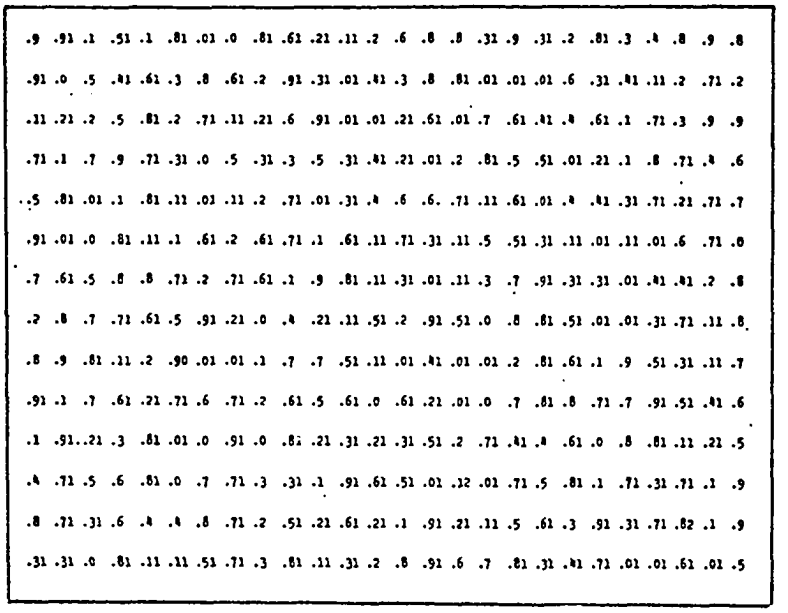

b)

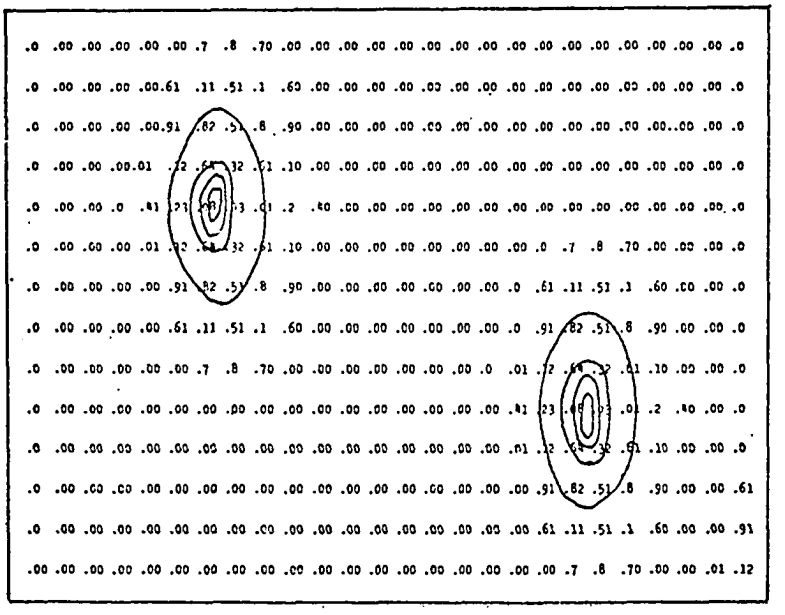

Contoured every 2 inches

Fig. 27 Typical rainfall patterns for frontal (a) and convective (b) type precipitation (inches per day).

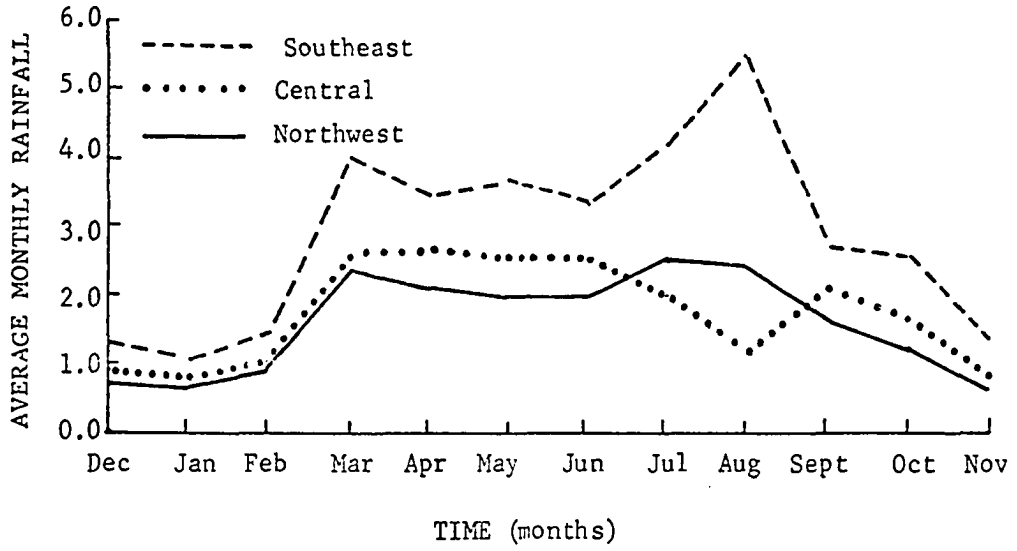

Fig. 28. The average monthly rainfall for three points in the ecosystem are illustrated. The data is calculated from the 14-year computer simulation.

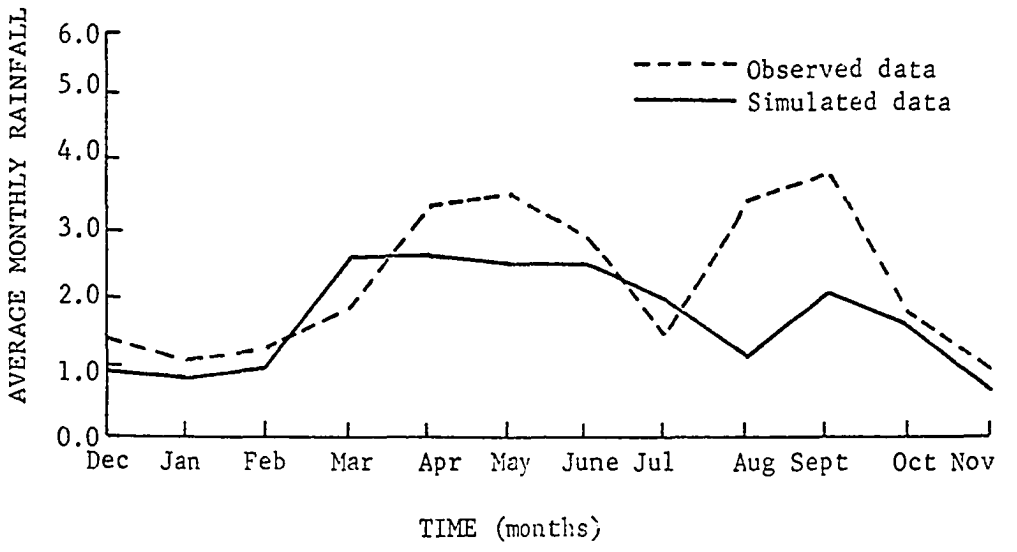

Fig. 29. The simulated and observed monthly average rainfall is illustrated in this figure. The simulated data are calculated from the 14-year computer simulation, while the observed data is determined from the 5-year time series of daily observations at Oklahoma City (1965-1969).

statistics generated from daily observations at Oklahoma City. Figure 29 shows a comparison of the observed and simulated average monthly rainfall. The observed and simulated average rainfall amounts compare favorably, however, during the months of August and September, the observed average monthly rainfall is much greater than the simulated average value. The "student's t test" was run to determine significance of the deviation between the observed and simulated average monthly rainfall amounts. The results showed that there is no significant difference at the 95% confidence level. However, the results did show that the difference between the observed and simulated average monthly means for August and September is significant at the 90% confidence level. This observed discrepancy is partially attributed to the fact that the average monthly rainfall for September and August that is calculated from the observed data is .75 inches greater than the long term average monthly rainfall amounts for Oklahoma City. It is important to note that the model is not able to predict a sharp peak in the rainfall for a given month because of the fact that the climatalogical input data is presently summarized over four month periods. The data would have to be summarized over monthly time periods in order to simulate large month to month variations in rainfall. The spring peak in rainfall (March, April, May and June), the September peak in rainfall and the low rainfall observed during the winter (December, January, and February) are features indicated for both the observed and simulated average amounts.

Figure 30 presents the rainfall amount cumulative frequency distributions for the simulated and observed data. The results of comparing

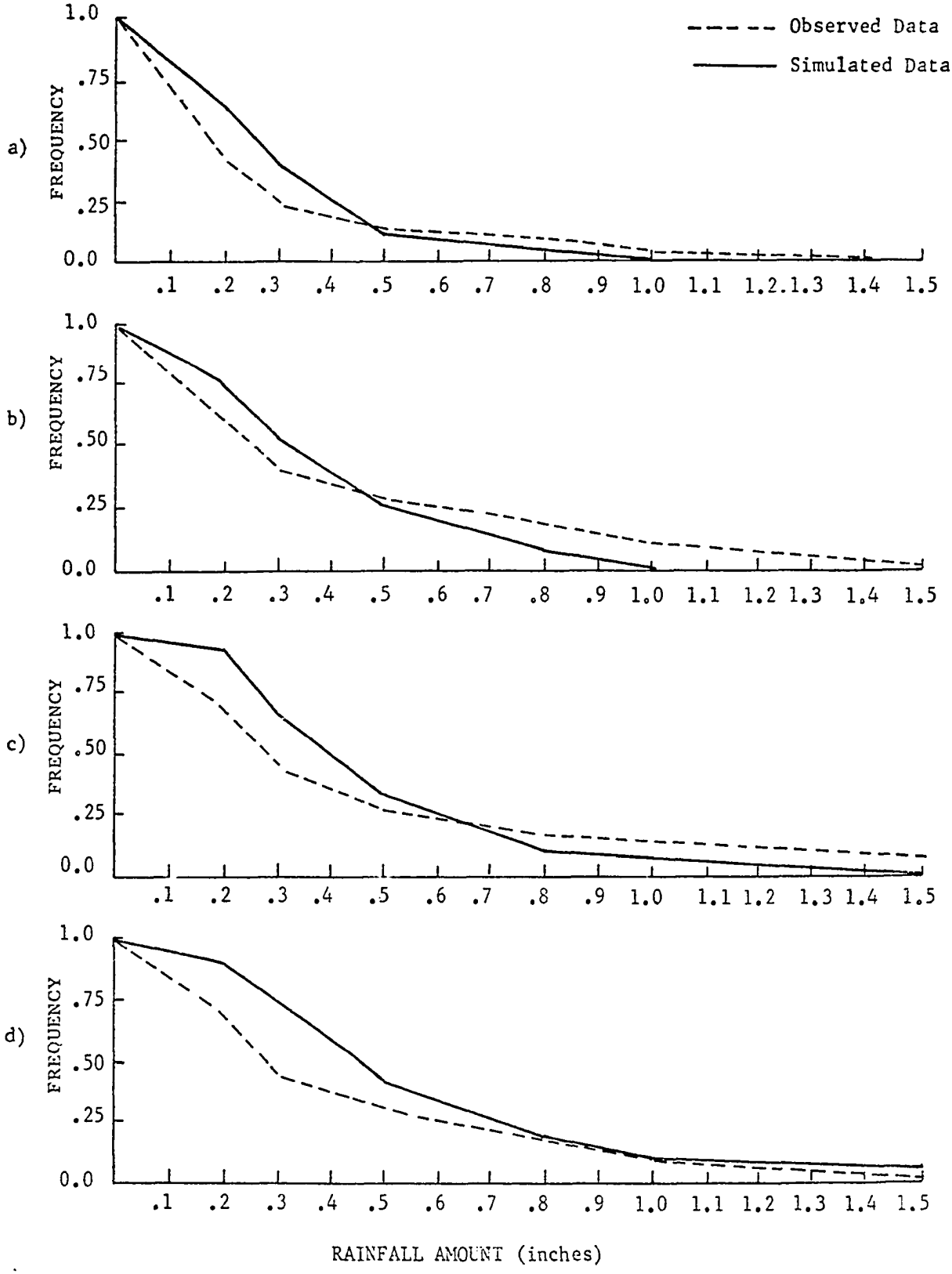

Fig. 30. The simulated and observed cumulative frequency distributions of rainfall amounts for Oct., Nov., and Dec. (a); Jan., Feb., and Mar. (b); Apr., May, and June (c); and July, Aug., and Sep. (d) are presented in this figure. The simulated cumulative frequency distributions are calculated from a 14-year time simulation, while the observed values are determined from a 5-year time series of daily weather observations at Oklahoma City (1965-1969).

the frequency distributions for the fall (October, November and December), winter (January, February and March) and spring (April, May and June) months showed that the frequency of the large rainfall amounts increased from a minimum in the fall months to a maximum in the spring months. One discrepancy in comparing these frequency distributions is that the simulated distributions have significantly lower probabilities for the higher rainfall amounts. This indicates that the technique used to determine rainfall amounts for frontal rainfall activity should be modified so that larger rainfall amounts have a higher probability of occurring. The comparison of the observed and simulated frequency distributions for the summer months (July, August and September) indicate the probability for rainfall greater than .8 inches compare favorably; however, the generated probability for rainfall greater than .3 and .5 inches is considerably greater than the probabilities indicated by the observed data. These results indicate that convective rainfall mechanism used to simulate rainfall during this time period is over-predicting rainfall events in the .3 to .8 inch category. A possible solution to this problem is to modify the rainfall mechanism so that the rainfall amounts decrease more rapidly moving away from the center of the convective storms.

Figure 31 illustrates a comparison of the observed and simulated average monthly number of rain days. The observed average number of rain days is calculated using the five year time series of observation at Oklahoma City (1965-1969), while the simulated average number of rain days is calculated from the 14 year series of simulated atmospheric data. The results show that the simulated data does not show a distinct

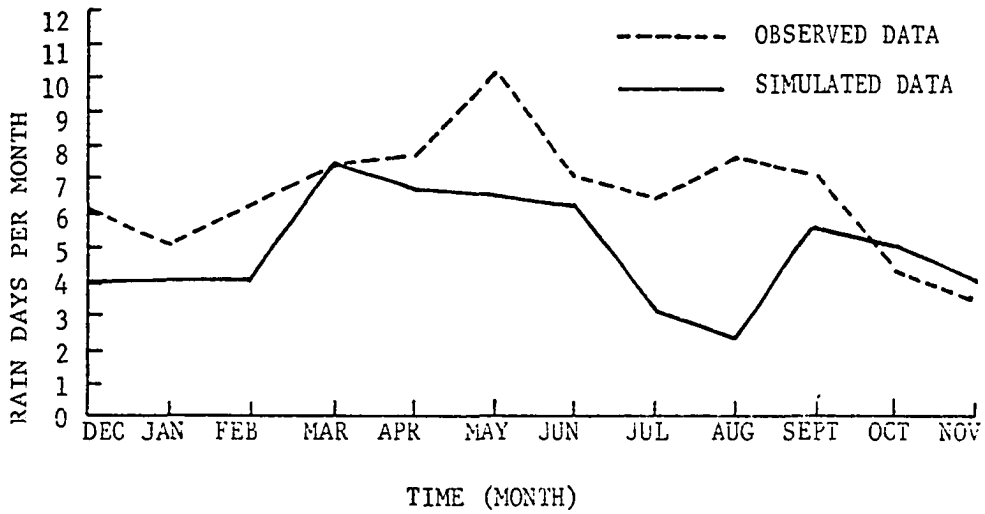

Fig. 31. The simulated and observed monthly average number of rain days are shown in this figure. The simulated data are calculated from the 14-year run of the ecosystem model, while the observed data are calculated from a 5-year time series of daily weather observations at Oklahoma City (1965-1969).

peak in the maximum number of rain days as indicated by the observed data and also that the average number of rain days for the months of July and August is much lower in comparison with the observed data. The simulation model is not capable of predicting monthly variations in the observed number of rain days since it combines the data for a four month period to determine the statistical controlling relationships. The significantly lower number of rain days for the simulated data during the months July and August can be attributed to the fact that the convective shower mechanism is used to distribute rainfall during this period of time. The model predicts the correct number of rain days for rainfall occurring anywhere in the ecosystem; however, since only 20% of the total area received rainfall using this mechanism, then the average number of rain days at any given point in the ecosystem will be less than the average number of rain days indicated by the observed data. This fact means that the convective shower mechanism will have to be modified so that a larger percentage of the ecosystem will receive rainfall. The results from Figure 31 show that both the observed and simulated data had the peak average monthly number of rain days occurring during the spring (March, April and May) while the minimum number of rain days occurred during the winter and fall months (November, December, January and February).

The influence of air pollution upon rainfall is incorporated in the overall rainfall model by assuming that areas which have air pollution levels greater than 40 $\mu g/m^3$ will have a 10% greater probability for rainfall to occur and also that if it does occur then the amount will be 10% greater than the rainfall amount in an area with

low air pollution. The effect of air pollution on rainfall is demonstrated by a 2-year computer simulation in which a constant air pollution field is superimposed over the rainfall grid. A comparison of average rainfall at a point with low air pollution (0.0 $\mu g/m^3$) and point with high air pollution (86 $\mu g/m^3$) are presented in Table 13. These results show that the point with high air pollution has a higher number of rain days and higher average monthly rainfall than the point with low air pollution.

In an attempt to validate the radiation balance model, the monthly average maximum and minimum air surface air temperature and the average monthly 6-inch soil temperature are calculated from the 14-year simulation of the model and compared with observed data from Oklahoma City. The values of the air and soil temperature simulated by the model are calculated at a point in the central section of the ecosystem. The rainfall data from this same point are compared with the observed data at Oklahoma City. The radiation balance model is modified slightly to obtain the simulated results that are used in this validation procedure. The model is altered by using the following equations to modify the values of U_2 (wind speed at the 30000 cm level) and Z_0 (roughness length) as a function of time of year. The model also assumes that $dq/dz \geq 0$ (no deposition of dew) and that RH (% of area evaporating water) never gets lower than .5.

TABLE 13

The effect of air pollution upon the average monthly rainfall, the number of rain days, and average monthly maximum air temperature are demonstrated in this table.

Seasons	[1]Average # of Rain Days Air Pollution = 86 $\mu g/m^3$	[1]Average # of Rain Days Air Pollution = 0.0 $\mu g/m^3$	[1]Average Monthly Rainfall Air Pollution = 86 $\mu g/m^3$	[1]Average Monthly Rainfall Air Pollution = 0.0 $\mu g/m^3$	[2]Average Maximum Air Temperature (F) Air Pollution = 398 $\mu g/m^3$	[2]Average Maximum Air Temperature (Air Pollution = 8.0 $\mu g/m^3$
Jan Feb Mar	2.3	2.5	.60	.73	49.7	51.8
Apr May Jun	6.5	6.3	3.04	2.84	63.3	67.3
Jul Aug Sept	5.8	4.6	3.45	2.38	84.2	88.6
Oct Nov Dec	6.2	5.3	2.21	1.93	65.8	69.3
Annual	5.2	4.67	2.32	1.97	65.6	69.25

[1]These values are calculated from a two-year computer simulation in which the rain is observed at two points that had different constant air pollution levels.

[2]These values are calculated from a two-year computer simulation in which the maximum air temperature is observed at two points that had different constant air pollution levels.

$$U = \begin{cases} = U_2^1 \text{ during the day time hours (06-19 LST) if the average surface wind speed is greater than 5 MPH.} \\ = .8\ U_2^1 \text{ during the night time hours (20-05 LST) from April to September.} \\ = .27\ U_2^1 \text{ during the night time hours (20-05 LST) from October to March.} \\ = U_2^2 \text{ during the day (06-19 LST) if the average surface wind speed is less than or equal to 5 MPH.} \end{cases} \quad (1)$$

$$Z_0 \quad \begin{cases} = 20 \text{ cm from April through September} \\ = 70 \text{ cm from October through March} \end{cases} \quad (2)$$

where

U_2^1 wind speed at 30000 cm predicted by the Atmosphere Model

U_2^2 wind speed at 3000 cm predicted by the Atmosphere Model for average surface wind speed between 5 and 10 MPH.

These modifications are used to lower the minimum air temperatures predicted by the radiation balance model and to keep the maximum air temperature from getting too large. Another modification is that the volumetric soil moisture content used by temperature model is set to a lower value than the actual volumetric soil content of soil ($\approx 1/2$). Figure 32 illustrates the comparison between the average monthly maximum and minimum air temperature determined from

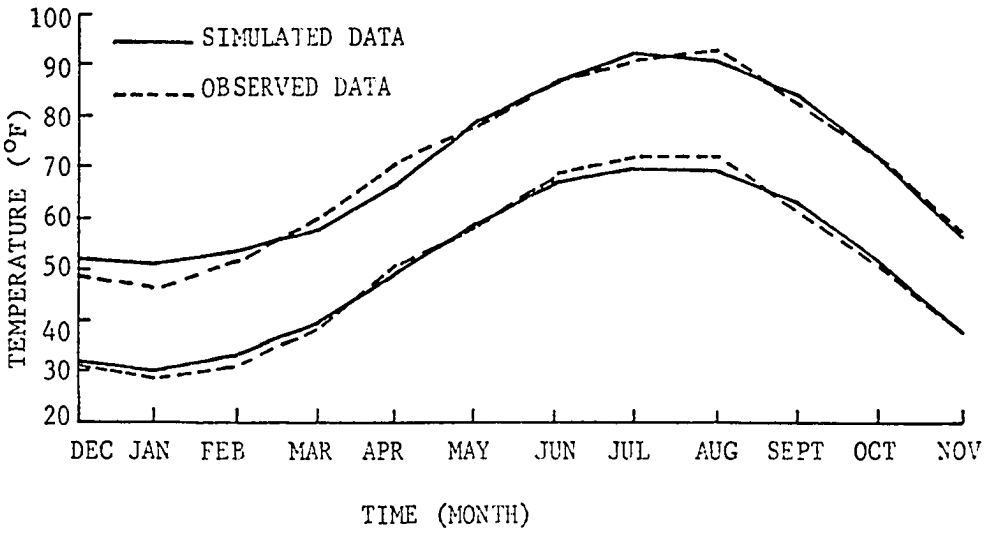

Fig. 32. A comparison of the observed and simulated average monthly maximum and minimum air temperature are shown. The 30-year average monthly maximum and minimum air temperatures observed at Oklahoma City are used as the observed data, while the simulated data are calculated from the 14-year computer simulation.

the computer simulated data and the average maximum and minimum air temperature observed at Oklahoma City (1931-1960). The results of the comparison show that there is very little difference between the observed and simulated mean monthly values. The most significant deviation is that the simulated mean maximum air temperature for the month of January is 5°F greater than the observed mean value. A detailed study of the results did not indicate any particular cause for the deviation. The average monthly 6-inch soil temperature determined for the simulated data is compared with the 1970 average monthly 25 cm (10-inch) soil temperature observed at the IBP Osage site in northeastern Oklahoma (Risser, 1971). The results shown in Figure 33 indicate a good comparison between the observed and simulated data. A more detailed comparison indicates a phase shift between the curves. This phase shift is consistent with the soil temperature gradients ($\partial Ts/\partial Z$) at the Osage site and the fact that the observed soil temperature is measured four inches lower in the soil profile. In the spring and early summer, the values of $\partial Ts/\partial Z$ are positive (5 to 10°F/25cm), while by the end of the summer, the average soil temperature is fairly homogenous in the top ten inches of the soil. $\partial Ts/\partial Z$ becomes negative in the late fall and winter as the top soil layers cool off more rapidly than the lower soil layers. Figure 34 presents the average monthly values of the net short wave solar radiation observed at ground surface at 11:00 LST. The results show the peak incoming solar radiation occurs during the month of July while the minimum value is observed in the month of December. The dashed lines on the graph show the standard deviation about the mean value and indicate that the months

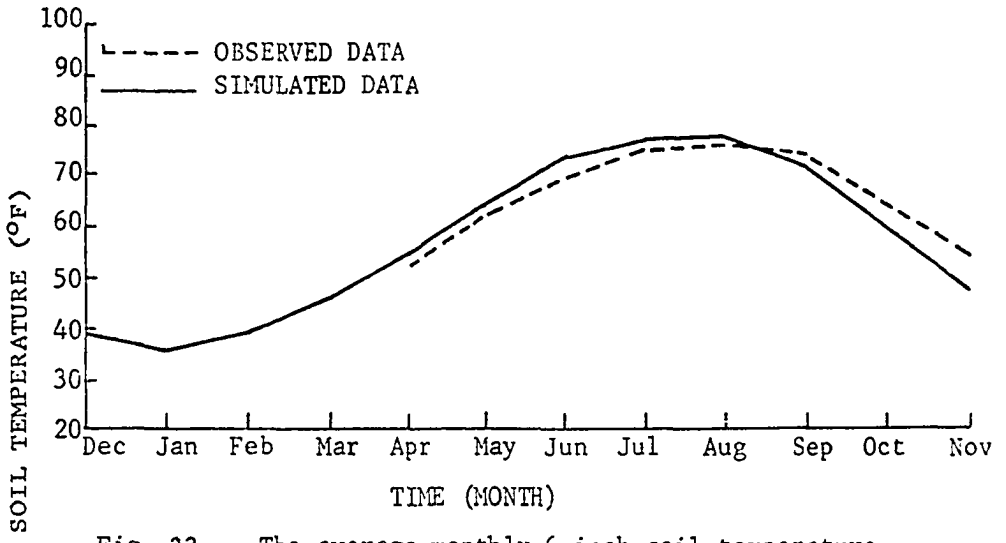

Fig. 33. The average monthly 6-inch soil temperature simulated by the model is compared to the average 25-cm soil temperature observed at the IBP Osage Site in northeast Oklahoma (Risser, 1971). The simulated data are calculated from the 14-year run of the ecosystem model.

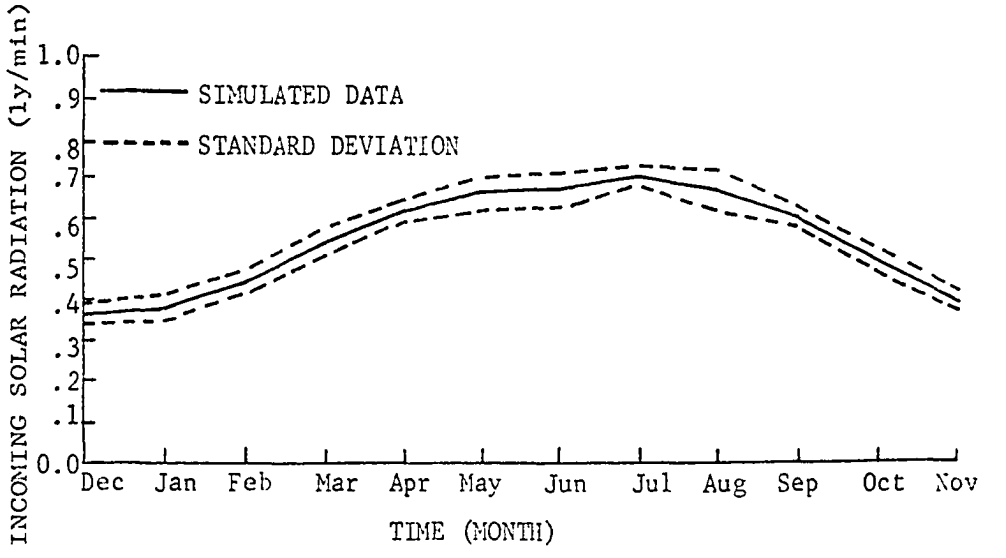

Fig. 34. The average monthly net incoming short-wave solar radiation at 11 (LST) and the standard deviation about the mean value are illustrated in this figure. The results are determined from the 14-year simulation of the ecosystem model.

of May, June and August have the greatest standard deviation for the mean values. Most of this variation is attributed to changes in the mean monthly cloud cover.

The radiation balance model also considers the effect air pollution has on the system. In particular, the model assumes that the incoming solar radiation is reduced by 1% for every 10 μg/m of particulate matter suspended in the air. The suspended particulate material primarily influences the maximum air temperature. Table 13 summarizes the results of a two-year simulation of the model in which the maximum air temperature is observed at points with low air pollution (8 $\mu g/m^3$) and one with high air pollution (98 $\mu g/m^3$). The results show that on the average, the maximum air temperature at point with high air pollution is $4^{\circ}F$ lower than the maximum temperature at point with low air pollution. These results are consistent with Bryson's theory that increasing concentrations of particulate matter will cause the mean air temperature to decrease over the long run (Singer, 1970).

Figures 35 and 36 illustrate how the average monthly mean rainfall and maximum and minimum air temperature vary about the group population mean values. The data presented in these figures are calculated from the 14-year time series of simulated atmospheric data. The results show that there is large variation in the mean monthly rainfall amounts simulated for the spring and summer months. In particular, the month of July has the greatest variance about the mean value and is attributed to the use of the convective shower mechanism to distribute rainfall during July. The results for the mean monthly minimum air temperature show that there is little variation in the mean monthly values; however,

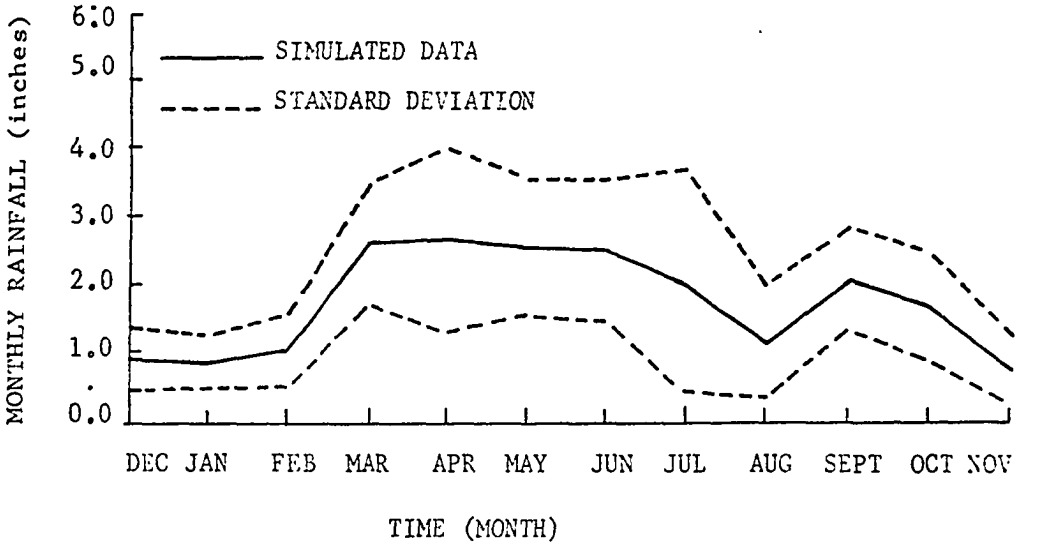

Fig. 35. The average monthly rainfall and the standard deviation about the mean are shown. The results are determined from a 14-year simulation of the model.

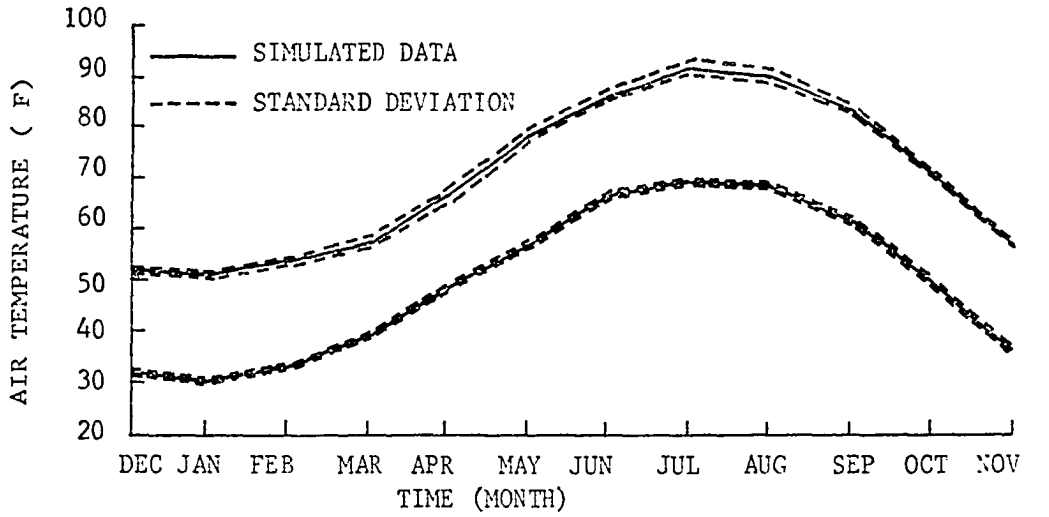

Fig. 36. The average monthly maximum and minimum air temperatures and the standard deviation about these mean values are illustrated. The results are determined from a 14-year simulation of the model.

the greatest variance that is observed occurs during the winter months (December, January and February). Most of the variation in the minimum air temperature during the winter months is probably caused by changes in the mean monthly cloud cover. The effect of varying the cloud cover during the remainder of the year (March - September) is partially masked by stronger night time wind speed during this time period. The lower wind speed during the winter months (October - February) is caused by the modification of the radiation balance model presented in Equation 1. This modification is specifically designed to lower the minimum air temperatures predicted by the radiation balance model during the winter months. The variance for the mean monthly maximum air temperature is fairly small, however, it is significantly greater than the variance for the minimum air temperature. The greater variation of the maximum air temperature is probably caused by the fact that incoming short wave radiation is subject to greater day-to-day variations than the radiative heat loss during the night time hours. The incoming short wave radiation has a strong influence upon the maximum air temperature, while the infrared radiative heat loss during the night hours is the predominate factor that influences the minimum air temperature. The standard deviation for the maximum air temperature is greatest for the months of March, April, and primarily attributed to variation in rainfall and cloud cover.

Table 14 presents a five-day sequence of the atmospheric parameters for 4 months during the year. This table is presented to show typical day-to-day variation of the atmospheric parameters. The effect of cloud cover upon the maximum (13:00 LST) and minimum (5:00 LST) air temperature

TABLE 14

This table presents four different simulated time series of the atmospheric parameters.

Date	Average Daily Wind Direction (degrees)	Average Daily Wind Speed (mph)	Average Daily Relative Humidity (%)	Max. Air Temp. (°C)	Min. Air Temp. (°C)	Average Daily Cloud Cover (%)	Daily Rainfall (inches)
1/21	143	8.6	40	11.1	-8.4	17	0.0
1/22	151	5.0	67	11.3	-10.4	12	0.0
1/23	180	16.1	82	9.5	1.1	85	.40
1/24	182	13.6	29	11.1	-2.1	10	0.0
1/25	190	8.7	67	10.7	.5	92	0.0
4/11	157	9.5	75	16.4	8.7	83	0.0
4/12	160	10.6	61	16.2	7.7	36	.60
4/13	200	24.9	53	13.6	8.9	84	.20
4/14	200	12.1	65	15.4	8.4	66	.20
4/15	349	16.3	74	14.2	8.7	77	0.0
8/21	190	6.0	56	30.9	21.7	99	0.0
8/22	160	8.8	68	34.7	20.1	42	0.0
8/23	195	5.6	49	34.9	19.9	38	0.0
8/24	137	4.9	50	32.2	20.8	75	0.0
8/25	151	7.9	42	36.8	18.7	3	0.0
12/21	271	14.4	48	11.4	-.2	11	0.0
12/22	310	12.7	41	11.4	-.8	1	0.0
12/23	165	10.6	73	10.9	.12	26	0.0
12/24	268	5.7	44	13.4	-4.0	7	0.0
12/25	349	10.1	69	9.9	1.9	78	0.0

is one of the most dramatic relationships demonstrated. The results show that as the cloud cover increases, the maximum temperature decreases and minimum air temperature increases.

Air Pollution Model

The sensitivity of the air pollution model to wind speed and stability is illustrated in Figures 37 and 38. Figure 37 shows that as the stability is changed from unstable to stable (stability categories A-D, Turner, 1961) the average pollution concentration increases dramatically, while the location of the maximum air pollution concentration moves farther down stream. Stable atmospheric condition cause an air pollution plume to diffuse less slowly and thereby maintain its identity for a long distance downstream from the source. Figure 38 shows the effect of varying the wind speed from 5 to 15 mph. The results show that an increase in wind speed causes a direct decrease in the air pollution concentration. It is important to note that in this experiment changing the wind speed does not change the stability category. In the working version of the model, stability is a direct function of the solar radiation, cloud cover, and wind speed (Turner, 1961). Figure 39 presents the contoured average annual SO_2 air pollution field determined by using the atmospheric model to drive the air pollution submodel for a two year simulation. The location of the air pollution sources and the air pollution emission rates are modelled to simulate the air pollution in Houston, Texas (see Figure 22 in the main text for the location of pollution sources). The shape of the air pollution field is primarily dependent upon the climatalogical wind rise and the location of the air pollution sources. A detailed discussion of the effect of the air

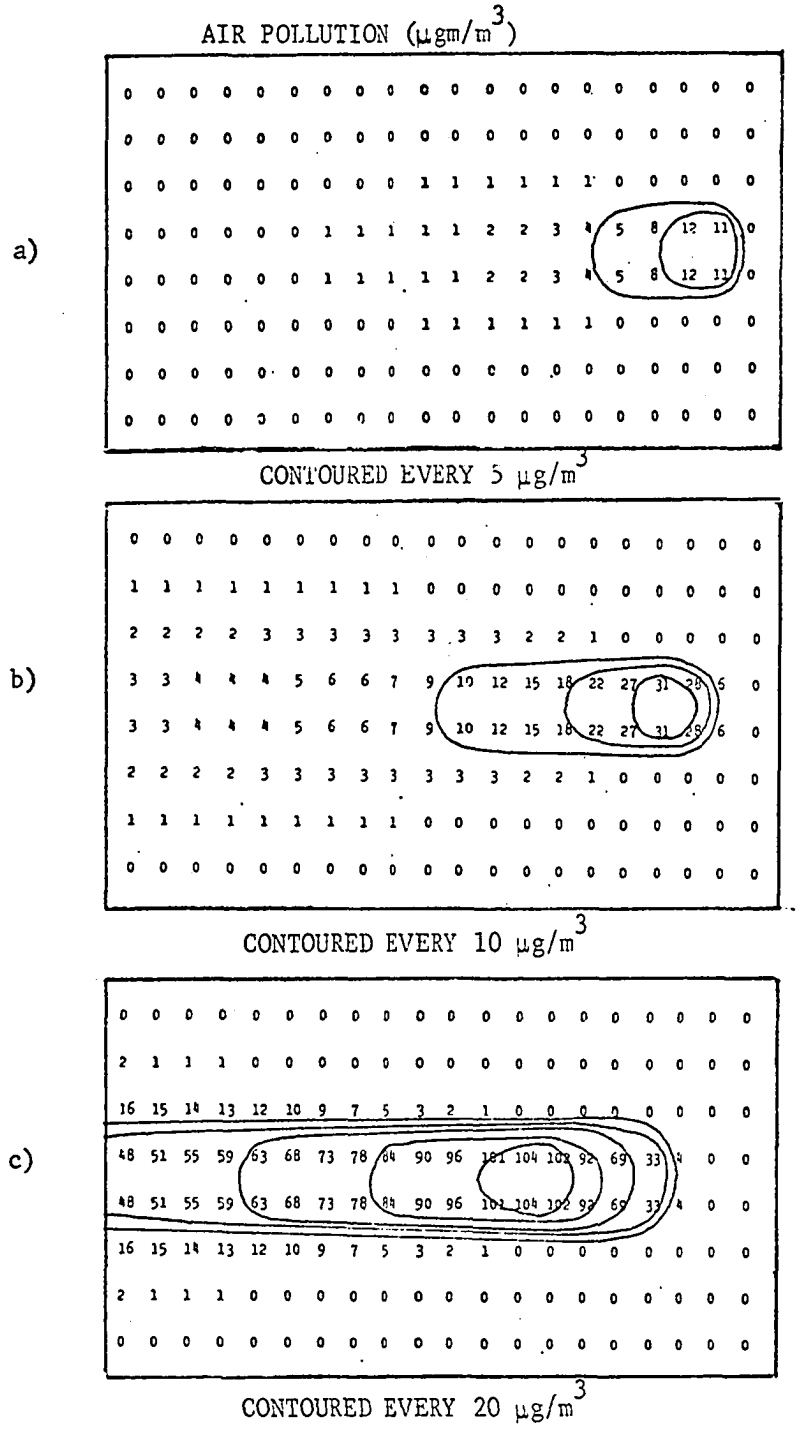

Fig. 37. The air pollution field for stability categories A (a), B (b), and D (c) are illustrated in this figure. The stability categories A, B, and D refer to the stabilities in Turner's (1961) stability classification system. The wind speed for (a), (b), and (c) is 10 kts, while the wind direction is 90 degrees.

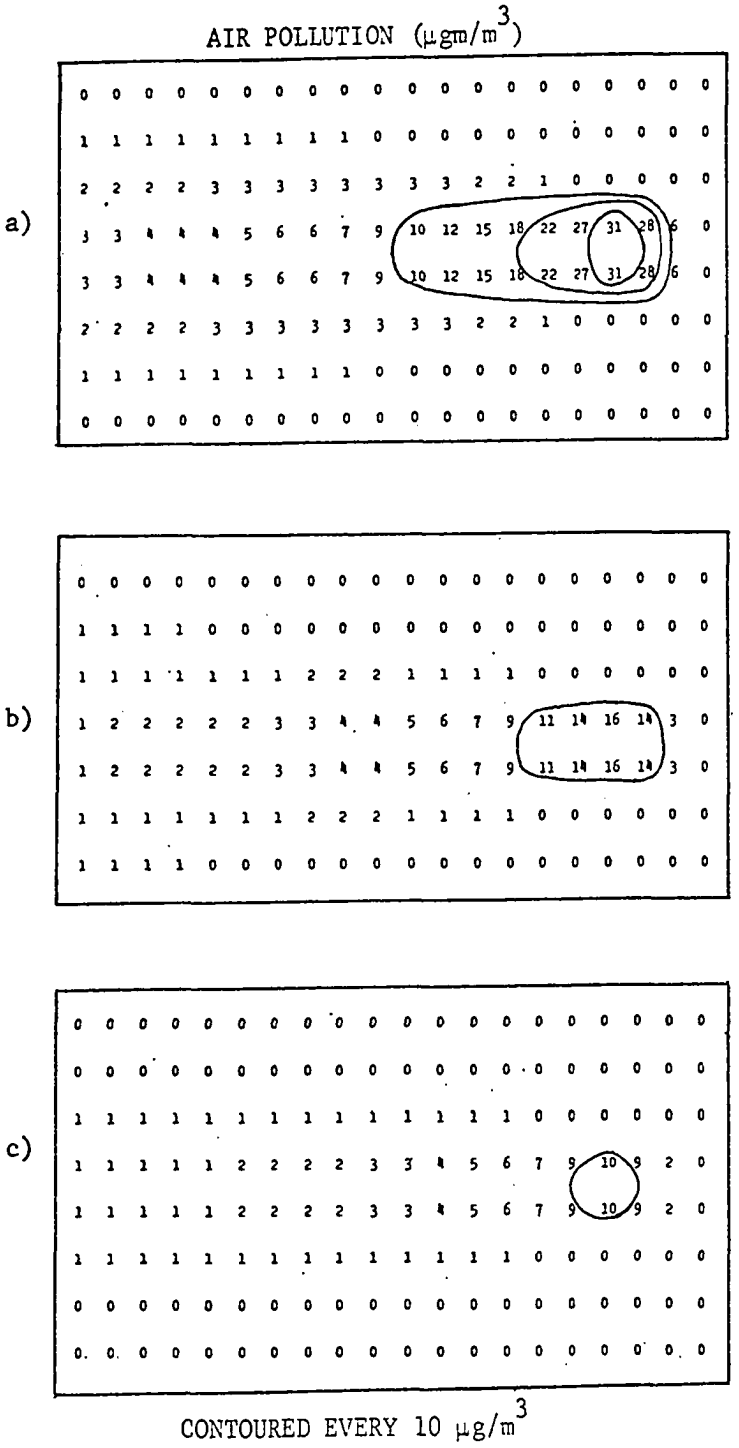

Fig. 38. This figure presents the air pollution field for three cases where the wind speed is set equal to 5 kt (a), 10 kt (b) and 15 kt (c). Stability category B was used for (a), (b), and (c), while the wind direction is 90 degrees.

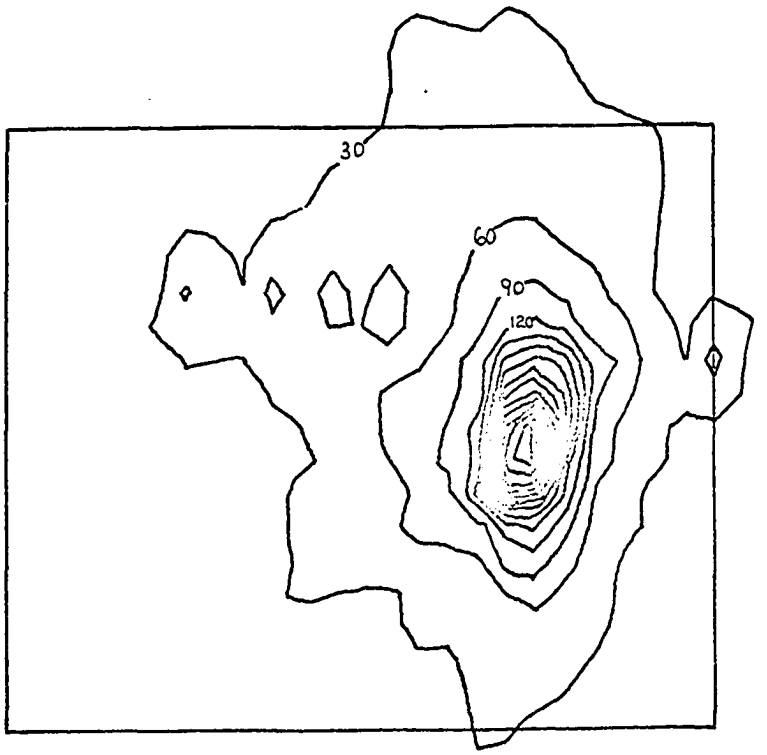

AIR POLLUTION CONTOURED EVERY 30 g/m^3

Fig. 39. This figure presents the contoured average annual SO_2 air pollution field determined by using the atmospheric model to drive the air pollution submodel for a two-year simulation. The location of the air pollution sources and the air pollution emission rates simulate the air pollution in Houston, Texas.

pollution control model upon the simulated air pollution fields is presented in Appendix F.

Radiation Balance Model

A sensitivity analysis is performed on the radiation balance model in order to demonstrate the response of the model to the control parameters. Specifically, the response of the maximum and minimum air temperature to variations of eight of the control parameters is demonstrated. The numerical experiment varied one of the parameters while the remaining parameters are kept constant (see Figs. 40, 41, 42, 43). The values for the input parameters used for this sensitivity exercise are summarized in Tables 15 and 16. Table 15 presents the constant input parameters for a point that represents a rural area and a point that represents an urban area. The values presented for the rural area are used in the sensitivity analysis. Table 16 presents the 1000 ft wind speed time series that is multiplied by the wind factor (wf) to get the wind speed at any time during the day. This wind speed time series is only used for the sensitivity analysis exercise. A comparison of the temperature simulated for the urban point with the rural point is presented in order to demonstrate some of the characteristics of the Urban-Heat Island effect.

The influence of wind speed and cloud cover upon maximum and minimum air temperature is presented in Fig. 40. The results show that increasing wind speeds cause the maximum air temperature to decrease and the minimum air temperature to increase. The maximum and minimum air temperature change very rapidly as the wind factor increases from .5 to 1.5, however, increasing the wind factor beyond 1.5 has little effect upon them. Increasing the cloud cover causes a continuous increase in the minimum air temperature and a continuous decrease in maximum air

(a)

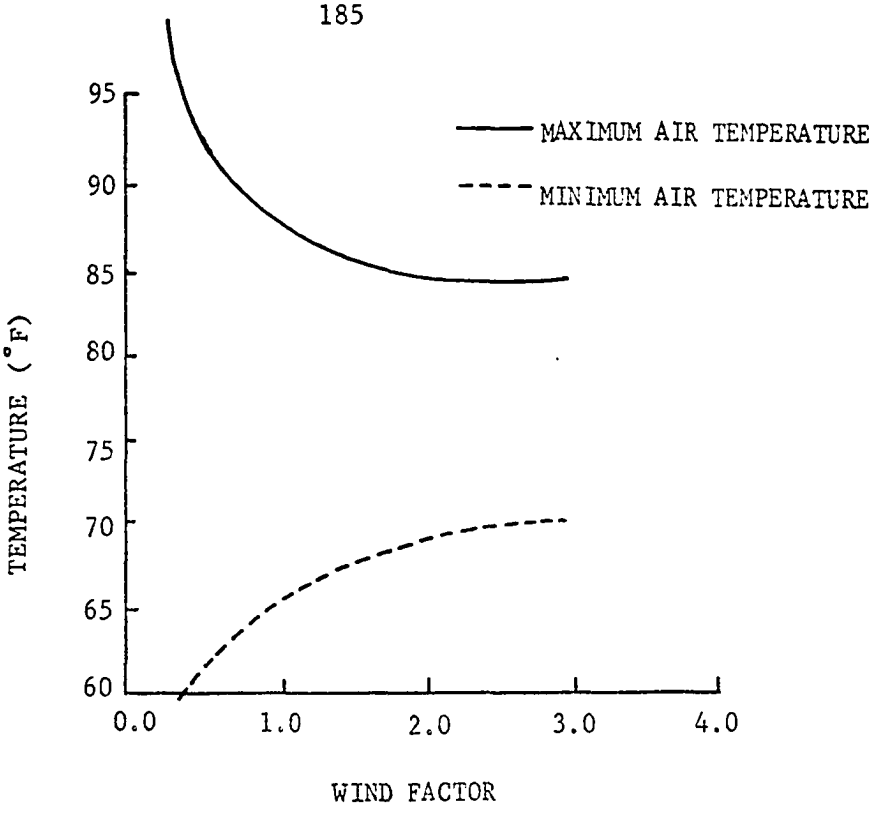

(b)

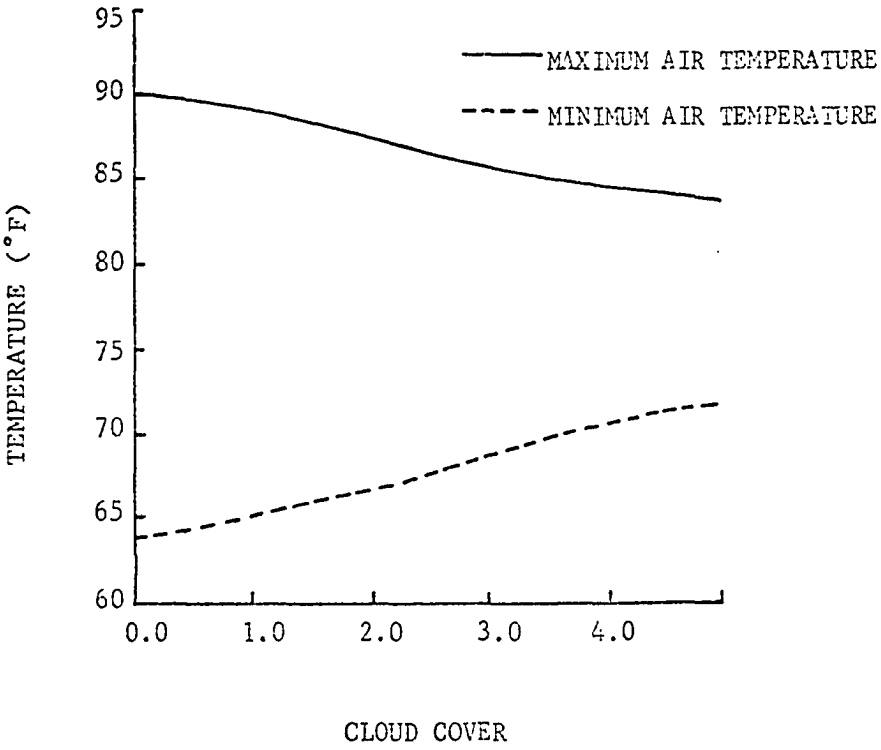

Fig. 40. The influence of wind speed (a) and cloud cover (b) upon the simulated maximum and minimum air temperature is presented here.

(a)

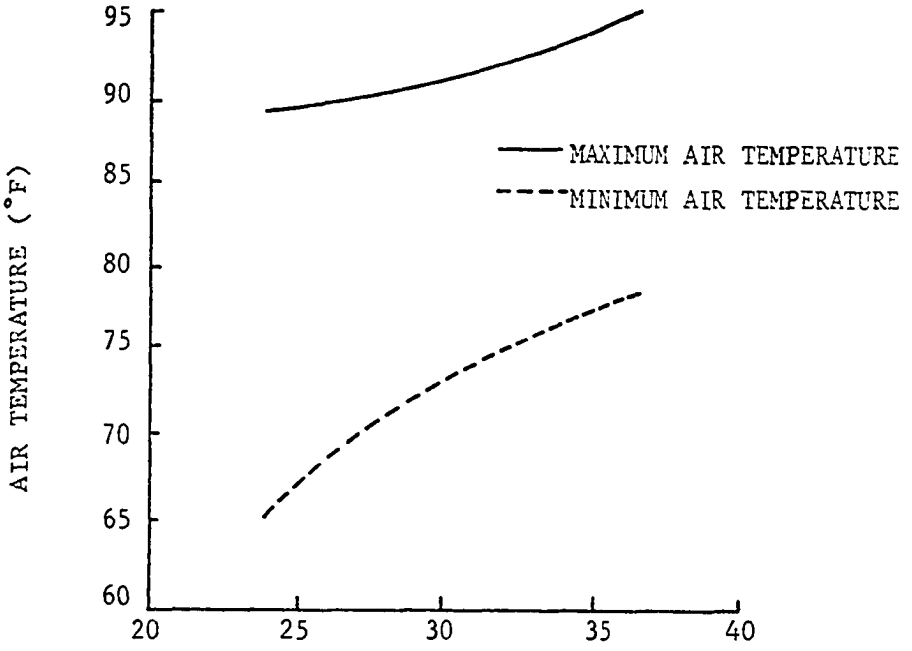

(b)

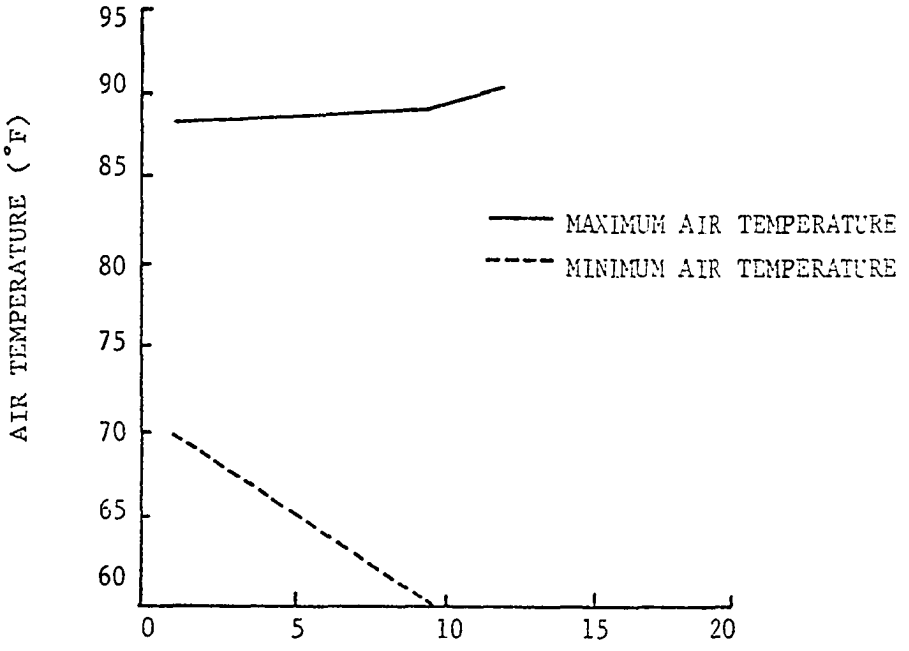

Fig. 41. The influence of the 1000 ft. air temperature (a) and the amplitude of the 1000 ft. air temperature oscillation (b) upon the maximum and minimum air temperature is illustrated in this figure.

(a)

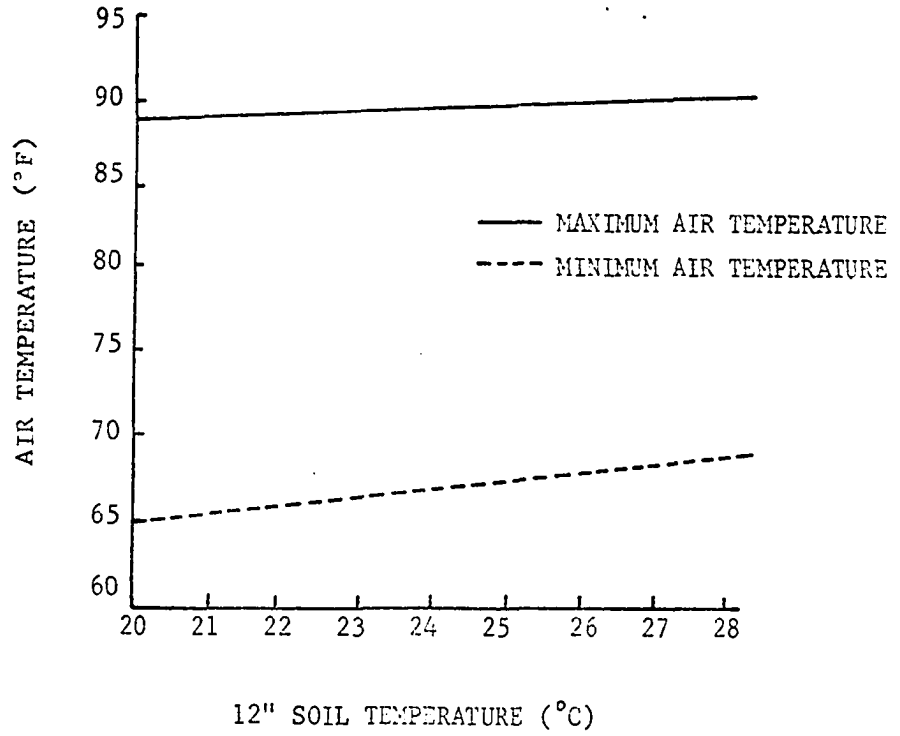

(b)

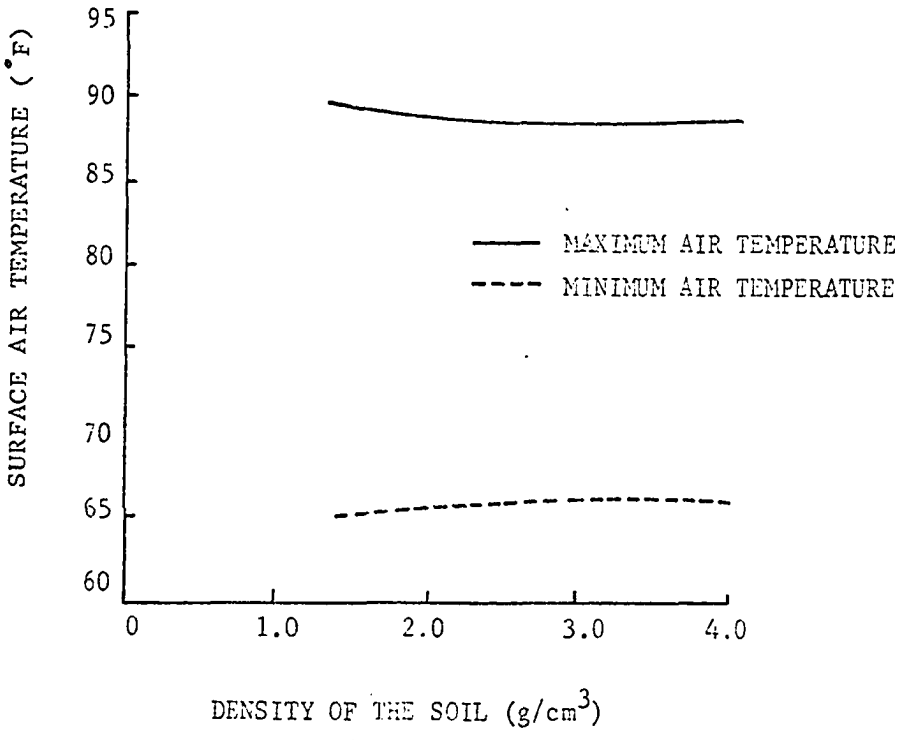

Fig. 42. The effect of the 12" soil temperature (a) and soil density (b) upon the maximum and minimum air temperature is illustrated.

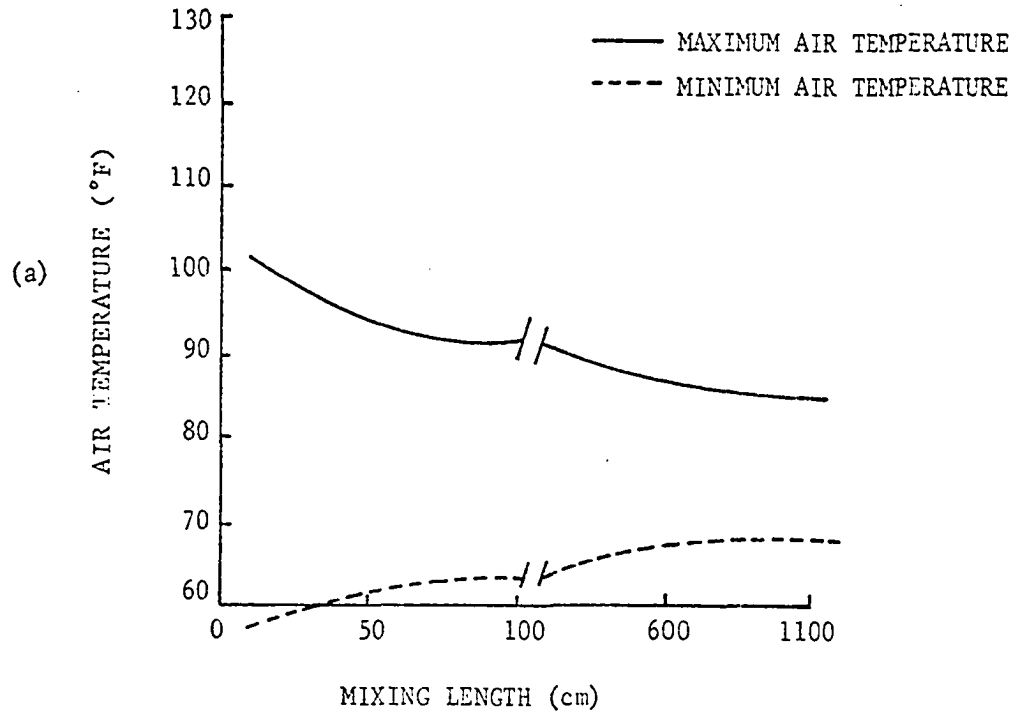

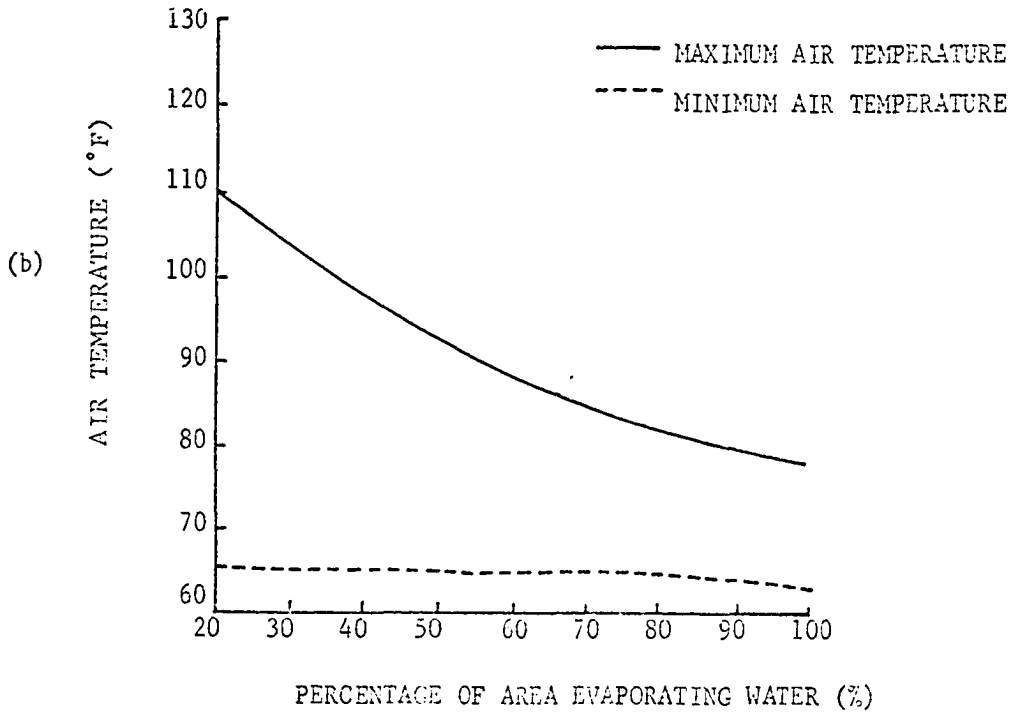

Fig. 43. The effect of mixing length (a) and the percentage of area evaporating water (b) upon the maximum and minimum air temperature is shown.

TABLE 15

Constant parameter values used in the sensitivity analysis of the radiation balance model.

	Rural	City
Particulate Concentration ($\mu g/m^3$)	15.8	110.0
Self Heating Term (ly/min)	-.005	+.060
IR Radiation Modification Term (non-dimensional)	1.17	.70
12" Soil Temperature (°C)	20.8	22.5
Cloud Cover (%)	20	20
Wind Factor (WF)	1	1
Conductivity (cal/cm sec °C)	.004	.017
Density (gm/m^3)	1.83	2.50
Evaporating Surface (%)	58	43
Mixing Length (cm)	253	500
1000 ft. Temperature (°C)	24.6	24.6
Amplitude of 1000 ft. Temperature (°C)	5.1	3.0
Specific Heat Capacity (cal/gm °C)	.18	.18

TABLE 16

Wind speed time series used in the sensitivity analysis of the radiation balance model.

Time (CST)	1000 ft. Wind Speed (MPH)
1	04
2	04
3	04
4	04
5	04
6	04
7	05
8	05
9	06
10	06
11	07
12	07
13	08
14	08
15	07
16	07
17	06
18	06
19	05
20	04
21	04
22	04
23	04
24	04

temperature.

The effect of the 1000 ft. air temperature and the amplitude of the 1000 ft. air temperature oscilation upon the maximum and minimum air temperature is presented in Figure 41. Increases in the 1000 ft. air temperature cause both maximum and minimum air temperature to increase. The results show that the minimum air temperature increases more rapidly than the maximum air temperature. Increasing the amplitude of the 1000 ft. air temperature oscilation causes the maximum air temperature to increase slowly while the minimum air temperature decreases rapidly. The maximum air temperature increases because increasing values of the amplitude of the 1000 ft. air temperature causes the maximum 1000 ft. air temperature to be higher and thus lower the upward sensible heat transfer loss in the late afternoon hours. The mean minimum air temperature decreases because increasing the amplitude of the 1000 ft. air temperature cause the minimum air temperature at 1000 ft. to decrease and thus lower the downward sensible heat transfer in the nocturnal hours. Figure 42 shows the effect of 12-inch soil temperature and the density of the soil upon the maximum and minimum air temperature. Increasing the 12-inch soil temperature causes both the maximum and minimum air temperature to increase slowly; however, the minimum air temperature increases at a much more rapid rate than the maximum air temperature. Increasing the density of the soil causes only a minor decrease in the maximum air temperature and a slow increase in the minimum air temperature. The influence of mixing length and percentage of area evaporating water upon the maximum and minimum air temperature is presented in Figure 43. The results show that increasing the mixing length causes the maximum

air temperature to decrease and the minimum air temperature to increase. With mixing length greater than 600 cm the changes in the maximum and minimum air temperature are small. Increasing the percentage of area evaporating water causes a rapid decrease in the maximum air temperature and a minor decrease in the minimum air temperature. The rapid decrease in the maximum air temperature is caused by the increase in the latent heat loss associated with the increase in the area evaporating water. The minimum temperature is only slightly influenced by the area evaporating water because the latent heat loss during the evening hours is minimal. A summary of the results shows that variation of some of the parameters have a significant influence in the response of the model while changes in other parameters have very little influence upon the model.

One of the primary reasons for developing the radiation balance model is to devise a mechanism that would be useful to study the "Urban-Rural Heat Island." The Urban-Rural Heat Island refers to the phenomenon whereby the center of an urban area is observed to have higher air temperatures than the surrounding rural area. The urban-rural temperature difference is observed to be greatest under conditions when the wind speed is light (less than 5 kts) and cloud cover is low. The greatest temperature difference is generally observed in the early morning hours. Fig. 44 presents a two-day air temperature time series for points in the urban rural area during August and January. These time series are generated by running the radiation balance model with the constant input parameter values presented in Table 15. The results for the month of August show that the greatest urban-rural temperature difference occurs just prior to sunrise ($10^{o}F$). During the daylight hours, the

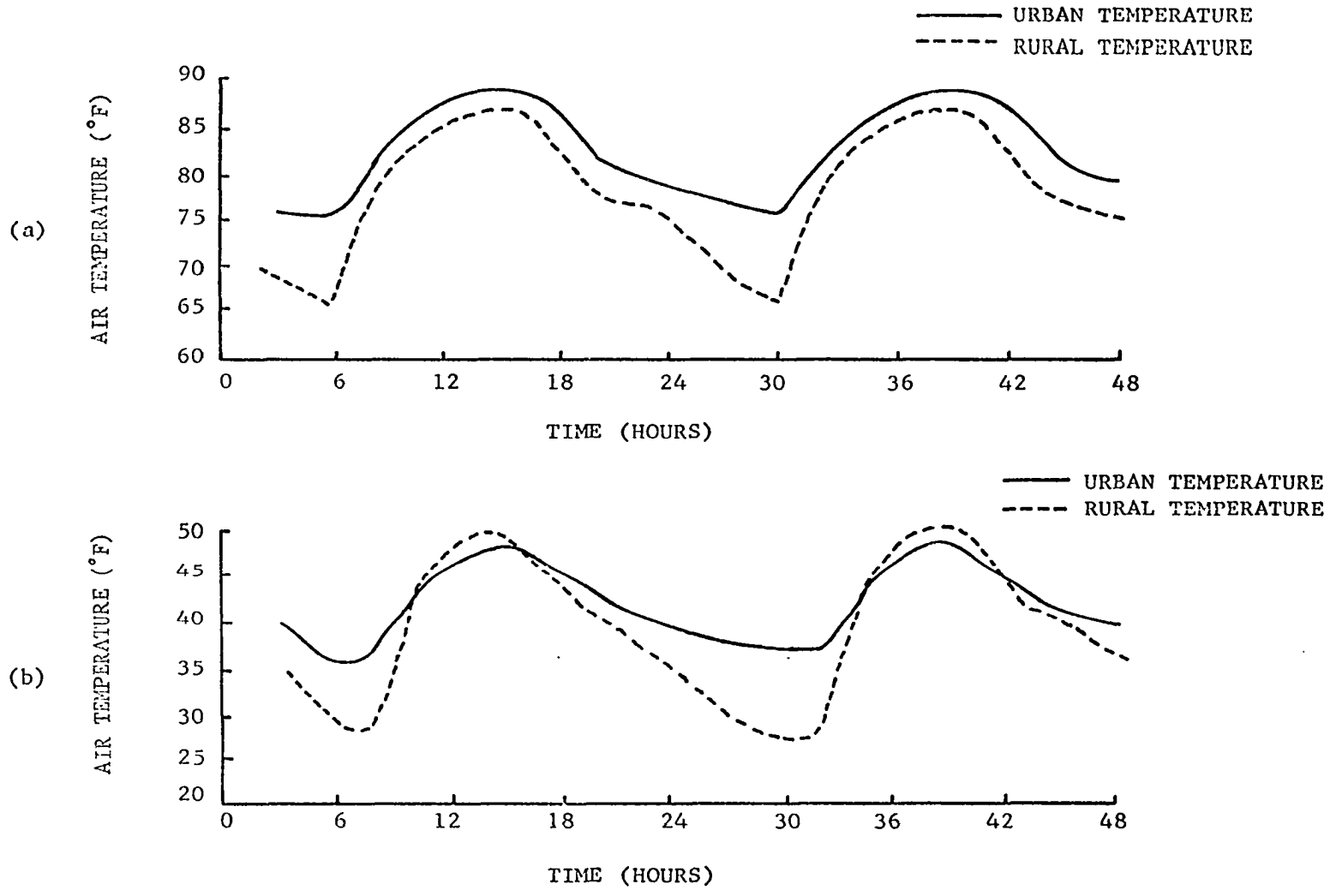

Fig. 44. This figure illustrates a two-day time sequence of air temperature simulated for an urban area and a rural area during August (a) and January (b).

urban-rural temperature becomes less significant (2 F). The results for January also show that the greatest urban-rural temperature difference occurs just prior to sunrise (10 F), however, during January there is a temperature excess (+2 F) observed in the rural area from 11:00 to 14:00 LST. The results simulated by the model are consistent with field observation of the Urban-Rural Heat Island. The effect of time of year, cloud cover, and wind speed upon the urban-rural temperature difference observed at the time of minimum air temperature (6:00 LST) and maximum air temperature (14:00 LST) is presented in Figure 45. These results are determined by running the radiation balance model during different times of the year and then varying the cloud cover and wind speed parameters. The results show that the urban-rural temperature difference decreases significantly with an increase in cloud cover or an increase in wind speed. The peak temperature difference during the early morning hours is observed to occur during early March while there is a secondary peak observed in the month of September. The temperature difference in the afternoon hours is shown to become negative only during December and January. The peak positive difference during the afternoon hours occurs during the summer months and is increased by increasing wind speed and cloud cover. During December and January, increasing the wind does not modify the temperature difference during the afternoon hours, however, increasing the cloud cover causes the urban-rural temperature difference to be decreased significantly. The results presented in Figure 45 are very interesting; however, they have not been validated by observed data.

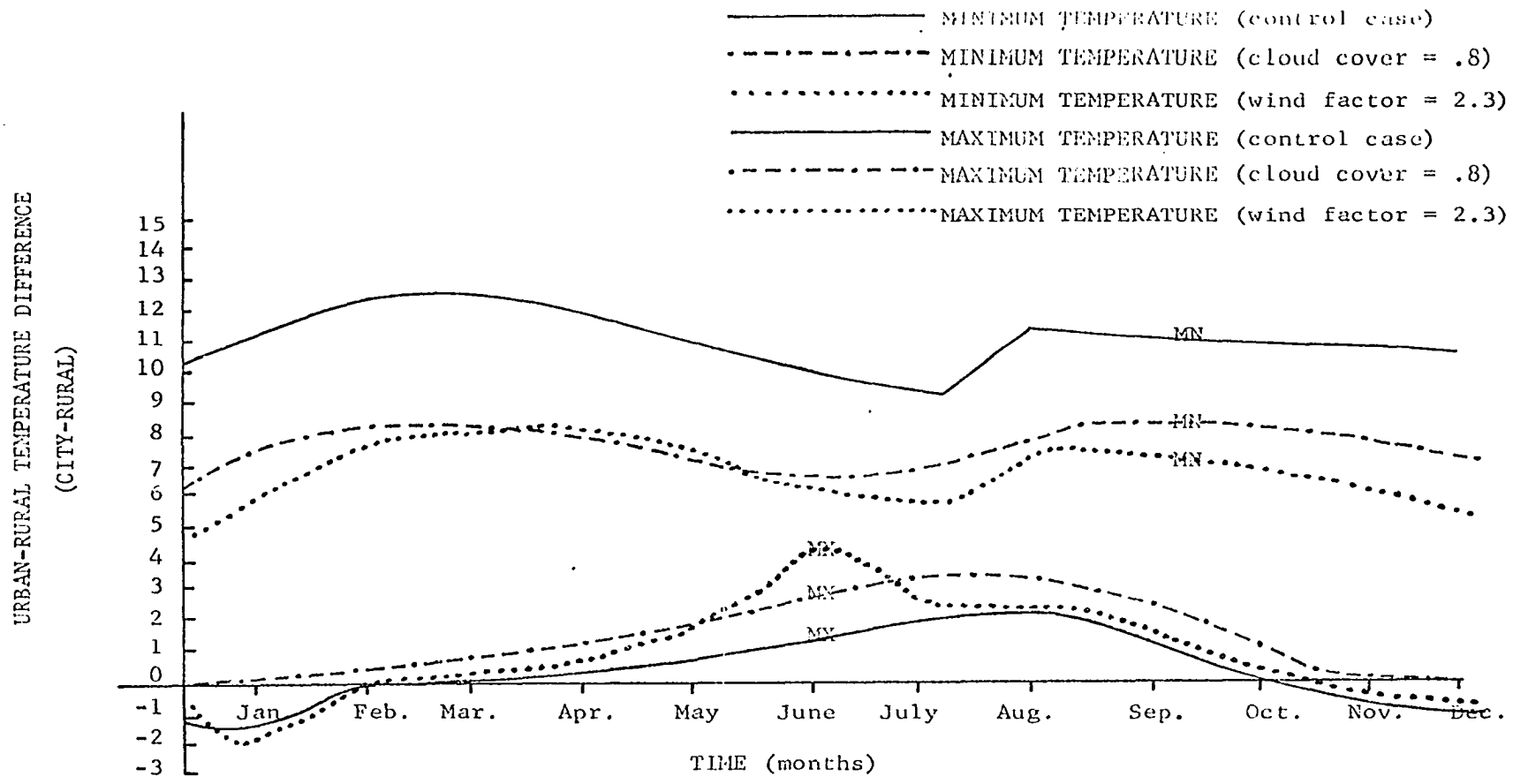

Fig. 45. The effect of cloud cover, wind speed, and time of year upon the urban minus rural temperature difference (Urban-Rural) for both maximum and minimum air temperature is presented in this figure.

Heat Island Wind Model

The urban-rural heat island wind model is tested by varying the most important driving parameter in the model, which is the urban-rural temperature difference. Fig. 46 presents the wind direction field and wind speed field for a case with an +8C temperature difference, while Fig. 47 presents the wind direction and speed fields for a case when the temperature difference is +4C. The roughness length field used to calculate Figs. 46 and 47 increased from a low value of 250 cm at the edge of the city to 1080 cm at the center of the city. The urban-rural temperature difference used in Figs. 46 and 47 represent typical temperature differences observed in the early morning. The mixing length field used as input for the model increased from the edge of the city into the center of the city. The top of Urban-Rural Heat Island dome is specified by a two dimensional sine wave that has the maximum value of the dome in the center of the city. A comparison of the two figures shows that maximum wind speed decreases one-third of the original peak value as the temperature difference is decreased by one-half, while the wind direction fields do not vary significantly. The most significant feature of the wind speed field is the increase of the wind speed from zero in the center of the city to peak value two miles from the center of the city. The wind speed then decreases continually out to the edge of the city. A study of the results from the model did not produce any information about the variation in the maximum wind speed belt. The wind direction field shows that the air is moving directly into the center of the city. The values of wind speed simulated in the model compare favorably with those indicated by observed data (Pooler, 1967). An error discovered in the procedure used to calculate

(a)

(b)

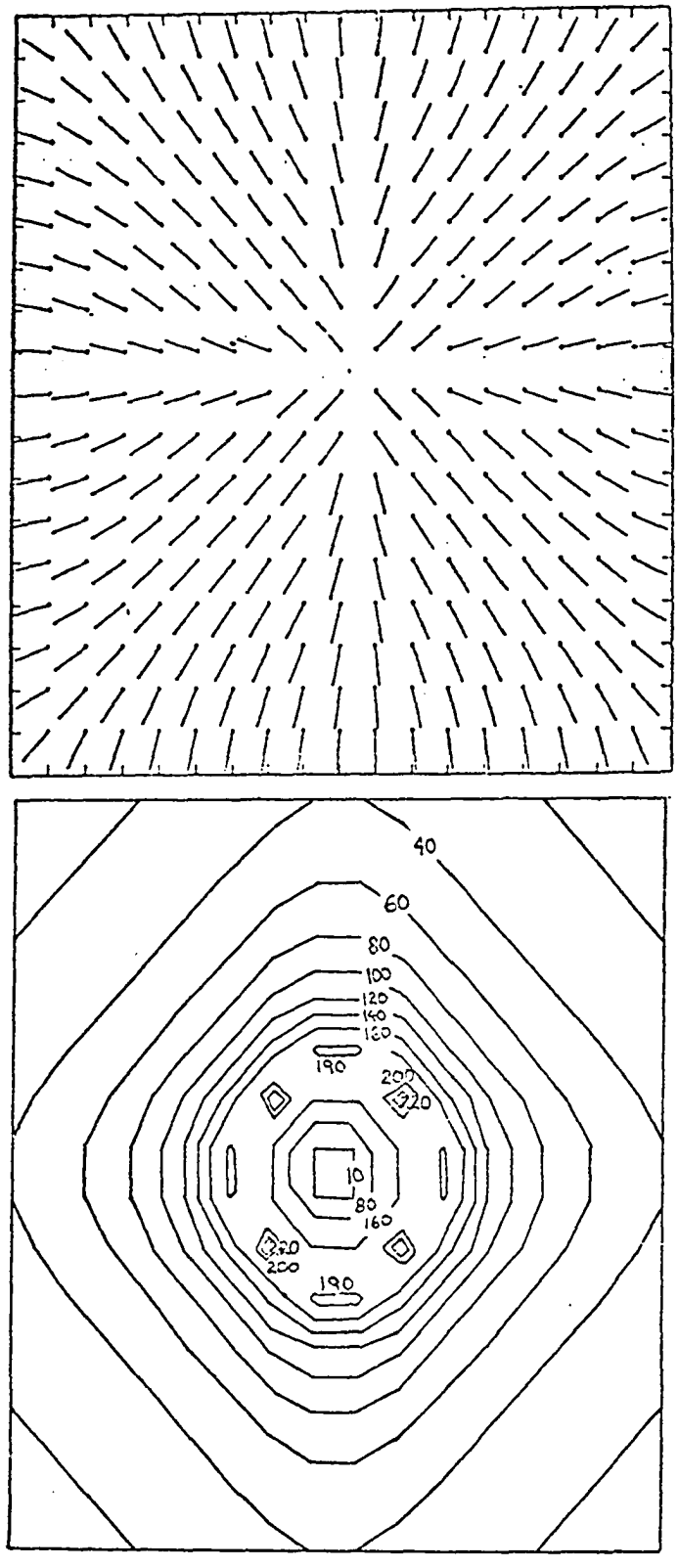

WIND SPEED (cm/sec)

Fig. 46. This figure presents the wind direction field (a) and wind speed field (b) for a case in which the urban minimum rural temperature difference is equal to +8 °C. The dots with straight lines connected to them indicate the direction that the wind blows from.

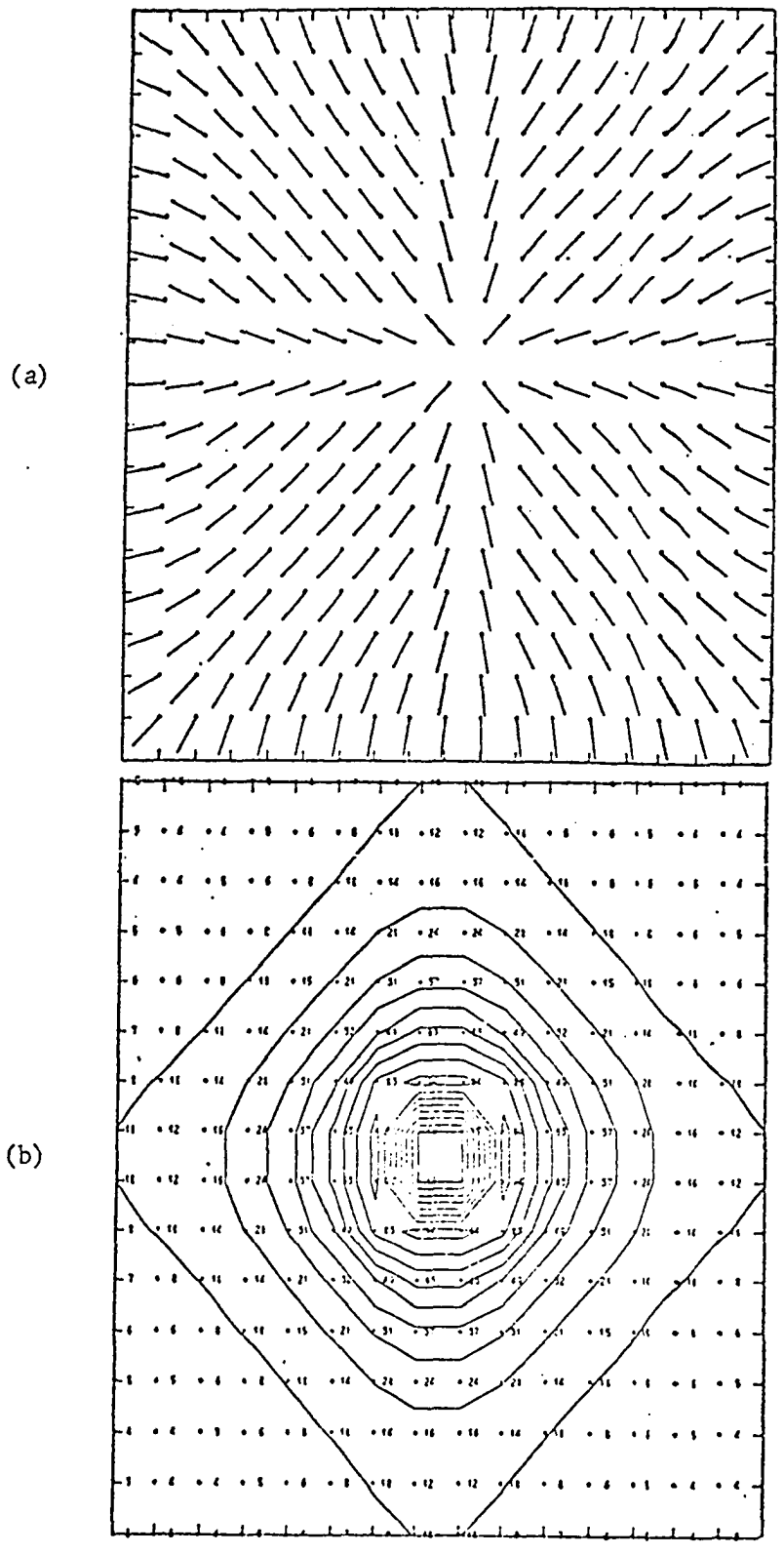

Fig. 47. The wind direction field (a) and wind speed field (b) for case in which the urban minus rural temperature difference equals +4°C is illustrated. The dots with straight lines connected to them indicate the direction that the wind blows from.

the drag coefficient field caused the estimates of the drag coefficient to be increased. The effect of error is to decrease wind speeds simulated by the model.

APPENDIX B

APPENDIX B

RESULTS OF THE TESTING SCHEME PERFORMED ON THE HYDROLOGY MODEL

The hydrology model is tested by demonstrating the response of its parameters to the driving atmospheric parameters. This is accomplished by using the data generated from the 14-year simulation of the evaluation of the ecosystem to determine mean monthly values the hydrology parameters. Some of the factors which influenced the hydrology model and are kept constant for the whole ecosystem during this simulation are presented in Table 17. Table 18 presents the monthly flow rates of water into and out of the lake which are used for the simulation. The mean monthly value of the parameters are determined for the point in the central section of the ecosystem where the mean monthly values of atmospheric parameters are determined (see appendix A). The effect of different soil types and hydrologic conditions upon storm runoff is presented along with a 30-day time series that demonstrates the day-to-day response of the hydrology parameters to the driving atmospheric parameters.

Figure 48 presents the average monthly values of the soil moisture parameters. The soil moisture from 0-24 inches has its peak value in March and decreases to a minimum value in August. The March peak in the soil moisture is associated with the heavy rainfall during the spring months, while the fairly rapid decrease in the soil moisture from

TABLE 17

THIS TABLE PRESENTS THE STATE OF THE CONSTANT HYDROLOGIC

PARAMETERS USED IN THE 14-YEAR COMPUTER SIMULATION

Vegetation Type	Hydrologic Condition of The Soil	Flow Velocity of the Stream	Flow Velocity of the River	Height of Vegetation	% of area Covered by Vegetation	Soil Type	Time Period When Transpiration Occurs
Pasture Land	Poor	3m/sec	4m/sec	1.5 ft.	70%	Sharkey Clay	April-October

TABLE 18

MONTHLY FLOW RATES OF WATER INTO AND OUT OF THE LAKE AND THE AVERAGE MONTHLY LAKE WATER TEMPERATURE AT THE AIR WATER INTERFACE

	Jan	Feb	Mar	Apr	May	June	July	Aug	Sept	Oct	Nov	Dec
Flow into the lake (CSF)	9000	9000	9000	9000	7000	7000	6000	6000	7000	9000	9000	9000
Flow out of the lake (CSF)	8000	8000	8000	8000	8000	8000	8000	8000	8000	8000	8000	8000
Average monthly lake water temperature (C^{o})	9	8	9	12	18	23	26	27	25	20	18	15

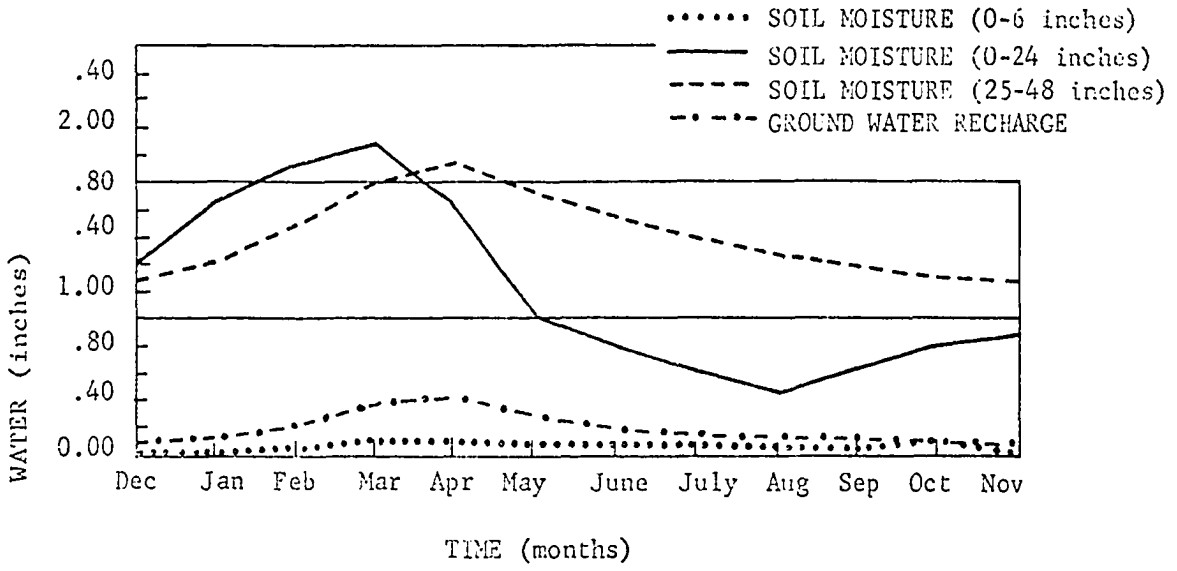

Fig. 48. The average monthly values of the soil moisture from 0-6 inches, 0-24 inches and 25-48 inches and the ground water recharge are presented in this figure.

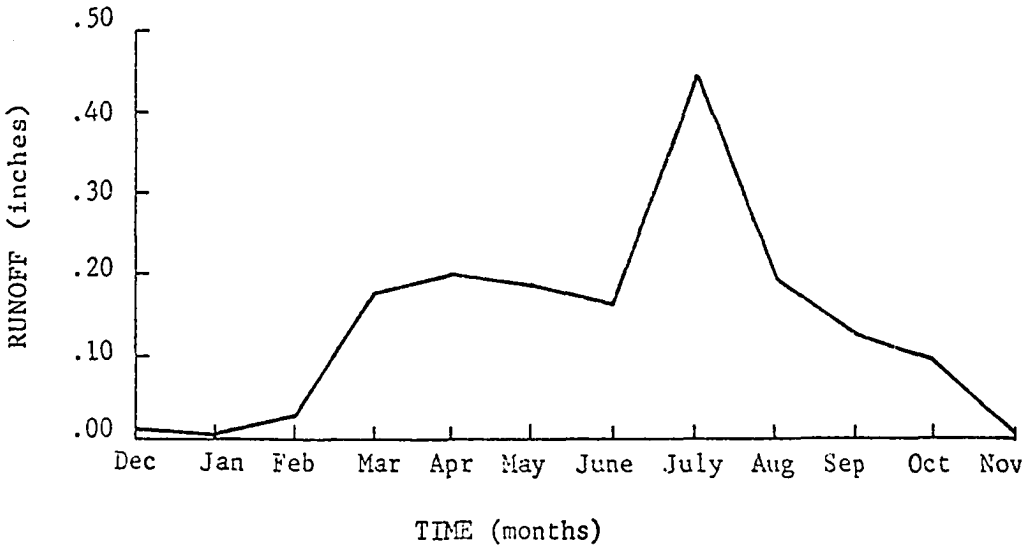

Fig. 49. The average monthly storm runoff is shown in this figure.

March until June is caused by a rapid increase in the potential evapotranspiration loss. The low soil moisture during the summer is caused by lower rainfall amounts and high potential evapotranspiration loss. The increase in the soil moisture from September until March is caused by low potential evapotranspiration values which allow the soil moisture to accumulate during this period. Another factor to consider in studying the soil moisture for 0-24 inches is the fact that from April until October, (growing season of the grass) the evaporation water loss from this layer occurs as transpiration by the plants, while during the remainder of the year, the evaporation water loss from the soil is limited to the top 6 in. of the soil (evaporation loss from bare soil). Part of the fairly rapid drop in soil moisture from March to April is attributed to the fact that evaporation water loss in March is limited to the top 6 in. of the soil, while in April, plant transpiration is losing water from the whole soil moisture layer (0-24 inches). The fairly rapid increase in the soil moisture from November until March is influenced by the fact that water loss by evaporation is limited to the top 6 in. of the soil. The soil moisture in the 25-48 inch layer has its peak values in April and decreases to minimum value in January. This layer is recharged by drainage from the upper soil moisture layer and loses water by drainage to the layer below 48 inches. The April peak in the soil moisture from 25-48 inches is caused by high values of soil water drainage from the upper soil moisture layer during January, February, March, and April. This drainage is caused by high values of soil moisture in the upper soil moisture layer. The observed decrease in the soil moisture of the 25-48 inch layer after March is associated with a rapid decrease in the soil moisture in the upper layer

(0-24 inches). The ground water recharge indicated in Figure 48 is the average monthly drainage out of the soil moisture layer from 24 to 48 inches. As expected, the results show that the drainage is directly proportional to the soil moisture in the layer. The average monthly soil moisture from 0 to 6 inches is less than .2 inches for the whole year and reaches its peak value in March. The average soil moisture in this layer is low because soil water evaporation loss is confined to the top 6 inches of soil if there is available water in this layer. Thus, after a rainfall recharges the soil, the soil moisture from 0-6 inches will be the first layer to lose water due to evaporation. A programming error in the model that predicts soil moisture in the layer was discovered. The effect of this error is to slightly increase the soil moisture from 0-24 inches during the winter (increase equals .15 inches) and also to decrease the soil moisture from 0-6 inches during all of the months of the year. The greatest decrease would occur during the late spring and early summer months (decrease equals .25 inches for late spring and summer, while the decrease equals .15 inches during the remainder of the year).

The average monthly runoff at the control point in the central section of the ecosystem is presented in Fig. 49. A primary peak in runoff is observed in July while there is secondary peak in runoff during April. The July peak in runoff is produced by the high ratio of runoff to rainfall that is associated with convective shower mechanism used to distribute rainfall for July and August. The runoff was much lower for the month of August because the average rainfall is lower. The secondary peak in runoff during April is caused by the heavy rainfall during the spring. The relatively low runoff during the winter months

(October, November, January and February) is associated with the low average monthly rainfall for this time period.

The average monthly values of evaporation parameters are illustrated in Figure 30. Variation in the lake evaporation rate and the potential evapotranspiration rate are directly related to changes in the atmospheric parameters while the variations in the soil evaporation loss are directly related to potential evapotranspiration rate and the soil moisture from 0 to 24 inches. The potential evapotranspiration rate increase from minimum value in December to a peak value in June. This increase is caused by increasing average air temperature and increasing short-wave solar radiation during this period. The potential evapotranspiration rate generally decreases from June until December. This is caused by a decrease in the net incoming short-wave solar radiation and the decrease in the average air temperature after the month of August. The lake evaporation rate increases from minimum value in March to maximum value in August, and then decreases until March. The dramatic increase in evaporation rate from March to August is caused by increasing lake surface temperatures (see Table 18) decreasing relative humidity. The decrease in the lake evaporation rate from August to March is primarily caused by increasing relative humidity. The minimum evaporation rate occurs in March because the lake surface temperature is still fairly low with the relative humidity being very high during that month. The major feature of the soil evaporation rate is that it increases from a minimum value in November to maximum value in April, while the rate then decreases steadily to the minimum value in November. The increase in the evaporation rate from November to March is caused by the fact that

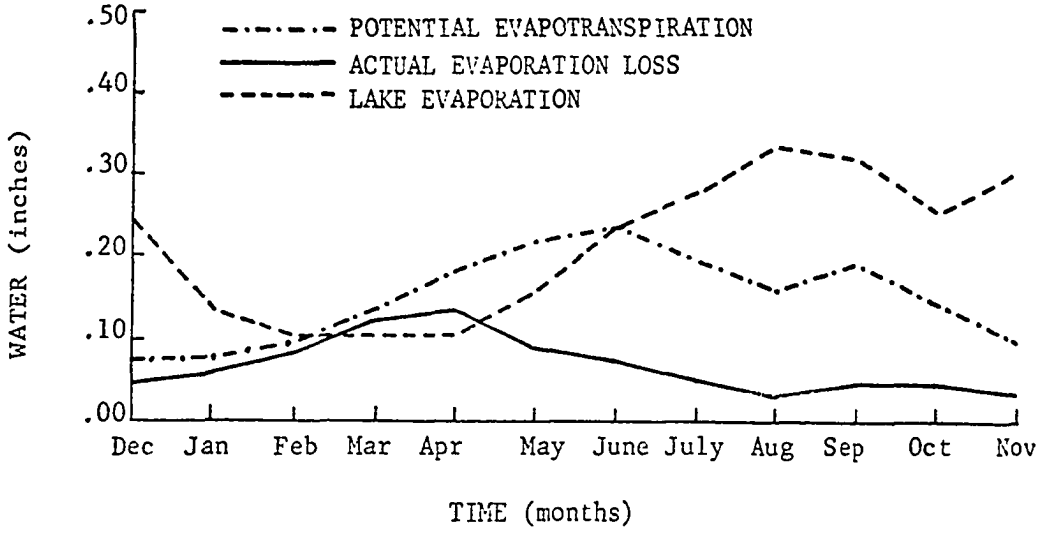

Fig. 50. The average monthly values for potential evapotranspiration, actual evaporation and lake water evaporation are illustrated in this figure.

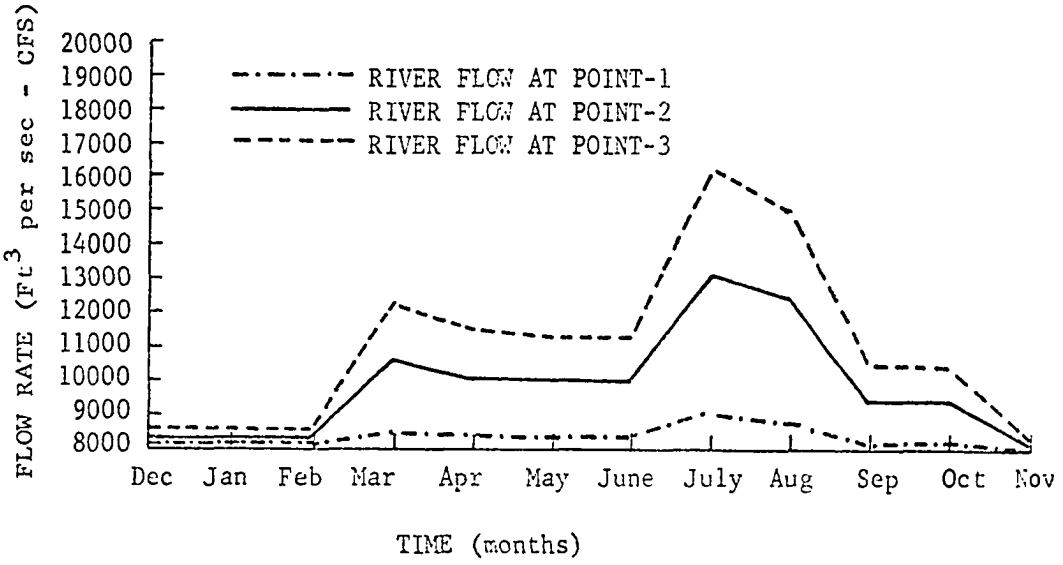

Fig. 51. This figure shows the average monthly flow rate at three points along the River system (point 1 - below the lake, point 2 - middle of the River system, point 3 - southern boundary of the ecosystem.).

the potential evapotranspiration rate increases throughout that period while the available soil water for evaporation remains at a high level. The decrease in evaporation rate after March is caused by a rapid decrease in available soil moisture for evaporation.

The average monthly flow rate at three points along the river system are presented in Figure 51. Point 1 (Point 3-Figure 14 in the main text) is the upstream point just below the dam Point 2 (Point 5-Figure 14 in the main text) is located in the middle of the ecosystem while Point 3 (Point 7-Figure 14 in the main text) is the farthest downstream point still in the ecosystem. The results show that the flow rate increases dramatically from February to March, decreasing slightly until June, increasing to a peak value in July and then decreasing to the base flow level (8000 cubic feet per sec-cfs) in December. As would be expected, the changes in the average flow rate correspond directly to the variations in the average monthly runoff (Figure 49). The average flow rate at Point 1 increases, at the most, 1000 cubic feet per second (cfs) over the base flow rate. This indicates that there is very little runoff of water into the river above Point 1 with most of the water at Point 1 flowing from the dam at the constant rate of 8000 cfs (base flow rate). The average flow rate at Point 2 is significantly higher than the flow rate at Point 1, indicating that a large amount of water runs into the river between Point 1 and Point 2. The comparisons of flow rate at Point 2 and Point 3 show that the flow rates continue to increase significantly because of runoff from the remainder of the ecosystem. The runoff from particular areas of the ecosystem is equal to the difference between the average flow rate at consecutive downstream point along the river. The results from Figure 51 show that on the

average, the runoff area above Point 1 contributes 10% of the runoff, runoff area between Point 1 and Point 2 contributes 52% of the runoff, while the runoff area between Point 2 and Point 3 provide 38% of the runoff. In this model, the water flowing through a particular upstream point must necessarily flow through all of the downstream points along the river. There is a lag between the peak flow rate at the three points in the river, however this does not show in the monthly average values since the runoff for a particular storm will flow completely out of the ecosystem in less than 6 days.

An error in the computer program caused the runoff into the watershed areas in Northern part of the grid to be increased while the runoff into the Southern watersheds was decreased. This error is responsible for a slight increase in the water flow rates at Points 1 and 2 along the river ($\approx$ 200 cfs).

Figure 52 shows the average monthly lake level (solid line) and the standard deviation of the average monthly lake level value about the mean value (dashed line). The standard deviation about the average monthly lake levels is calculated using the 14 average monthly means determined from the 14-year time series of simulated data. The lake level increases from a minimum in December to a peak in May and then decreases continually to the minimum value observed in December. The peak lake level occurs in May because of an accumulation of storm runoff from March, April and May and the fact that lake evaporation rate is at its lowest value for the three months prior to May. Part of this increase is also attributed to the fact that water is coming into the lake at rates greater than the water is leaving the lake for the months from December to March (see Table 18). The decrease in the lake level after May is caused by relatively high lake evaporation rate from May until

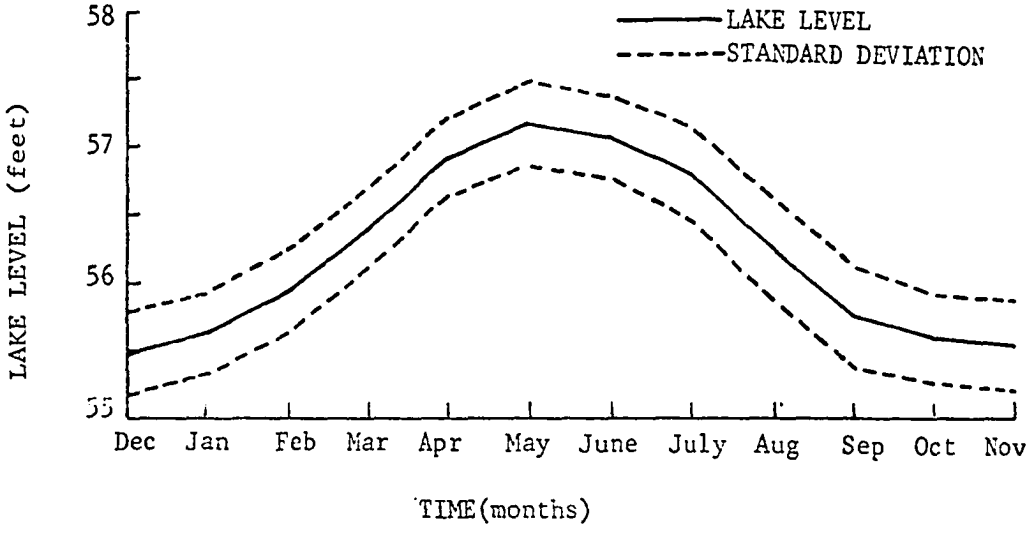

Fig. 52. The average monthly lake level and the standard deviation about the mean values are illustrated.

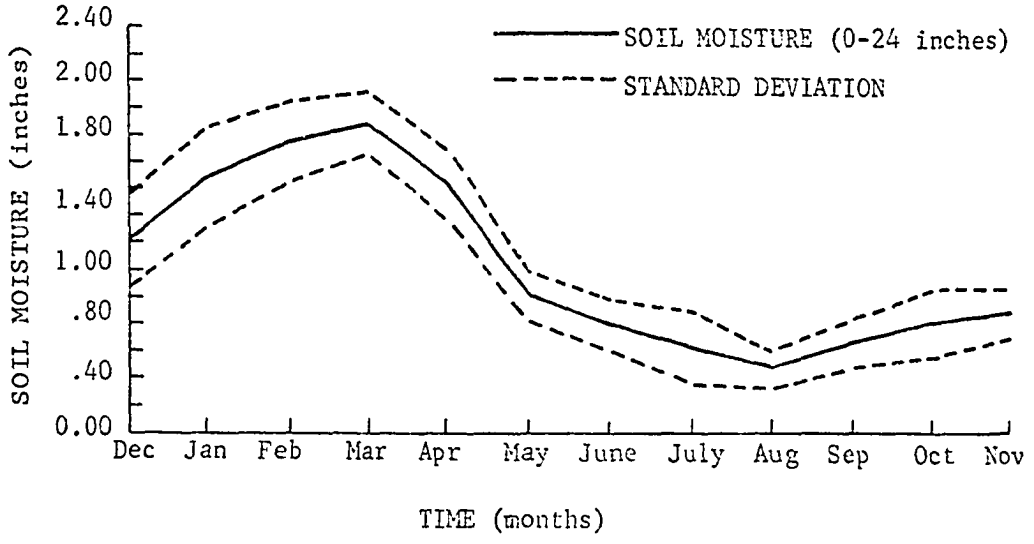

Fig. 53. The average monthly soil moisture for 0-24 inches and the standard deviation about the mean values are presented in this figure.

the end of the year and also because water is leaving the lake at a more rapid rate than it is coming into the lake from May until September. The standard deviation about the mean monthly lake level is uniform for all of the months of the year and has an average value equal to $\pm$ .35 ft. Figure 53 shows the standard deviation of monthly mean values of soil moisture from 0-24 inches. The standard deviation about the mean monthly values is calculated by using the 14 average monthly values of soil moisture determined from the 14-year computer simulation. The results show a fairly uniform distribution of the standard deviation for the different months of the year, however, the greatest values occur during the months of December, January and February. The variations during these months are caused by non-uniformities in the average monthly rainfalls.

The influence of different soil types and the hydrologic condition of the soil upon average storm runoff is determined by running the hydrology model for two years and calculating the monthly average runoff values for five different case studies (Table 19). The hydrologic condition of the soil refers to the ability of the soil to infiltrate rainfall. Poor hydrologic conditions mean that the infiltration rate is low. The results show that sharkey clay has greater average runoff values than commerce silt loam and that the average runoff decreases as the hydrological condition of the soil changes from poor to fair to good. The greatest average runoff is observed for a simulated urban area in which 50% of the area consisted of concrete, blacktop or roofing material.

Figure 54 illustrates a 30-day time sequence in which the soil moisture from 0-24 inches, the potential evapotranspiration rate, the actual evaporation rate and the river flow rate at 3 points in the river flow system respond to rainfall in the ecosystem.

TABLE 19

THE AVERAGE MONTHLY RUNOFF[1] (INCHES) CALCULATED AS A FUNCTION OF THE SOIL TYPE AND THE HYDROLOGIC CONDITION OF THE SOIL

		Dec Jan Feb	Mar Apr May	Jun Jul Aug	Sept Oct Nov
#1	Commerce Silt Loam with Fair Hydrology Conditions	0.0	.016	.057	.0005
#2	Sharkey Clay with Poor Hydrology Conditions	.015	.150	.279	.068
#3	Sharkey Clay with Fair Hydrology Conditions	.006	.069	.058	.018
#4	Sharkey Clay with Good Hydrology Conditions	0.0	.030	.061	.009
#5	City Area (50% Soil Area 70% of the Soil Area has live vegetation)	.307	.843	1.11	.684

[1]The average monthly runoff values are determined by running the ecosystem model for two years and calculating average values for five case studies with different soil types and hydrologic conditions.

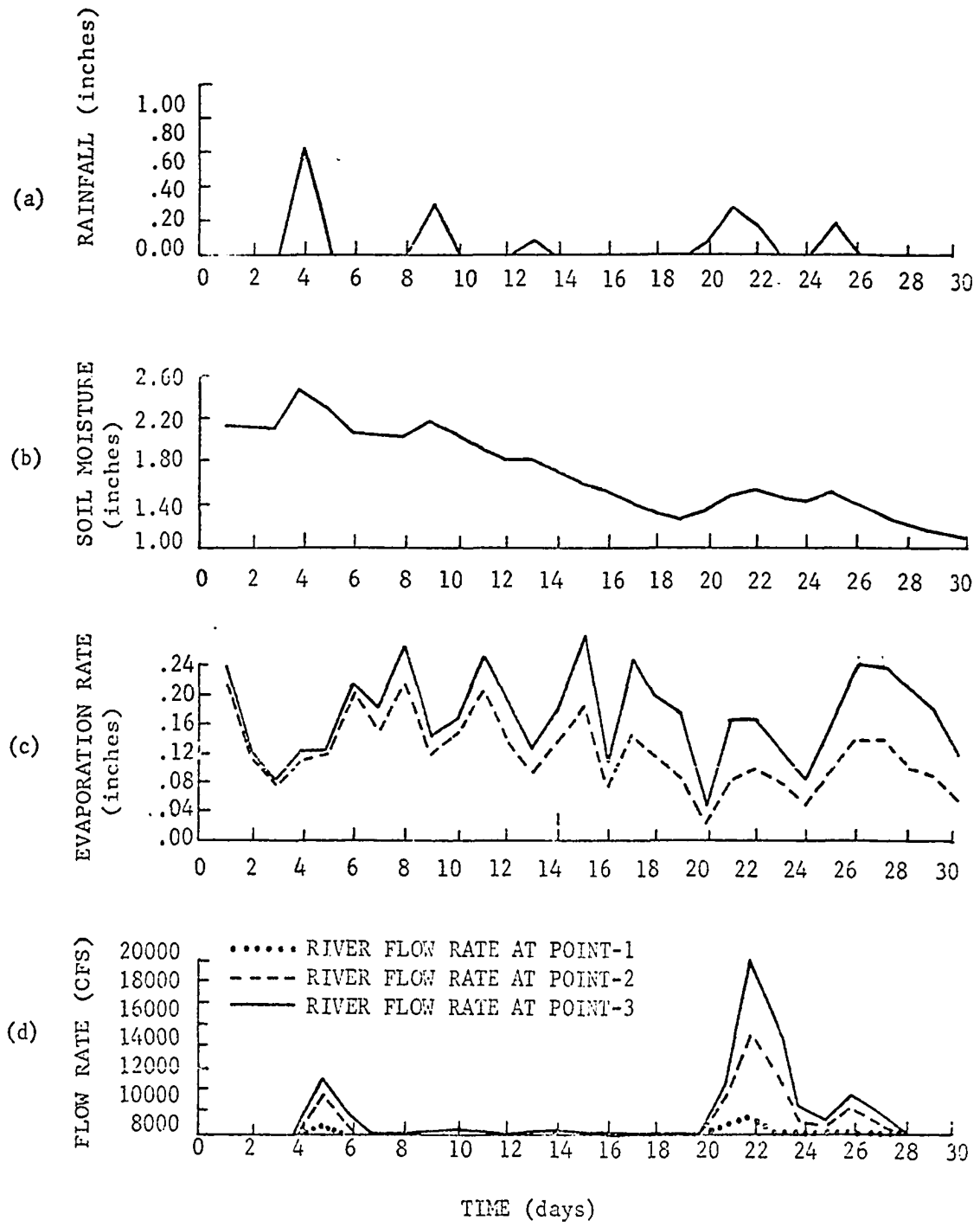

Fig. 54. A 30-day sequence of rainfall (a), soil moisture from 0-24 inches (b), potential evapotranspiration (solid line) and actual evaporation (dashed line) (c), and the flow rate at three points in the river system (d) are presented in this figure (the three points in the river system are the same three points listed in Figure 51).

Point 1 is the upstream point just below the dam, Point 2 is located in the middle of the ecosystem while Point 3 is the farthest down stream point in the ecosystem. The soil moisture for 0-24 inches shows a general decreasing trend from the beginning of simulation to the end of the simulation. The temporal increases in the soil moisture are all related to rainfall events. The time series of the potential evapotranspiration rate shows that it is subject to large day-to-day variations. These variations are produced by changes in wind speed, air temperature and cloud cover. A comparison of the potential evapotranspiration rate (solid line) to the actual evaporation rate (dashed line) shows that the ratio of the actual evaporation rate to the potential evapotranspiration rate is close to 1. at the beginning of the time simulation and decreases to less than .6 at the end of the simulation. The decrease in this ratio is caused by the fairly continuous decrease in the available soil moisture for evaporation (soil moisture from 0-24 inches). The time series of the river flow rate at the three points along the river system show that the flow rate responds directly to the rainfall events. The result shows that the rainfall events on day #4, day #21, and day #25 of the simulation caused significant increase in the flow rates along the river system. Some of the significant features of the flow rate time series associated with rainfall events are that

a) peak average flow rate is lagged one day from the rain event,

b) the flow rate at Point 1 recedes to the base level (8000 CFS) after one day while it takes two days for this to occur at Points 2 and 3 along the river system.

c) the flow rate increases going from Point 1 to Point 3 along the river with the greatest increase occurring between Point 1 and Point 2.

The river flow rates at Point 2 and Point 3 take longer to recede back to the base flow rate because the water continues to flow out of the upstream watersheds for up to five days after the occurrence of a rainfall event. The amount of time that it takes for the runoff from a particular rainstorm to flow out of a watershed is determined by the unit hydrograph for the rainfall event. Figure 54 shows that the peak flow rate at the three points on the river occurs at the same time. A more detailed look at the data shows that the peak flow rate after a rainfall event occurs earlier at the upstream point along the river. This detail in the flow rates along the river does not show up in Figure 54 since only daily average values of the parameters are shown.

The results presented in this appendix are determined from a computer simulation in which the atmospheric and the botany models are the only ones that interacted with the hydrology model. Specifically, the atmospheric model simulated the parameters which drive the hydrology model, while the botany model influenced the results through the effect of transpiration water loss by the plants. Some of the important interaction with the rest of the ecosystem not considered in the 14-year simulation are listed below:

1) Botany Model - this model utilizes water from the lake for irrigation of crop land.

2) Zoology Model - the model influences the hydrology model by emitting water pollution into the river.

3) Urban Model - the urban model uses water from the river for municipal and industrial use and then dumps water pollution into the river. The expansion of the city into the rural areas influences rainfall runoff and evaporation water loss.

The hydrology model considers water pollution in a very elementary manner. The model determines the amount of water pollution emitted into the river and then calculates the weight of the water pollution

material per cubic foot of water in the river. The water pollution material is carried down the river without considering any sinks for the pollution material. To a great extent, the influence of the Botany, Urban, and Zoology models upon the hydrology model is controlled by the linear program water control model. A detailed discussion of the influence of the Botany, Zoology, and Urban models upon the hydrology model is presented in the description of the testing procedure run on the water control model (Appendix F).

The effect of droughts of different length upon the evolution of the ecosystem is an interesting problem that is not directly studied in testing procedures performed on the ecosystem model. However, the results of the testing procedure performed on the water control model (Appendix F) give some indication of the possible effect of drought upon the ecosystem. In a drought situation, the water supply in the lake would decrease in response to the increased demand for water by the consumers (agriculture, industry, and the city), to the increase in the evaporation water loss from the lake and to the decrease in the amount of water flowing into the lake as runoff. The feedback mechanism in the model limits the amount of water allowed to flow out of the lake when the lake level decreases below a certain level. This will result in a decrease in the water allocated to the consumers. Eventually, the lake level would stabilize, however, the amount of water allocated to the consumers would be considerably less than the amount of water needed for their normal activity. The allocation of water within the city would be further complicated by the growth of the city and the consequent increase in water demand by all of the consumers. A long term drought would cause the growth of the city to be limited by the amount of water resources available.

APPENDIX C

APPENDIX C

RESULTS FROM THE URBAN MODEL

This appendix presents the results of the scheme used to test the Urban Model. The testing scheme demonstrates the response of the model to its four primary driving mechanisms which include boundary movement, population dynamics, industrial development and suburb dynamics. The effects of these four forcing functions upon the model are determined by a series of ten 16-year computer simulations in which the appropriate control parameters are altered individually. These parameters influence the evolution of the cities external and internal boundaries, the geographical distribution of the population, industrial development of the city, and the frequency distribution of the attributes associated with each suburb. The initial conditions for the frequency distribution and parameters used in the model are derived from the 1960 census data for Houston, Texas and are presented in Tables 20-29. Tables 30-32 illustrate the conditional relationships that are used to choose the attributes of individuals in the suburbs. Table 33 summarizes the values of the control parameters used in the ten simulations. The 10 case studies used the frequency distributions of the middle class suburb to generate the properties of people born in both the poor black and poor white suburbs.

Case #1 is the control case study, case #2 and #3 are concerned with

TABLE 20

Percent of people in the different age categories for the four suburbs in the city.[1]

Age Categories	Suburbs in the city				
	Poor Black	Poor White	Middle Class	Rich	Rural Farm
0-5	15.46	14.48	10.73	13.97	9.9
5-10	12.73	12.97	10.49	15.17	11.0
10-15	9.22	19.47	8.30	9.87	11.6
15-20	6.65	7.49	5.93	5.14	9.4
20-25	[illegible].93	6.29	6.91	.354	4.3
25-30	7.63	6.51	6.94	6.47	4.1
30-35	7.86	7.21	8.20	11.13	4.9
35-40	7.23	6.79	8.49	11.11	5.8
40-45	5.86	5.54	7.68	7.99	6.3
45-50	5.25	5.29	6.65	5.61	6.8
50-55	4.33	4.33	5.97	3.55	6.2
55-60	3.66	3.68	4.91	2.16	5.6
60-65	2.48	2.85	3.49	1.39	4.6
65-70	2.01	2.42	2.24	.83	3.8
70-75	1.24	1.76	1.46	.61	2.7
75-80	.35	1.06	.88	.32	1.5
80-85	.15	.48	.47	.16	.9
> 85	.10	.22	.19	.08	.5
	100%	100%	100%	100%	100%

[1]The statistics presented in the table are determined from 1960 census data for Houston, Texas.

TABLE 21

Summary of the initial conditions for several attributes of the four suburbs in the city.[1]

General Properties	Suburbs in the City: Poor Black	Poor White	Middle Class	Rich	Rural Farm
No. of People	201,561 (18.29%)	177,886 (16.14%)	450,000 (40.83)	272,495 (27.72%)	90,000
Area (sq. miles)	54	58.5	184.5	135	Rest of the Ecosystem
Population Density (per sq. mi.)	3732	3040	2439	2018	
Population Per Small Grid	457	380	304	252	
% of White	13.4	87.5	93.8	99.10	89.0
% of Non-White	86.6	12.5	6.2	.90	11.0
	100%	100%	100%	100%	100%
% of Male	48.27	49.0	49.13	49.13	51.7
% of Female	51.73	51.0	50.87	50.87	48.3
	100%	100%	100%	100%	100%

[1]The data presented in this table is based upon the 1960 census data for Houston, Texas.

TABLE 22

Percent of people in the different education categories for the four suburbs in the city.[1]

Education Categories	Suburbs in the City				
	Poor Black	Poor White	Middle Class	Rich	Rural Farm
0-School	5.10	3.74	1.33	.37	2.3
1-4 years	14.65	11.00	4.20	1.21	9.0
5-7 years	22.84	24.38	12.18	4.48	18.6
8 years	12.37	14.67	10.17	4.77	25.1
HS - 1-3	22.50	23.92	22.33	13.51	15.5
4 years	14.32	15.43	26.95	28.0	20.6
College 1-3	5.15	4.56	12.96	21.91	6.1
4 or more	3.11	2.26	9.84	25.71	2.8
	100%	100%	100%	100%	100%

[1]The data presented in this table are determined from the 1960 census data for Houston, Texas.

TABLE 23

Percent of people in the different family income categories for the four suburbs in the city.[1]

Family Income Categories (Annual Income)	Suburbs in the City				
	Poor Black	Poor White	Middle Class	Rich	Rural Farm
$1000. <	13.03	4.93	3.27	2.05	19.0
1000.-1999.	16.81	8.22	4.36	1.79	17.3
2000.-2999.	19.05	10.35	5.51	2.66	14.4
3000.-3999.	17.79	13.19	8.0	3.36	12.0
4000.-4999.	13.43	14.94	10.24	4.97	9.7
5000.-5999.	7.38	14.42	12.88	7.76	7.7
6000.-6999.	4.76	11.03	12.96	9.89	5.4
7000.-7999.	3.17	7.21	11.82	9.45	3.7
8000.-8999.	1.57	5.04	8.68	9.15	2.7
9000.-9999.	1.15	4.09	5.73	7.78	1.9
10000.-14999.	1.56	5.29	12.77	21.91	4.2
15000.-24999.	.16	.91	3.15	10.43	1.5
< 25000	.06	.32	.58	8.74	.5
	100%	100%	100%	100%	100%

[1]The data presented in this table are determined from the 1960 census data for Houston, Texas.

TABLE 24

Percent of people in the different occupation categories for the four suburbs in the city.[1]

Occupation Categories	Suburbs in the City				
	Poor Black	Poor White	Middle Class	Rich	Rural Farm
Professional	2.07	1.66	5.64	9.06	1.36
Managerial	1.01	2.00	4.44	7.22	.88
Clerical	1.83	5.36	11.35	8.47	1.58
Sales	.48	2.11	4.84	5.27	.84
Craft	2.30	7.12	6.87	4.03	2.02
Operators	7.63	10.10	5.43	2.55	3.85
Private Household	7.20	1.39	.69	.45	.66
Service Workers	9.45	4.21	3.78	1.38	1.08
Labor	6.70	3.56	1.59	.37	.38
Not-Employable	61.7	62.5	55.4	61.2	63.0
Farmers	0	0	0	0	15.25
Farm Labor	0	0	0	0	5.31
	100%	100%	100%	100%	100%

[1]The data presented in this table are determined from the 1960 census data for Houston, Texas.

TABLE 25

The number of housing units and percent of housing units in the different categories is presented for the four suburbs in the city.[1]

	Suburbs in the City			
Housing	Poor Black	Poor White	Middle Class	Rich
No. of Housing Units	66,381	63,764	150,000	87,374
% of Underemployed Housing Units	59.37	70.35	35.74	11.50
% of Worker Housing Units	37.59	27.91	54.65	59.51
% of Quality Housing Units	1.67	.93	8.76	29.10
	100%	100%	100%	100%

[1]The data presented in the table are determined from the 1960 census data for Houston, Texas.

TABLE 26

Percent of people in the different health categories for the four suburbs in the city.

Health Categories (Mortality Rate Per 1000 Population)	Poor Black	Poor White	Middle Class	Rich	Rural Farm
0-5	1.0	1.0	0	5.0	1.0
5-6	4.0	4.0	2.5	10.0	4.0
6-7	10.0	10.0	25.0	40.0	10.0
7-8	15.0	15.0	50.0	30.0	15.0
8-9	50.0	50.0	20.0	10.0	50.0
>10	20.0	20.0	2.5	5.0	20.0
	100%	100%	100%	100%	100%

TABLE 27

The total number of industries in the different categories and the number of jobs in the different occupation categories is presented in this table.

	New Enterprise	Mature Business	Declining Industry	Total
Number of Industries	15,000	10,000	5,000	30,000
Number of Managerial and Professional Jobs	75,000 5/	30,000 3/	5,000 1/	120,000
Number of Worker Jobs	195,000 13/	100,000 10/	35,000 7/	330,000
Number of Underemployed Jobs	120,000 8/	60,000 6/	200,000 4/	200,000

5/ This symbol indicates the number of jobs in an occupational category that a particular type of industry will employ.

TABLE 28

Five year mortality rates[1] for the four suburbs in the city.

Age	Poor Black	Poor White	Middle Class	Rich	Rural Farm
0-5	.027	.026	.025	.024	.026
5-8	.006	.005	.004	.003	.005
10-14	.003	.003	.002	.002	.003
15-19	.003	.003	.003	.003	.003
20-24	.008	.007	.006	.005	.007
25-29	.006	.006	.006	.006	.006
30-34	.008	.008	.007	.007	.008
35-39	.011	.011	.010	.009	.011
40-44	.015	.015	.014	.014	.015
45-49	.025	.024	.023	.023	.024
50-54	.037	.037	.036	.035	.037
55-59	.058	.057	.055	.052	.057
60-64	.085	.084	.081	.080	.084
65-69	.128	.126	.121	.120	.126
70-74	.179	.178	.174	.170	.178
75-79	.250	.249	.246	.245	.249
80-84	.360	.360	.355	.350	.360
85 →	.400	.400	.395	.394	.400

[1]The five year mortality rate is fraction of people in each age category that will die in a five year period, data determined from the 1960 census data.

TABLE 29

Birth and death rates for the four suburbs in the city.

	Poor Black	Poor White	Middle Class	Rich	Rural Farm
No. of People Born per 1000 Population	31.5	27.1	22.7	22.7	24.0
No. of People that Die per 1000 Population	9.9	9.8	9.4	9.3	9.6

TABLE 30

Percent of people in the different occupation categories[1] as a function of their sex and annual income.

	Male Income			Female Income		
Occupation	0-5000	5000-10000	>10000	0-5000	5000-10000	>10000
1.Professional	6.59	14.51	30.18	11.36	43.23	32.22
2.Managerial	6.96	13.30	39.13	2.95	10.11	34.93
3.Clerical	8.4	8.52	2.50	32.07	31.87	12.99
4.Sales	7.52	7.14	12.31	8.27	2.78	8.68
5.Craft	17.29	29.10	10.13	1.26	2.04	1.64
6.Operators	28.98	20.59	3.53	19.06	6.44	2.42
7.Private House	.29	.01	.01	9.01	.23	.65
8.Service Workers	10.49	3.47	.96	15.37	3.05	5.26
9.Laborers	13.45	3.33	.59	6.20	.21	.15

[1]Data determined from the 1960 U.S. Census data. Occupation 1 and 2 comprise the professional-managerial category, occupations 3-6 comprise the worker category, while 7-9 comprise the underemployed category.

TABLE 31

Percent of people in each age and sex category that are members of the working force.[1]

	Rural Farm		Urban	
Age	Male	Female	Male	Female
14-17	31.5	10.3	26.8	15.5
18-24	81.6	35.0	79.3	48.7
25-34	95.7	25.5	95.4	37.7
35-44	96.3	29.4	96.3	45.2
45-64	91.5	25.3	90.1	45.0
65 →	49.7	7.6	30.4	11.3

[1]Data determined from the 1960 U.S. Census data.

TABLE 32

Percent of people in different income categories as a function of their educational level and age category.[1]

Income Categories	Under 25 Years Old (Education)				25-64 Years Old (Education)				≥ 65 Years Old (Education)			
	≤8 Years	1-3 HS	4 HS to 3C	≥ 4C	≤8 Years	1-3 HS	4 HS to 3C	≥ 4C	≤8 Years	1-3 HS	4 HS to 3C	≥ 4C
0- 1000	10.8	5.0	2.6	2.7	6.2	2.0	1.4	.7	12.8	6.6	5.9	3.7
1000- 1999	16.3	10.0	6.5	5.3	8.0	2.9	1.8	1.0	25.3	15.7	13.7	6.0
2000- 2999	19.8	16.2	12.0	10.1	10.2	5.2	3.5	1.4	18.6	16.9	14.5	7.9
3000- 3999	18.5	19.1	16.8	14.2	12.1	8.7	6.6	2.5	11.5	13.3	12.0	8.0
4000- 4999	14.5	17.6	18.7	16.8	13.5	12.3	10.5	4.6	8.2	10.3	9.9	8.3
5000- 5999	9.4	13.5	16.8	16.2	13.5	15.9	15.4	7.5	6.2	8.5	8.4	7.9
6000- 6999	4.8	8.2	11.4	12.7	10.3	13.9	14.8	9.5	4.6	6.6	7.0	6.7
7000- 7999	3.0	6.0	7.0	8.0	9.0	14.0	15.0	15.0	3.0	6.5	6.0	7.0
8000- 8999	1.0	1.8	4.0	5.0	5.0	6.0	7.0	7.0	2.4	3.0	5.0	5.0
9000- 9999	.8	1.0	3.0	3.6	3.1	5.0	6.1	6.2	2.0	2.5	3.3	4.1
10000-14999	.9	1.3	1.8	4.2	7.2	11.0	13.3	25.2	3.9	6.5	8.8	15.6
15000-24999	.08	.16	.24	.8	1.2	2.5	3.2	15.0	1.2	3.2	5.0	15.0
225,000	.02	.04	.06	.3	.7	.7	1.3	4.3	.5	1.0	1.5	4.8
	100%	100%	100%	100%	100%	100%	100%	100%	100%	100%	100%	100%

[1]Data determined from the 1960 U.S. Census (HS = high school, C = college, 4C = four years of college completed).

TABLE 33

This table presents the control parameter values used in the 10 urban model case studies.[1]

PARAMETERS	Control Case Study #1	Boundary Movement Case Studies #2	#3	Population Dynamics Case Studies #4	#5	#6	Suburb Dynamics #7	#8	Industry Development #9	#10
Critical Boundary Stress	5000	25000								
Boundary Stress Eqn. (Eqn.38)										
a) Race Factor (C)	40		90							
b) Population Factor (B)	2.0									
c) Land Use Factor (A)	100									
Livability (Eqn. 51(b))										
a) Population Factor (L4)	.50									
b) Air Pollution Factor (L1)	0.0			$3x10^6$	0					
c) Race Factor (L3)	60									
d) Housing Factor (L2)	70									
Gradient of Livability (Eqn. 51(c))										
a) Population Factor (P_3)	6				0.0					
b) Air Pollution Factor (P_1)	0.0			$15x10^6$						
c) Race Factor (P_4)	150									
d) Housing Factor (P_2)	130									
Suburb Livability (Eqn. 54)										
a) Population Factor (R_1)	1.0									
b) Air Pollution Factor (R_2)	0.0			2.0						
c) Race Factor (R_3)	130									
% of Blacks Moving to New Suburbs (PR)	100									
% of People Moving by Discontinuous Movement (P)	80%					5%				
Industry Model (Rate Parameters)										
a) Growth of New Industries (H_c)	10%								5%	15%
b) Decline of New Industries (H_o)	8%									
c) Decline of Mature Industries (Q_d)	5%									
d) Death of Old Industries (Q_c)	3%									

[1] The control parameter values for case studies 2-10 are only indicated when the values are different from the values in the control case study. The equation numbers and the symbols next to control parameter refer to those used in the main text description of the urban model. -1,-2, -3, -4 after a parameter value refer to the parameter value for suburb 1, 2, 3, and 4.

Table 33 continued

		#1	#2	#3	#4	#5	#6	#7	#8	#9	#10
Suburb Dynamics											
a) Quality Housing Construction Rate	P_c-1	6%									
	P_c-2	6%									
	P_c-3	6%							8%		
	P_c-4	6%							8%		
b) Quality Housing Loss Rate	P_d-1	3%									
	P_d-2	3%									
	P_d-3	2%							3%		
	P_d-4	3%									
c) Worker Housing Construction Rate	W_c-1	6%							8%		
	W_c-2	6%							8%		
	W_c-3	6%							8%		
	W_c-4	6%							8%		
d) Worker Housing Loss Rate	W_d-1	5%									
	W_d-2	5%									
	W_d-3	2%									
	W_d-4	2%									
e) Underemployed Housing Construction Rate	U_c-1	5%							8%		
	U_c-2	5%							8%		
	U_c-3	1%									
	U_c-4	0%									
f) Underemployed Housing Loss Rate	U_d-1	5%									
	U_d-2	5%									
	U_d-3	1%									
	U_d-4	2%									
g) Underemployed to Worker Transfer Rate	I_v-1	4%							10%		
	I_v-2	4%							10%		
	I_v-3	4%									
	I_v-4	4%									
h) Worker to Professional Transfer Rate	I_w-1	3%							7%		
	I_w-2	3%							7%		
	I_w-3	3%									
	I_w-4	3%									

boundary movement. Cases #4, #5 and #6 study the population dynamics. Cases #7 and #8 looked at suburb dynamics, while cases #9 and #10 study the effect of industrial development. The results for the control case study (case #1) are presented in a fairly detailed manner, while the results from the other case studies are compared with these results. New figures are only presented when the results of the different case studies are significantly different from the results of the control case study.

The initial city and suburb boundary configuration and population density for the control case study (case #1) are presented in Figure 55. These are the same initial conditions used for the other case studies. The most important feature to note in Figure 55 is that suburbs #1 and #2 have much higher population density than suburbs #3 and #4. Figure 56 shows the change in the total suburb populations with evolution of model. The discontinuous changes in the suburb population every five years is caused by the fact that every fifth year the model ages the people five years, allows the population to die as a function of the survival rate and then adds the people born during the last five years to the total population of the particular suburb. It is interesting to note that the population of suburbs #1 and #2 decrease in the five-year periods that precede each five-year update of the suburb population. This decrease is caused by the movement of people from suburbs #1 and #2 into the other two suburbs which have better livability conditions.

The greatest increase in the suburb population is observed in suburb #4 and can be attributed to the fact that suburb #4 had the best livability conditions. Figure 57 shows the contoured population field

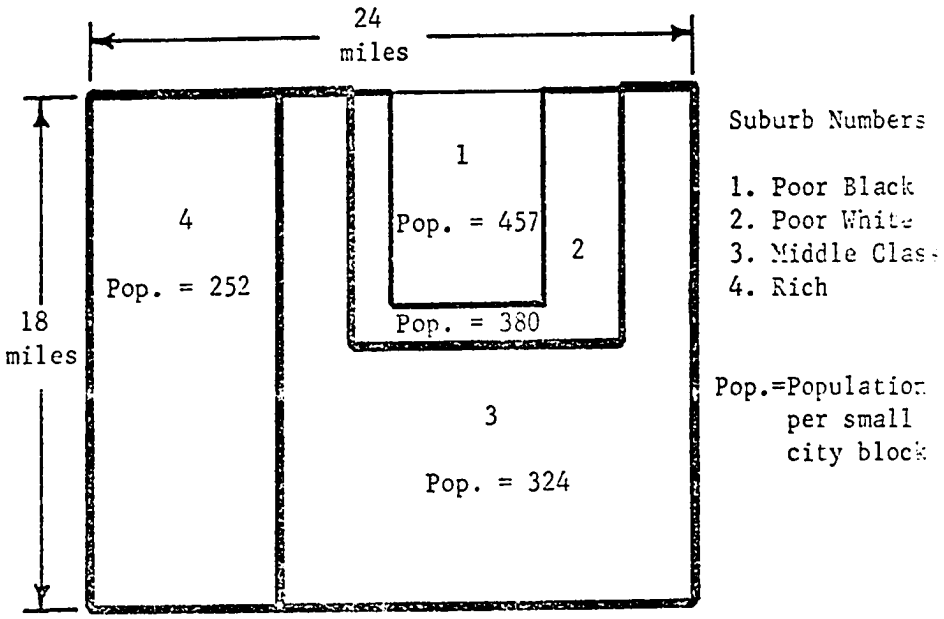

Fig. 55. The initial city and suburb boundary field and the initial population of the small city blocks are presented in this figure. The particular configuration of the city boundaries and population densities are set up to approximate the conditions found in Houston, Texas (1960 census data).

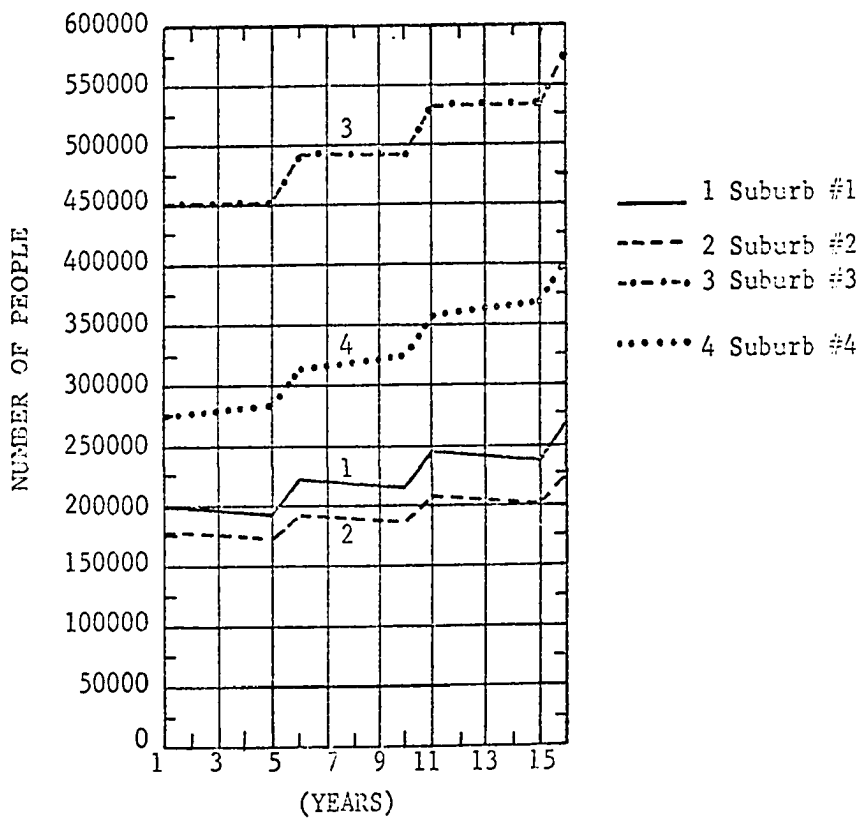

Fig. 56. Population growth of the four suburbs for case #1 is presented.

(a)

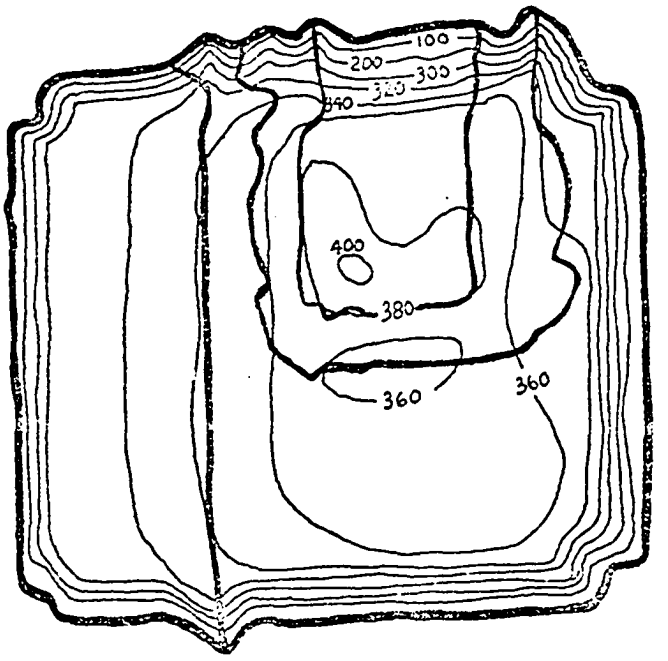

CONTOURED POPULATION
(number of people per small city block)

(b)

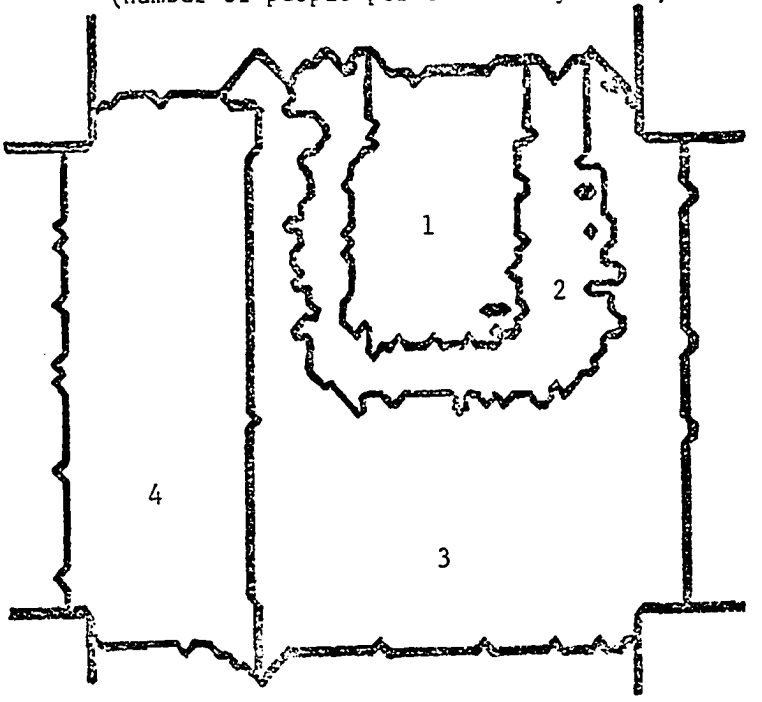

BOUNDARY FIELD

Fig. 57. The contoured population field (a) and the city and suburb boundary field (b) for the last time step (16 years) in case #1 are illustrated in this figure.

and the city and suburb boundary field at the end of the time simulation. The results indicate that the city expanded in area with all of the suburbs increasing in size. While all suburbs expanded into the rural areas, suburb #1 and #2 also expanded into the center of the city at the expense of suburb #3. Population stress across the boundaries is the parameter primarily responsible for the expansion of the city into the rural area and the expansion of suburb #1 into suburb #2 into the center of the city. The most significant changes in the boundary configuration occurred during the first 10 years of the simulation. The population field shows that the people moved into the rural area as the city expanded. A comparison of the initial and final population density (original city boundaries) shows that the population density of suburbs #1 and #2 decreases while the population density of suburbs #3 and #4 increases. The decrease in the population density of suburbs #1 and #2 is caused by the rapid increase in the size of the suburbs, while the population density in suburbs #3 and #4 is increased because of the immigration of people from suburbs #1 and #2 and the fact that these suburbs did not expand into the rural areas as fast as local population increased. The immigration of people from suburbs #1 and #2 is prompted by the more favorable living conditions in suburbs #3 and #4.

The most important effect of the 16-year evolution upon the population field is that the strong population gradients found in the intital state of the model are diffused to such an extent that the population density in the city is fairly uniform. The predominate features of the population field are the strong population gradients that exist at the outer edges of the city and the gradual population

density decrease that is observed going west from suburb #3 into suburb #4.

Fig. 58 presents the initial (dashed line) and final (solid line) race distributions for the four suburbs. At the end of the 16-year simulation, the percentage of the non-white population of suburb #1 decreased, while the percentage of non-white population increased in the other three suburbs, with the greatest increase occurring in suburb #2 and suburb #4. The decrease in the percentage of non population in suburb #1 is caused by the movement of rich non-white people into the other suburbs and the slow movement by diffusion of white people from suburb #2 into suburb #1. This movement of people from suburb #2 into suburb #1 occurs in the last 8 years of the simulation, after the livability of the suburb #1 has improved because of the decrease in the population density (see Fig. 57). The increase in the non-white population in suburb #2 is caused by movement by diffusion of middle-class black population in suburb #1 into suburb #2. The increase in the black population in suburbs #3 and #4 is caused by discontinuous movement of the very rich non-white population from suburb #1 into these suburbs. As people move from one suburb to another, they take with them attributes selected from the frequency distribution of attributes associated with the suburb they are moving from. This selection process promotes the integration of the city since the race attribute of the people moving away from the poor livability conditions in suburb #1 is selected from a frequency distribution in which over 80% of the people are non-white. The poor livability conditions in suburb #1 is the factor which initiates the movement of people out of this suburb and thus promotes the racial integration of the city. The net effect at the end of of the time simulation is that the city is more integrated with respect

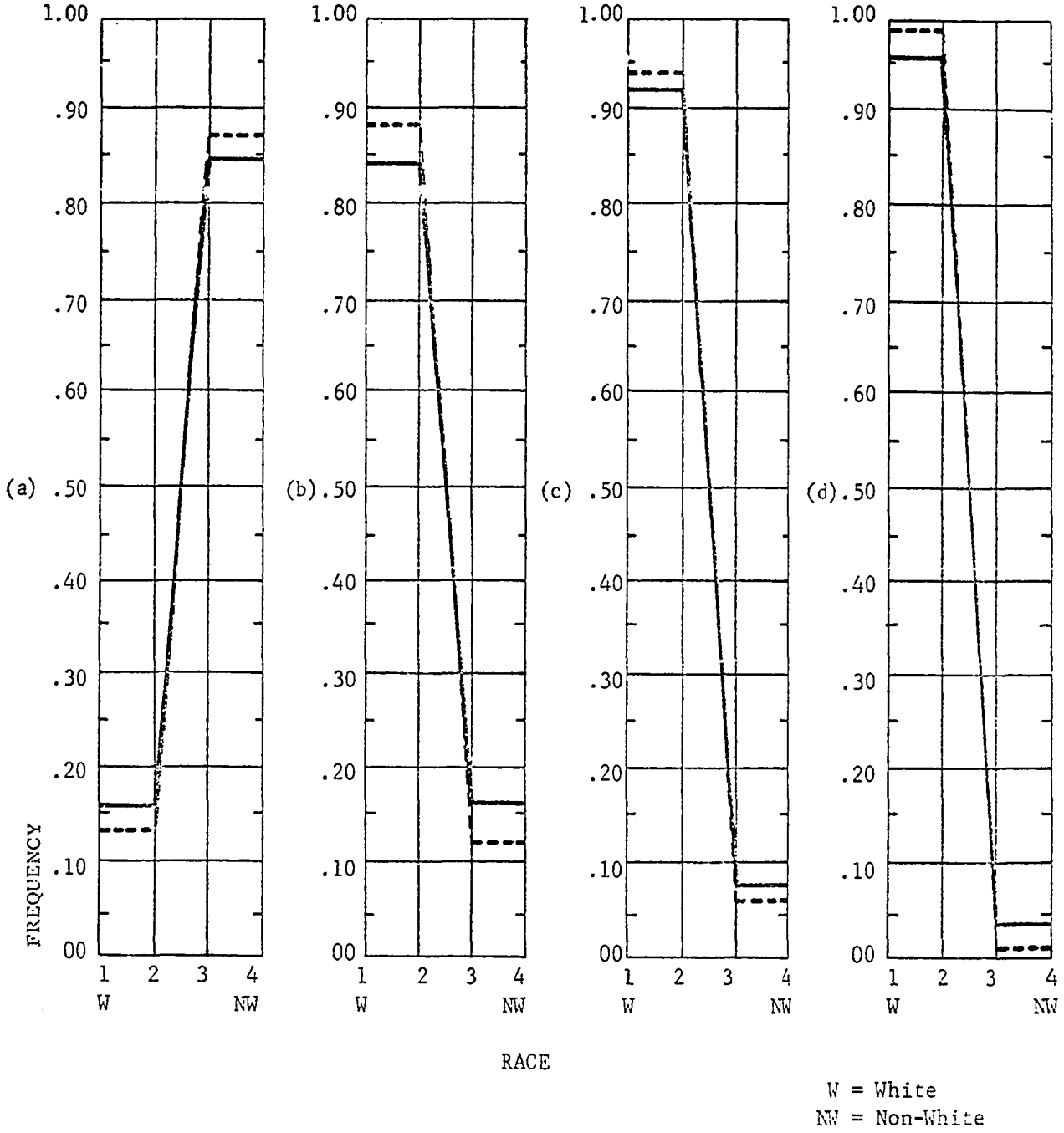

Fig. 58. Initial (dashed line) and final (solid line) race frequency distribution for suburb #1 (a), suburb #2 (b), suburb #3 (c), and suburb #4 (d) are given for case study #1.

to racial distributions in the suburbs.

The initial (dashed line) and final (solid line) occupation frequency distributions for the four suburbs are presented in Fig. 59. The results show that in all of the suburbs the relative frequency of the higher occupational levels increase significantly. This is produced because the occupation submodel assumed that 4% per year of the people in the under-employed category are upgraded to the worker category while 3% of the people in the worker category are upgraded to the managerial-professional category. The above assumptions are only valid if money for the job training programs is available and if there is an increase in the number of jobs in the worker and managerial-professional occupation categories. In reality, the money for the education programs is not available and the jobs do not exist. This case study is designed to demonstrate the influence of a job training program upon a city that has a growing job market in the worker and managerial-professional categories. When people are upgraded to a higher occupational level, their family income could be generated by an increase in industrial activity. A complete ecosystem model of an urban-rural ecosystem requires a detailed economic model that is capable of handling the monetary problems associated with the industrial growth and the utilization of capital for projects such as job training programs. The effect of increasing the number of people in higher occupational levels upon the initial (dashed line) and final (solid line) family income and educational level frequency distribution is shown in Figs. 60 and 61. The results show that for all of the suburbs the relative frequency of higher income and higher educational levels are increased significantly. The family income distribution

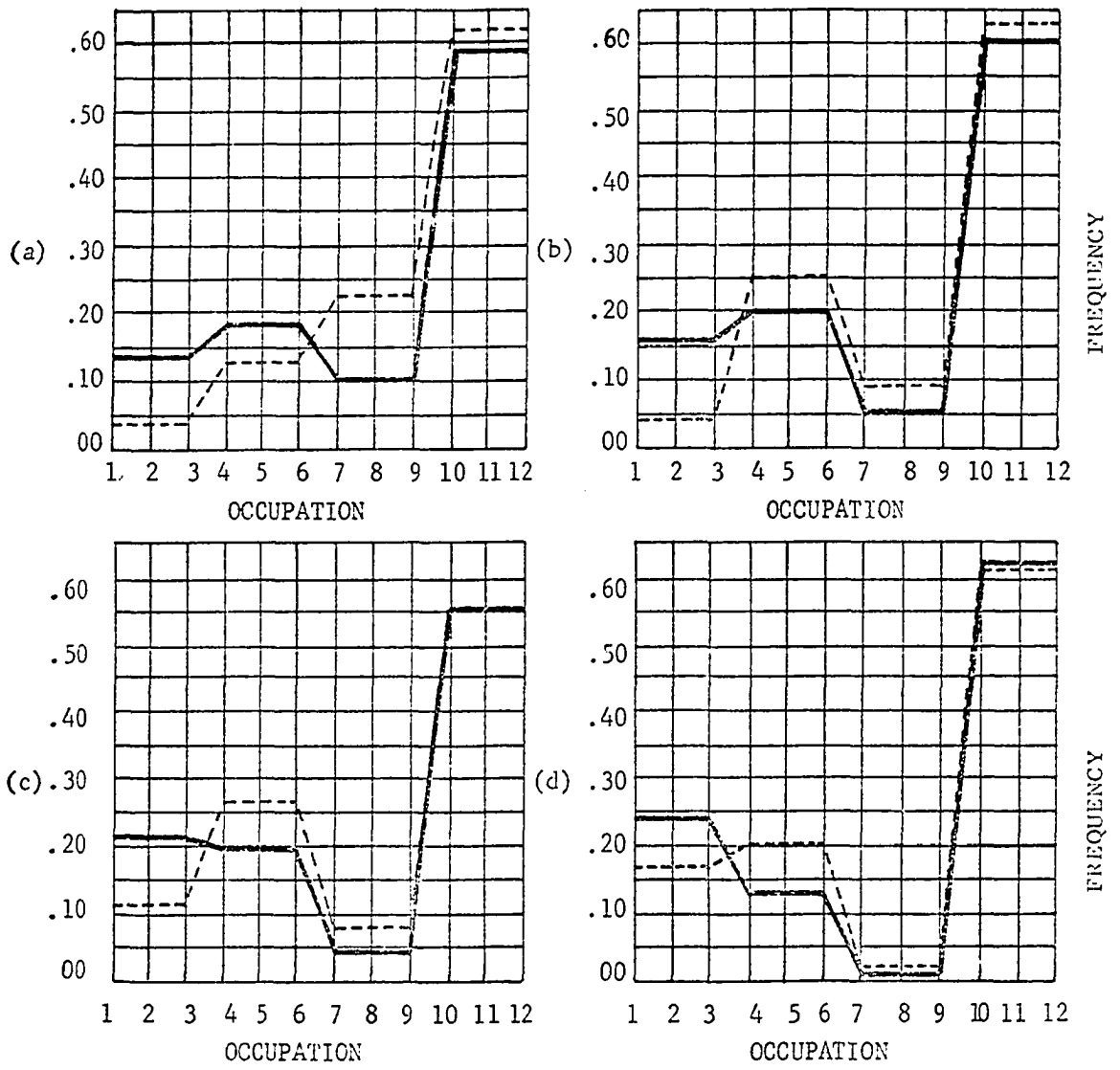

Fig. 59. Initial (dashed line) and final (solid line) occupation distribution for suburb #1 (a), suburb #2 (b), suburb #3 (c), and suburb #4 (d) are illustrated for case study #1.

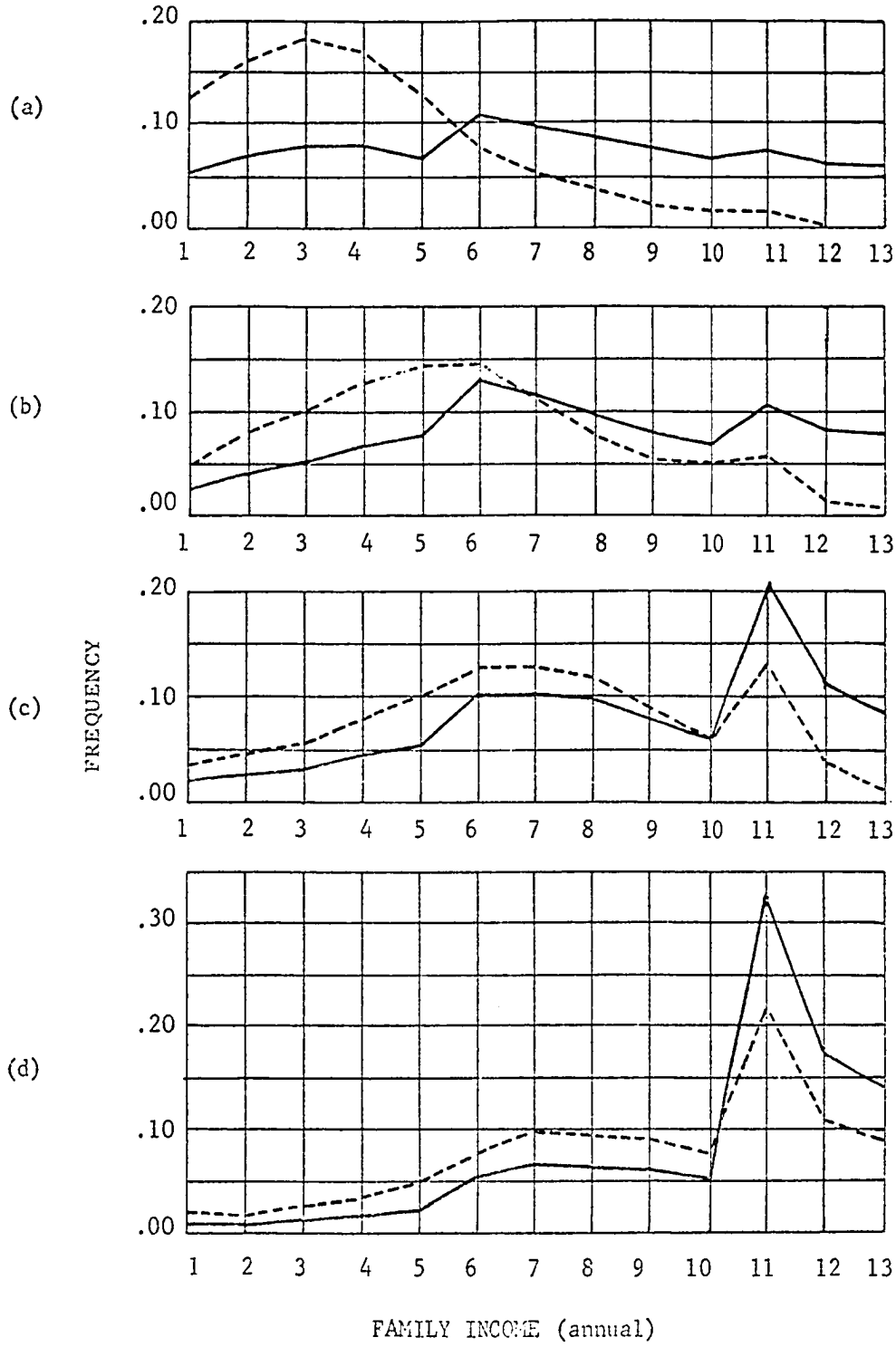

1	1000	6	5000-5999		
2	1000-1999	7	6000-6999	11	10000-14999
3	2000-2999	8	7000-7999	12	15000-24999
4	3000-3999	9	8000-8999	13	25000
5	4000-4999	10	9000-9999		

Fig. 60. Initial (dashed line) and final (solid line) family income distribution for suburb #1 (a), suburb #2 (b), suburb #3 (c), and suburb #4 (d) are shown for case study #1.

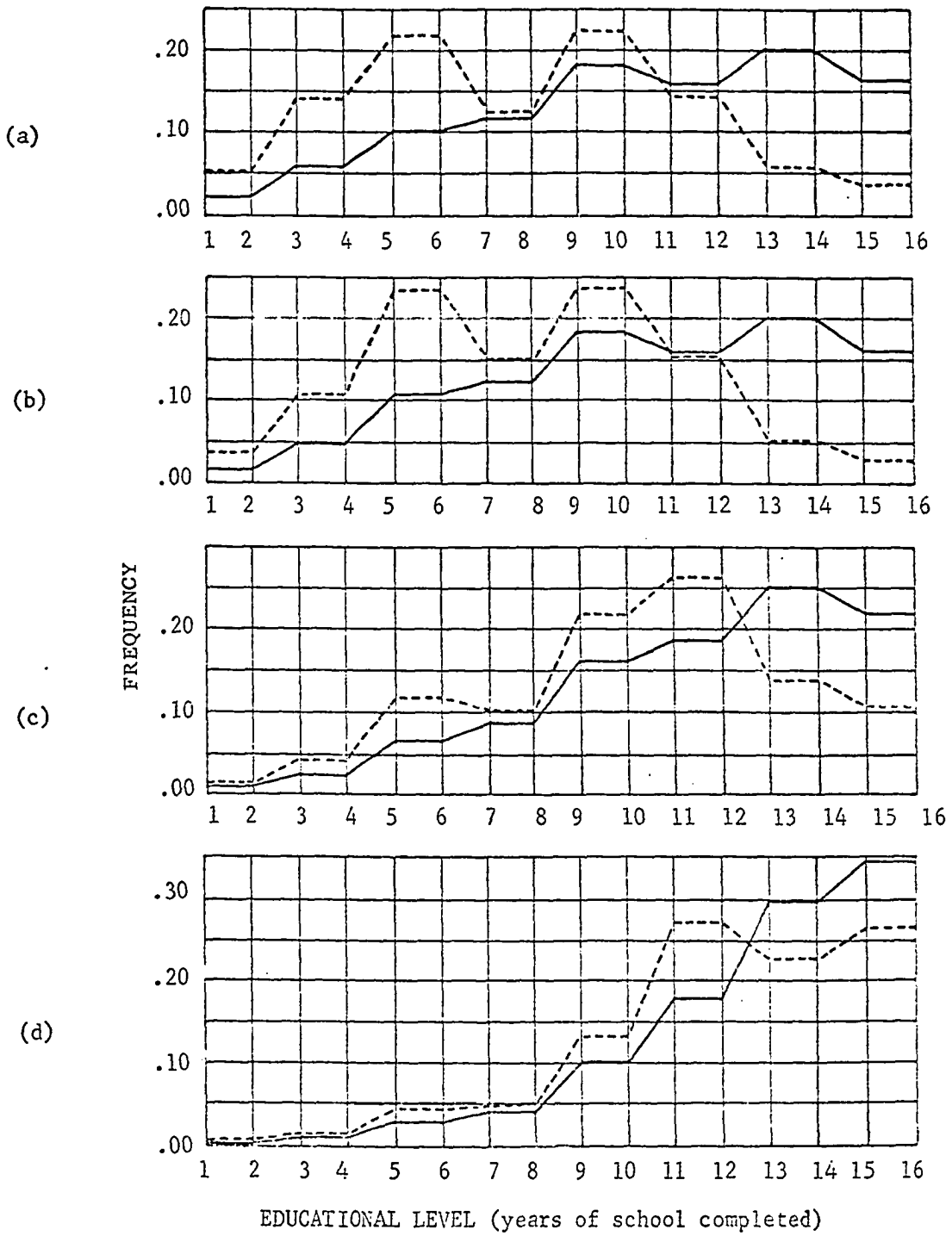

Fig. 61. Initial (dashed line) and Final (solid line) education frequency distribution for suburb #1 (a), suburb #2 (b), suburb #3 (c), and suburb #4 (d) are presented for case study #1.

for suburbs #3 and #4 show that the family income in the $10,000 to $15,000 category increases much more rapidly than the family income in this category for suburbs #1 and #2. This is caused by the movement of high income families from suburbs #1 and #2 into suburbs #3 and #4.

Fig. 62 illustrates the initial and final housing frequency distributions for the differenc suburbs. A comparison of the initial and final frequency distribution for suburbs #1 and #2 show that there is a significant increase in the relative frequency of the underemployed housing. This is caused by a fairly high construction rate for new underemployed housing and a high transfer rate of worker housing into underemployed housing. This transfer rate can be considered as an again process in which houses deteriorate with age and thereby lose value. The housing distribution for suburb #3 shows that there is a significant increase in the percentage of worker housing. This is attributed to a fairly low transfer rate of worker to underemployed housing. The use of a lower transfer rate of worker to underemployed housing in suburb #3 than in suburbs #1 and #2 simulates the situation in which a middle-class neighborhood would take better care of its houses than the lower income level neighborhood. A comparison of the initial and final housing distribution for suburb #4 showed that there is an increase in the percentage of the worker housing and a fairly sharp decrease in the percentage of quality housing. This decrease in the percentage of quality housing resulted from a higher transfer rate from quality housing to worker housing in suburb #4 than in suburb #3. The increase in the percentage of the worker housing in suburb #4 is produced by the higher transfer rate of quality housing to worker housing and the fact that

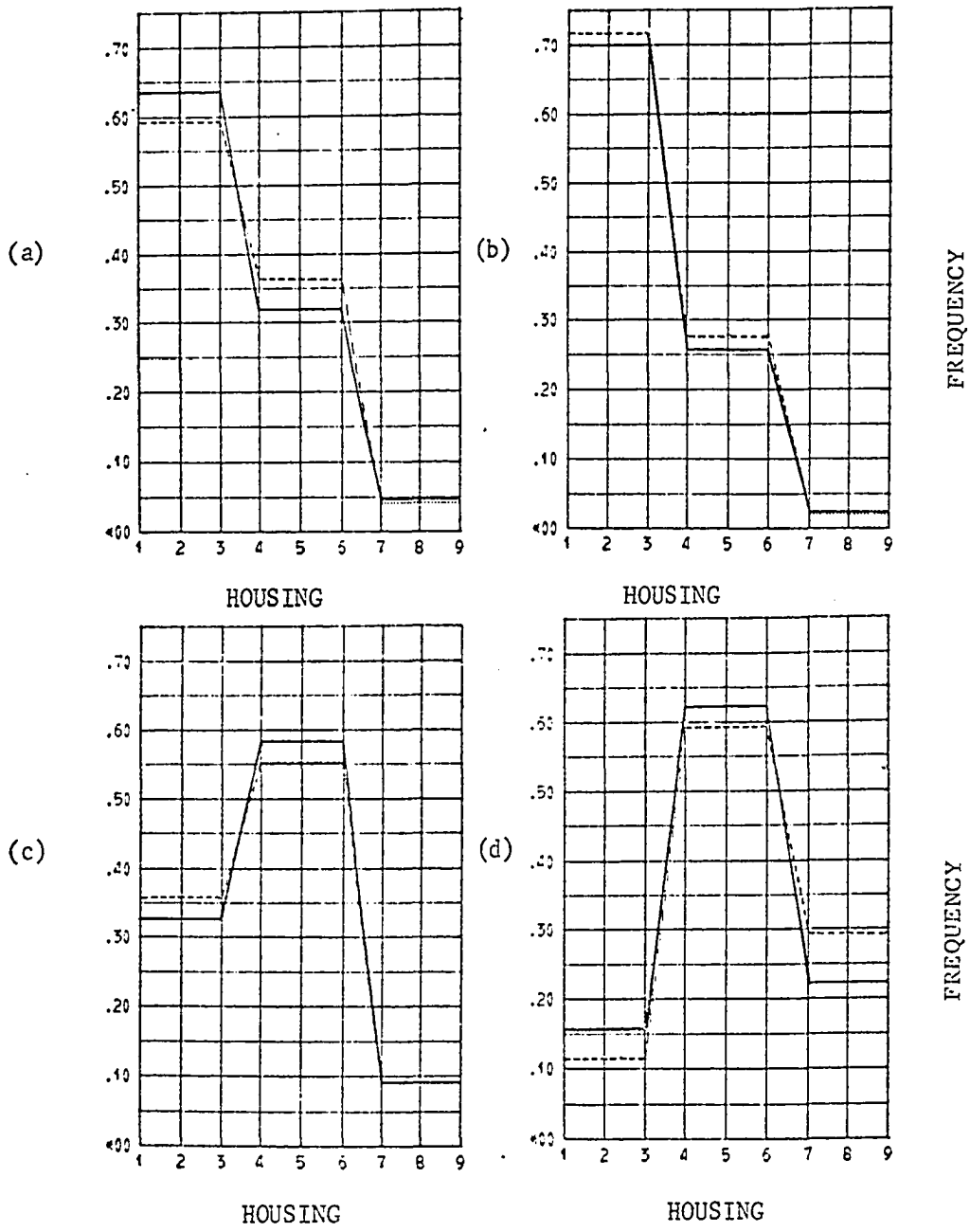

1-3 Underemployed Housing
4-6 Worker Housing
7-9 Quality Housing

Fig. 62. Initial (dashed line) and final (solid line) housing frequency distributions for suburb #1 (a), suburb #2 (b), suburb #3 (c), and suburb #4 (d) are shown for case study #1.

the transfer rate from worker housing to underemployed housing is fairly low in comparison to the new construction rate for worker housing. A comparison of the initial and final percentage of area occupied by housing units show that in suburbs #1 and #2 there is a decrease in the percentage of area occupied, while in suburbs #3 and #4 there is a sharp increase in the percentage of area occupied by housing units. The decrease in suburbs #1 and #2 is caused by the fact that these suburbs increase in area much more rapidly than the growth of new housing facilities, while the increase in the percentage area occupied by housing units in suburbs #3 and #4 occurs because the number of housing facilities increased more rapidly than the area occupied by the suburbs.

Boundary Movement

Case studies #2 and #3 are designed to demonstrate the effect of the boundary movement mechanisms upon the evolution of the urban model. In particular, case #2 demonstrates the influence of the critical boundary stress parameters, while case #3 demonstrates the effect of the race factor in the boundary stress equation. Specifically for case #2, the critical boundary stress values are increased to such a level that the city boundaries are not allowed to expand during the time simulation. The model is set up so that the critical boundary stress values between the city and rural areas must be exceeded before the city can expand into the rural areas. The boundary configuration and contoured population field at the end of the 16 years of evolution for case #2 are presented in Fig. 63. The city boundaries did not change from the initial condition, however, the suburb boundaries within the city changed significantly.

(a)

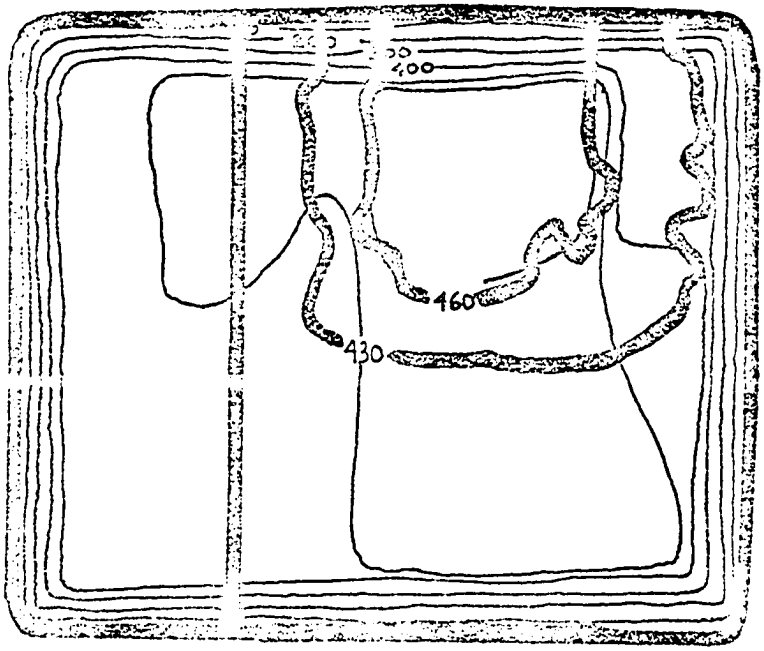

CONTOURED POPULATION
(number of people per small city block)

(b)

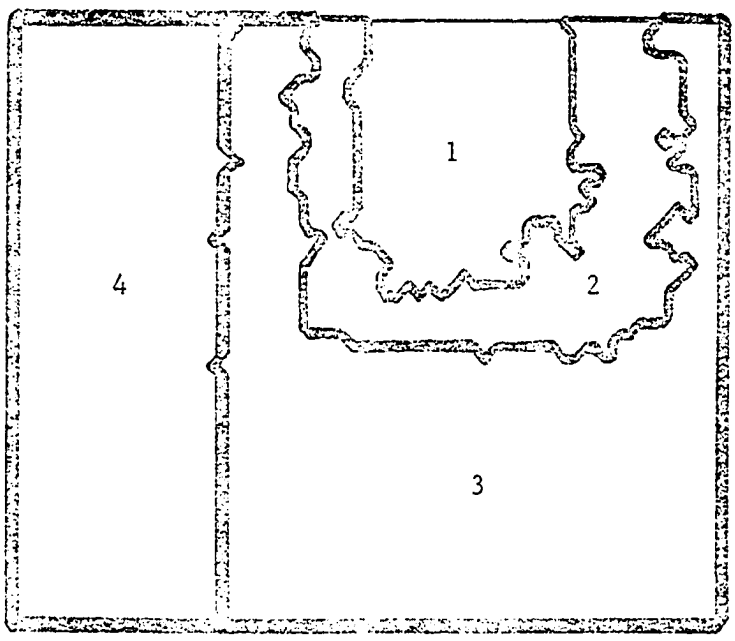

BOUNDARY FIELD

Fig. 63. The contoured population field (a) and the city and suburb boundary field (b) for the last time step in case study #2 are shown in this figure.

Suburb #1 and #2 expanded in area by 11% and 7% respectively while suburbs #3 and #4 decreased in area by 2% and 5% respectively. Suburbs #1 and #2 took on new area because of the very poor livability conditions that initially existed in these suburbs. A comparison of the suburb boundaries in the center of the city area with the suburb boundaries in the same region for case study #1 shows very little difference; however, a comparison of the population field for case study #1 and #2 indicates a significant difference. The most striking feature is that the population densities for all suburbs are greater in case study #2. This would be expected since the overall area of the city is not expanding during the 16-year simulation. A comparison of the population density between the different suburbs for case #2 shows that suburb #1 and #2 have higher population densities, however, the difference between the population density in suburbs #1 and #2 and the population density in suburbs #3 and #4 decreases significantly from the difference observed at the beginning of the time simulation. Stopping the city growth into the rural area has little effect upon the education distribution, income distribution, occupation distribution, and the housing distribution for the suburbs; however, it did influence the race distributions for the two case studies. The results for suburb #1 show that the percentage of the non-white population decreases more rapidly in case #2. This decrease associated with a more rapid increase in the percentage of non-white population in suburbs #2, #3 and #4. The net effect is to cause the city to become more racially integrated. This occurred because the number of people moving within the city is greater than in case #1. The

increase in movement within the city is prompted by the lower level livability which occurred in case #2 because the population density is much greater. The percentage of land occupied by housing units in the different suburbs increases significantly for case #2 since the area occupied by the suburbs is smaller than is case study #1.

Case #3 is organized to demonstrate the effect of the race factor in the boundary stress equation (Equation 38 of the main text) upon the evolution of the model. Specifically, in this case, the race parameters "C" ("C" refers to the race parameter used in Equation 38 of the main text) is increased from 40 to 90 (see Table 33). Increasing the race parameter causes the boundary stress between two suburbs to be increased when the percentage of non-white population in one of the suburbs is significantly different from the percentage in the other suburb. Figure 64 shows the contoured population and boundaries for the end of the 16-year period in case study #3. A comparison of boundaries for case #1 with the boundaries for case #3 shows that the most significant difference between them is that the area closed within the boundary of suburb #1 is considerably larger for case study #3. The area enclosed within boundary of suburb #1 increased 95% in case #3 while the area only increased 74% for case study #1. The increase in area for suburb #2 is lower for case #3, while suburbs #3 and #4 are not influenced by the change in the race parameter. These results could be expected since the increase in the race parameter in the boundary stress equation caused the boundary stress along the boundary of suburb #1 to increase because of the large non-white population in this suburb. The increase in the boundary stress around this suburb causes it to expand more rapidly

(a)

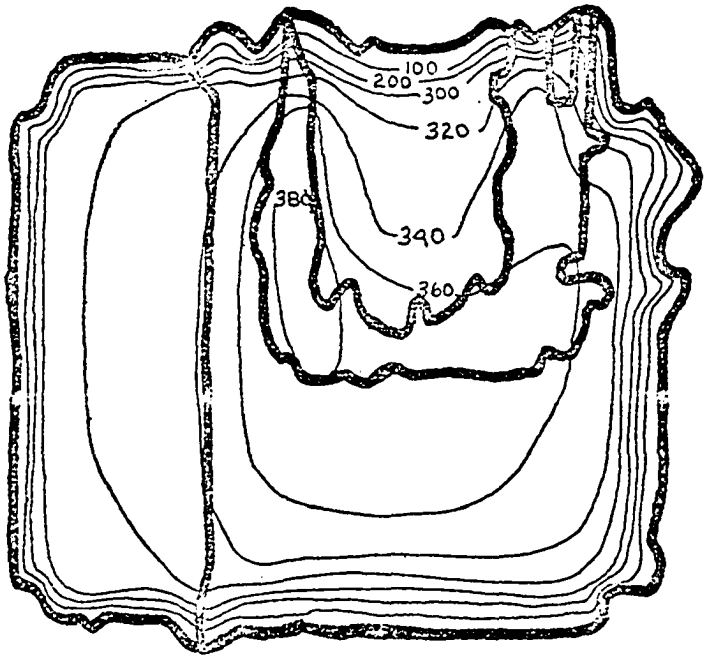

CONTOURED POPULATION
(number of people per small city block)

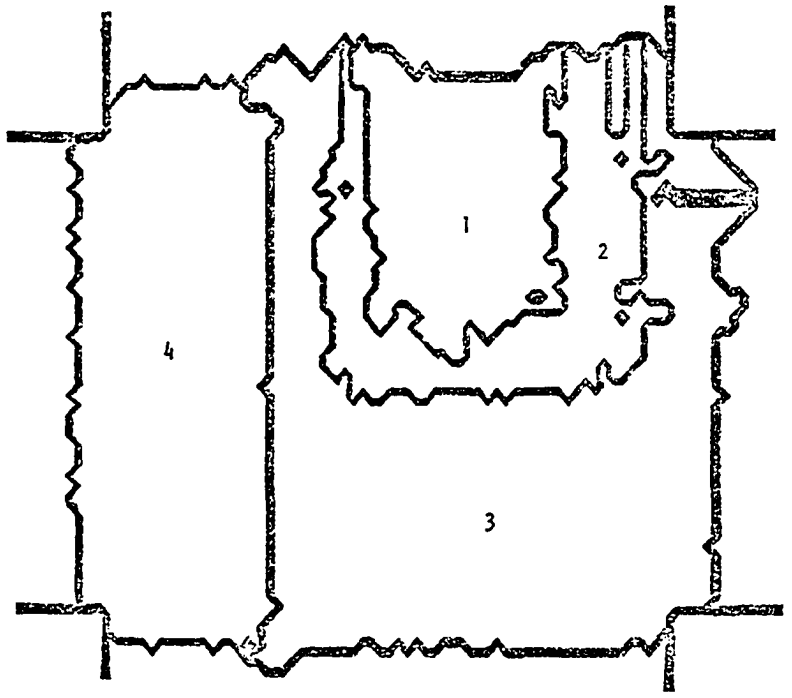

BOUNDARY FIELD

Fig. 64. The contoured population field (a) and city and suburb boundary field (b) for the last time step in case #3 are presented.

because the critical boundary stress required for its movement is exceeded more often. The significant difference between the contoured population fields for case #1 and case #3 is that the population density in suburb #1 is significantly lower for the latter. In fact, the population density for suburb #1 is lower than for suburbs #2 and #3, while in case #1 the population density is greater in suburb #1. The decrease in population density of the suburb #1 is primarily attributed to the increase in the area of the suburb.

Modifying the race parameter does not significantly affect the frequency distributions for the attributes of the people in the different suburbs. The most noticeable effect is that there is a slight decrease in the percentage of non-white population in suburb #2. This decrease is caused by a decrease in the number of people moving from suburb #1 to suburb #2. The movement between suburbs is decreased because the population density in suburb #2 is greater than the population in suburb #1.

Population Dynamics

The influence of population dynamics upon the evolution of the model is demonstrated by case studies #4, #5 and #6. Case #4 demonstrates the influence of an air pollution field upon the movement of people in the city. Case #5 shows the effect of setting the population density parameters "L1" and "P3" (see Table 33) equal to zero, while case #6 illustrates the effect of decreasing the percentage of people who are allowed to move in the discontinuous model (see Table 33).

Urban case study #4 is set up to demonstrate a possible effect of an air pollution field upon the evolution of a city. The model assumes

that high air pollution level creates poor livability conditions and that as a consequence, people try to move away from high concentrations of air pollution. The air pollution field used in this simulation is presented in Figure 65 and shows that the highest pollution level is in the center of the urban area. The rectangular box in the figure represents the initial location of the boundary between the urban and rural area. Figure 66 presents the contoured population field and city and suburb boundary field for the last time step in case study #4. A comparison of the city and suburb boundary field for case study #1 and #4 shows (see Figures 57 and 66) only very small differences. A more detailed analysis indicates that suburbs #1, #2 and #4 expanded more rapidly in case #4 than in the control case. The increase in the area of the suburbs is caused by an increase in the stress along the outer city boundaries. The outer city boundary stress is greater because of people moving away from the highly polluted areas in the center of the urban area. The areas of low population density correspond very well with the maximum concentration of air pollution (see Figures 65 and 66). Another important feature of the population field is that the regions of high population density surround the heavily polluted air in the center of the city. In this experiment, it is clear that the air pollution field is the most influential parameter in determining the population density distribution across the city. The addition of this pollution field did not appreciably modify the evolution of the education, housing or occupation frequency distributions for the different suburbs; however, it did modify the income and the race frequency distributions. A comparison of the race distribution for case studies #4 and #1 show

AIR POLLUTION CONTOURED EVERY 30 g/m^3

Fig. 65. This figure presents the contoured average annual SO_2 air pollution field determined by using the atmospheric model to drive the air pollution submodel for a two-year simulation. The location of the air pollution sources and the air pollution emission rates simulate the air pollution in Houston, Texas.

(a)

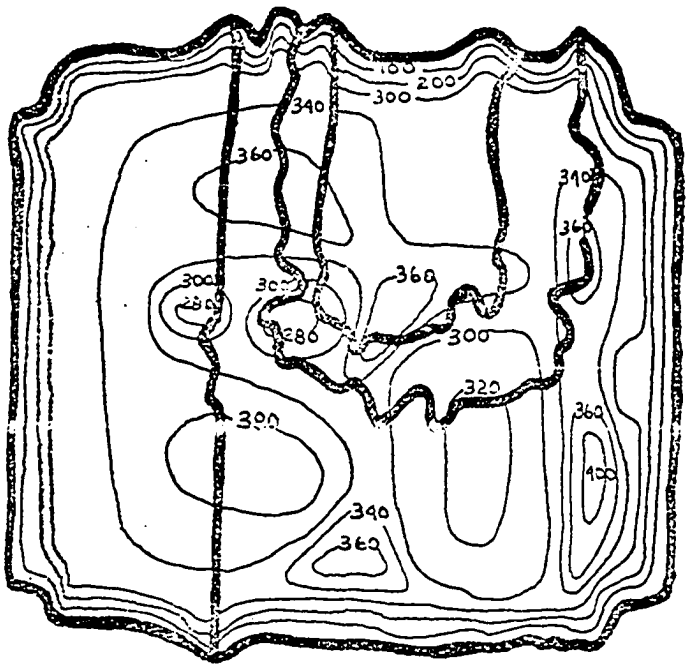

CONTOURED POPULATION
(number of people per small city block)

(b)

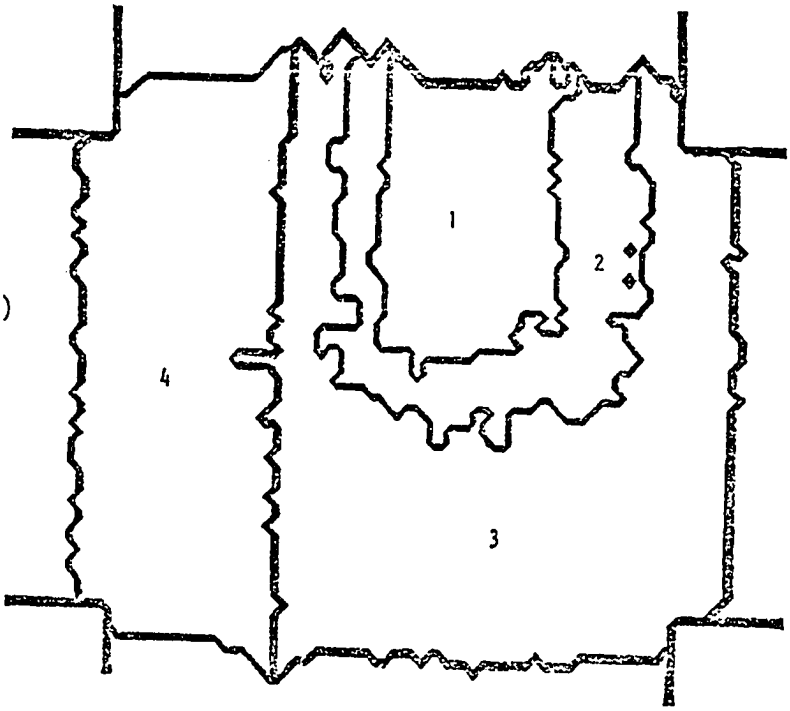

BOUNDARY FIELD

Fig. 66. The contoured population field (a) and the city and suburb boundary field (b) for the last time step in case study #4 are illustrated.

that the percentage of non-white population in suburb #1 decreases more rapidly in case #4 while the non-white population in suburbs #2, #3 and #4 increased more rapidly in case #4. The change in the race distribution suburbs #2, #3 and #4 are caused by the increase in the immigration rate of people from suburb #1 to these suburbs. The high air pollution levels observed in suburb #1 lowered the already poor livability conditions in this suburb and thus increased the percentage or people in the suburb that are allowed to move out by discontinuous and diffusion movement. The diffusion movement of people from this suburb is increased by the fact that the air pollution field decreases going from the eastern part of the suburb to the western part (compare Figures 65 and 66) and thus causes livability gradient in which the people are moving away from the suburb #1 into the western part of suburb #2 which is predominately white. The decrease in the air pollution concentration from the center of the city to the outer boundaries of the city sets up a livability gradient such that livability improves going away from the center of the city and thus causes the people to move by diffusion in all directions away from the center of the city. The northward movement of white people from the center of the city is responsible for the increase in the white population in suburb #1 which is predominately non-white and is located in the northern part of the city. A comparison of the income distribution for case studies #1 and #4 show that for case #4 the relative frequency of the average annual family incomes greater than $10,000 increased more rapidly for suburbs #2 and #4 because these two suburbs have the best livability conditions and thereby attract the high income families whose influx is

the result of both continuous and discontinuous movement. The best livability conditions are found in suburbs #2 and #4 because of the location in reference to the air pollution field. Suburb #4 is in the western part of the city where the air pollution concentration is low, while suburb #2 is located to the North of the center of the maximum air pollution. Suburb #3 has poor livability conditions because the center of maximum air pollution is located in this suburb.

For case study #5 the population term and the air pollution term in the livability equation and the livability gradient equation are set equal to zero. This leaves the race factor and housing factor as the only terms that influence the gradient of livability of the city. This gradient is critical to the population dynamics of the model since it directs the diffusion of people to better livability conditions. The race and housing factor in the livability equation will cause people to move toward an area that has the lowest percentage of underemployed housing, the lowest percentage of non-white population. The contoured population field and city and suburb boundary field for the last time step in case #5 is illustrated in Figure 67. A comparison of boundary field for case #1 and case #5 shows very little difference. It also shows that the increase in area for the four different suburbs is almost identical for these two case studies. A significant feature of the population field for case #5 is that just outside the boundary between suburbs #1 and #2 there is a distinct minimum in population density. This is caused by the diffusing movement of people in suburb #2 away from the poor livability conditions in suburb #1. The large non-white population in suburb #1 is responsible for the poor livability conditions

(a)

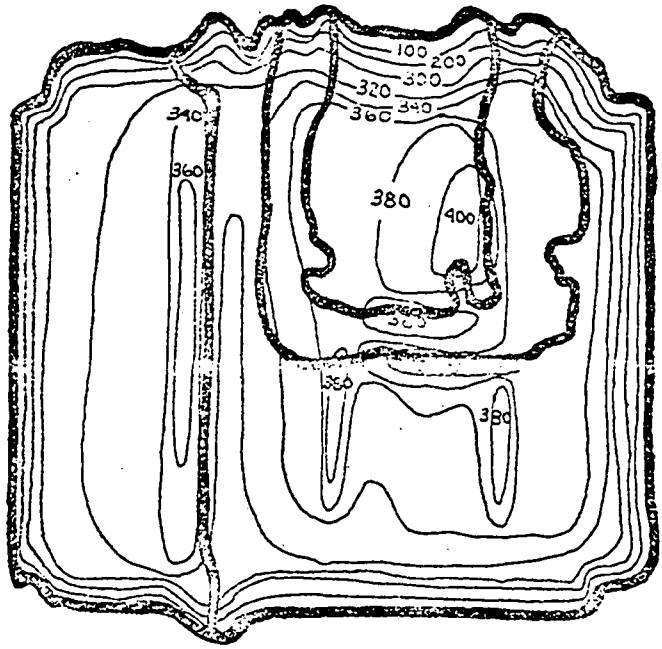

CONTOURED POPULATION
(number of people per small city block)

(b)

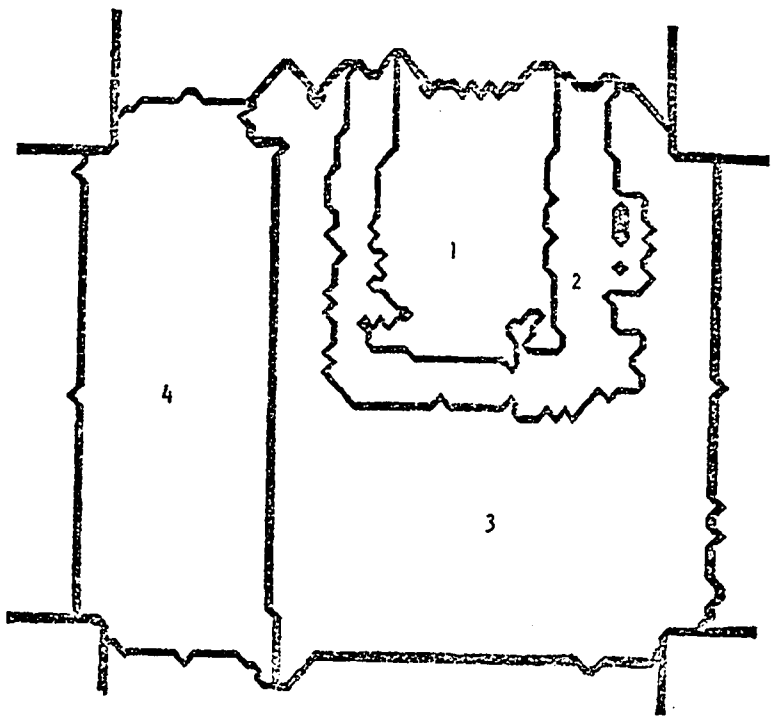

BOUNDARY FIELD

Fig. 67. The contoured population field (a) and the city and suburb boundary field (b) for the last time step in case study #5 are shown.

in this suburb. The loss of people in suburb #3 and the gain of people in suburb #4 is caused by the movement of people to find better livability conditions. In suburb #4, immediately along its border with suburb #3, the livability condition improves because suburb #4 has a lower percentage of underemployed housing. The race factor is not significant along this boundary since neither suburb #3 or #4 has a large non-white population. The population field shows that the most significant changes in the population density feature occurs just along the boundary between the different suburbs. This would be expected since the livability gradient which directs the diffusive movements of people in the City is only influenced by parameters that are characteristic of a whole suburb and thus only change across the boundaries between suburbs. In the previous case studies, the population density air pollution fields are the predominant factors that influence the diffusive movement of people in the city. A comparison of the characteristic frequency distributions for the different suburbs in case #1 and #5 shows only small differences.

Case study #6 is set up to demonstrate the effect of limiting the number of people moving within the city by discontinuous technique. Specifically, for this case the percentage of people allowed to move by discontinuous movement of people within the city is limited to movement by diffusion. The contoured population field and boundary field for the last time step in case study #6 is presented in Figure 68. In case #6, the area within all of the suburbs did not expand as rapidly as it did in case #1. A comparison of the population fields for case #1 and #6 shows that in case #6, the average population density in suburbs

(a)

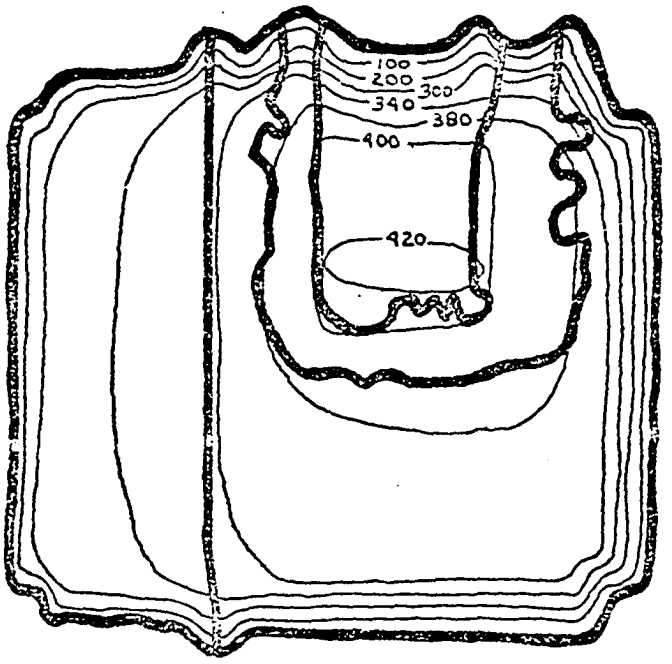

CONTOURED POPULATION
(number of people per small city block)

(b)

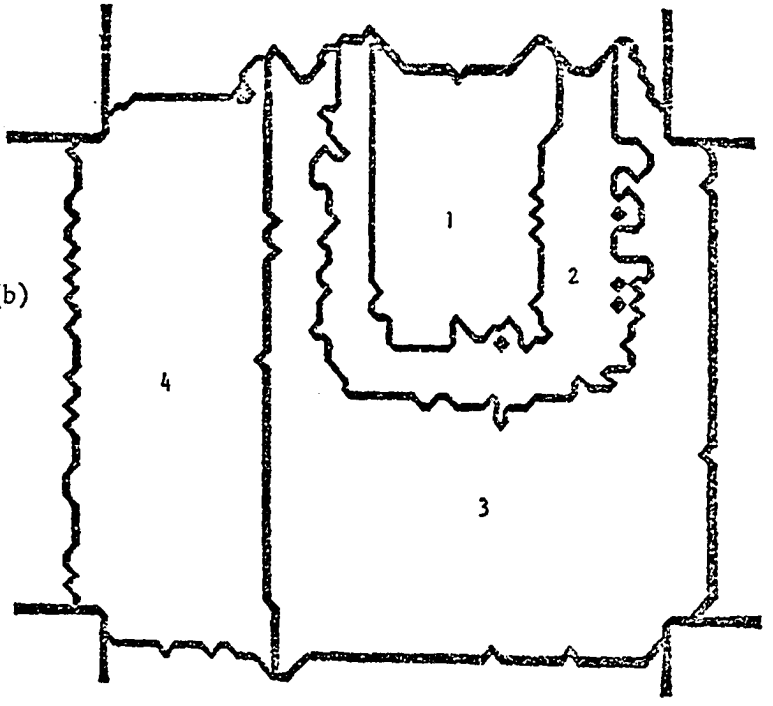

BOUNDARY FIELD

Fig. 68. The contoured population field (a) and the city and suburb boundary field (b) for the last time step in case study #6 are illustrated.

#3 and #4 are slightly lower, while the population density in suburbs #1 and #2 is significantly higher. It is also observed that in case study #6, the total population for suburbs #3 and #4 decreases while the total population in suburbs #1 and #2 increases significantly. The change observed in the local population density and total population of the suburbs are caused because the number of people allowed to move by discontinuous movement is decreased to a very small number of people. The primary effect of the discontinuous movement technique would be to take people from the poor livability suburbs which are suburbs #1 and #2 and place them in suburbs #3 and #4 which have better livability conditions. By drastically limiting the use of discontinuous technique, the primary mechanism for causing racial integration of suburb #3 and #4 is limited. This is demonstrated by comparing the racial frequency distribution for suburbs in case study #6 and #1. The comparison shows that in case #6, (Figure 69), the percentage of the non-white population in suburbs #3 and #4 increased very little compared to the increase observed in case study #1. The comparison for suburbs #1 and #2 shows that in case #6, there is a slight decrease in non-white population in suburb #1 and slight increase in the percentage of the non-white population in suburb #2. This means that the increase in the movement by diffusion between suburbs #1 and #2 caused an increase in rate at which suburb #1 and #2 are racially integrated. The net effect of suburb #1 and #2 to be more racially integrated while in suburbs #3 and #4 the racial integration is slowed down. A comparison of the other frequency distribution for case #1 and #6 shows that there is very little difference between them.

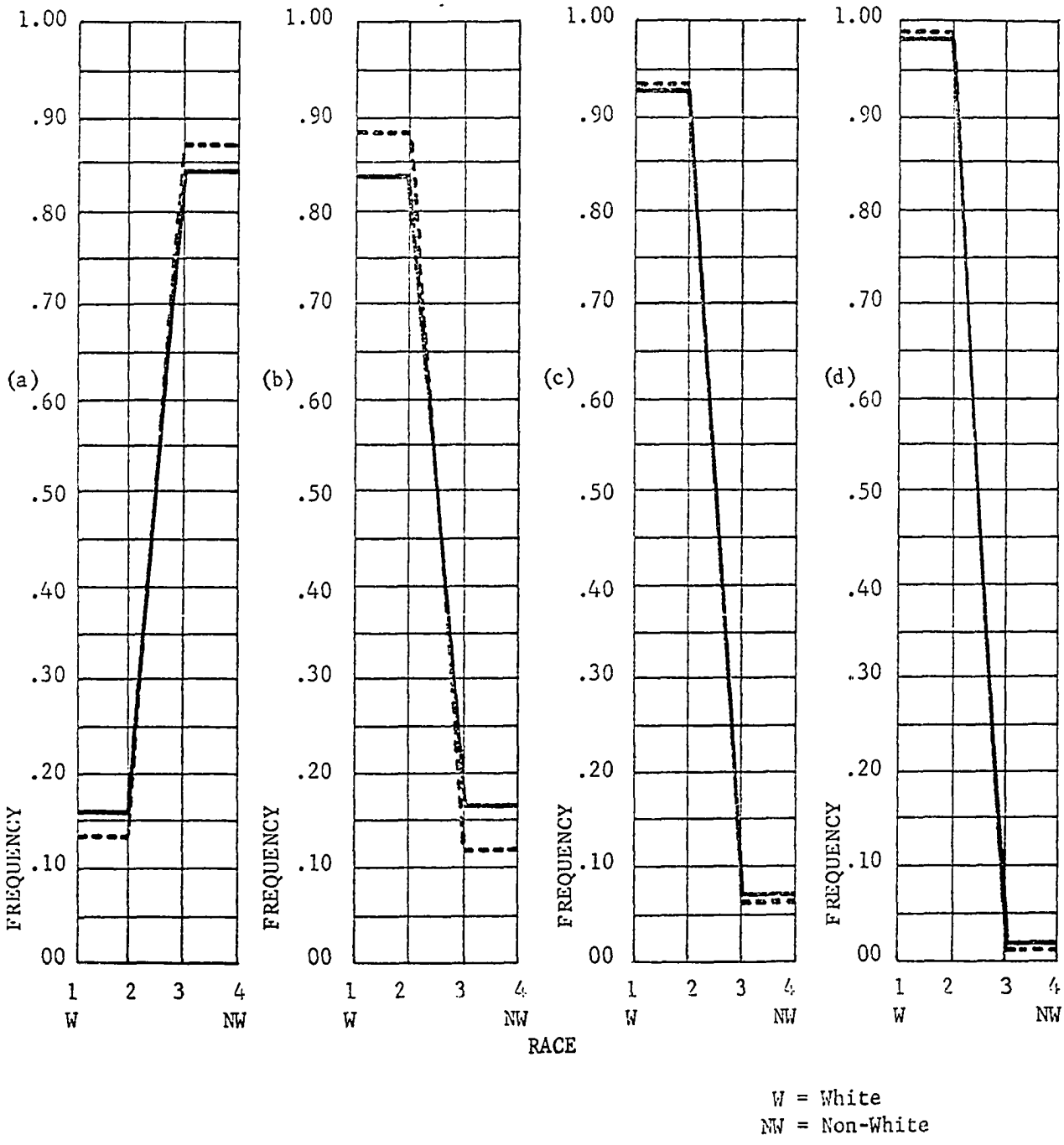

Fig. 69. The initial (dashed line) and final (solid line) race frequency distribution for suburbs #1 (a), suburb #2 (b), suburb #3 (c), and suburb #4 (d) are presented for case study #6.

Suburb Dynamics

Case studies #7 and #8 are organized to demonstrate the effect of the suburb dynamics subsection upon the evolution of the model. In case #7 the underemployed to worker transfer rate is increased from 4% to 10% for suburbs #1 and #2 and similarly the worker to professional transfer rate is increased from 3% to 7%. The transfer rates for the other suburbs are not changed. In case study #8, the transfer rate that influenced the housing distributions are modified so as to increase the new construction rate for quality housing, worker housing and underemployed housing.

Case #7 is run in order to demonstrate the effect of increasing the rate of transfer of lower class (underemployed people) in suburbs #1 and #2 into the upper class categories (worker and professional). A comparison of the boundary field and population field in case #1 and #7 show that there is very little difference between them. In comparing the results between the two cases, the significant differences are seen in the occupation, family income and education frequency distributions for suburbs #1 and #2 (Figures 70, 71 and 72). A comparison of the occupation frequency distribution for case #1 and #7 (Figure 59 and 70) shows that in case study #7, there is a much higher percentage of people in the higher level occupational categories. A similar comparison of the family income and education level frequency distributions (Figure 60, 61, 71 and 72) shows that in case study #7 there is a much higher percentage of people in the upper income categories and the more advanced educational levels than in case study #1. This result is expected since an increase in the transfer of people from the lower level occupation

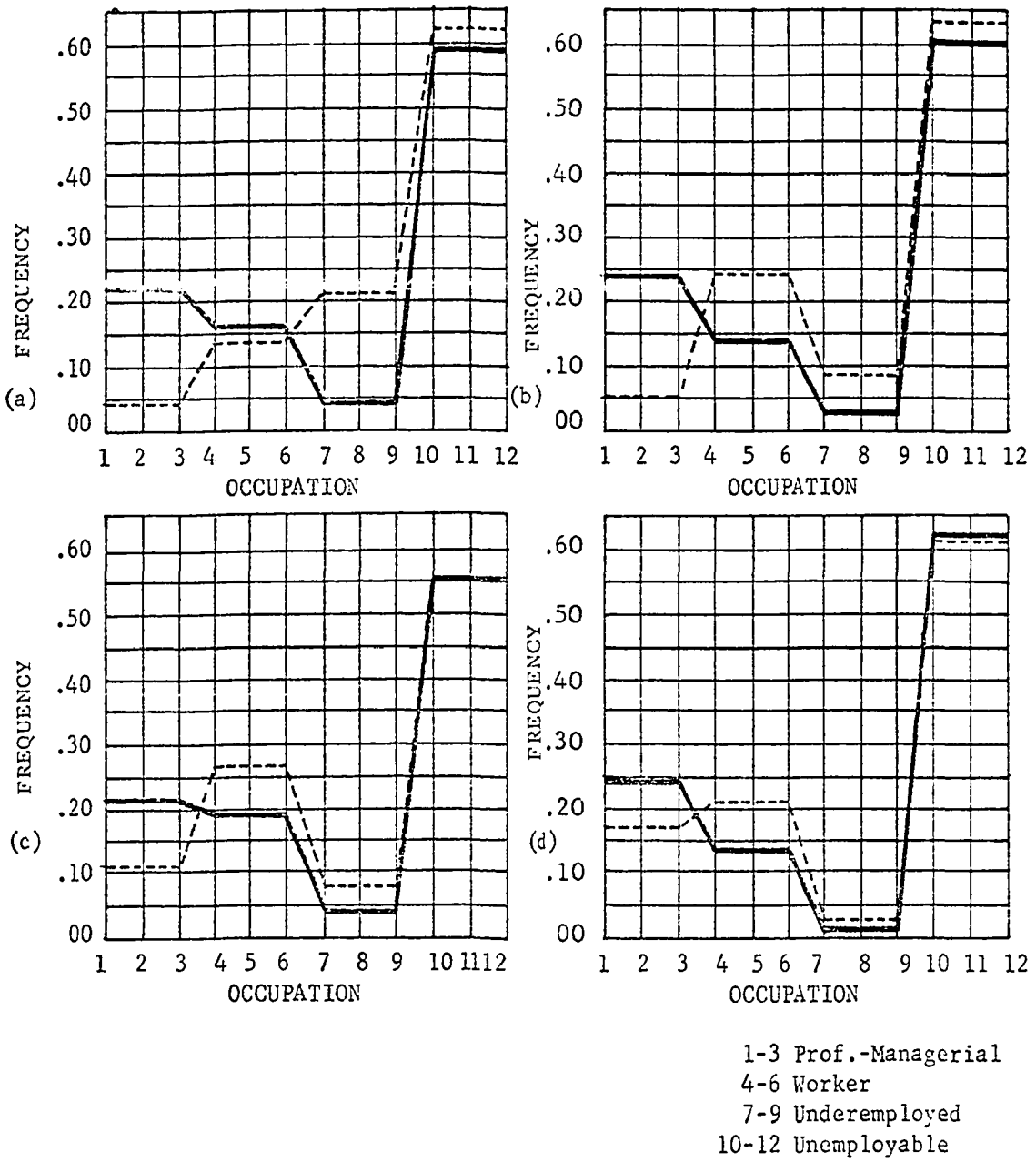

Fig. 70. The initial (dashed line) and final (solid line) occupation frequency distribution for suburb #1 (a), suburb #2 (b), suburb #3 (c), and suburb #4 (d) are presented for case study #7.

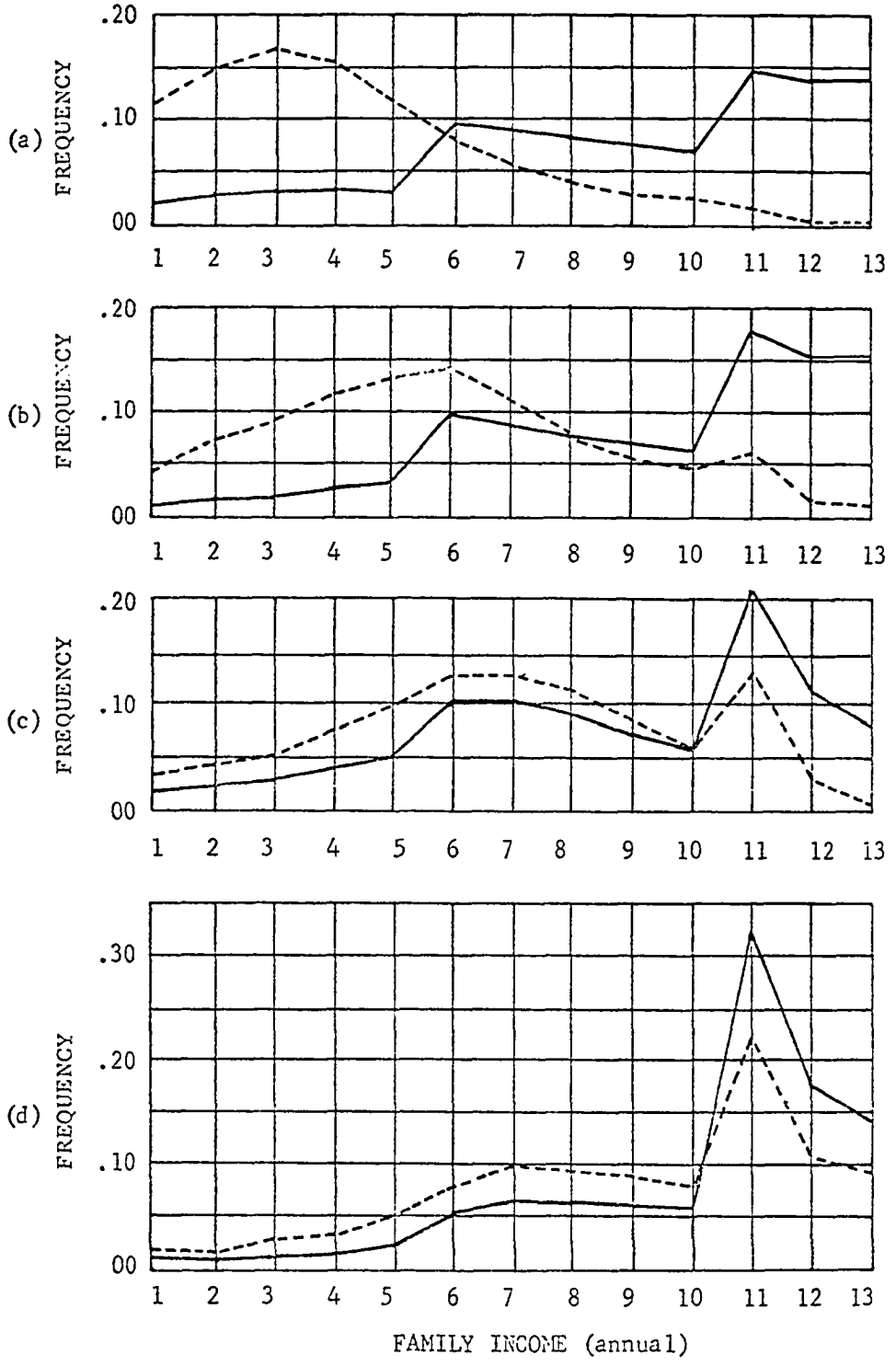

1	1000	6	5000-5999	11	10000-14999
2	1000-1999	7	6000-6999	12	15000-24999
3	2000-2999	8	7000-7999	13	25000
4	3000-3999	9	8000-8999		
5	4000-4999	10	9000-9999		

Fig. 71. The initial (dashed line) and final (solid line) family income frequency distribution for suburb #1 (a), suburb #2 (b), suburb #3 (c), and suburb #4 (d) are shown for case study #7.

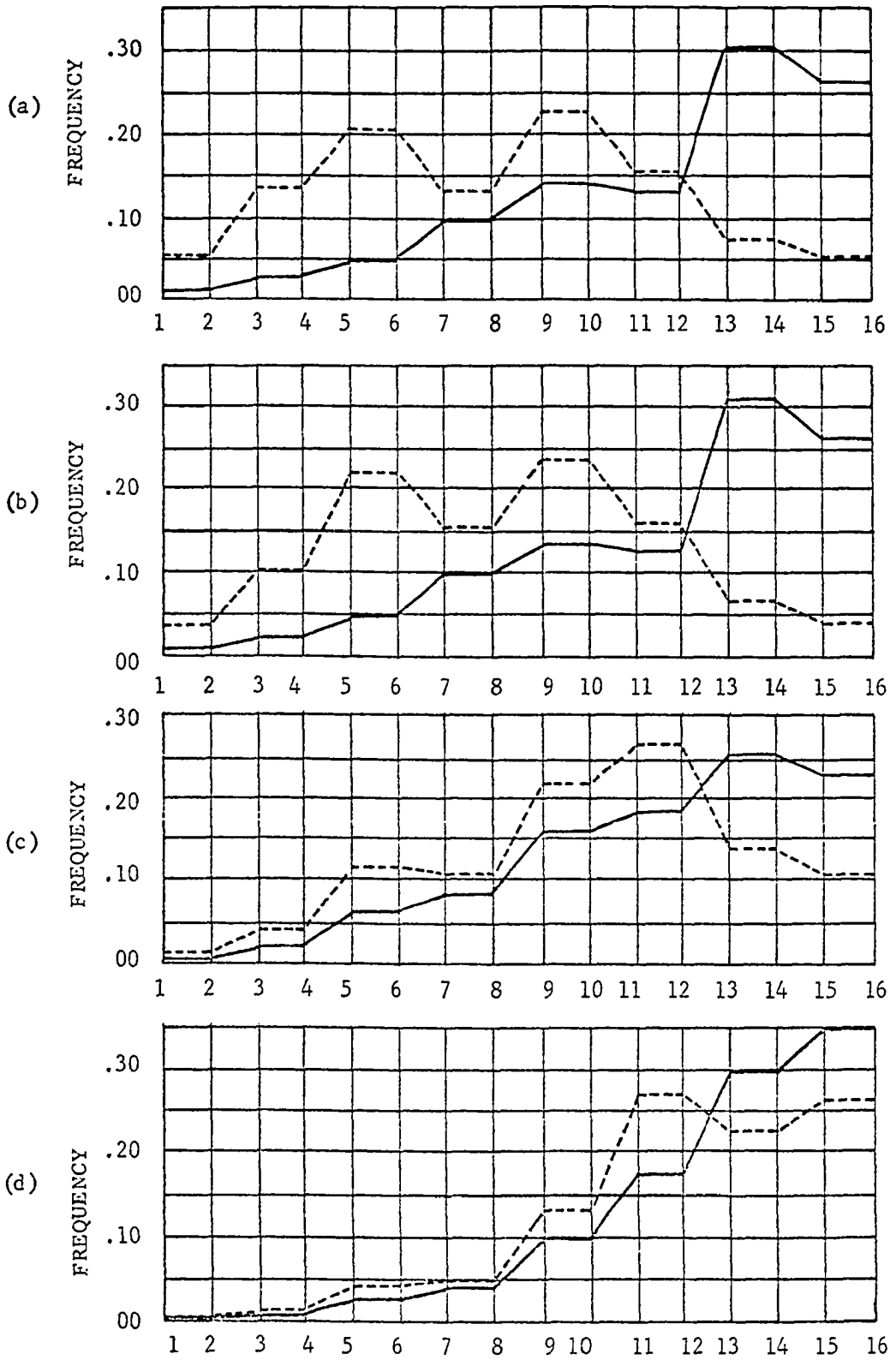

1-2	0 School	9-10	1-3 High School
3-4	1-4 Grade	11-12	4 High School
5-6	5-7 Grade	13-14	1-3 College
7-8	8 Grade	15-16	College

Fig. 72. Initial (dashed line) and final (solid line) education frequency distribution for suburb #1 (a), suburb #2 (b), suburb #3 (c), and suburb #4 (d) are presented for case study #7.

categories to the higher level categories is associated with an increase in their educational level and family income. A comparison of the occupational, family income and educational level frequency distribution in the different suburbs shows that at the end of the last time step in case study #7 the frequency distributions for all four suburbs are very similar. The net effect of running case study #7 is to produce a city in which the attributes of the people in the different suburbs are very similar, except for the racial segregation that exists in the city. It is interesting to note that increasing the educational level, occupational level and family income of the non-white minority in the city did not significantly increase the rate at which the city is racially integrated: clearly no mechanism is provided to bring this integration about as simple consequence of increased education level.

Case study #8 demonstrates the influence of increasing the construction rate of the different types of housing upon the evolution of the model. Specifically, the new construction rate for quality houses is increased for suburb #3 and #4, the worker housing construction rate is increased for suburbs #1, #2, #3 and #4, while the underemployed housing construction rate is increased for suburbs #1 and #2. A comparison of the housing frequency distributions for case study #1 and #8 (see Figures 73 and 63) show that for case #8 the relative frequency underemployed housing increases in suburbs #1 and #2, while in suburbs #3 and #4 the relative frequency of the worker housing increases. The most important influence of increasing the new construction rates for the different categories of housing units is to increase the total number of housing units in the city and thereby decrease the amount of

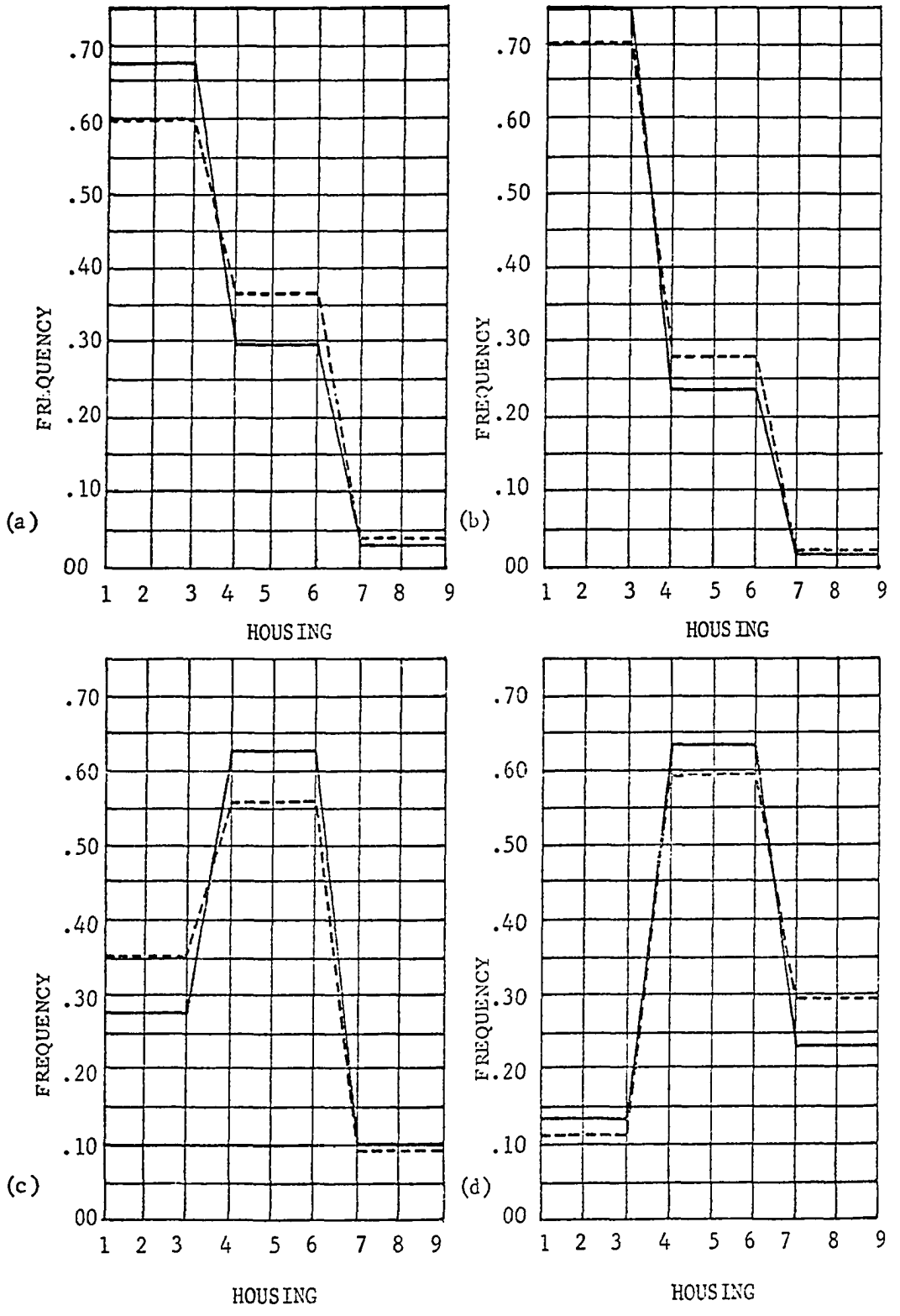

Fig. 73. The initial (dashed line) and final (solid line) housing frequency distribution for suburb #1 (a), suburb #2 (b), suburb #3 (c), and suburb #4 (d) are illustrated for case study #8.

open land area in the city.

Industry Model

The effect of the industry model upon the evolution of the urban model is demonstrated by running case studies #9 and #10. In case #9, the rate of growth of new industries is decreased from 10% to 5%, while in case #10, the rate of growth of new industries is increased from 10% to 15%. The effect of the different case studies upon the output parameters of the industry model are summarized in Table 34, which presents the output parameters at the end of the time simulation for case studies #1, #9 and #10. Comparing the results from case #9 with the results for case #1 show that decreasing the rate of growth of new industries causes a decrease in the number of industries in all of the categories with a particular decrease in the number of new industries. This decrease also causes a significant decrease in the number of jobs sustained by industry. The comparison of case #10 with case #1 shows that increasing the rate of growth of new industries produces a significant increase in the number of industries in all of the categories with a particularly large increase in the number of new industries. As would be expected, the total number of people employed by industry also increases. It is interesting to note that for case #1, #9 and #10 there are approximately 600,000 people available for working the different industries. A comparison of the number of people needed by industry and the number of people available shows that in case #1 there are twice as many jobs as there are people to fill these jobs, while in case #10, there is almost three times as many jobs as there are people available for work. Case #9 is the only one in which the number of jobs

TABLE 34

This Table Presents The Industry Model Output Parameters

At The End Of 16-Year Simulation For Case Studies #1, #9, and #10

	Number of New Industries	Number of Mature Industries	Number of Declining Industries	Number of Prof.-Managerial Jobs	Number of Worker Jobs	Number of Underemployed Jobs	Total Number of Jobs
Case #1 (Control Case)	20,591	20,389	12,965	177,093	562,347	338,933	1,078,373
Case #9	9,213	14,848	11,701	102,317	350,178	209,609	662,104
Case #10	44,282	29,521	14,760	324,738	974,214	590,432	1,899,384

available and the number of people looking for work are comparable. This indicates a 5% growth rate for new industries is sufficient to provide enough jobs for the people in the city, while growth rates greater than 5% create an excess of the number of jobs which only could be filled by importing people into the city. In case #9, a comparison of the number of jobs in the particular job categories with the number of people in the city who are trained for that job category shows there are twice as many people looking for professional managerial jobs than are jobs available, while there are three times as many underemployed jobs available in comparison to the number of people looking for underemployed jobs. The discrepency between the number of people looking for jobs and the number of jobs available in the underemployed professional managerial categories is caused by the fact that each year during the 16-year simulation, 4% of the people in the underemployed category are upgraded to the worker category and 3% of the people in the worker category are upgraded to the professional managerial categories. These results show that job training programs that improve the occupational level of the people in the city must proceed along with the changes in industry manpower needs.

APPENDIX D

APPENDIX D

RESULTS OF THE TESTING SCHEME PERFORMED ON THE BOTANY MODEL

The detailed results of the testing procedure performed on the botany model are given in this appendix. Validation of the model is performed by comparing simulated results with the 1970 grassland data for the IBP Osage site (Risser, 1971), while a sensitivity analysis demonstrates the response of the model to the driving abiotic variables. In particular, the sensitivity of the primary state variables (above ground live biomass (ABM), standing dead (SD), and litter(LIT)) to variations in soil moisture, air temperature, wind speed, and solar radiation is demonstrated by running a numerical experiment that shows how these parameters influence the primary state variables. The numerical experiment comprised several one year time simulations using different data sets for the driving variables. In addition to the sensitivity analysis and validation, the botany model is tested by running a ten-year simulation of the overall ecosystem model. A summary of the results from this simulation is presented, in order to demonstrate the feedback loops between the botany model and the rest of the ecosystem. The values assigned to the constant parameters in the botany model for this simulation are presented in Table 35. For this simulation the model assumed that vegetation height remained constant (1.5 ft.).

TABLE 35

CONSTANT VALUES USED FOR THE VARIOUS PARAMETERS IN THE BOTANY MODEL

Parameter	Constant Value	Parameter	Constant Value
CPH	.5	PTC2	.20
HAR	0.0	PMS1	.166
HS	0.0	PMS2	.10
HL	0.0	ABM1	.026
HM	0.0	ABM2	.024
HB	0.0	ZM1	7.1
NS	.8	ZM2	.90
LA	1.0	PRP10	.5
CR	1.0	PBT1	4×10^{-7}
PPH1	3.36×10^{-4}	PBT2	1×10^{-6}
PPH2	59	PBT4	1.0×10^{-7}
PRP	1.70×10^{-3}	PBT5	5×10^{-1}
PTC	44	PDA1	$.43 \times 10^{-6}$
PPH3	.125	PDA2	35.0
Z1	2.10	PDA3	42.0
Z2	1.12	PDA4	7.1
PPH4	6.94×10^{-8}	PDA5	.3
PPH5	.40	PRB	1.5×10^{-8}
PPH6	.50		

Validation Process

Figure 74 presents the observed and simulated time series for above ground biomass (ABM) and below ground biomass (BBM), while Figure 75 gives the observed and simulated time series for the litter (LIT) and standing dead (SD). A comparison of the observed and simulated time series of ABM, BBM, SD and LIT is satisfactory. The most apparent deviation between the observed and simulated time series of ABM is that at the end of the growing season the observed ABM decreases much more rapidly than the simulated ABM. The importance of this deviation is questionable since a comparison of the observed ABM and SD time series at the end of the growing season shows that the sharp decrease in ABM is not consistent with the slow increase in the SD biomass. It is generally observed that the ABM that dies is transferred into SD biomass. The simulated BBM curve predicts the observed maximum and minimum values of BBM; however, there appears to be a phase lag between the observed and simulated peak and minimum. The simulated litter time series does not show the two distinct peaks indicated by the observed data and also indicated a trend towards increasing litter in the fall, while the observed data indicates that litter decreases in the fall. The significance of these deviations is difficult to determine because of the experimental error in observing the data and the fact that some of the physical processes which influence the transfer of SD to LIT are not taken into account by this model. Heavy rainstorm and hailstones are two such physical processes that can have a significant influence upon transfer of SD to LIT.

A comparison of the observed and simulated time series is made on

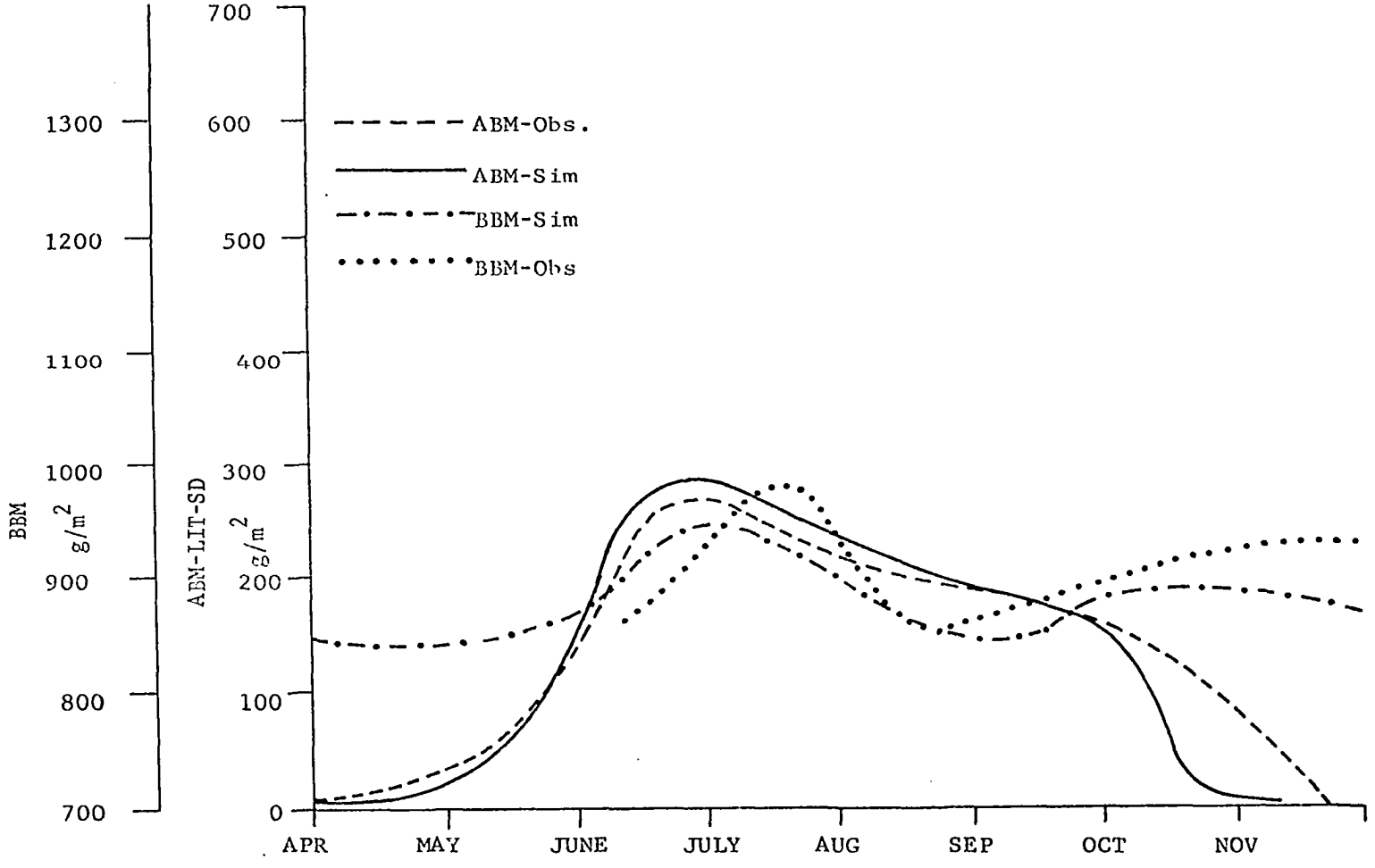

Fig. 74. Comparison of the simulated and observed time series for above-ground live biomass (ABM) and below-ground biomass (BBM).

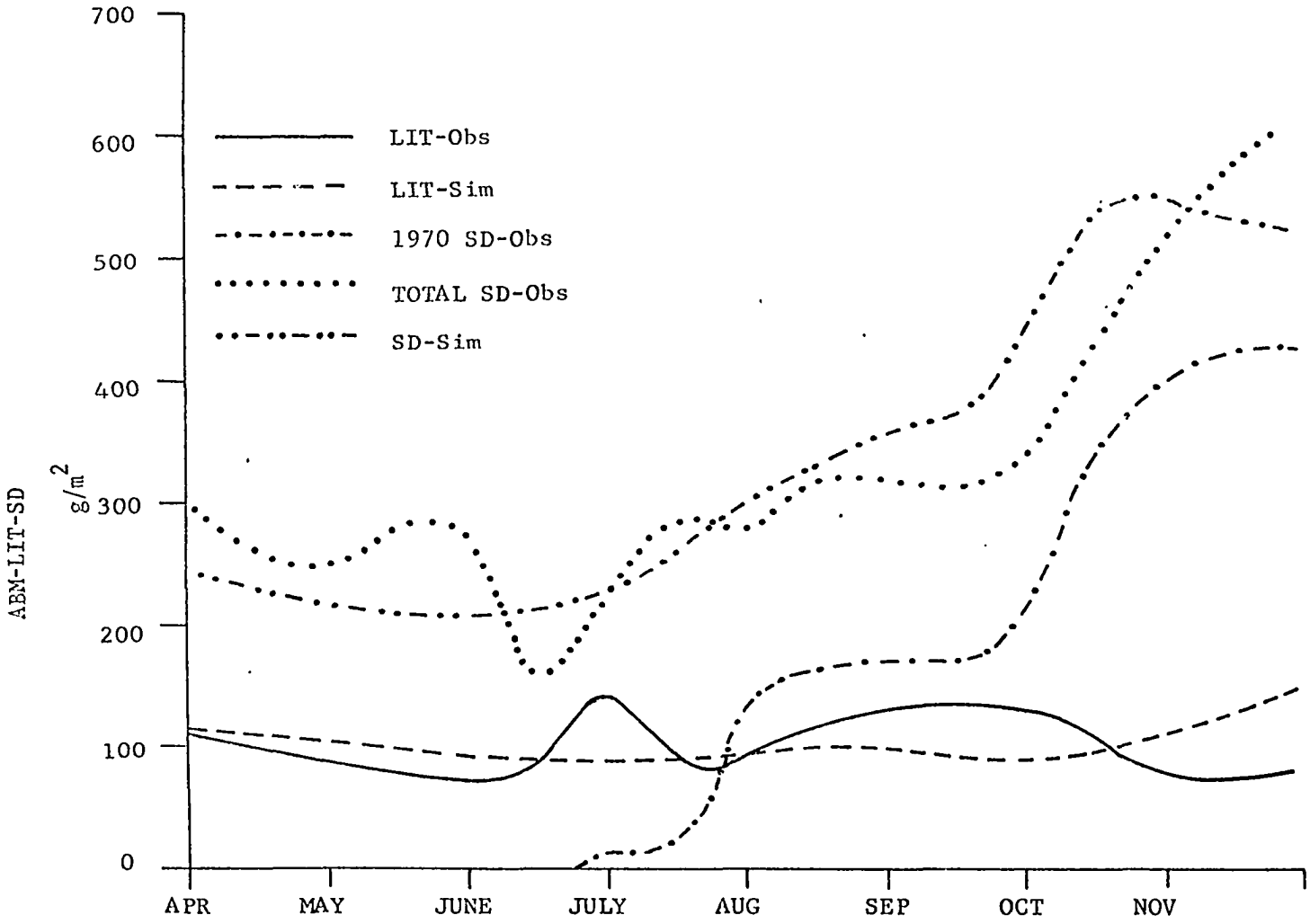

Fig. 75. Comparison of the simulated and observed time series for litter biomass (LIT) and standing dead biomass (SD).

trends indicated by the time series. A point to point comparison of the observed and simulated data is unrealistic when the experimental error in observing biological samples is considered (Francis, 1971; Cochran, 1963).

Sensitivity Analysis

A sensitivity analysis of the model is performed in order to validate the model subjectively. This type of analysis is considered necessary because only one year of observed data is available for the validation process. A numerical experiment is set up to test the ability of the model to respond to variation in four critical abiotic parameters (wind speed, solar radiation, precipitation, and soil moisture). The numerical experiment varies the observed time series for each of the abiotic parameters in an organized manner and observed the influence of these variations upon the simulated time series of the primary state variables. The simulated response of the primary state variables is compared to the expected response anticipated for a particular time series of abiotic parameters.

The sensitivity of the model to soil moisture is demonstrated by running five different case studies that used different soil moisture time series (see Figure 76). The influence of the different soil moisture time series upon the simulated time series of ABM, and SD are summarized in Figure 76 and 77. In general, the results show that increasing the soil moisture causes ABM to increase significantly. This is particularly true when the soil moisture is added in the spring and early summer. As would be expected decreasing soil moisture in the spring causes a large decrease in the peak value of ABM. The simulated results

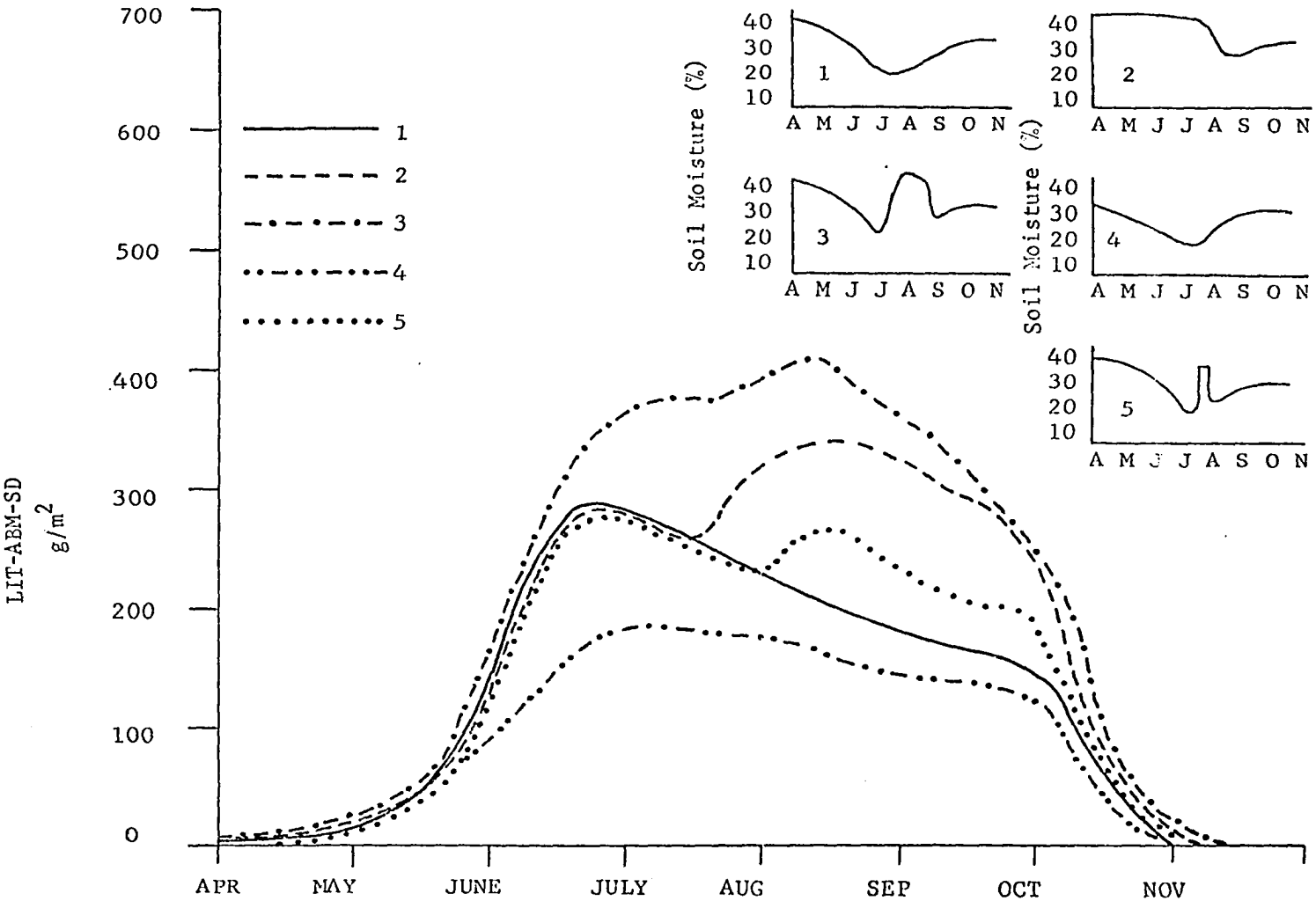

Fig. 76. Simulated time series for live above-ground biomass (ABM) for five soil moisture case studies: Case #1 observed moisture data; case #2 moist July and August; case #3 moist growing season; case #4 dry spring; case #5 moist August 1-15.

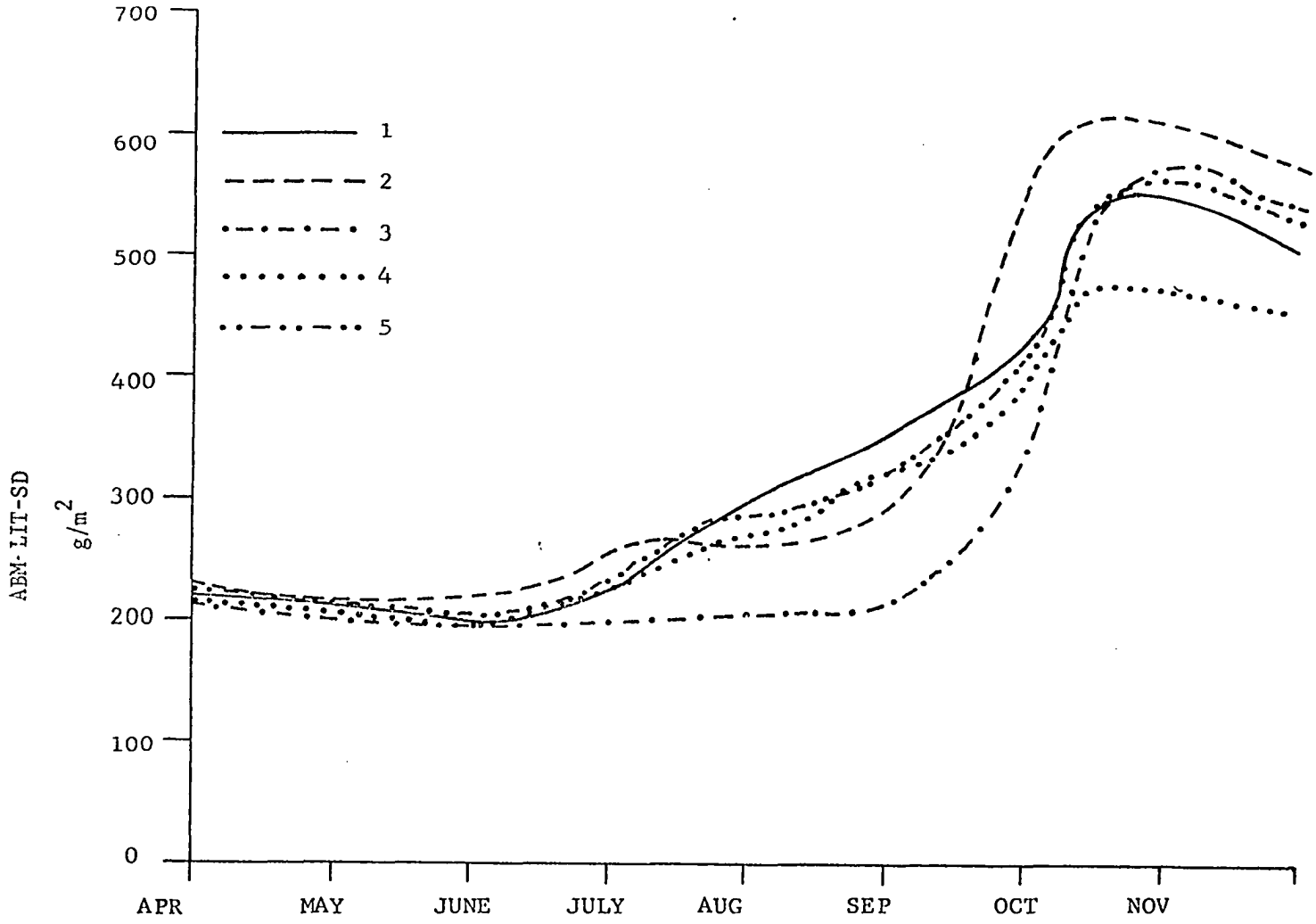

Fig. 77. Simulated time series of standing dead biomass (SD) for the five soil moisture case studies: case #1, observed moisture data; case #2, moist July and August; case #3, moist growing season; case #4, dry spring; case #5, moist August 1-15.

for the case studies compare favorably with the expected results anticipated for the different moisture time series. It is interesting to note that the ABM time series generated by case #3 (Moist yearly growing season) and case #4 (Dry spring growing season) form an envelope that contains the ABM time series for all other time series. An unanticipated result is the fact that case #2 (Moist July and August) generated the greatest amount of SD in comparison with the other case studies. This fact is surprising since case #3 (Moist yearly growing season) generated a significantly greater amount of ABM than case #2 (Moist July and August). The testing procedure demonstrated that the Botany model is extremely sensitive to variation in soil moisture content.

The influence of the surface air temperature upon the model is demonstrated by running three case studies that use different time series of maximum air temperature. Case #1 uses the observed values for the abiotic parameters, while Case #2 and Case #3 modify the maximum air temperature by adding and subtracting 5 F respectively to the observed values of the maximum air temperature. The simulated time series of ABM and SD are presented in Figure 78. The computer results show that increasing the temperature causes ABM to peak earlier in the year and decrease more rapidly in the summer, while decreasing the air temperature caused the peak in ABM to occur later in the year, with ABM decreasing more slowly in summer. These results agree with the expected results associated with increasing and decreasing the mean air temperature. It is interesting to note the phase lag of the maximum value of ABM for the three cases and the fact that the case with coldest mean air

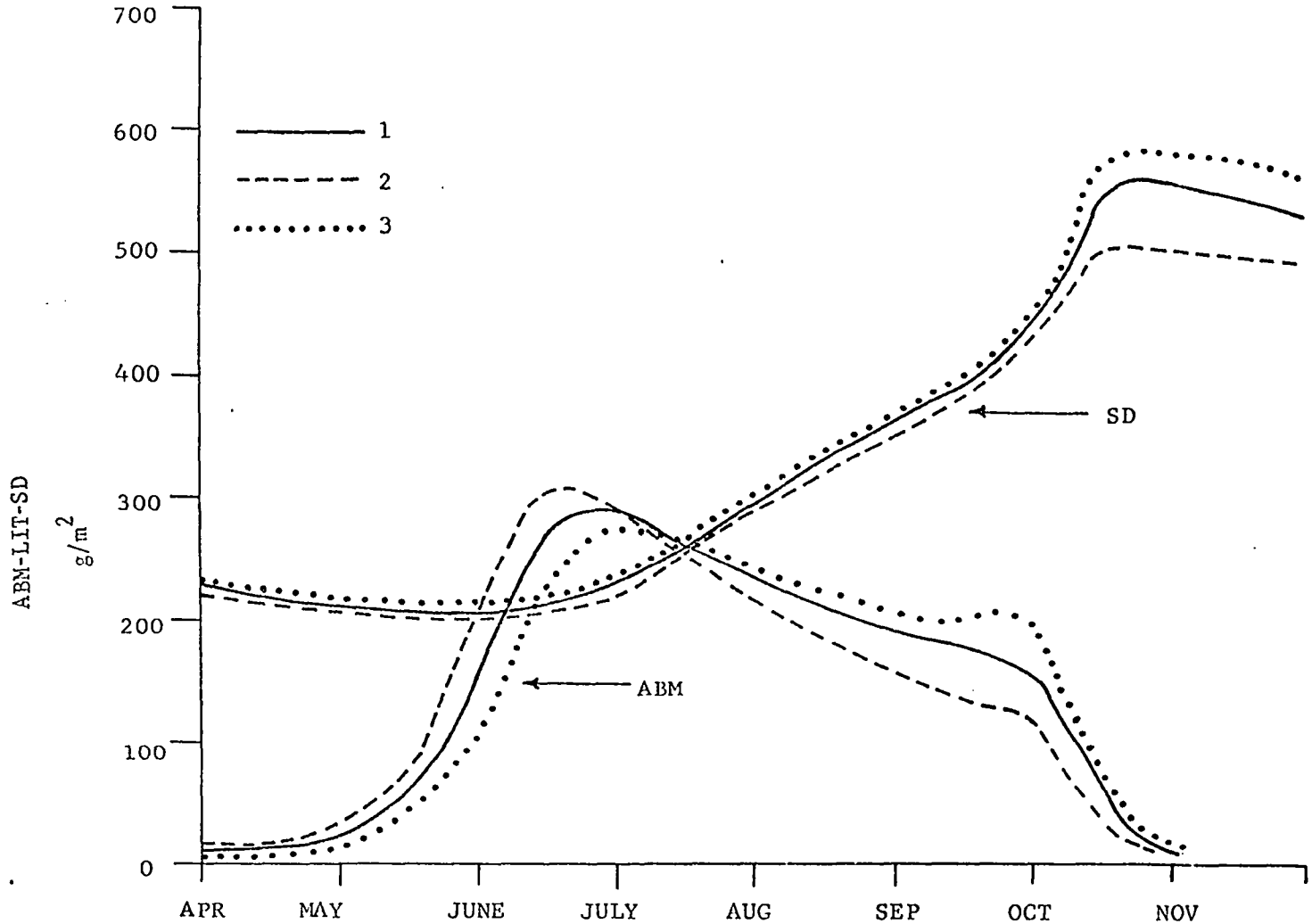

Fig. 78. Simulated time series of above-ground live biomass (ABM) and standing dead biomass (SD) for the three surface air temperature case studies: case #1, observed temperature data; case #2, warm air temperatures; case #3, cool air temperatures.

temperature (Case #3) produced the greatest amount of standing dead biomass at the end of the growing season.

The response of the model to different wind speed constants is demonstrated using three case studies. Case #1 will use the unaltered observed data for the abiotic parameters while Case #2 and Case #3 assign the average wind speed to be zero to 5 kts and 6 to 10 kts respectively for the complete growing season. The time series of primary ABM, SD and LIT for the different cases are presented in Figure 79. The simulated computer results agree with expected results associated with changes in the average wind speed. The most important observations from the results are the facts that, a) increasing wind speed causes the same effect on the ABM time series as decreasing the surface air temperature and, b) that increased wind speed will cause more standing dead to be transferred to litter.

The influence of different solar radiation conditions is demonstrated by running three case studies in which Case #1 used the observed data while Case #2 and Case #3 increase and decrease respectively the observed maximum solar radiation by 20%. The simulated time series of ABM and SD are illustrated in Figure 80 and show that decreasing solar radiation decreases the peak in ABM, while increasing solar radiation increases the peak in ABM. The simulated time series correspond fairly well with expected time series for the different cases. An interesting observation is that decreasing the maximum solar radiation by 20% causes a greater change in the peak values of the ABM curve than a 20% increase in the maximum solar radiation.

A preliminary time step sensitivity analysis for this model indicated

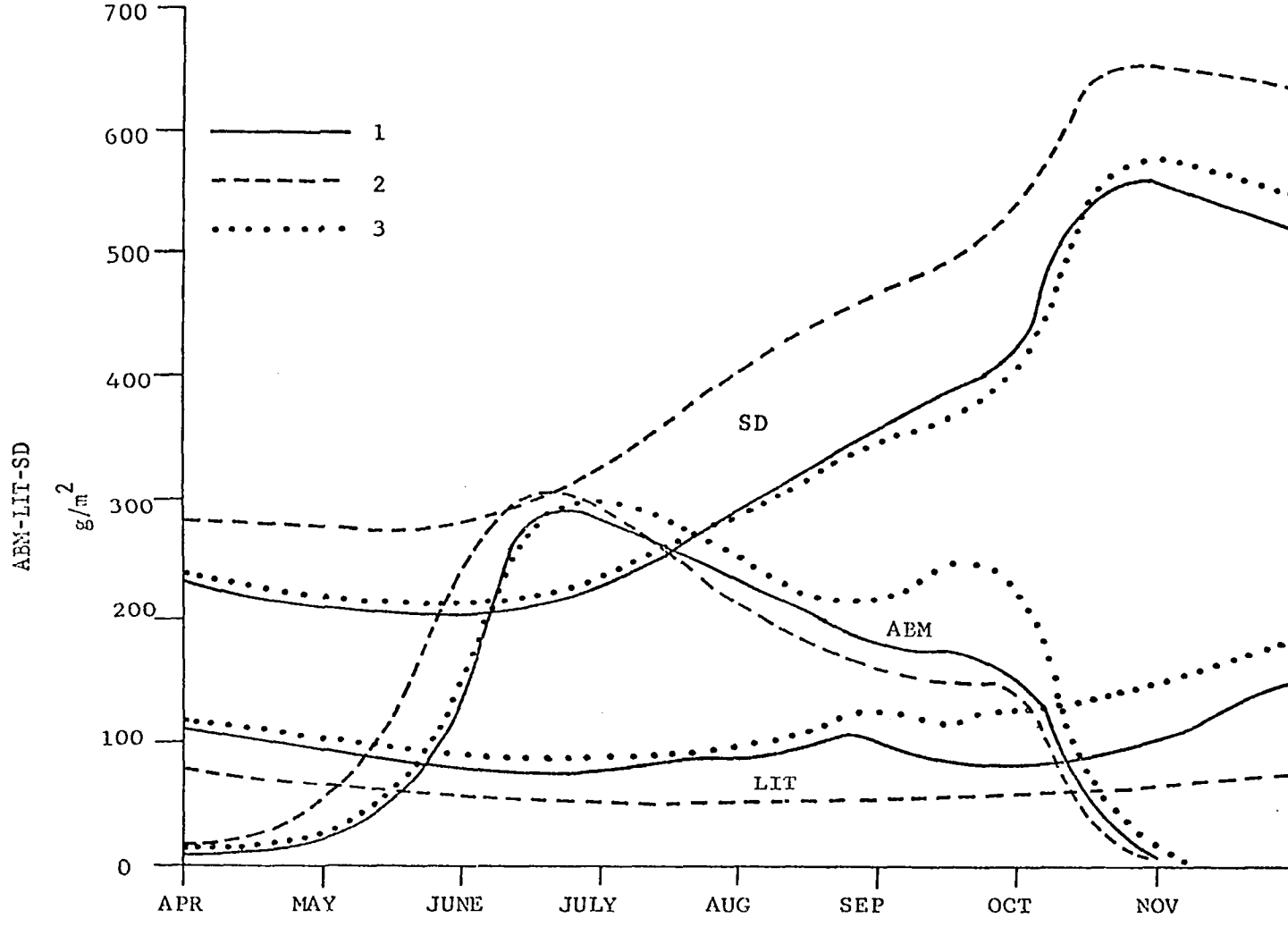

Fig. 79. Simulated time series of above-ground biomass (ABM), litter biomass (LIT), and standing dead biomass (SD) for the three wind speed case studies: case #1, observed wind data; case #2, lighter winds; case #3, stronger winds.

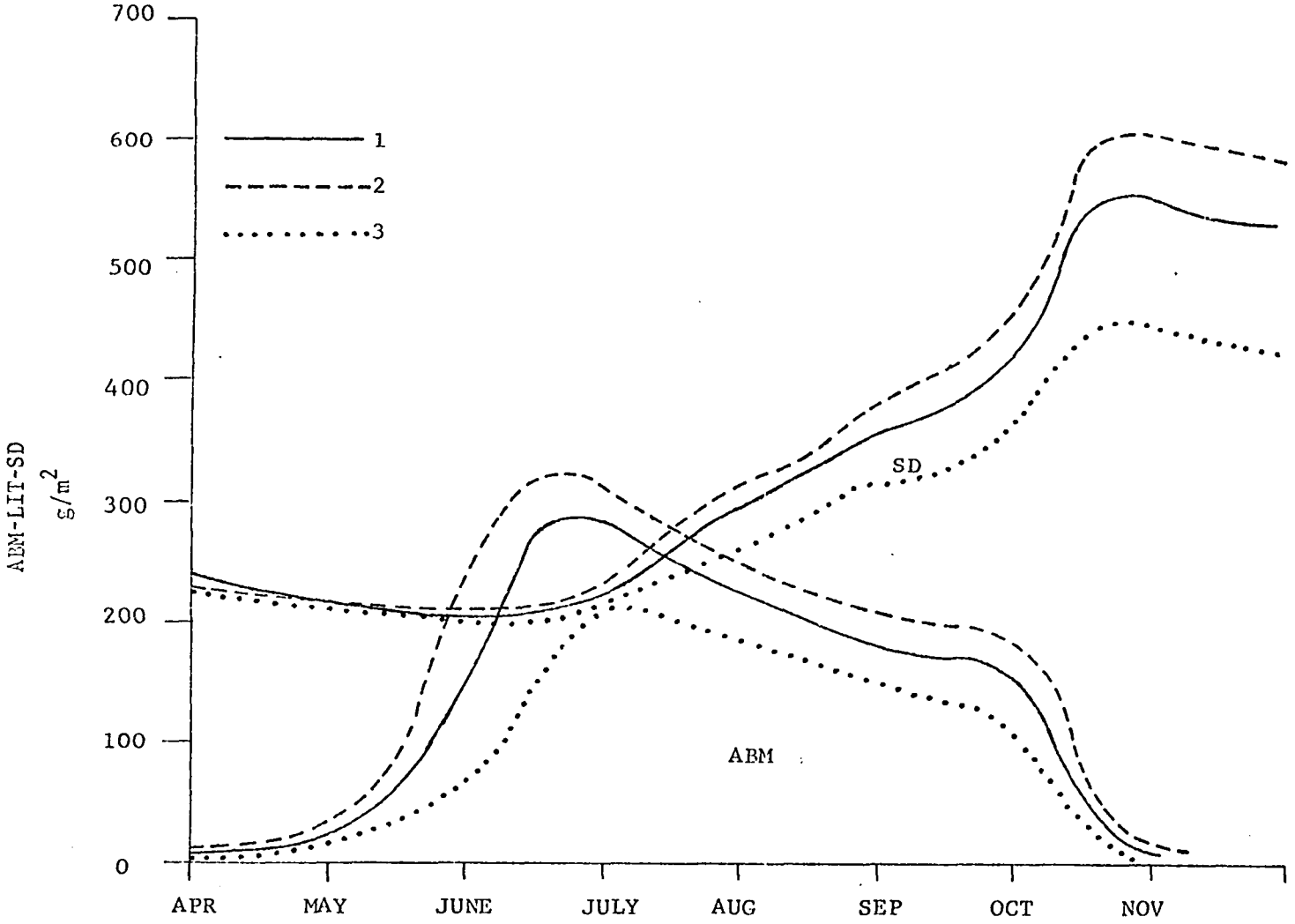

Fig. 80. Simulated time series of above-ground biomass (ABM) and standing dead (SD) for the three solar radiation case studies: case #1, observed solar radiation data; case #2, increased solar radiation (+20%); case #3, decreased solar radiation (-20%).

that one hour steps are optimal. The optimality criterion is based upon the numerical stability of the model and the amount of time required to run the model on the computer. The results also indicated that a more sophisticated finite difference scheme, such as the Runge-Kutta Method, should be used to increase numerical stability.

The results of the sensitivity analysis and validation procedure provide a preliminary validation of the model. A more convincing validation of the model would require a much longer time series of observed data and an extended sensitivity analysis. A more thorough sensitivity analysis should include numerical experiments in which more than one of the parameters is varied simultaneously in the experiment and a sensitivity analysis in which varying an abiotic parameter influences both the primary state variables and the other abiotic variables.

Simulation Results

A ten-year simulation of the botany model in conjunction with the whole ecosystem model is run in order to show the interacting feedback loops between them. These feedback loops are demonstrated by simulating the above ground live biomass, (ABM), standing dead, (SD), litter and below ground live biomass, (BBM) for four separate grass fields that are subject to different management practices. Field #1 is irrigated and not grazed by cattle, field #2 is not irrigated and not grazed, while field #3 and #4 are not irrigated and alternately grazed during the spring and summer. The decision to graze either field #3 or field #4 is decided by the decision theory process in the executive management submodel. Fields #1 and #2 are harvested at the end of each growing

season (day 300), while the resulting forage is used to feed the cattle in the feed lot. The detailed day-to-day variations of the state variable (ABM, LIT, BBM, and SD) and the average soil moisture for the four fields are presented for the first two years of the ten-year simulation. These detailed graphs demonstrate the effect of different management practices and growing condition upon the state variables for each of the fields. The long-term effect of the management decision and growing conditions upon the different fields is demonstrated by presenting the average monthly values for the state variables in the four fields.

Figure 81 and 82 present the two-year time series of the above ground live biomass, standing dead and litter for the four different fields. ABM in field #1 increases very rapidly in the spring, reaches a peak values in early September and then decreases very rapidly in the fall. The spring increase in ABM is caused by good growing conditions in the spring, while the leveling off of the ABM in mid summer is caused by the biological limitation upon the peak value for ABM. The growth of grass in field #1 is never limited by soil moisture because of irrigations and thus is permitted to grow to its peak value. The fall decrease in ABM is caused because of the aging process where ABM is transferred to standing dead (SD) (simessence). The standing dead for field #1 curve shows that SD decreases from the start of the simulation until the beginning of September, when it increases dramatically for a month and then decreases discontinuously to 25 gm/m^2. The decreased SD through August is caused by the loss of standard dead material into the litter category, while the dramatic increase in the SD in September

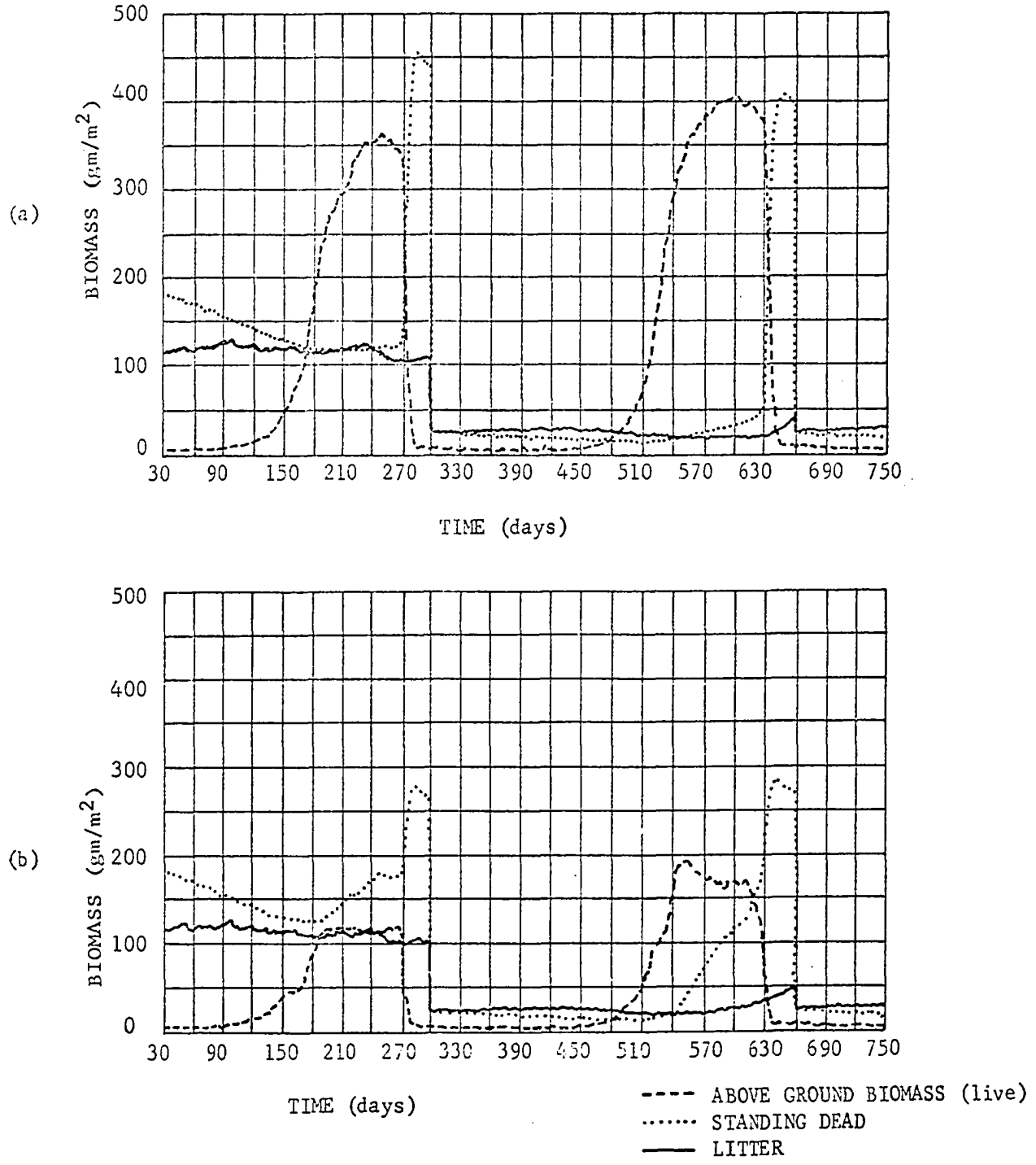

Fig. 81. A two-year simulation of live above-ground biomass, standing dead biomass, and litter for field #1 (a) and field #2 (b) is presented in this figure.

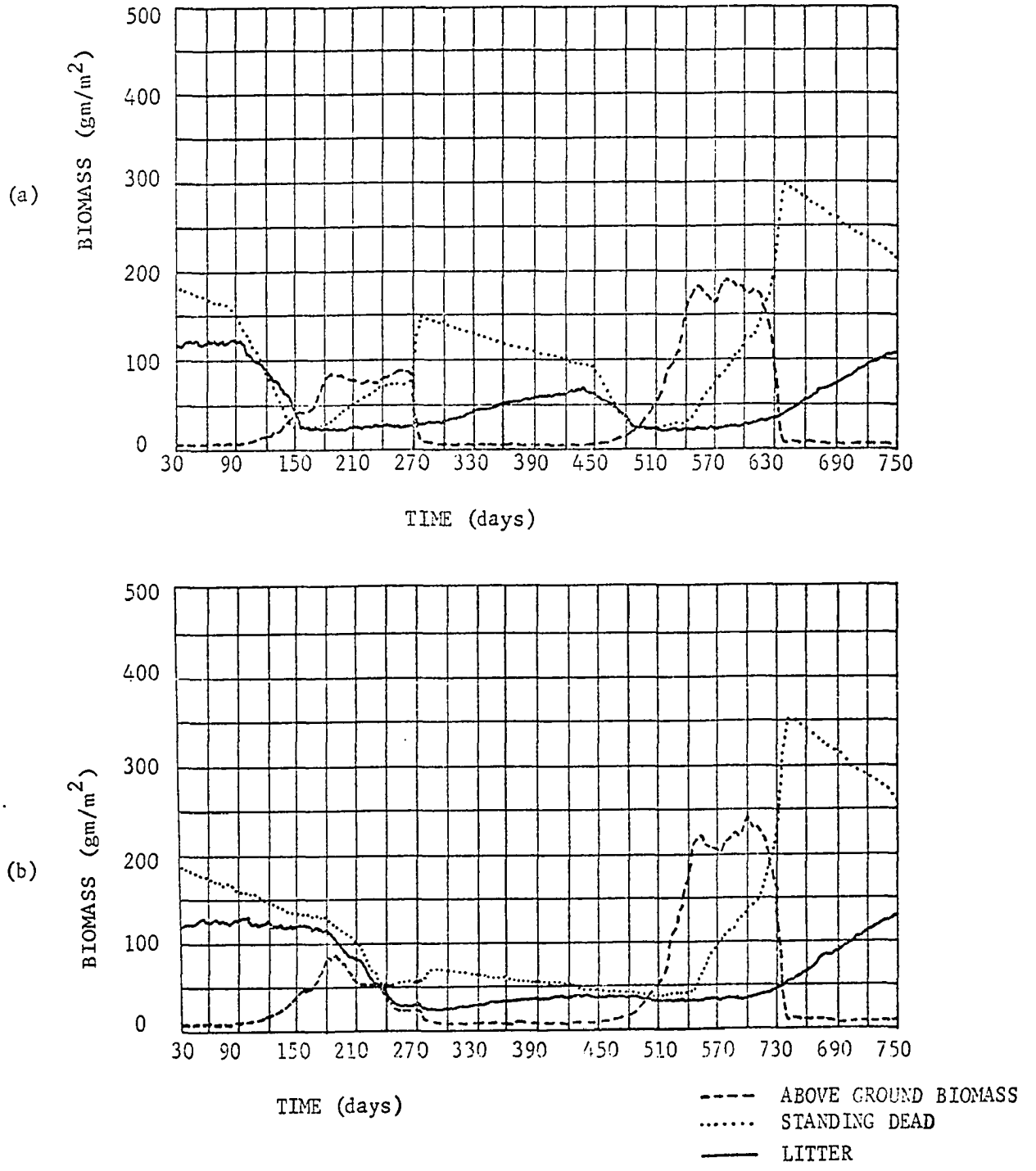

Fig. 82. A two-year simulation of live above ground biomass, standing dead biomass and litter for field #3 (a) and field #4 (b) is presented.

is caused by the transfer of ABM into SD. The discontinuous decrease in SD is produced by harvesting the grass for utilization by the feed lot cattle. The litter curve shows very little variations through the year, except for the dramatic decrease in the fall which is caused by harvesting the grass. Comparing the time simulation for the first year and second year for field #1 shows that the major difference is that in the second year ABM peaks at a higher level. The increase in ABM for the first year to the second is caused by the increase in the below ground biomass (see Figure 83). Increasing below ground biomass allows above ground biomass to maintain higher peak values by lowering the rate of translocation of photosynthetic material to BBM. The major difference between field #1 and field #2 is that field #1 is irrigated when the soil moisture starts to limit growth, while in field #2 no moisture is added when soil moisture becomes a limiting factor. The overall characteristics of the response of the state variable in field #2 is the same as field #1, except for the fact low soil moisture values limit growth of ABM during the summer. Thus the most significant difference between field #1 and #2 is that the value for ABM is much lower in field #2. A comparison of the time simulation for the first and second year for field #2 shows that the peak in the ABM curve is almost twice as high in the second year. This increase is caused by a significant increase in the available soil moisture during the early summer (see Figure 84 . The herbage dynamics in fields #3 and #4 are identical to the dynamics in field #2, except for the fact that cattle alternately graze field #3 and #4. Figure 82 demonstrates that the effect of grazing on the herbage dynamics is significant. In the first

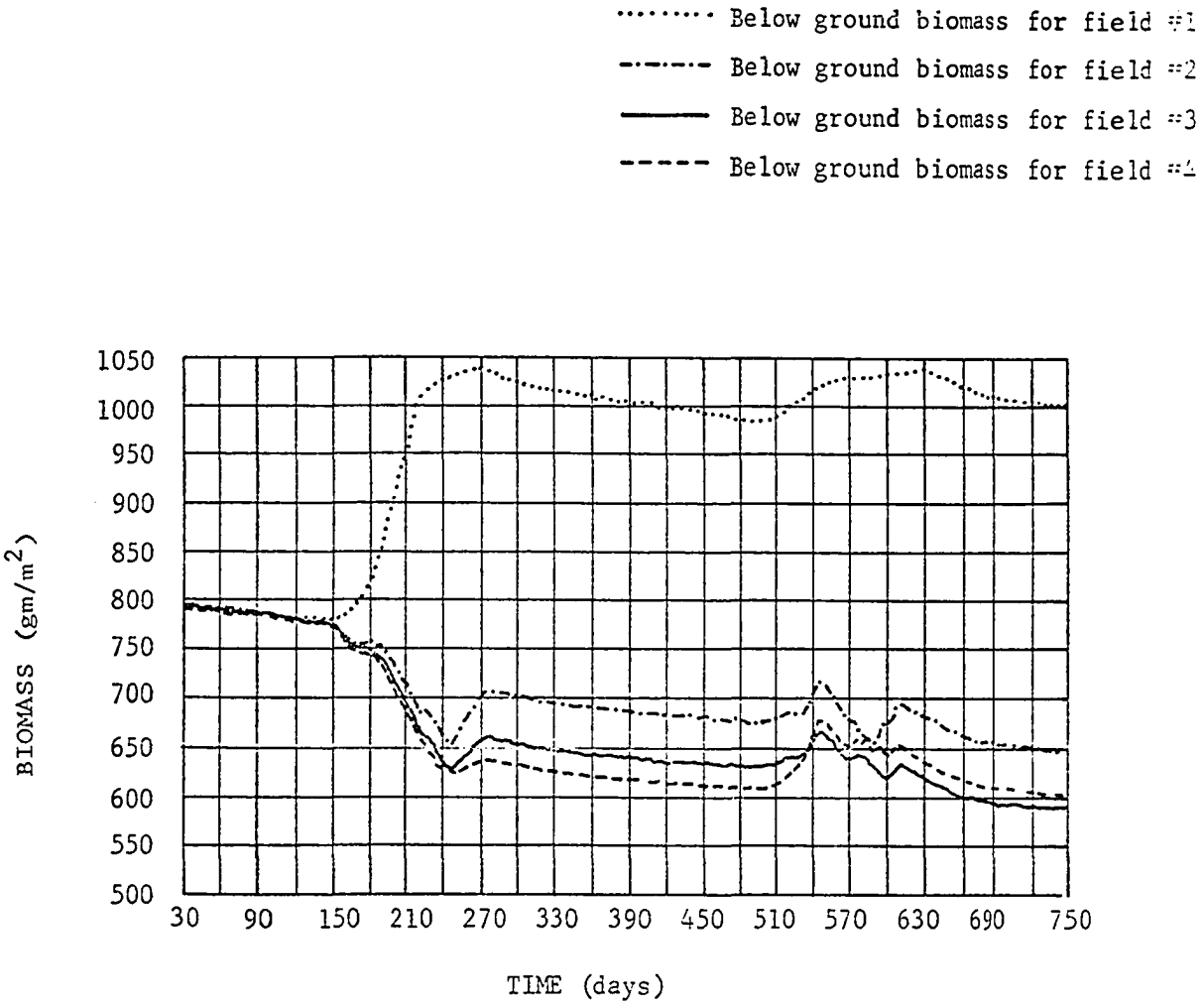

Fig. 83. A two-year simulation of below ground biomass for fields #1, #2, #3, and #4 is illustrated in this figure.

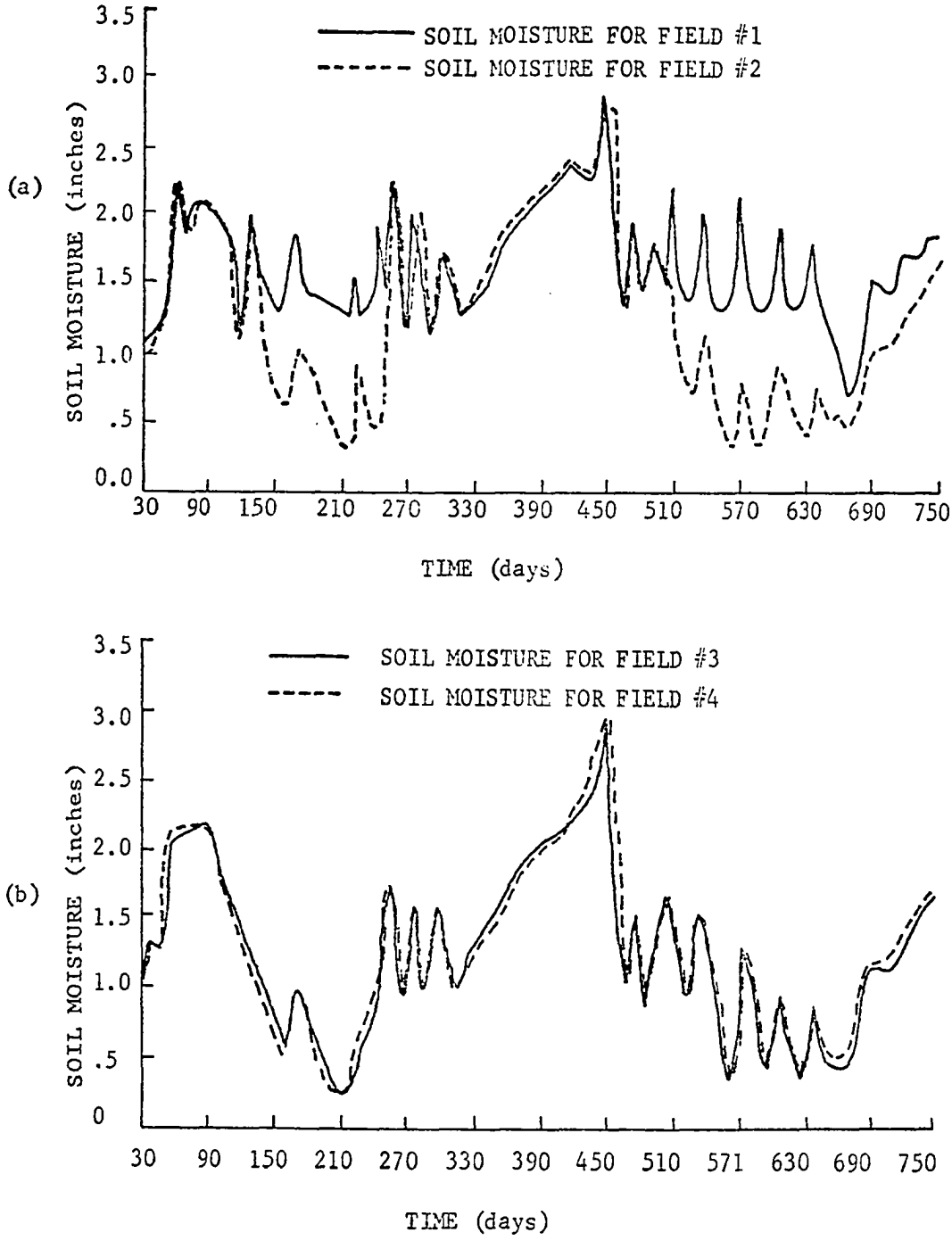

Fig. 84. A two-year simulation of the soil moisture available for evaporation from 0-24 inches for field #1 and #2 (a) and for field #3 and #4 (b) is shown.

year simulation the cattle are placed on field #3 at day 90. The amount of standing dead and litter began to decrease as soon as the cattle were placed on field #3, and by day 160 there is insufficient grass for the cattle and a decision must be made to relocate the cattle. The management decisions process decided to move the cattle to field #4. The total above ground forage in field #3 then starts to decrease rapidly. After the cattle leave field #3 ABM and SD increase to peak values which are much less than the peak values found in field #2. In the second year the cattle are again placed on field #3 in April and promptly start eating the standing dead and litter in field #3. Within two months the amount of grass is insufficient for grazing and a decision must be made to relocate the cattle. In checking field #4 the decision process notes that the total above ground forage is less than 150 gm/m^2 and decides to move the cattle to the feed lot, permanently. After putting the cattle in the feed lot, fields #3 and #4 respond to the available soil moisture and grow peak values of ABM similar to the peak ABM observed in field #2 for that year. This discussion demonstrates how grazing management policies decisions dramatically influence the herbage dynamic in fields #3 and #4.

Figure 83 presents the time simulation of live below ground biomass (BBM) for the different fields. The BBM time series for fields #2, #3 and #4 decreases significantly for the first year, and continue to decrease slowly during the second year. The below ground biomass increase for a short time period in the late spring and early summer and also in the early fall. The increase in early summer and early fall is caused by an increase in the transfer of above ground photosynthate material

to the below ground biomass. The below ground biomass in field #1 increases dramatically the first year and then stabilizes by the end of the second year. After stabilizing the BBM for field #1 tends to increase during the spring and summer and decrease during the remainder of the year. This increase is caused by high translocation rates of above ground photosynthate material to below ground biomass during the spring and summer. The decrease in BBM during the fall and winter is caused by net respiration (translocation minus respiration is negative) during this time period. Comparison of the BBM curves for the different fields shows that field #1 has the highest biomass. The BBM time series in field #2, #3 and #4 is very similar, however, the biomass in field #2 is significantly greater than fields #3 and #4. This is expected since grazing of field #3 and #4 reduces the translocation of photosynthate material to the below ground biomass. Figure 84 presents the average soil moisture for the four fields. The most important feature observed in comparing the time series is that field #1 has the higher average value of soil moisture during the summer. This is expected since field #1 is irrigated when the available soil moisture from 0-24 inches gets below 1.5 inches. A comparison of the average soil moisture for fields #2, #3 and #4 shows that there is very little difference. Comparing the first year with the second year shows that the soil moisture in the early summer is much higher in the second year, and causes the increased growth observed in fields #2, #3 and #4. The low soil moisture during the summer months limits the growth of grass in fields #2, #3 and #4.

Figures 85, 86 and 87 present the average monthly values of ABM,

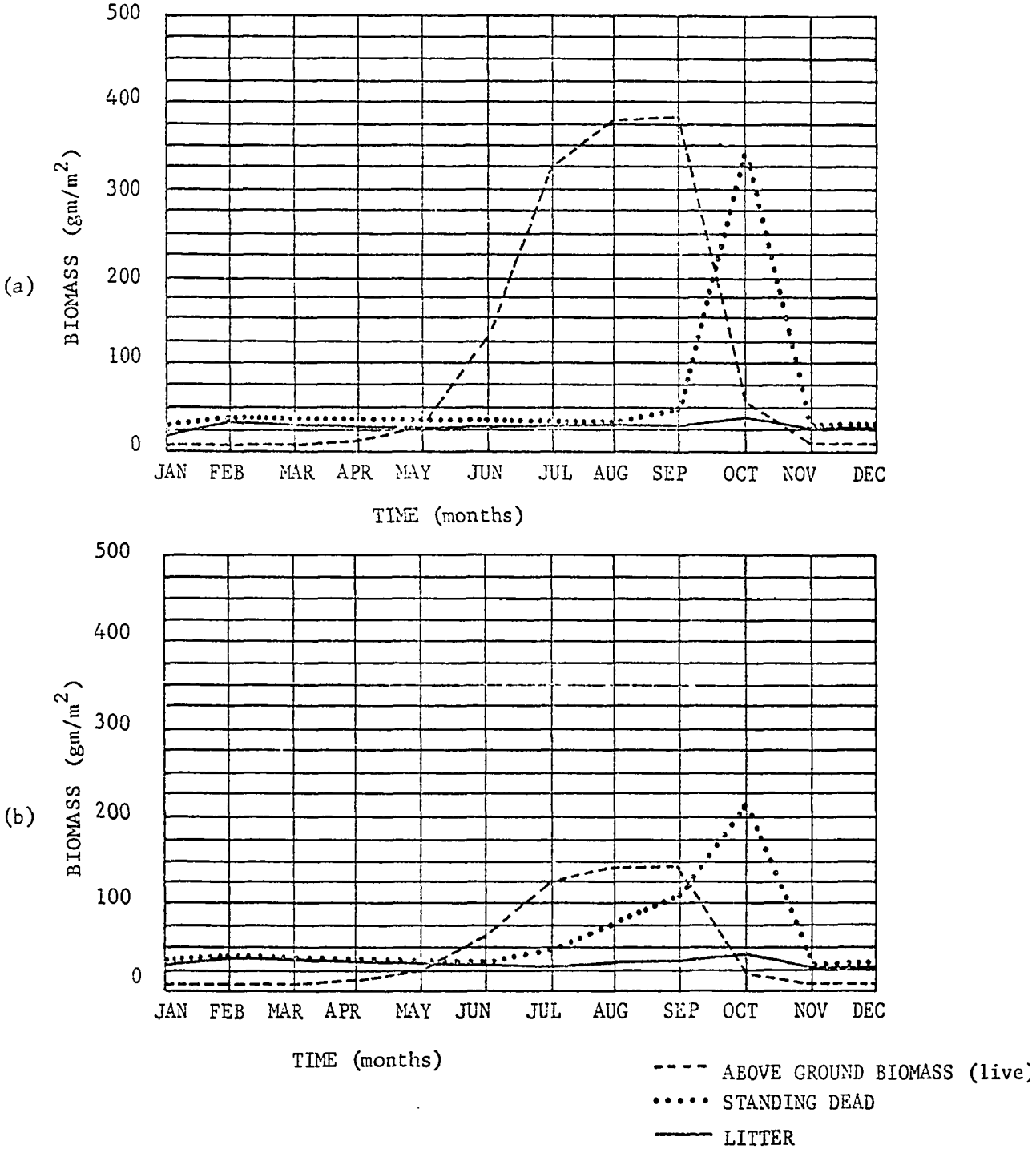

Fig. 85. The average monthly live above-ground biomass, standing dead biomass, and litter for field #1 (a), and field #2 (b) is presented in this figure.

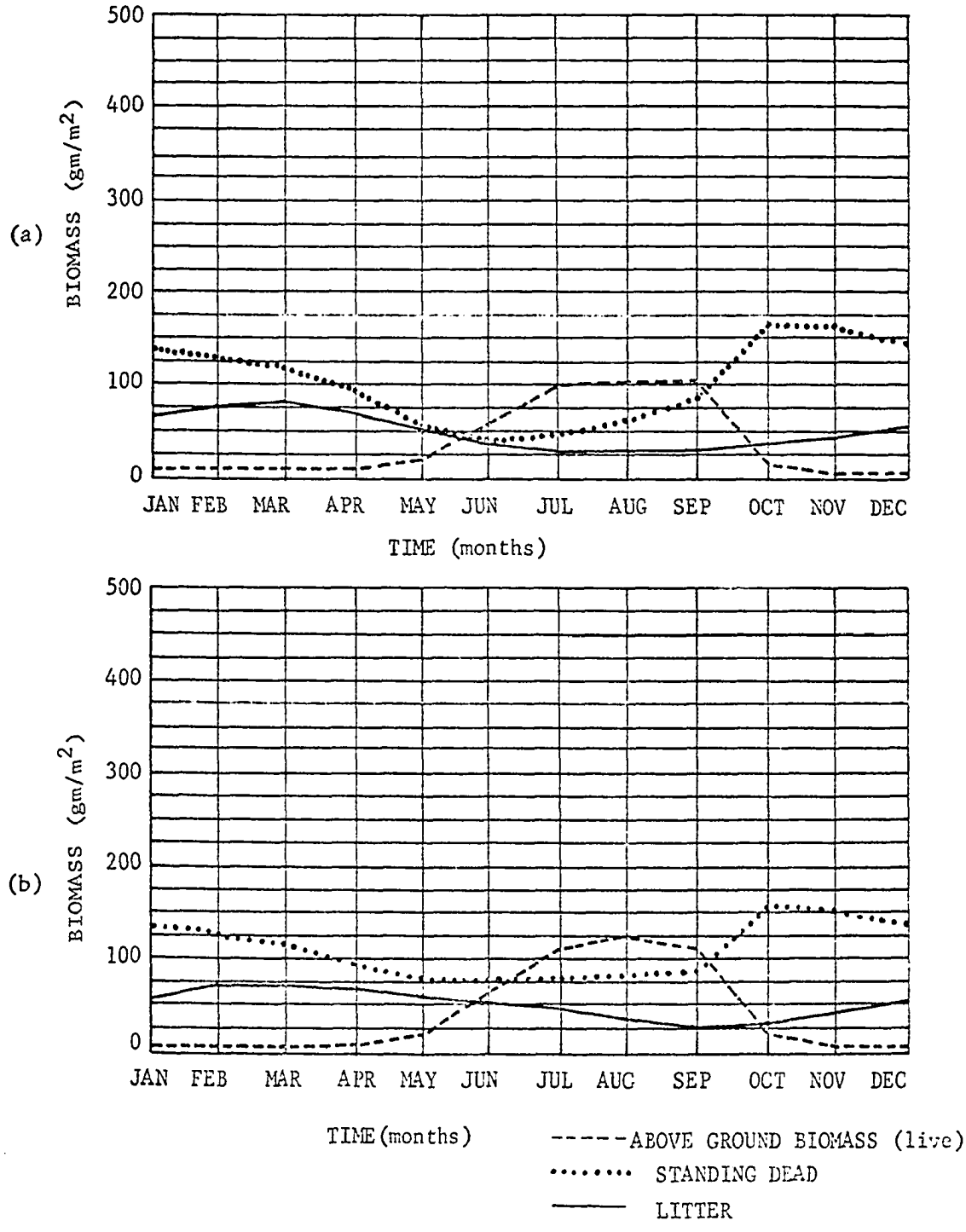

Fig. 86. The average monthly live above-ground biomass, standing dead biomass and litter for field #3 (a) and field #4 (b) is illustrated.

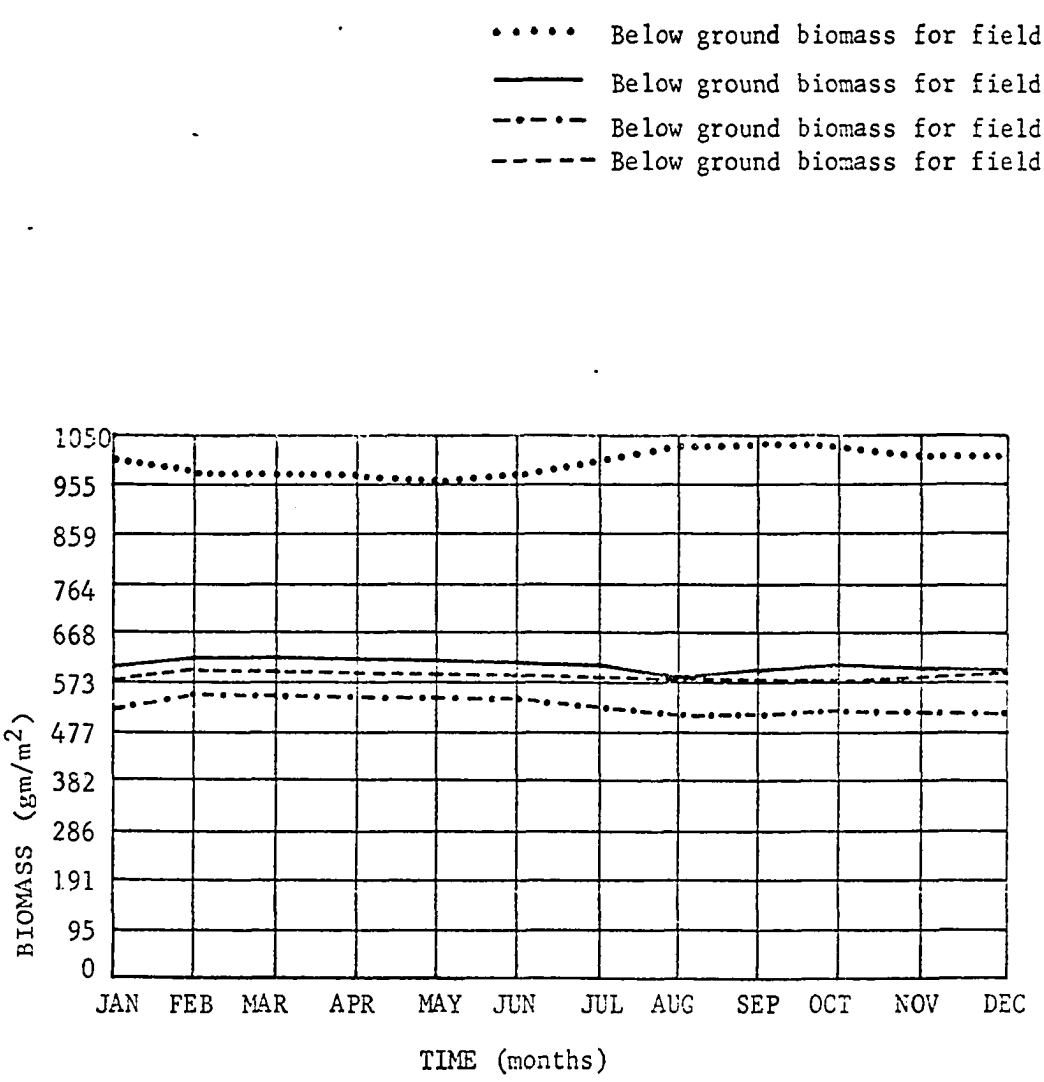

Fig. 87. The average monthly below ground biomass for field #1, #2, #3 and #4 is shown in this figure.

SD, LIT and BBM for fields #1, #2, #3 and #4. A comparison of the peak values of the above ground biomass for the different fields shows that fields #1 and #2 has the highest peak values of ABM, with the highest values of ABM observed in field #1. This is expected since field #1 is irrigated during low soil moisture conditions. A comparison of the peak value ABM in fields #3 and #4 shows that field #4 has a significantly higher peak value. This results because at the beginning of each year the cattle are first put on field #3, and are not moved to field #4 unless the forage is insufficient in field #3. The most important herbage dynamics demonstrated for all four fields is that the ABM increases to a peak value in mid summer and decreases rapidly in the fall with the transfer of ABM to standing dead. The transfer of standing dead to litter during the winter months in field #3 and #4 is shown by the fact that the peak value of litter lags the peak value of standing dead by four months. The average monthly below ground biomass curves for the fields show that BBM in field #1 is distinctly greater than BBM in the other fields. The below ground biomass for fields #2, #3 and #4 are very similar, with the average below ground live biomass decreasing from field #2 to field #4 to field #3. The fact that field #3 has the lowest average biomass is caused by the fact that it is grazed more often than the other fields. The relative difference between field #1, #2, and #4 are explained using arguments previously discussed.

APPENDIX E

APPENDIX E

RESULTS OF THE TESTING PROCEDURE PERFORMED ON THE ZOOLOGY MODEL

This appendix presents the results of the testing procedure performed on the zoology model. The testing demonstrates the response of the model to the input variables and the decision making process that controls the movement of cattle. This is accomplished by using the results from a ten-year simulation of the total ecosystem model to demonstrate the feedback loops between the zoology model and the overall ecosystem. The month-to-month variation of the zoology parameters are shown for the first 4 years of the time simulation in order to demonstrate the detailed workings of this subsystem. The average monthly values of zoology parameters are presented to illustrate the long-term influence of the range management practices upon the model.

Figure 88 presents the four-year time series of the number of grazing and feedlot cattle, weight of the yearling and feedlot cattle at the end of each month and the amount of forage available (ABM, SD, and LIT) in fields #3 and #4. The grazing cattle herd consists of breeding cattle herd (15,000) and yearling cattle that are born each spring. The breeding cattle are older than two years old and are mated during the summer months of the previous year. The herd is located in the grazing field each spring and calving proceeds to provide 15,000

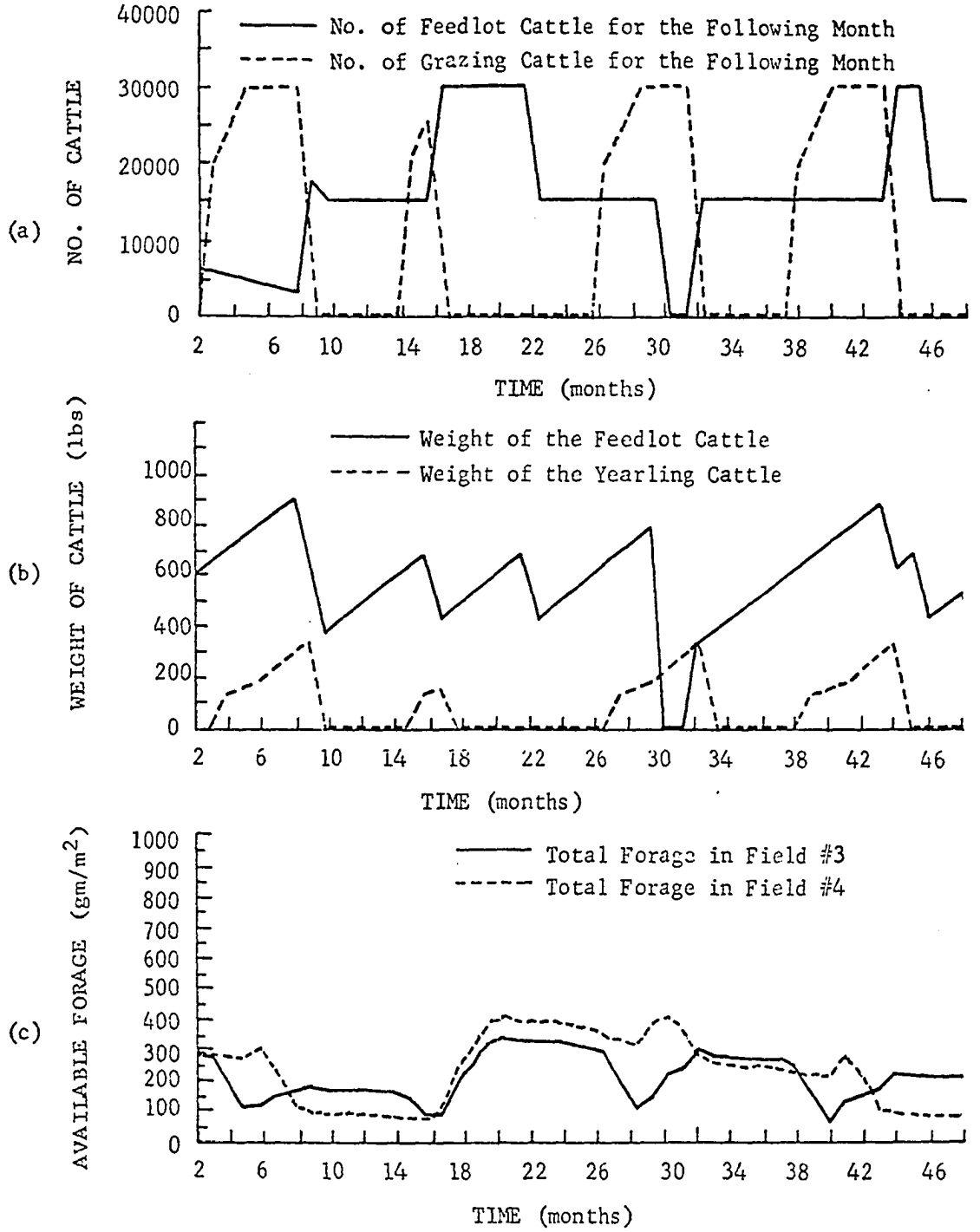

Fig. 88. A four-year simulation of the number of grazing and feedlot cattle (a), the weight of the yearling and feedlot cattle at the end of each month (b), and the amount of available forage (LIT, ABM, and SD) for grazing (c) is presented in this figure.

yearling cattle (range cattle) during the first three months of the spring (April, May, and June). By the end of September the grazing cattle herd is taken off the range. The yearling cattle are transferred to feedlots and the breeding cattle are transferred to temporary storage locations until the spring. The time series of the grazing cattle (Fig. 88(a)) shows this sequence with the number of grazing cattle increasing in the spring, stabilizing in the summer months and then decreasing to zero at the end of September. The transfer of yearling cattle to feedlots shows up as the discontinuous increase in the number of feedlot cattle at the end of September. The feedlot cattle gain weight and age in the feedlots and are slaughtered if they get older than 21 months or if they reach the critical age for slaughtering. By the end of September the number of cattle increased in response to the transfer of yearling cattle into the feedlot. During the second year of the simulation, the number of feedlot cattle doubled in May with the early transfer of yearling cattle into feedlots. The transfer is initiated by the lack of sufficient forage in field #3 and #4 (see Figure 88(c)). Six months later the number of feedlot cattle decreased by 15,000 as the first year yearling cattle reached critical weight for slaughtering. The continuous time series of the number of feedlot cattle is a function of when yearling cattle are located in the feedlot and when the yearling cattle placed in the feedlot reach their critical weight or age for slaughtering. The number of cattle in the grazing herd follow the same pattern for every year of the four-year simulation except for the second year when there is insufficient forage in fields #3 and #4 to support the grazing cattle. The chart of the average weight of the feedlot cattle shows a series of time segments with

increased average weights that are periodically interrupted by discontinuous decreases in the average weight. These decreases in the average weight are caused by the addition of light weight yearling cattle to the feedlot or by the slaughtering of full-grown feedlot cattle. The decrease due to the addition of yearling cattle is demonstrated by the dramatic decrease in the average weight during September of the first year simulation. The decrease in the average weight of the feedlot cattle in October of the second year of the simulation is caused by slaughtering of the yearling cattle from the first year. Similarly, the remainder of the discontinuous decrease in the average weight can be attributed to changes in the number of feedlot cattle. Increases in average weights of the feedlot cattle are caused by the continuous weight gain of cattle in the feedlot (50 lbs. per month). The average weight of the yearling grazing cattle for each year show a continuous increase for the 6-month period of time they are on the grazing fields (50 lb./month). While the grazing cattle are on a grazing field (16 x 16 sq. mi. field) they consume 31 lbs. of grass per lb. of weight gain. Similarily the feedlot cattle consume 31 lbs. of grass per lb. of weight gain. The water comsumption by feedlot cattle and grazing cattle is not considered in this model. The weight gain pattern of the yearling cattle is identical for each year of the four-year simulation except for the second year in which the yearling cattle are prematurely transferred into the feedlot. The effect of the cattle on the available forage in field #3 and #4 is demonstrated in Figure 88(c). In the spring of the first year the forage in field #3 decreased until the beginning of June when the cattle have eaten all of the available forage. The cattle are transferred to field #4 and the available forage started to decrease in that field until the end of September. In the second year when the available forage is insufficient, the cattle are not

transferred to field #4 because there is not sufficient forage in field #4 (less than 150 gm/m^2). Since the cattle are in the feedlot both field #3 and #4 respond by increasing their available forage. The changes observed in the available forage for year 3 and 4 are very similar to the changes observed in year 1. It is interesting to note that in the years after year #2 the average available forage in both fields decreases from year to year. If this forage decrease continued into year 5 the available forage would reach the critical level that forces the cattle to be prematurely transferred to the feedlots.

Figure 89 shows the average monthly number of feedlot cattle and grazing cattle and the average monthly weight of the feedlot cattle and yearling cattle at the end of each month. The results show (Figure 89) that the month of May has the highest average number of yearling cattle. The premature removal of the grazing cattle because of insufficient forage causes the average number of yearling cattle in the grazing fields to decrease after May. The average monthly number of feedlot cattle shows a peak in June and one in October. The peak in June is caused by the early transfer of grazing cattle into the feedlots while the peak in October is caused by the normal transfer of the yearling grazing cattle into the feedlot. The sharp decrease in the number of feedlot cattle in December is caused by the slaughtering of yearling cattle that are transferred to the feedlots in October of the previous year. The second minimum value of the number of feedlot cattle observed in August and September is produced by the slaughtering of the yearling feedlot cattle prematurely placed in the feedlots during the early summer months. The average monthly weight of the feedlot cattle shows an increase in weight from November until the early summer months, with a sharp decrease observed at the end

(a)

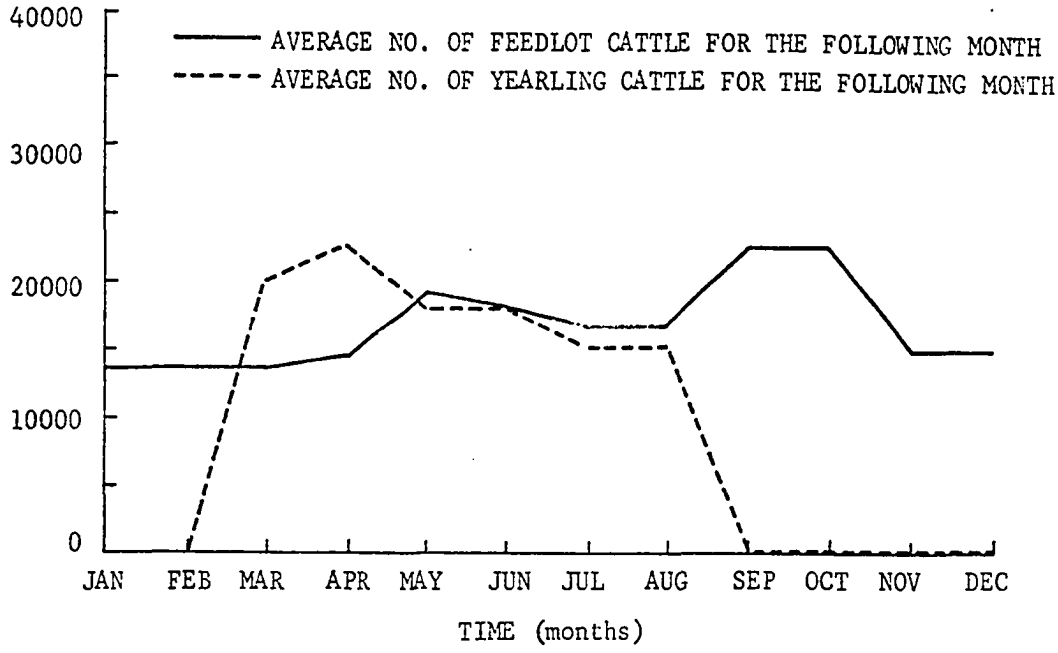

(b)

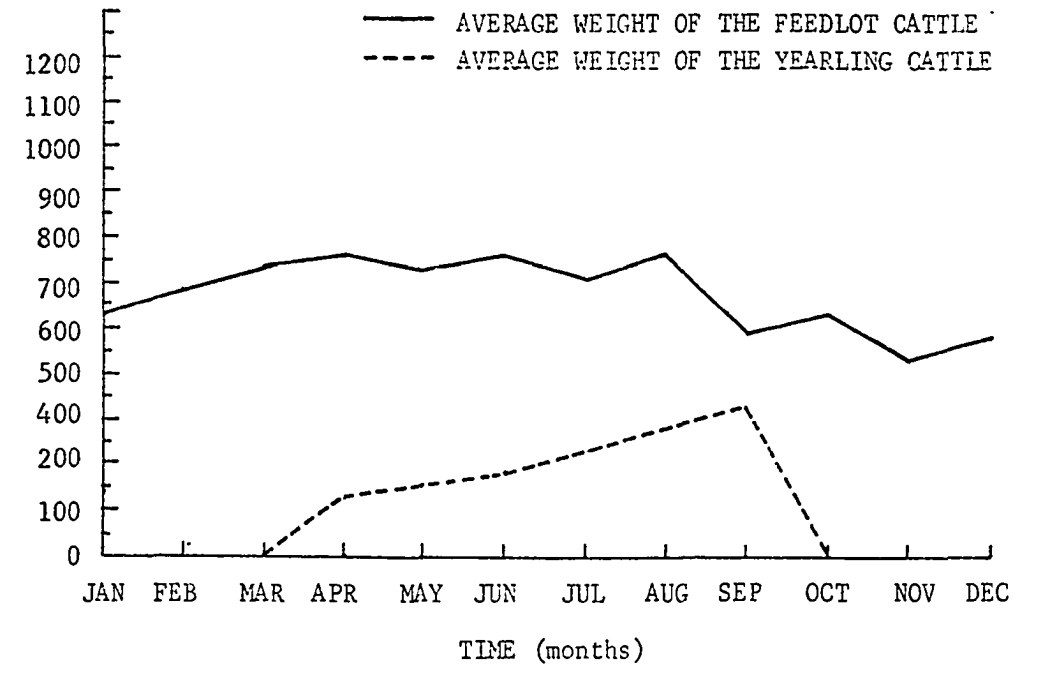

Fig. 89. The average monthly number of grazing cattle and feedlot cattle (a) and the average monthly weight of the yearling cattle and feedlot cattle at the end of each month (b) are illustrated.

of September and November. The sharp decrease at the end of September is caused by the transfer of yearling grazing cattle into the feedlots, while the sharp decrease at the end of November is caused by the slaughtering of the yearling cattle from the previous year. The increase from November to April is produced by the continuous weight gain by cattle in the feedlots. The average weight of the yearling cattle increases while they are on the grazing fields (April through September). A minor error in the computer program caused the total number of yearling cattle to be low by 5,000 for year #7 of the ten year simulation. This error does not significantly influence any of the results presented in this section.

The breeding cattle consume 1,550 lbs. of grass per month while they are grazing with the yearling cattle. They consume 930 lbs. of cut grass per month during the remainder of the year. The 1,000 milk cattle in the milk cattle herd consume 300 lb. of cut grass per month from January to December. Each milk cow produces 75 lb. of milk per month.

APPENDIX F

APPENDIX F

RESULTS OF THE TESTING SCHEME PERFORMED ON THE EXECUTIVE ROUTINE

This appendix is concerned with the testing procedure performed on the decision making executive model. The executive model consists of three submodels which include an air pollution control submodel, water control submodel and a range management submodel. These submodels are examined by running sensitivity analyses on them and by demonstrating the influence of the submodels on the overall ecosystem.

Air Pollution Control Submodel

The air pollution control model demonstrates sensitivity of the model to wind direction, maximum air pollution levels permitted at the monitoring points and objective function coefficients. It also considers the long term effect of the air pollution control model upon the resulting average annual air pollution field. The sensitivity of the submodel to the three parameters mentioned above is demonstrated by altering these parameters separately and observing their influence upon the production level permitted for each factory and on the total industrial production. It is important to note that this model assumes that factory production is directly proportional to the air pollution emitted. The initial condition for all of the parameters that are set

in the air pollution model are summarized in Table 36 and 37. These tables show the maximum air pollution levels permitted at air pollution monitoring points, the values assigned to the objective function coefficients for each factory, the maximum air pollution emission rates and the minimum profitable air pollution emission rates for each factory. The sensitivity of the model to wind direction, maximum level of air pollution allowed at the monitoring points and the objective function coefficients is shown by running 9 case studies in which the parameters were varied and the effect upon the production levels of the individual factories and the total system is observed and presented in Table 38. Specifically Case #1 is the control case, Case #2-5 demonstrate the effect of wind direction, Case #6 and #7 show the effect of altering the maximum air pollution level permitted, while Case #8 and #9 show the effect of changing the objective functions coefficients. The objective function coefficients are a measure of relative worth of the products produced by the individual factories.

The results from case studies #2 through #5 show that by changing the wind direction the production levels of the individual factories vary significantly. As the wind direction shifts from 150 to 190 the total production of the factories increases from 68% to 91%. The variations observed in the production levels with the different wind directions are caused by the specific location of the air pollution monitoring points relative to the air pollution source. For example, with case #5 the production level is highest because the air pollution for most of the factories does not flow over the air pollution monitoring points with the wind direction from 190, while with the wind direction

TABLE 36

Maximum Air Pollution at the Air Pollution Monitoring Points (mg/m^3)

#1	#2	#3	#4	#5	#6	#7	#8	#9	#10
50	50	50	50	50	50	100	100	50	50

TABLE 37

Air Pollution Sources[1]

	#1	#2	#3	#4	#5	#6	#7	#8	#9	#10	#11	#12	#13	#14	#15	#16
Objective Function Coefficients	2	2	2	2	2	2	2	2	2	2	4	4	2	2	2	2
Maximum Production level for the ith factory (P_i^{MX}- units/sec)	25	25	25	25	25	180	180	180	80	80	460	460	70	70	70	70
Minimum Production level for the ith factory (P_i^{MX}- units/sec)	11.25	11.25	11.25	11.25	11.25	81	81	81	36	36	207	207	31.5	31.5	31.5	31.5

[1]The value of x_i (see air pollution control model) is set equal to one.

TABLE 38

Production Level (%) for Each Factory for the Sensitivity Analysis Case Studies

Case Studies	1	2	3	4	5	6	7	8	9	10	11	12	13	14	15	16	Total Production (%)
#1 Control Case WDR = 140	100	100	100	0.0	0.0	0.0	100	100	98.5	100	100	100	100	100	100	0.0	85%
#2 WDR = 150	100	100	100	100	100	0.0	100	100	100	100	100	0.0	100	100	100	100	68%
#3 WDR = 160	100	100	100	100	100	100	100	100	100	100	0.0	100	100	100	100	100	77%
#4 WDR = 170	100	100	100	100	100	100	0.0	0.0	100	100	100	100	100	100	100	100	82%
#5 WDR = 190	100	100	100	100	100	100	100	0.0	100	100	100	100	100	100	100	100	91%
#6 - Mx Pollution Level Increased (+30 mg/m^3)	100	100	100	100	100	100	100	100	100	100	100	100	100	100	100	0.0	97%
#7 - Mx Pollution Level Decreased (-30 gm/m^3)	100	100	100	0.0	0.0	0.0	76	100	69	100	0.0	69	100	100	100	0.0	52%
#8 - Decrease Objective Function Coef. for Factory #12 (-2)	100	100	100	0.0	100	100	86	100	98.5	100	100	0.0	100	100	100	0.0	71%
#9 - Increase Objective Function Coef. for Factory #6 (+4)	100	100	100	0.0	0.0	100	82	100	98.5	100	100	100	100	100	100	0.0	92%

from 150 the air pollution from the factories is advected toward some of the air pollution monitoring points. Thus it is important to note that the location of the monitoring points relative to the air pollution sources and the prevailing wind direction will have a significant influence upon the effect of the air pollution control model upon production level permitted and the resulting air pollution field.

Case study #6 demonstrates the effect of increasing the maximum air pollution level permitted at the monitoring points by 30 $\mu g/m^3$, while case study #7 shows the effect of decreasing the maximum air pollution level by 30 g/m^3. The results show that increasing the pollution level causes the total production to increase from 85% to 97% while decreasing the maximum air pollution level causes the total production level to decrease to 52%. The fact that decreasing the maximum allowable air pollution concentration by 60 g/m^3 produces a 45% decrease in total production, emphasizes the economic importance of determining realistically, the maximum air pollution levels for urban areas.

Case #8 demonstrates the effect of decreasing the objective function coefficients for factory #12, while case #9 shows the effect of increasing the objective function coefficient of factory #6. Decreasing the coefficient for factory #12 causes the production level in factory #12 to go from 100% to 0% while the production levels in factories #5 and #6 increased from 0% to 100%. Increasing the objective function coefficient for factory #6 enabled the production level to increase from 0% to 100% while the production level at factory #7 is lowered from 100% to 82%. It is interesting to note that decreasing the

objective function coefficient of factory #12 causes the total production to decrease to 71% while increasing the objective function coefficient for factory #6 caused the production level to increase to 92%. In a real life situation, the effect of increasing or decreasing an objective function coefficient is equivalent to making the value judgment that the product produced by a factory is either worth more or less. If one factory has higher value for its objective function coefficient than another factory, then an equivalent statement is that the air pollution from one factory is more critically associated with the economy of the community than the air pollution from the other sources. Thus factories that produce products of high relative value have preference in the allocation of air pollution emission rates. In case #8, the decision that the product produced at factory #12 is of low relative value causes the air pollution control model to determine that the product volume produced at factory #12 is decreased in preference to production by factories #5 and #6. This decision causes the total production for the city to decrease from 85% to 71%, with the justification that the products of factories #5 and #6 are more valuable to the total system than the products of factory #12. Cases #8 and #9 demonstrate the importance of assigning relative economic values to the different factories.

The effect of the air pollution control model upon the average air pollution level in the city is shown in Figure 90, which illustrates the average annual air pollution field generated with all the factories in operation at 100% production and the average air pollution field when the production levels are controlled by air pollution control model.

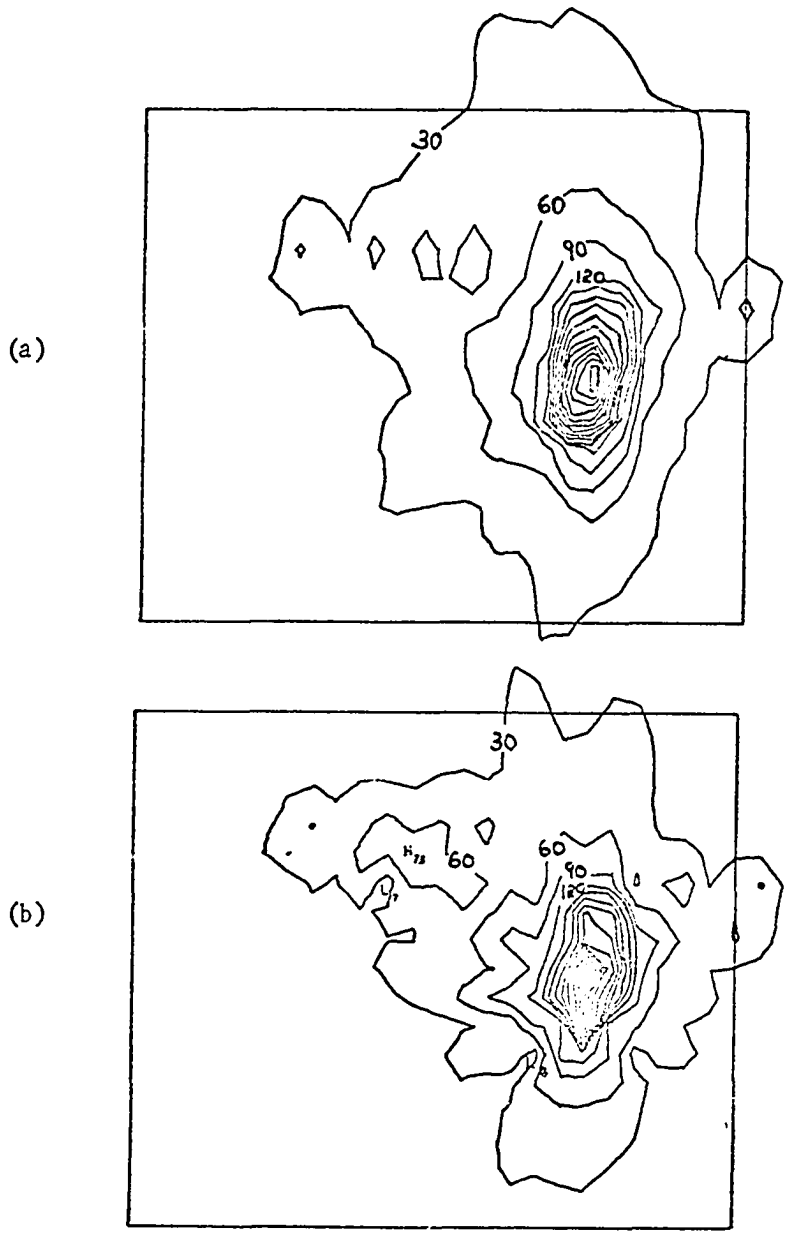

Fig. 90. A comparison of the average annual SO_2 air pollution fields for uncontrolled (a) and controlled (b) air pollution emission rates are presented. The uncontrolled air pollution field is determined by using a two-year simulation of the air pollution submodel in which the air pollution emission rates are constant. The controlled air pollution field is determined by using a two year simulation in which the air pollution control model influences the air pollution emission rates. The location of the air pollution sources and the air pollution emission rates simulate the SO_2 air pollution in Houston, Texas.

The most important effect observed in comparing the two air pollution fields is that the air pollution field directly to the north and south of the center of maximum air pollution concentration is lower for the case where the air pollution control model is used. This indicates that when the wind direction is from the north or south some of the factories have their production levels decreased because of excessive air pollution levels. When the wind direction is from the east or the west, the air pollution control model does not significantly reduce the production levels of the factory. These results are explained by the particular location of the air pollution monitoring points and climatology wind rose for Oklahoma City.

Seasonal effects upon the production level of the factories regulated by the air pollution control model is demonstrated by a two-year simulation in which the average monthly production level for the city is determined (see Table 39). The results show that the lowest production levels are observed in February, March and April, while the maximum production levels are observed in May, June and July. Interpretation of these results is difficult because there are many factors that could influence the results. Two of the most important factors are 1) that the atmospheric stability changes as a function of the time of year and 2) that climatology wind rose changes as a function of the time of year. Stable atmospheric conditions force the production level to be decreased because of higher air pollution levels, while unstable atmospheric conditions enable production levels to be high because the air pollution is dispersed over a much larger volume (reduce air pollution level). The effect of changing wind direction

TABLE 39

Average monthly production levels for the city[1] (% of total production capacity)

		Jan	Feb	Mar	Apr	May	Jun	Jul	Aug	Sep	Oct	Nov	Dec
Production Level (%)	1-Yr.	85	76	81	77	85	87	84	85	79	79	78	87
Production Level (%)	2-Yr	83	86	79	76	89	86	89	76	86	88	84	84
2-Year Average		84	81	80	77.5	87	86.5	86.5	80.5	82.5	83.5	81	85.5

[1]The results are determined from a two-year simulation of the air pollution control model.

upon production levels has already been demonstrated. In interpreting these results it is most likely that the low production levels in February, March and April are caused by the relatively stable atmospheric conditions, while the high levels of production in May, June and July are caused by a high frequency of unstable atmospheric conditions. The implication of such knowledge for industrial planning would seem to be important.

Water Control Submodel

The water control model is tested by running a sensitivity analysis and demonstrating the effect of water management decisions upon the overall ecosystem. The sensitivity of the model to the objective function coefficients and maximum amount of water permitted to flow out of the lake is demonstrated by changing these parameters separately and observing their influence upon the ratio of the water allocated to the consumers to the water desired by the consumers (industry, city and agriculture), the agriculture water pollution level and the actual water flow from the dam. The results are summarized in Table 40, while the values for the control parameters in the water control model are presented in Table 41. The sensitivity analysis is performed by running six case studies in which case study #1 is the control case, case study #2 through #4 vary the maximum water flow from the dam, while case studies #5 and #6 change the objective function coefficients. The results for case #2 show that with maximum flow rate from the dam set equal to 7000 cfs the water demands of the consumers and the water pollution emission rates desired by the consumers are allowed without

TABLE 40

Results from the Sensitivity Analysis of Water Control Model

Case Studies	Ratio of the water allocated to the water desired for: Municipal Use	Agricultural Use	Industrial Use	Pollution (lb/sec)	Water from the Dam (CFS)	Water Flow Below the City (CFS)
#1 - Control Case Max WFD = 5000 CFS	1.	1.	.73	47.	5000.	3645.
#2 - Max WFD = 7000 (CFS)	1.	1.	1.	70.	6865.	5400.
#3 - Max WFD = 6000 (CFS)	1.	1.	1.	43.4	6000.	4535.
#4 - Max WFD = 4500 (CFS)	1.	1.	.58	47.0	4500.	3203.
#5 - Decrease Objective Function Coef. for Agricultural Use (-1.)	1.0	.33	.86	47.0	5000.	4035.
#6 - Increase Objective Function Coef. for Industrial Use (+2.)	1.0	.33	.86	47.0	5000.	4035.

TABLE 41

Values for the Linear Program Control Parameters Used in the Sensitivity Analysis of the Water Control Model

	Municipal Water Use	Agricultural Water Use	Industrial Water Use	Municipal Water Pollution	Agricultural Water Pollution	Industrial Water Pollution	Water Flow Below The City	Water Flow From the Dam
Objective Function Coefficients	3	2	3	1	1	1	0.0	-.03
Maximum Water Utilization Rate and Water Pollution Rates	2000 (CFS)	1000 (CFS)	2000 (CFS)	50 (lbs/sec)	70 (lbs/sec)	50 (lbs/sec)		
Minimum Water Utilization Rate and Water Pollution Rates	700 (CFS)	233 (CFS)	500 (CFS)	25 (lbs/sec)	23.3 (lbs/sec)	50 (lbs/sec)	3000 (CFS)	
Percentage of Water Returned to the River	80%	5%	80%					
Maximum Water Pollution Allowed				.05 (lb/ft^3)	.05 (lb/ft^3)	.05 (lb/ft^3)		

any restrictions. The results also show that 6865 cfs of water is all of the water that is needed to satisfy the demands of the consumers. This fact is verified because the water management model only needed 6865 cfs of the 7000 cfs of water that is available from the lake to satisfy the water demands for all the consumers. Comparing this with case #1 shows that in case #1 the industrial water use is limited and the agricultural water pollution rate is reduced. The difference between case #1 and #2 is attributed to the fact that in case #1 there is insufficient water flowing from the dam to satisfy the water needs of all of the consumers. Similarly, a comparison of the case #2 with cases #3 and #4 shows that the agricultural water pollution rate is the first parameter to be reduced by a reduction of the water flow from the lake, while with further reduction of the water allocated to industry is limited.

Comparing the results for case #5 with case #1 shows that by decreasing the value of the objective function for agriculture water, the water allocated to agriculture is reduced from 100% to 33%, while the water allocated to the industry is increased. For case #6 the objective function coefficient for industry is increased. Making this change produced results that are identical to the results in case #5. It is not surprising that increasing the objective function coefficient for industry has the same effect as decreasing the coefficient for agricultural water use. Studying the results for the six case studies shown that for all of the case studies the use of water by the city remained at the peak rate. This shows that the city water use is least sensitive to variations of the parameters altered in this sensiti-

vity analysis. This occurs because municipal water pollution rates are low enough such that they do not require as much excess water to dilute the water pollution that is emitted by the city. The sensitivity analysis shows that changing the relative values of water utilization can cause dramatic shifts in the allocation of water to the consumer. Choosing values for the objective function coefficients in the water management model is equivalent to the real life problem of deciding which consumers contribute more to the total system through their utilization of water resources.

Simulation Results

The effect of water control model upon the overall ecosystem is demonstrated by presenting the results from a ten-year simulation of the overall ecosystem model. The parameters that are studied include:

1) the average monthly values of water desired by the consumers and the average monthly water pollution emission rates desired by agriculture,
2) the average monthly values of ratio of the water received by the consumers to the water desired by the consumers and the ratio of the water pollution emission rate allowed to the water pollution emission rate desired by agriculture,
3) the ten-year trend of the desired water consumption by consumers,
4) a ten-year trend in the ratio of the water consumption to water demand and the ratio of the water pollution received by agriculture to the water pollution desired by agriculture,

5) the average monthly lake level and a ten-year trend in the yearly average lake level,

6) average monthly values of water flow from the lake and a ten-year trend in average annual water flow from the lake.

The ratio of the water pollution rate received by the city and industry to the water pollution rate desired by them is not presented because this ratio has the same value as the ratio of the water received to the water desired by the city and industry. Tables 41, 42 and 43 present the values for the control coefficients that are used in the ten-year simulation. The maximum water utilization rate for the consumers and water pollution rates by the consumers changed in simulation with time, however, the minimum values for these coefficients are the same as those presented in Table 41 (minimum water pollution emission rate and water demand by agriculture is set equal to 1/3 the desired rate).

Figure 91 shows the average monthly values of the water demand by the consumers and the desired water pollution emission rate by agriculture. The results show the flow rate desired by industry and the city in this test are constant throughout the year, while the irrigation water need by agriculture increases in the spring to a peak value in July and then decreases in the fall. The water demand for irrigation peaks in the summer since this is the time of year when soil moisture depletion is the greatest. The water pollution needed by agriculture has two peaks with one in June and July and the other in October and November. The water pollution generated by agriculture comes from the feedlots adjacent to the rivers and thus the water

TABLE 42

The Maximum Flow Rate from the Dam as Function of Lake Level

	LK>60	60≥LK>58	58≥LK>56	56≥LK>54	54≥LK>52	52≥LK>48	48≥LK
Maximum Water Flow from the Dam (cfs)	9000	8000	7500	7000	6500	5500	4500

TABLE 43

Controlled Flow into the Dam (cfs)

Jan	Feb	Mar	Apr	May	Jun	Jul	Aug	Sep	Oct	Nov	Dec
9000	9000	9000	9000	7000	7000	6000	6000	7000	9000	9000	9000

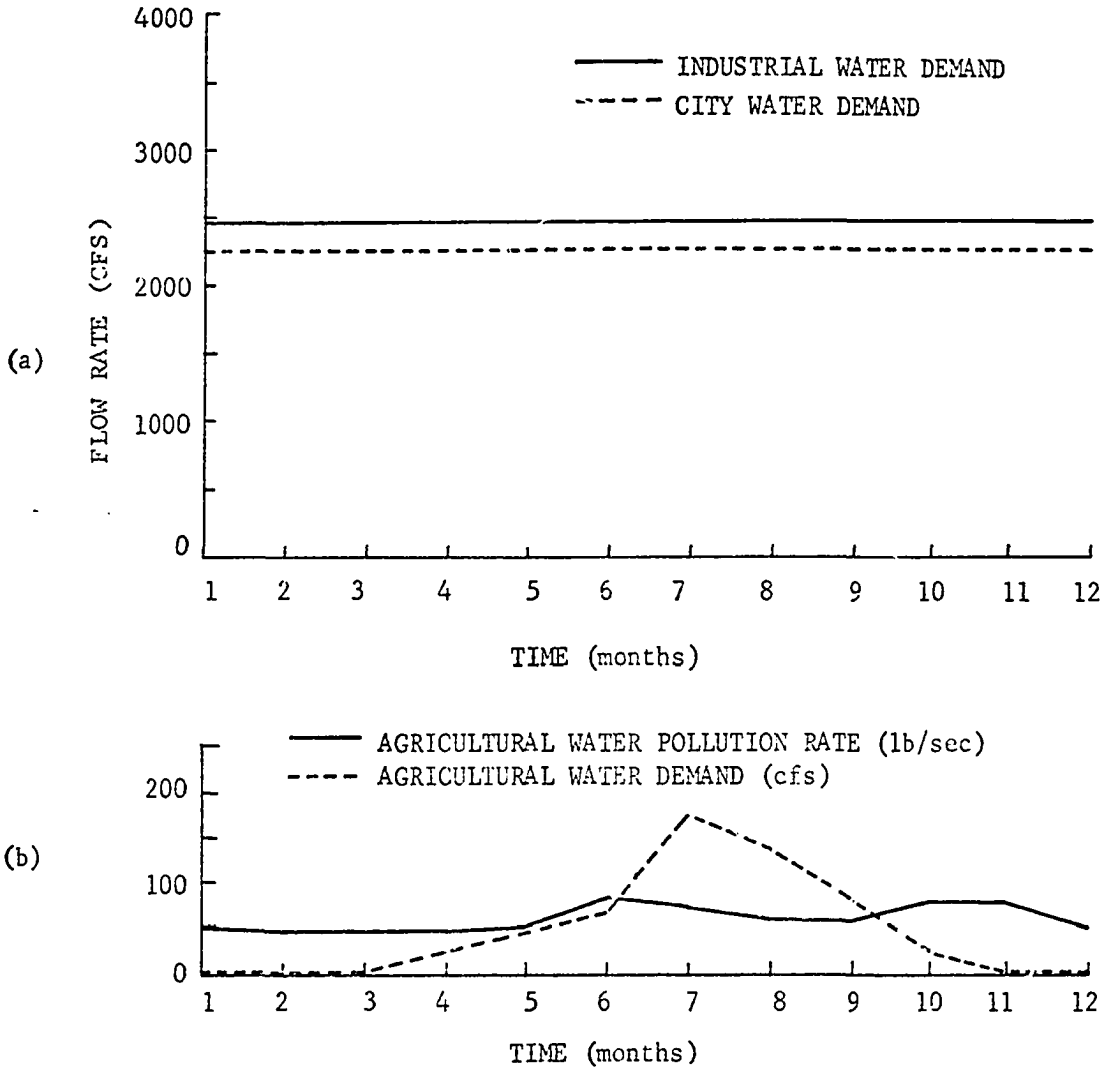

Fig. 91. This figure presents the average monthly water flow rates desired by the city and industry (a), and agriculture (b) and also the desired water pollution emission rate for agriculture (b).

pollution level is a direct function of the number of cattle in the feedlot. Comparing these results with the results in Figure 88 (Appendix E) show that the peak values of water pollution correspond to the peak values in the average number of cattle on the feedlots.

Figure 92 presents the average monthly ratio of the water received by the consumers and also the similar ratio of the water pollution rates allocated for agriculture to the water pollution desired by agriculture. The results for water consumption by the city and agriculture show that the ratio is equal to 1 for the complete year. This indicates that the water received by the city and by agriculture is always equal to the water desired by them. The average monthly ratios of the water received by industry to the water desired by industry and ratio of water pollution rates allowed for agriculture to the water pollution rates desired by agriculture show that they are less than one for the whole year and changes significantly within the year. These results show that the water allocated to industry is at its peak value in the winter and spring months and reaches minimum values in September, October and November. Changes in the water allocation for industry are related to the availability of water which is a direct function of the average lake level (at lower lake levels the water flow from the dam is reduced). During the spring months the average lake level is at its peak and the availability of water is increased, while during the fall the lake level is lower and water flow from the dam is reduced.

The ratio of actual water pollution rate to the water pollution rate desired by agriculture is at its peak value in the spring and decreases to its minimum values in October and November. Changes in

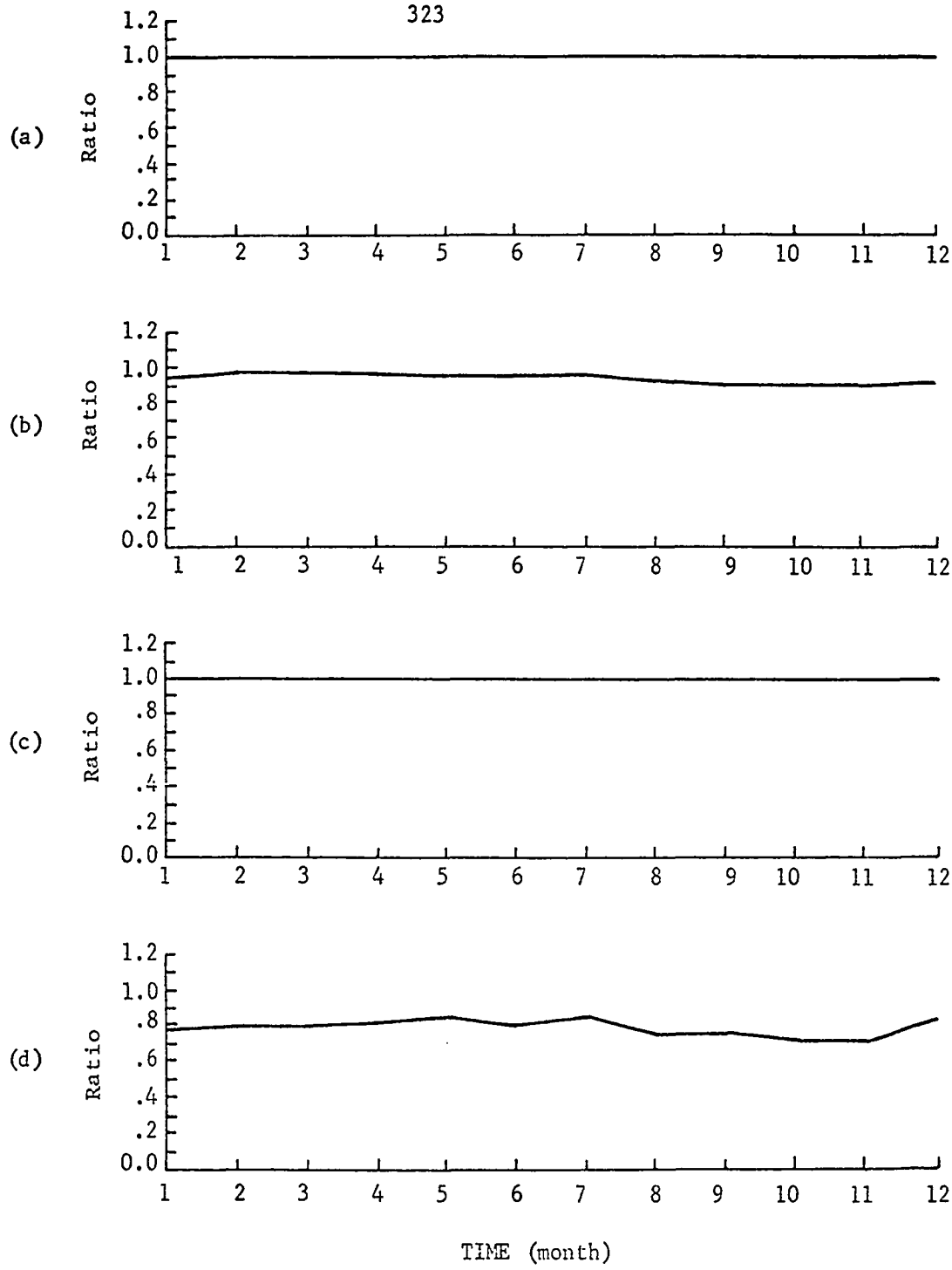

Fig. 92. This figure presents the average monthly values of the ratio of the water received by the city, industry and agriculture to the water desired by the city (a), industry (b), and agriculture (c) and also a similar ratio of the water pollution emission allowed for agriculture to the water pollution emission rate desired by agriculture (d).

the ratio are attributed to variations in the lake level and the fact that the average agriculture water pollution rate is at its peak value in October and November.

Figure 93 shows the average monthly flow rate of water from the dam. The peak values occur during June and October and November. These two peaks occur because of increases in the water demand by agriculture during these time periods. The June peak is caused by an increase in the water pollution emission rates by agriculture and an increase in the irrigation water demand. Increasing water pollution rates requires an increase in the river flow rates so that the water pollution concentration level will not exceed the critical level. The October and November peak values in flow rate are caused by the increase in the water pollution emission rate desired by agriculture during October and November. Comparing the average monthly water pollution flow rates desired by agriculture with the average monthly flow rates from the lake shows that there is a one-to-one correlation between changes in the water pollution emission rate and changes in the flow rate from the lake.

Figure 94 shows the average monthly lake level for the ten-year simulation. The results indicate that the peak lake level occurs in May while the minimum lake level occurs in November. The lake level is highest in the spring because of an accumulation of runoff from the spring rainfall, low lake evaporation rates until June and the fact that water is coming into the dam at a faster rate than leaving the lake during the late winter and spring months (compare Figure 93 with Table 43). The decrease in the lake level from May until November is produced by

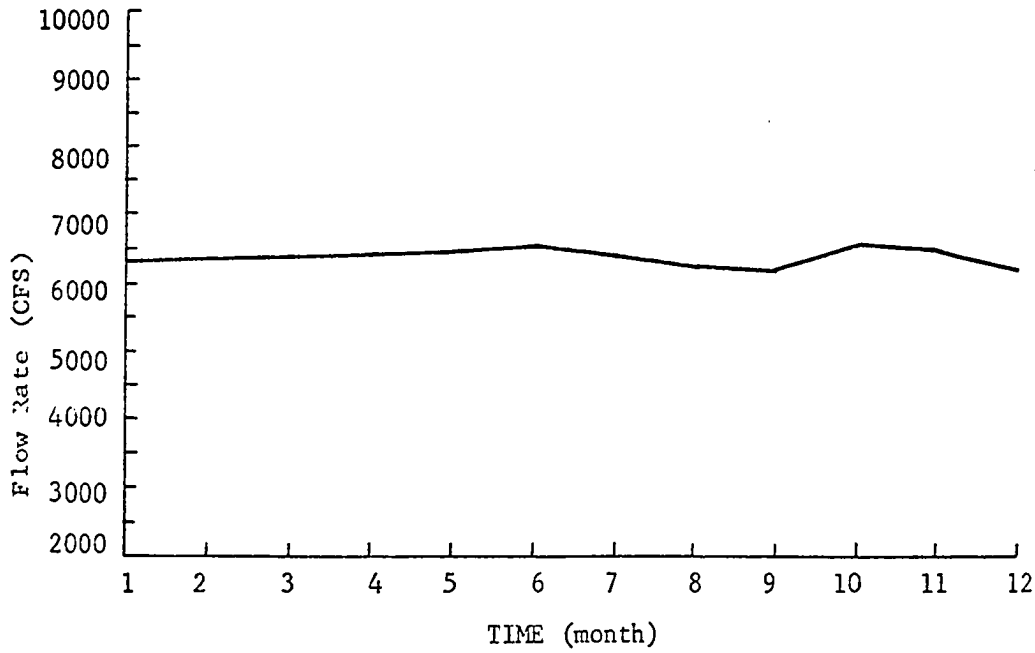

Fig. 93. The average monthly values of the flow rates in the river just below the lake are presented for the ten year simulation.

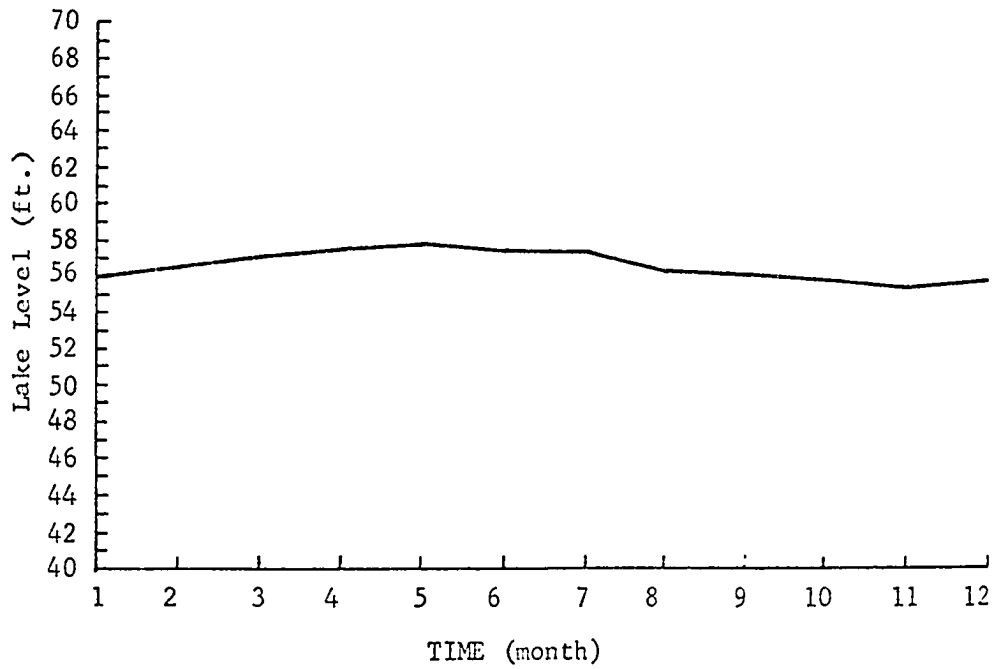

Fig. 94. The average monthly lake level is presented for the ten year simulation.

high lake evaporation rates during the summer, relatively low rainfall during the period, and an increase in the water demand by agriculture.

Figure 95 presents the average yearly demand for water by the consumer and water pollution by agriculture. The water demand by industry and the city shows a continuous increase with time. The increase in the water demand by the city is produced by a 20% increase in the population of the city, while the increase in the industrial water needs is caused by a 50% increase in the number of industries. The increase in the city population and the number of industries are estimated by looking at the results of the control case study for the Urban Model presented in Appendix C. The demand for agriculture irrigation water shows minor ossilation within the ten-year period. Years with relatively low demand for irrigation water have more favorable soil moisture conditions. The ten-year trend for desired water pollution emission rates by agriculture shows significant year to year variation which are caused by changes in the average number of cattle in the feedlots. In particular, years #2, #6 and #9 have the highest average number of cattle because the e are years when the grazing cattle are prematurely removed from the grazing area and put in the feedlots (see Table 47).

The ten-year trend in the lake level (Figure 96(b)) shows that the lake level decreases continually with greatest decrease occurring from year 4 to year 7. The lake level then stabilizes in the ninth and tenth year. The decrease in the lake level is caused by an increase in the water demand by the city and industry and also because the lake is loosing more water by evaporation than it is gaining from storm runoff.

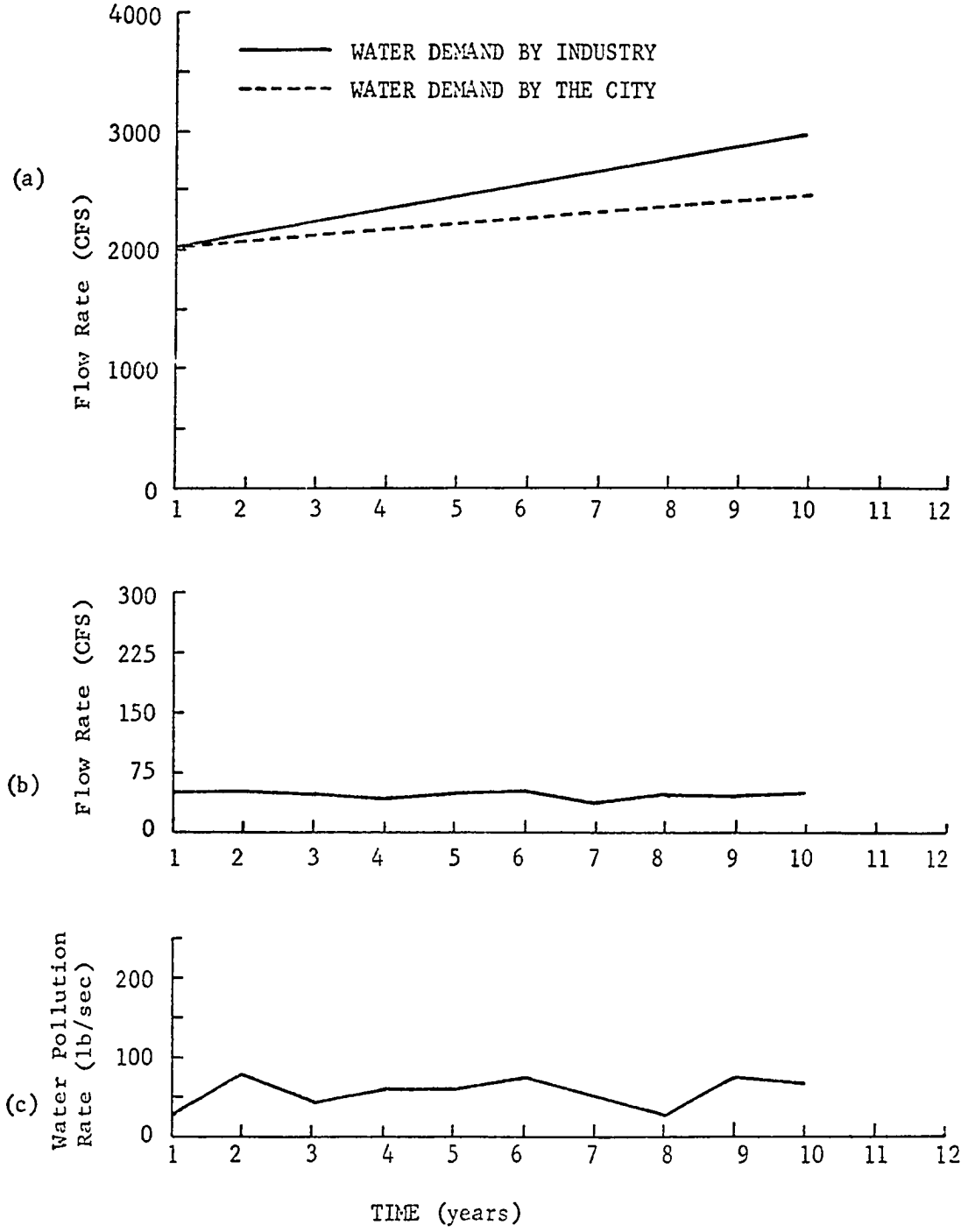

Fig. 95. The average yearly demand for water by the city and industry (a), by agriculture (b) and the demand for water pollution by agriculture (c) is presented for the ten year simulation.

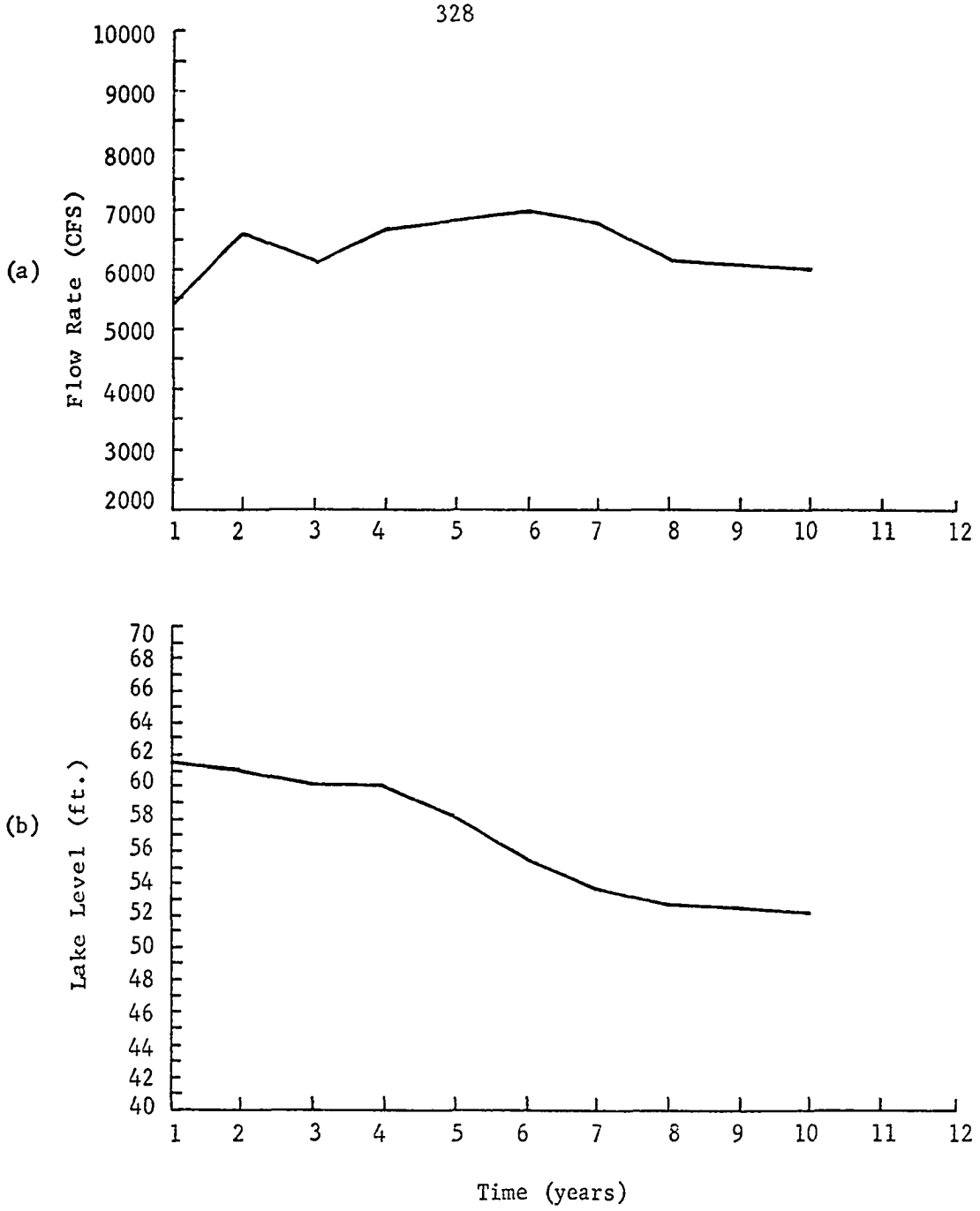

Fig. 96. The average yearly water flow rate below the dam (a) and the average yearly lake level (b) are presented for the ten year simulation.

The sharp decrease in the lake level from year 4 through year 6 corresponded very well with the sharp increase in the flow of water from the lake (see Figure 96(a)). The increase in the water flow from the dam is to a greater extent caused by the increase in the water demand by the city and industry. The leveling off of the lake level after year 7 is produced because a continued decrease in the lake level triggers a mechanism in the water control model that limits the amount of water allowed to flow out of the dam. Thus, by the tenth year, the water permitted to flow from the dam is limited to such an extent that the lake level is stabilizing.

Figure 96 (a) presents the average flow rate of water from the lake. In the first 6 years there is a general increasing tendency in the water flow from the dam. This increase is caused by the steady increase in the water demands by industry and the city (Figure 95). There is a temporary decrease in the water flow from the dam in year 3 which is caused by a significant decrease in the annual water pollution rate desired by agriculture (see Figure 95). The decrease in the flow rate from the dam after year 6 is produced by the decrease in the lake level that automatically limits the amount of water permitted to flow out of the dam. The interaction between the flow rate from the dam and the lake level tends to stabilize the flow rate from the dam and the lake level.

Figure 97 shows the ten-year trend in the average annual ratio of the water received by the consumers to the water desired by the consumer, and the ratio for the water pollution emission rate permitted by agriculture to the water pollution rate desired by agriculture.

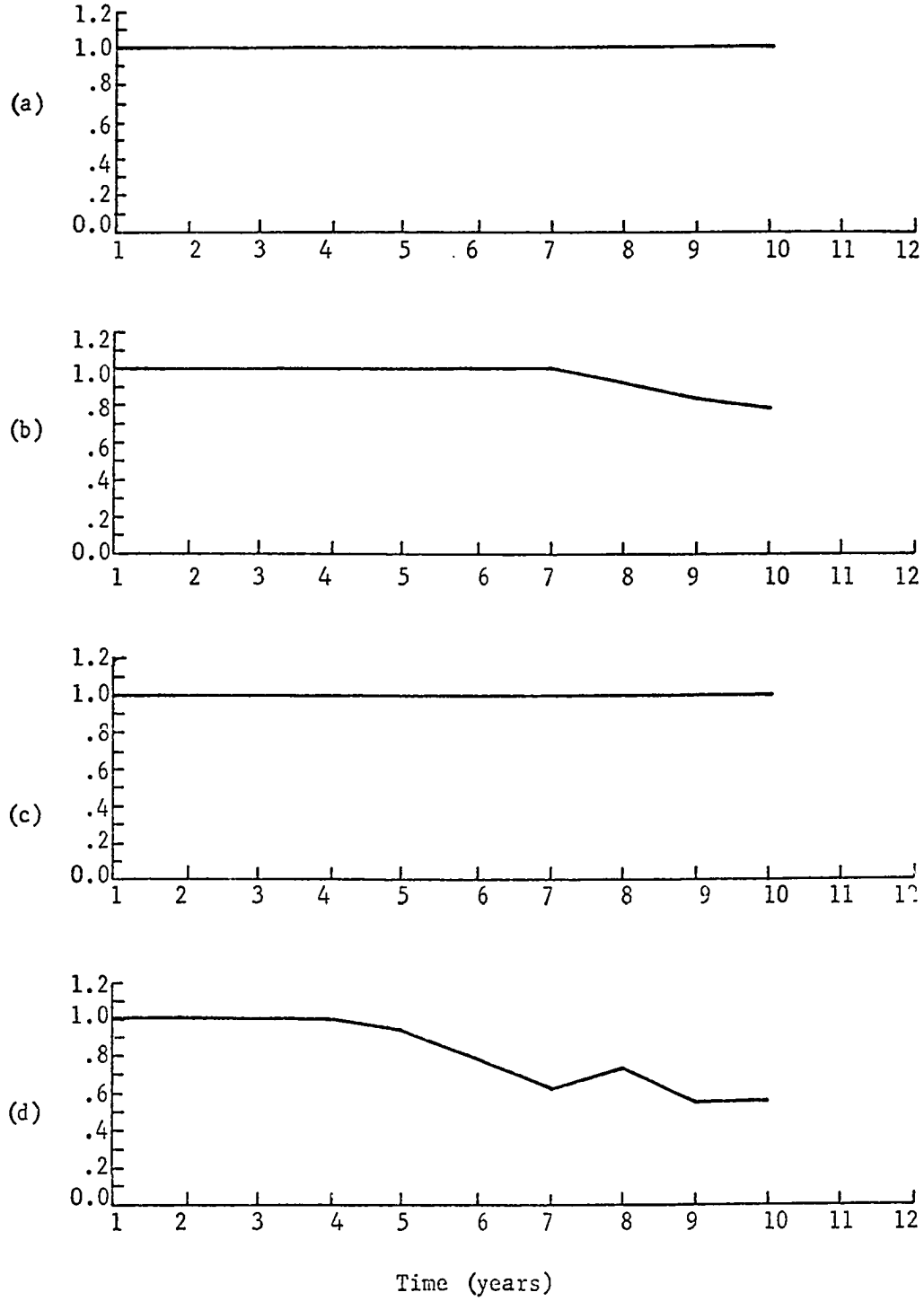

Fig. 97. The average yearly values of the ratio of water received by the city, industry and agriculture to the water desired by the city (a), industry (b), and agriculture (c) and also the ratio of the water pollution allowed by agriculture to the water pollution desired by agriculture (d) is presented for the ten year simulation.

The results show the ratio of the water used to the water desired for city use and agricultural irrigation remains at 1 for all ten years. Thus during the ten-year period the water needs for the city and agricultural irrigation are completely satisfied. The ratio for industrial water demand is one for the first seven years and then continued to decrease steadily for the next three years. The reduction of available water flow from the lake is responsible for this decrease. The ratio of the water pollution emission rate permitted to the water pollution emission rate desired by agriculture stay at 1 for the first four years and then decreases to .55 by the tenth year. A temporary increase in the ratio during year 8 (see Figure 95) is caused by a significant reduction in the average number of feedlot cattle for that year. It is interesting to note that the ratio of the water pollution received to the water pollution desired by agriculture is the first ratio to be affected by limiting the water supply, while the ratio of the water received to the water desired by industry is the second ratio to be influenced.

In a real life situation, the fact that industry is not allowed to have the water supply needed, would possibly cause industry to close down some operations and to move to a more favorable area. This could have a devastating effect upon the economy of the city. Similarly, not permitting the feedlot to pollute the water at the desired rate would cause the feedlot to reduce the number of cattle maintained in the feedlot or to develop a technology for reducing the water pollution caused by the feedlot.

Range Management Submodel

The range management model is tested by performing a rudimentary sensitivity analysis on the decision theory part of the submodel and also by observing the influence of the range management decisions upon a ten-year simulation of the model. The sensitivity of the decision theory aspect of the range management model is performed by running numerical experiments in which different cost matrices and the climatology matrices are used to determine optimal strategies. Five different case studies are run in the numerical experiment, with case study #1 being the control case study. Case study #2 shows the effect of increasing the cost of moving the cattle, case study #3 demonstrates the effect of increasing the cost of not moving the cattle, case studies #4 and #5 illustrate the effect of changing the climatology matrix. The parameter values and the matrices used by the decision theory process are illustrated for the different case studies in Tables 44 and 45. The cost matrix, climatology matrix, the probability matrix presented for case study #1 are used for the running version of the total ecosystem model. Table 46 shows the optimal decision theory strategies as a function of soil moisture categories for the 5 different case studies. The results for case study #1 show that for soil less than 1.25" the optimal strategy is to move the cattle while with soil moisture greater than 1.25" the optimal strategy is to keep the cattle in the same location. This means that with soil moisture greater than 1.25 inches the grass field grass is likely to grow enough grass to provide food for the grazing cattle. With the soil moisture less than 1.25" this is not likely. The decision to move or not to move the

TABLE 44

The cost, climatology and probability matrices used in the sensitivity analysis of the range management model are presented.[1]

CASE #1 Control Case

COST MATRIX

States of Nature	Decision 1	Decision 2
1	0	20
2	1	10
3	15	10
4	20	10
5	30	10

CLIMATOLOGY MATRIX

States of Nature	Soil Moisture for the Following Month 1	2	3	4	5
1	.10	.15	.20	.35	.20
2	.10	.15	.30	.30	.15
3	.10	.25	.30	.20	.15
4	.20	.30	.30	.10	.10
5	.25	.30	.30	.10	.05

PROBABILITY MATRIX For the States of Nature

States of Nature	
1	.20
2	.20
3	.20
4	.20
5	.20

CASE #2 (Increase cost of moving)

COST MATRIX

States of Nature	Decision 1	Decision 2
1	0	30
2	1	20
3	15	20
4	20	20
5	30	20

CASE #3 (Increase cost of not moving)

COST MATRIX

States of Nature	Decision 1	Decision 2
1	0	20
2	10	10
3	20	10
4	30	10
5	40	10

TABLE 44 continued

	Soil Moisture for the Following Month				
	1	2	3	4	5
CASE #4 (Less diagonal climatology matrix)					
1	.10	.20	.25	.25	.20
2	.10	.15	.25	.25	.25
3	.10	.25	.25	.25	.15
4	.20	.25	.25	.20	.10
5	.25	.25	.20	.20	.10

	Soil Moisture for the Following Month				
	1	2	3	4	5
CASE #5 (More diagonal climatology matrix)					
1	.10	.15	.20	.25	.30
2	.10	.10	.25	.35	.20
3	.08	.25	.34	.25	.08
4	.25	.30	.25	.15	.05
5	.35	.25	.15	.15	.10

Decision #1 Do not move the cattle	Categories of Soil Moisture (inches of water in the top 24")
Decision #2 Move the cattle	#1 SM .5" #2 .75 SM .5 #3 1.25 SM .75 #4 2.00 SM 1.25 #5 SM 2.0

[1]The matrices presented for the control case study are used for the other case studies unless another matrix is presented in this table.

TABLE 45

The Average Monthly Change in Soil Moisture from the Beginning of the Month to the End of the Month

Jan	Feb	Mar	Apr	May	Jun	Jul	Aug	Sep	Oct	Nov	Dec
+.4	+.6	+.6	+.4	+.4	-.4	-.8	-.6	+.6	+.4	+.4	+.4

The values presented in this table are used to estimate ΔSML in Equation 75 in the main text.

TABLE 46

Optimal Strategies

	Soil Moisture During the Next Month				
	1	2	3	4	5
Case #1 Control Case	2	2	2	1	1
Case #2 (Increase cost of moving)	1	1	1	1	1
Case #3 (Increase cost of not moving)	2	2	2	1	2
Case #4 (Less diagonal climatology matrix)	2	2	2	1	1
Case #5 (more diagonal climatology matrix)	2	2	2	1	1

1 - No Movement of Cattle

2 - Move Cattle

Categories of Soil Moisture

#1 SM < .5"

#2 .75 > SM ≥ .5

#3 1.25 > SM ≥ .75

#4 2.00 > SM ≥ 1.25

#5 SM ≥ 2.0

grazing cattle is made when there is insufficient grass for grazing in the field where the cattle are located. A decision to keep the cattle in the field means that the grass field where the cattle are located is able to grow enough grass to support the herd if it is left ungrazed for a month, while the cattle are fed cut grass in a closed area within the grass field. A decision to move the cattle means that the grass field is unlikely to grow sufficient grass to support the cattle and therefore should be moved. The effect of increasing the cost of moving the cattle is simulated in case study #2 and the results show that the optimal strategy is to keep the cattle in the field they are located for any soil moisture conditions. The optimal strategy indicates that it costs less to keep the cattle in the present grazing field and feed them cut grass if there is sufficient grass for grazing. Case study #3 simulates the effect of increasing the cost of keeping the cattle in a field when there is insufficient grass for them to eat. The results show that for all of the soil moisture categories, except #4, the optimal strategy is to move the cattle from the field they are grazing. In cases #4 and #5 the climatologic matrices are changed to see if the optimal strategies are sentitive to variation of this matrix. In case #4 the probability for the states of nature is independent of soil moisture, while in case #5 the probability for the states of nature is highly correlated to soil moisture. The results show that for both cases the optimal strategies predicted by the decision theory model are identical with the optimal strategies of the control case (case #1), thus indicating that this model is fairly insensitive to changes in the climatology matrix.

The results of a ten-year simulation of the total ecosystem model are used to demonstate the effect of the range management model upon the location of the grazing cattle herd during the summer months. Table 47 shows the location of the grazing herd during each month of the ten-year simulation. The grazing herd is placed on the grazing field in April and are then controlled by the range management submodel until the end of September. The cattle will remain on the grazing areas from April until the end of September if there is sufficient forage. At the end of September the cattle are automatically placed in the feedlots. The range management model has several options that can be used in managing the cattle. These include:

1) moving the cattle to another field when the forage is insufficient in the field where the cattle are located,
2) feeding the cattle cut grass for a month while the grass field they are located in grows enough grass to support them,
3) moving the cattle to the feedlot when there is insufficient forage to support the cattle in either of the two grazing fields.

The results for the first year show that the grazing cattle are placed in field #3 for April, May and June and are then transferred to field #4 for the rest of the grazing period. The transfer of the cattle from field #3 to field #4 is initiated because of the depletion of forage in field #3. In year #2 the cattle are then placed on field #3 for April and May and are then transferred to the feedlots. This premature transfer of cattle to feedlots is initiated because both grazing fields

TABLE 47

Status of Grazing Cattle Herd

Time on the Range

Years	Jan	Feb	Mar	Apr	May	Jun	Jul	Aug	Sep	Oct	Nov	Dec
1	2	2	2	3	3	3	4	4	4	2	2	2
2	2	2	2	3	3	2	2	2	2	2	2	2
3	2	2	2	3	3	3	4	4,5	4,5	2	2	2
4	2	2	2	3	3	3	4	4	4	2	2	2
5	2	2	2	3	3	1	3	3	4	2	2	2
6	2	2	2	4	4	2	2	2	2	2	2	2
7	2	2	2	4	2	2	2	2	2	2	2	2
8	2	2	2	3	3	3	4,5	4,5	4,5	2	2	2
9	2	2	2	4	1	4	3	2	2	2	2	2
10	2	2	2	4	4	2	2	2	2	2	2	2

Code

#1 - Cattle are fed cut forage in the grazing area

#2 - Cattle are placed in the feedlots

#3 - Cattle are grazing in field #3

#4 - Cattle are grazing in field #4

#5 - No cattle are in the feedlot

did not have sufficient forage to support the cattle.

In studying the results of the range management decisions upon the deployment of the cattle, two predominant patterns emerge. Pattern #1 is the location of the cattle in one field for the first few months and then the transfer of the cattle to the other grazing field for the remainder of the normal grazing sequence. In Pattern #2 the cattle are placed on a grazing field for the first two or three months and are then transferred to the feedlot. The amount of rain occurring during the spring and early summer months is the dominant factor in deciding which of the two patterns will occur. A year in which the spring and early summer rainfall is above normal will provide enough soil moisture for sufficient growth of the grass so that the cattle will not run out of grass during the grazing period. Below normal rainfall in the spring and early summer does not provide the soil moisture needed to grow the amount of forage required by cattle herd for the complete grazing period. In general, the rainfall that occurs in April, May and June decides which range management pattern will evolve.